Numerical Analysis of Crack Induced Debonding Mechanisms in FRP-Strengthened RC Beams

by

Agostino Monteleone

A thesis
presented to the University of Waterloo
in fulfilment of the
thesis requirement for the degree of
Master of Applied Science
in
Civil Engineering

Waterloo, Ontario, Canada, 2008

Author's Declaration

I hereby declare that I am the sole author of this thesis. This is a true copy of the thesis, including any required final revisions, as accepted by my examiners.

I understand that my thesis may be made electronically available to the public

ABSTRACT

The continual deterioration of infrastructure has motivated researchers to look for new ways of repairing and monitoring existing structures. A particularly challenging problem confronting engineers in the revival of the infrastructure is the rehabilitation of reinforced concrete (RC) structures. Traditionally, the repair of RC beams has been achieved by bonding steel plates to the structure. Although this technique has proven to be reasonably effective, it has several distinct disadvantages such as susceptibility of the steel plates to corrode and the excessive weight of steel plates when used in long-span beams. Recently, there has been an emergence of structural engineering applications employing fibre reinforced polymer (FRP) composites as an alternative to steel plates. FRP composites are well known for their high strength- and stiffness-to-weight ratios, corrosion resistance, durability, and ease of application. Numerous studies have been conducted to prove the efficiency of bonding FRP on structural elements. In spite of this, industrial practitioners are still concerned about premature debonding of the plates before reaching the desired strength or ductility. Premature debonding initiates from the ends of the plate or from intermediate cracks (IC) in the concrete. While end initiated debonding and peeling mechanisms have been researched extensively, researchers have unanimously recognized the lack of data for the FRP-RC structural members subjected to IC debonding. The scarcity of data compiled exemplifies the need to develop more refined numerical analysis tools to reduce the high cost and significant time required to conduct full-scale physical testing.

In this study, the results of a comprehensive numerical investigation are presented to assess the failure mechanisms caused by different types of flexural and shear crack distributions in RC beams strengthened with FRP composites. The model is based on damage mechanics modeling of concrete and a bilinear bond-slip relationship with softening behaviour to represent

the FRP-concrete interfacial properties. A discrete crack approach was adopted to simulate crack propagation through a nonlinear fracture mechanics based finite element analysis to investigate the effects of crack spacing and interfacial parameters such as stiffness, local bond strength, and fracture energy on the initiation and propagation of the debonding and structural performance. Results from the analysis reveal that the debonding behaviour and load-carrying capacity are significantly influenced by interfacial fracture energy and crack spacing. The debonding propagation is mainly governed by mode II fracture mechanisms. The results provide an insight on the long-term behaviour of a repair system that is gaining widespread use and will be of interest to researchers and design engineers looking to successfully apply FRP products in civil engineering applications.

Acknowledgments

My most grateful appreciation goes to Professor S. Potapenko for his knowledgeable insight, continuing patience and motivating words, without which this thesis would not have been possible.

A special thanks to both Professor S. Walbridge and J.R. Craig for taking the time to review the thesis.

Finally, I would especially like to thank my parents and family for their love and support throughout my studies. They have always wholeheartedly supported me in all my endeavours and for this I am truly grateful.

Table of Contents

List of Tables

CHAPTER 2

CHAPTER 5

CHAPTER 6

List of Figures

CHAPTER 2

CHAPTER 3

CHAPTER 4

CHAPTER 5

CHAPTER 6

Notation

a	crack length
b	member's width
[B]	strain-displacement matrix
b_c	width of concrete
b_f	width of FRP plate
b_p	width of FRP
C	inverse of the gradient of the load-deflection curve
[C]	material properties (constitutive) matrix
c_m	thickness of concrete cover
d	degradation variable
d_p	distance between the top of the beam to the centre of the plate
d_v	viscous stiffness degradation variable
$\dot{d}_v$	viscous stiffness degradation rate variable
$d\lambda$	scalar plastic multiplier
{D}	load vector
$[D]^{el}$	degraded elastic stiffness
$[D]_0^{el}$	initial (undamaged) elastic stiffness
E	elastic modulus
E_c	elastic modulus of concrete
E_p	elastic modulus of FRP
$F\left(\tilde{\sigma}, \bar{\varepsilon}^{pl}\right)$	yield function
F_p	plate force
F_u	ultimate load of the un-repaired beam
F_{ur}	ultimate load of the FRP repaired beam
f_c'	concrete compressive strength
f_c''	peak concrete compressive stress
f_t'	ultimate tensile stress
G	shear modulus
G	flow potential
G_{IIC}	critical strain energy release rate for the interface
H_p	strain-hardening parameter
[*I*].	unit matrix.
I_c	cracked equivalent moment of inertia of composite beam
k	constant
K	element stiffness
[K]	global stiffness matrix
L_e	effective bond length
l_{dev}	bond development length
M_e	applied bending moment at transition point
N_i	Lagrangian interpolation shape functions

p/a	length-to-shear span ratio
$\overline{p}$	effective hydrostatic pressure
P	applied load
P_u	ultimate bond strength
P_λ	row matrix
{q}	global displacement vector
$\overline{q}$	Von Mises equivalent effective stress
$\overline{q}_{(CM)}$	ratio of second stress invariant on compressive meridian
$\overline{q}_{(TM)}$	ratio of second stress invariant on tensile meridian
R	external forces
{R}	global stiffness matrix
s_N	normal deviatoric stress
s_τ	shear deviatoric stress
$\overline{\mathrm{S}}$	deviatoric part of effective stress tensor
t	thickness
t_n^0	peak value of normal traction
t_s^0	peak values of shear traction
t_p	thickness of FRP plate
T_0	original thickness of interface element
u_o	crack width at ultimate tensile strength
u_{ot}	ultimate crack width
w_p	width of FRP plate
x	distance from the top of the beam to the neutral axis
g,h,r	local element coordinate system position
u, v, w	local displacement as a function of nodal displacements
x, y, z	global coordinates as a function of local position
α	dimensionless material constant
β_w	effective width of FRP-to-concrete
δ_m^f	effective displacement at complete failure
$\delta_m^{\max}$	maximum value of the effective displacement
δ_m^0	effective displacement at initiation of damage
ε	total strain
{ε}	element strain vector
ε^{el}	elastic strain
ε^{pl}	inelastic (plastic) strain
ε_{cu}	maximum strain in concrete
$\tilde{\varepsilon}_c^{pl}$	equivalent compressive plastic strain
$\tilde{\varepsilon}_t^{pl}$	equivalent tensile plastic strain

$\dot{\varepsilon}_c^{pl}$	equivalent compressive plastic strain rates
$\dot{\varepsilon}_t^{pl}$	equivalent tensile plastic strain rates
$\dot{\varepsilon}_v^{pl}$	viscoplastic strain rate tensor
γ	dimensionless material constant
θ	temperature
σ_c	uniaxial compression
σ_f	axial stress in the FRP plate
σ_m	maximum tensile stress
σ_m	mean normal stress
σ_t	uniaxial tension
σ_{to}	uniaxial tensile stress at failure
$\bar{\sigma}_{eff(c)}$	effective uniaxial cohesion compressive stress
$\bar{\sigma}_{eff(t)}$	effective uniaxial cohesion tensile stress
$\hat{\bar{\sigma}}_{max}$	maximum principle effective stress
τ	shear stress
ν	Poisson's ratio
μ	viscosity parameter
э	eccentricity
ψ	dilation angle
Ω	domain over which integration is preformed

1 INTRODUCTION

1.1 BACKGROUND

In recent year, there has been an increased need for the strengthening or rehabilitation of reinforced concrete (RC) structures, due to the aging of infrastructure, demand for higher vehicle loads, updates in design codes or inadequate original design. An effective method for increasing the capacity of RC beams is through the use of externally bonded reinforcement. Traditionally, steel plates have been bonded on the soffits of beams to raise their flexural strengths. However, over the last two decades, the application of fibre reinforced polymers (FRP) as external reinforcement has received much attention from the structural engineering community. FRP plates or laminates are preferred over steel plates mainly due to their high tensile strength, high strength-to-weight ratio and corrosion resistance. Due to their light weight, field use of FRP plates or fabrics requires less labour and equipment, resulting in shorter periods of disruption to services. Although the material costs may be high, they can be offset by the low installation and long-term maintenance costs.

The main problem associated with FRP strengthened RC beams is premature debonding or peeling of the plate from the existing structure before reaching the desired strength or ductility. This form of failure is unique to plated structures and despite the fact that this observation has been made by various researchers, there exists a lack of literature focused on developing a rational and consistent model to accounts for factors that control debonding and the interfacial behaviour during the debonding process. The lack of such understanding may hinder the wide scale implementation of FRP repair methods in rehabilitating or strengthening existing structures. To help overcome this drawback, this study looks into clarifying the debonding

behaviour, failure mechanisms, and interfacial properties that limit the composite system from achieving its desired goal.

1.4 RESEARCH OBJECTIVES AND SCOPE

The principal objectives and scope of this investigation are as follows:

- To provide a detailed review of the state-of-the-art in FRP strengthening RC structures.
- To develop an efficient and sound numerical model to simulate global and interfacial behaviour in the strengthened composite.
- To investigate how load capacity, debonding behaviour and failure mechanisms are influenced by various flexural crack distributions in FRP strengthened RC beams.
- To investigate the effect of normal and shear stress concentrations developed at the toe of intermediate cracks and establish a clear understanding how they influence failure.
- To investigate how interfacial parameters influence debonding and strengthening, and incorporate these findings into practical engineering applications.

1.3 OUTLINE

This report is divided into seven chapters and an appendix. The remaining six chapters are organized as follows:

Chapter 2 – presents a state-of-the-art review of the existing work on FRP applications in structural strengthening critical to this study.

Chapter 3 – provides an overview of the numerical approach employed in the study, constitutive laws used to model of each, and formulations used to model the interaction between the materials.

Chapter 4 – outlines the finite element modelling approach, verification of the finite element model, and any special modelling considerations and modifications made to the calibrated model.

Chapter 5 – presents a numerical investigation to study FRP debonding under the presence of various flexural crack distributions along the concrete beam. The main parameters investigated in this chapter are crack spacing, interfacial stiffness, local bond strength, and fracture energy.

Chapter 6 – presents a numerical investigation in study FRP debonding induced under mixed-mode fracture behaviour. Interfacial properties such as initial shear stiffness, initial normal stiffness, bond strength and fracture energy are examined through a detailed parametric study.

Chapter 7 – summarizes conclusions from the investigation, contributions, engineering implications of findings, and recommendations for further research.

2 LITERATURE REVIEW

2.1 INTRODUCTION

Due to the many advantages of using FRP as external reinforcement for RC members, extensive research has been carried out regarding their performance. To expedite the use of FRP in field applications, numerous experiments were required to buildup a database of results, leading to large volumes of published literature regarding such tests. Much of the earlier research focused on flexural strengthening, where FRP laminates are bonded to the top or bottom of the beams in the maximum moment region. The number of experiments in which the FRP is bonded on the beam webs as shear reinforcement has also increased in recent years. In addition to studying the global response of strengthened beam, researchers have focused their attention on the local behaviour at the interface where premature failures initiate. In spite of the numerous experimental studies that have been achieved over the last two decades, the disagreement among researchers over analytical and numerical modelling techniques indicates that much further research is required before a widely acceptable model emerges. As for numerical modelling employing the finite element (FE) method, successful attempts have been reported in the area of flexural strengthening, while models simulating crack propagation and debonding are limited in number. The following presents an overview of the characteristic of FRP, field applications, common modes of debonding failure, and comprehensive review of notable research in the field of FRP-RC specimens.

2.2 MECHANICAL PROPERTIES OF FRP

FRP are composite materials obtained by reinforcing a polymer matrix with fibrous materials such as glass or carbon. The most common FRP in civil engineering are glass fibre reinforced polymers (GFRP), carbon fiber reinforced polymers (CFRP), and aramid fiber reinforced

polymers (AFRP). When combined with a matrix, these fibres have the ability to enhance a structure's load-carrying capacity. Strength related properties mainly depend on the fiber volume, mechanical properties of constituents, and procedures used to fabricate the composites. Typical properties of matrix materials and fibers are given in Tables 2.1 and 2.2, respectively. The properties of composites are shown in Table 2.3. Final performance of FRP can be controlled to generate a wide range of physical and mechanical properties for the composite materials.

Material	Density	Modulus of elasticity in tension E_t	Strength in tension f_t	Strength in compression f_c	Poisson's Ratio ν	Co-efficient of thermal expansion α
	kg/m^3	MPa	MPa	MPa		$10^{-6}/°C$
Polyester	1200-1400	2500-4000	45-90	100-250	0.37-0.40	100-120
Epoxy	1100-1350	3000-5500	40-100	100-250	0.38-0.40	45-65
P.V.C	1400	2800	58	-	-	50
Nylon	1140	2800	70	-	-	100
Polyethylene	960	1200	32	-	-	120

Table 2.1: Typical matrix properties (Mufti, 1991).

Material	Density	Modulus of elasticity E	Strength in tension f_t	Strain in tension ε_t
	kg/m^3	MPa	MPa	%
E-Glass	2500	70000	1500-2500	1.8-3.0
S-Glass	2500	86000	4800	-
High-Modulus Carbon	1950	380000	2000	0.5
High-Strength Carbon	1720	240000	2800	1.0
Carbon	1400	190000	1700	-
Boron	2570	400000	3400	-
Graphite	1400	250000	1700	-
Kevlar49	1450	120000	2700-3500	2.0-2.7
Kevlar	1450	60000-130000	2900	-

Table 2.2: Typical fibre properties (Mufti, 1991).

Material	Fibre content	Density	Modulus of elasticity in tension E_t	Strength in tension f_t
	% by weight	kg/m^3	MPa	MPa
Unidirectional GFRP/Polyester laminate	50-80	1600-2000	20000-50000	400-1250
GFRP/Polyester Randomly Oriented Hand lay-up	25-25	1400-1600	6000-11000	60-180
GFRP/polyester Material Metal Dye	25-50	1400-1600	6000-12000	60-200
GFRP/Polyester Woven Roving Hand Lay-ups	45-62	1500-1800	1200-2400	300-350
Sheet Molding Compound, Unidirectional Laminate	20-25	1750-1900	9000-13000	60-100
Carbon/ Epoxy	70	1930	120000	800
Aramid/ Epoxy	50-80	-	70000-80000	1000-1400

Table 2.3: Typical mechanical properties of GFRP and CFRP (Mufti, 1991).

2.2.1 Advantages of FRP over Conventional Materials

Traditionally, the repair or rehabilitation of RC beams has been achieved by bonding steel plates to the beams (Ross et al., 1999). Although this technique has proven to be reasonably effective, it has several disadvantages such as the susceptibility of steel plates to corrode and excessive weight used in long-span applications. Recently, FRP plates have become an attractive alternative due to its superior characteristics such as:

- high strength and stiffness-to-weight ratio
- long-term durability
- ease of fabrication
- low maintenance costs
- high strength is feasible as elevated temperatures
- oxidation, corrosion and fire resistant
- high impact resistance (high fatigue properties)
- potential for cost savings as large components can often be carried out at lower costs than metals.

The ease of application of FRP composites has made them extremely attractive for use in civil infrastructure applications, especially in cases where dead weight, space, or time restrictions exist.

2.2.2 Applications of FRP

FRP are commonly used an external reinforcement in civil engineering applications for new construction and rehabilitation of deteriorating structures.

Application of FRP in New Construction

Recently, FRP has been introduced in construction mainly as internal reinforcement in the form of reinforcing bars, grid reinforcement, and pre-stressing tendons. FRP bars can substitute conventional steel reinforcement and utilize its lightweight, corrosive resistant, high strength and durable properties.

Application of FRP in Rehabilitation

FRP is a proven material for the repair and rehabilitation of deteriorating structures. Structural rehabilitation involves:

- seismic retrofit
- repair of damaged structures
- strengthening of structural members

Techniques adopted for rehabilitation are (Teng et al., 2002):

- wrapping of columns to provide lateral confinement and enhanced ductility
- wrapping of flexural members for strengthening and deflection control

In terms of field applications, Japan has been reported to be leading the way in number of beams rehabilitated with FRP laminates, followed by Switzerland (Meier and Winistorfer, 1995). As more knowledge is being generated through comprehensive research and testing, the use of FRP in Canada and the US is rapidly increasing. The use of carbon fiber for structural applications was first studied at the Swiss Federal testing Laboratories (EMPA) (Meier and Winistorfer, 1995). The first application using CFRP laminates involved the repair work of a pre-stressed concrete bridge in Lucerne, Switzerland in 1991, where several steel tendons were severed when the bridge was drilled to mount new traffic signs. The bridge was strengthened with four CFRP

sheets 150 mm wide and 5.0 m long, epoxy-bonded to the tension face of the span. Approximately 6.2 kg of CFRP was used instead of 175 kg of steel.

A bridge deck in Hiyoshikura on the Tokando Highway, Japan, required strengthening to increase the load rating of the structure in 1994. The bridge deck consisted of a reinforced concrete deck supported by steel girders, where the soffit of the deck was affected by considerable cracking. As part of the surface preparation, all cracks were sealed before application of FRP and a total area of 164 m^2 was covered with two plies of CFRP placed parallel and perpendicular to the roadway. The bridge was monitored after completion using strain gauges and test results revealed a 30 to 40% reduction in tensile strains in the steel reinforcement (Nanni, 1995).

CFRP laminates were chosen as a cost saving alternative in a shear-strengthening project of ten pre-cast concrete girders on a bridge in Edmonton, Alberta, Canada during 1996. The three-span bridge spanned a total length of 18 meters and ten girders wide. The utilization of FRP helped to reduce downtime for repair from one month (if conventional external steel was used) to 16 days and the cost of repair was reduced from $100,000 (for repair with external steel stirrups) to $70,500 (Alexander and Cheng, 1996).

2.3 FAILURE MODES IN FRP STRENGTHENED BEAMS

Over the last two decades, a great deal of experimental studies has been focused on RC beams strengthened with FRP plates. The main reason for the introduction of FRP laminates into structural engineering applications was to replace the heavy and corrosive-prone steel plates traditionally used for the flexural strengthening of RC beams (Wong, 2001). Thus, a significant amount of research has been conducted in an effort to gain a better understanding of the flexural

and local behaviour of RC strengthened beams. Different failure modes of RC strengthened beams using FRP laminates have been reported and summarized as follows:

1. FRP Rupture – Flexural failure with yielding of longitudinal steel reinforcing bars followed by rupture of FRP as shown in Figure 2.1.

Figure 2.1: FRP rupture

2. Crushing of Concrete – Crushing of compressive concrete before or after yielding of tensile steel without any damaged to the FRP laminate as shown in Figure 2.2.

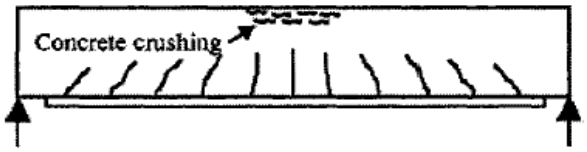

Figure 2.2: Crushing of concrete

3. Concrete Shear Failure – In practical applications, the plate bonded to the concrete substrate does not extend to the support of the beam. This may lead to the formation of a nearly vertical crack that might initiate at the plate-end and propagate as an inclined shear crack as shown in Figure 2.3.

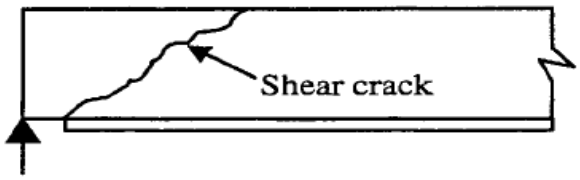

Figure 2.3: Concrete shear failure

4. Concrete Cover Separation – A common failure mode that usually results from of the formation of a crack at or near the end of the plate, due to the high interfacial shear and

normal stress concentrations caused by the abrupt termination of the FRP plate. Once a crack occurs in the concrete near the plate-end, the crack will propagate to the level of tensile reinforcement and extend horizontally along the bottom of the tension steel reinforcement (Garden and Hollaway, 1998). With increasing external load, the horizontal crack may propagate to cause the concrete cover to 'peel-off' with the FRP plate as shown in Figure 2.4.

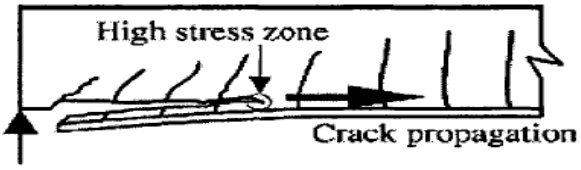

Figure 2.4: Concrete cover separation

5. Plate-End Interfacial Debonding – Failure occurs in the concrete adjacent to the concrete-adhesive interface and is generally believed to be the result of high interfacial shear and normal stresses near the plate-end that exceeds the strength of the weakest element, usually concrete (Smith and Teng, 2002). This mode involves the failure at the adhesive-fiber interface and usually has a very thin layer of concrete attached to the fiber after failure as shown in Figure 2.5.

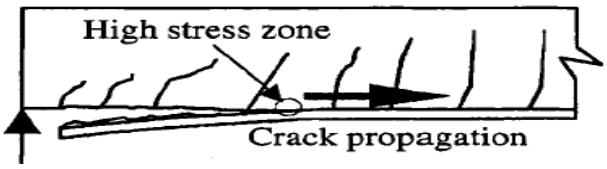

Figure 2.5: Plate-end interfacial debonding

6. Intermediate (Midspan) Crack Induced Debonding – Failure is by crack propagation in the concrete parallel to the bonded plate and adjacent to the adhesive-to-concrete interface, starting from the critically stressed portions towards one of the ends of the plate

(Bizindavyi and Neale, 1999). It is believed to be the result of high interfacial shear and normal stresses concentrated at a crack along the beam as shown in Figure 2.6.

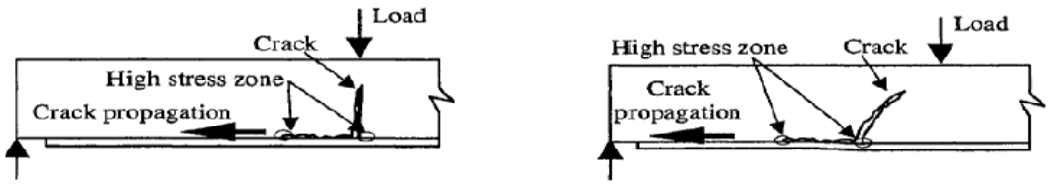

Figure 2.6 - Flexure or flexure/shear (diagonal) crack induced interfacial debonding.

Generally, FRP rupture and concrete crush can be regarded as flexural failures where the full composite action between concrete and FRP is achieved. Failure modes such as concrete cover separation, plate-end debonding and intermediate crack-induced debonding are regarded as local failures where the composite action between concrete and FRP is lost and prevents the strengthened beam from reaching its ultimate flexural capacity due to debonding. Thus, local failures must be considered in design to ensure structural integrity.

2.4 FLEXURAL FAILURES

Flexural failures, such as FRP rupture and concrete crushing, have been studied extensively since the 1990s. While earlier studies were predominately experimental, more recent investigations have been focused on analytical or numerical modeling. This section will review the work that has been undertaken pertaining to flexural failures.

Arduini and Nanni (1997) conducted a parametric analysis to investigate the effects of FRP on strength and failure mechanisms of repaired RC beams. The analysis aimed to investigate the effect of FRP parameters such as stiffness, bond length, thickness and adhesive stiffness when employed as a repair material. An analytical model used in a previous study published by the authors was used herein that employs constitutive laws for four constituent materials: concrete, reinforcing steel, FRP laminate, and the adhesive. Compressive concrete is

nonlinear and influenced by the confinement action due to closed stirrups according to CEB-FIB Model Code 90 (Arduini and Nanni, 1997). Tensile concrete is bilinear elasto-softening, reinforcing steel is bilinear elasto-hardening, and FRP and adhesive are perfectly linear elastic. The authors suggest that the model is capable of detecting the mode of failure that occurs in the strengthened RC beam if the conditions in Table 2.4 are met. The results of the analysis are shown in Figure 2.1 in terms of ultimate load of the FRP repaired beam (F_{ur}) to the ultimate load of the un-repaired beam (F_u). Four curves for a given FRP stiffness at the variation of the FRP bonded length-to-shear span (p/a) ratio are provided. The results indicate that for p/a values less than 0.65, there is no practical benefit in repairing the beam for strength, since $F_{ur}/F_u \approx 1$. Points on the diagram at FRP thickness values of 0.0, 0.1, 0.5, 1.0, and 2.0 mm are labeled with a letter that indicates the type of failure where R, S, and D represent FRP rupture, shear-tension, and debonding failure, respectively. When no FRP material is used ($\tau_p = 0$), the dominant failure mode is concrete crushing. When the thickness of FRP is 0.1 mm, the dominant failure mode is rupture of the FRP, independent of the p/a ratio. For the FRP thickness of 0.5mm, rupture of the FRP is only obtained for the case of p/a equal to 0.95mm. In all other cases, shear-tension failure is dominant leading to a brittle and therefore undesirable result. The authors also reported that employing a higher FRP stiffness reduces deflection at service loads. However, the occurrence of shear-tension or debonding failure no longer make it possible to increase the flexural capacity of the member by increasing the FRP stiffness and/or thickness.

Table 2.4: Failure mechanism detection as per Arduni and Nanni (1997) model.

Condition	**Failure Mechanism**
Ultimate strain of material is reached	FRP Rupture
Shear stress, τ, reaches τ_u	Shear Failure
Maximum tensile stress, σ_m ,reaches f_t	Tensile Fracture of Concrete
Ultimate tensile strain, $\epsilon_{u,}$ is reached	Local Adhesive Failure

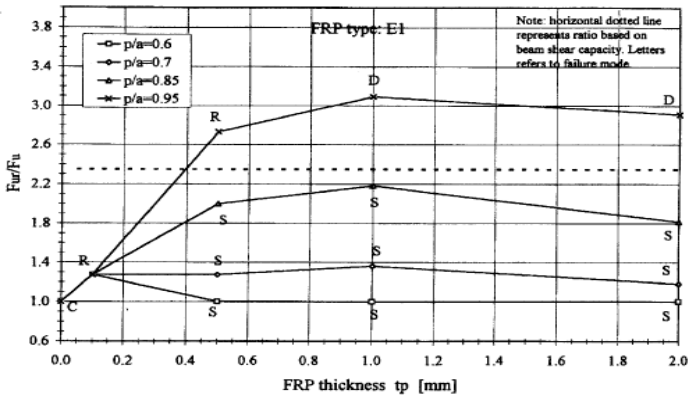

Figure 2.7: Ratio of F_{ur}/F_u vs FRP plate thickness (Adruini and Nanni, 1997).

The behaviour of RC beams strengthened with GFRP laminates was investigated by Grace et al. (1999). Each of the 14 simply supported rectangular cross-section beams were initially loaded above its cracking load. The cracked beams were strengthened with GFRP laminates and then tested until complete failure. Two strengthening systems were used in this research project using different arrangements of GFRP sheets to reinforce the beams for flexure, and the combination of flexure and shear. The reinforcing ratio at their midsection was kept constant to investigate how vertical layers of reinforcement affect their flexural failure modes. The first system was strengthened for both flexure and shear with vertical GFRP layers extending 0.15L from each support towards the midspan. The second system was strengthened in a similar manner except that each vertical layer was extended to cover half the span. The first system failed in a tensile mode by rupture of the GFRP sheets, while the second system failed in a compressive mode by crushing of concrete as shown in Figure 2.8. The authors reported that two vertical layers extending across the side of the beam, as in the second system, affected the mode of failure. Rupture lines experienced in the GFRP sheets on both sides of the first system were only present in the span between the two vertical layers. The elimination of the span in-between the two vertical layers, as in the second system, eliminates these rupture lines. The

authors concluded that the presence of vertical layers of FRP sheets limits the propagation of cracks to the un-strengthened area of the beam and prevents rupture in the flexural strengthening fibers.

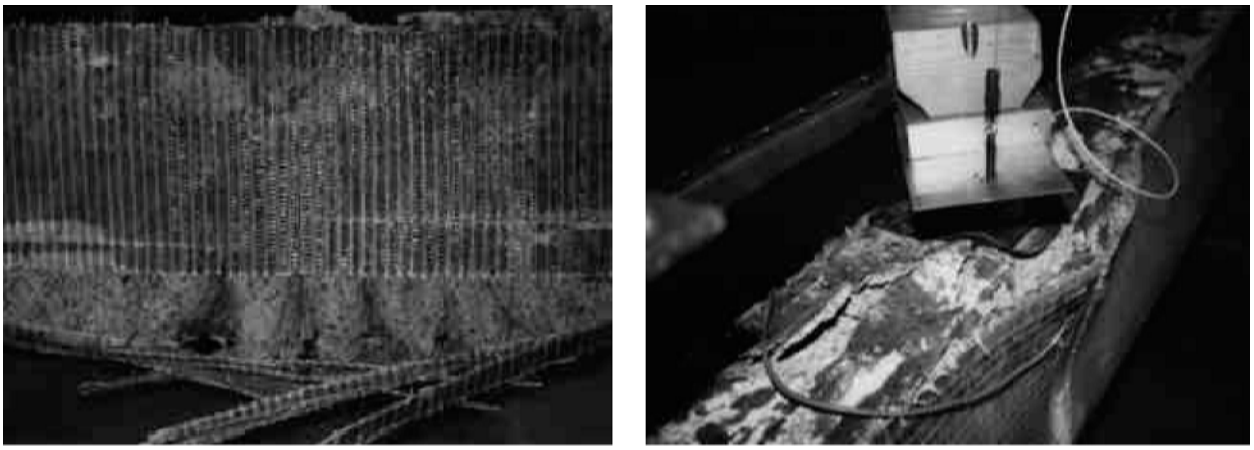

Figure 2.8: Failed section of beams (a) FRP rupture; (b) Crushing of compressive concrete (Grace et al., 1999).

An experimental program was carried by Ross et al. (1999) to test large-scale RC beams strengthened in flexure with three-ply uniaxial CFRP laminates. Based on experimental observations, an inelastic section analysis procedure was developed to predict the load-displacement response of retrofitted beams. The results were then compared with those obtained from a nonlinear FE analysis. The experimental study consisted of twenty-four rectangular concrete beams divided into six groups of four, according to their percentage of flexural reinforcement, ρ. For beams that were lightly to moderately reinforced with longitudinal steel (reinforcement ratio less than 1.5%), failure was dominated by delamination between the CFRP plate and the adhesive layer, otherwise known as mode II failure. For the heavily reinforced beams (reinforcing ratio's ranging from 1.8 to 3.3%), failure was dominated by crushing of the concrete in the compression zone accompanied by horizontal cracking in the tension zone in the vicinity of the reinforcing steel, commonly known as mode I failure. An elastic-plastic section analysis was used to produce the load-deflection curves for the beams tested. A multi-linear

load-displacement relationship is illustrated in Figure 2.9, where each element is divided into four regions and terminated by a similarly numbered point. The points defining the load-displacement curve were determined using appropriate assumptions for the beam's behaviour within each region. A trilinear curve is used to approximate the stress-strain behaviour of concrete, an elastic-plastic response is assumed for steel, and CFRP is considered linear elastic until failure. Point 4 in Figure 2.9 is not expected to necessarily reach its calculated value, but serves to determine the slope of the load-displacement curve in region 4. This is attributed to the likelihood that concrete may crush before FRP fails or the FRP may debond at the FRP-adhesive interface (due to inadequate bond strength) or at the concrete-adhesive interface (due to low she shear strength). A nonlinear FE analysis was then conducted using the commercial software ADINA to assess the results from the experimental study and inelastic sectional analysis. The model was comprised of a two-dimensional, eight-node plane stress element to represent concrete, and three-node truss elements to represent reinforcing steel and FRP plates. A hypo-elastic model based on a uniaxial stress-strain relation was employed to represent concrete and take into account biaxial and triaxial conditions. Material models for reinforcing steel and FRP are the same as those employed in the sectional analysis. The load displacement curves obtained from the FE analysis are compared with the results from the section analysis and experimental tests as shown in Figure 2.10a and b for the lightly reinforced and heavily reinforced beams, respectively. Although both predicted curves are close to the actual response, the expected behaviour in region 4 is not achieved in the experimental results. This is attributed to the delamination of the FRP plate in the beams with the lower reinforcement ratio. For the more heavily reinforced beams, failure induced by crushing of concrete in the compression zone results in the inability of the beam to transfer significant load to the FRP plate and use its high

strength capacity (Ross et al, 1999). In an attempt to prevent delamination and utilize the full capacity of the plate, the authors suggested the use of an anchorage system. Thus, it was concluded that the most important parameter affecting the beam's response is the bond strength between concrete and FRP.

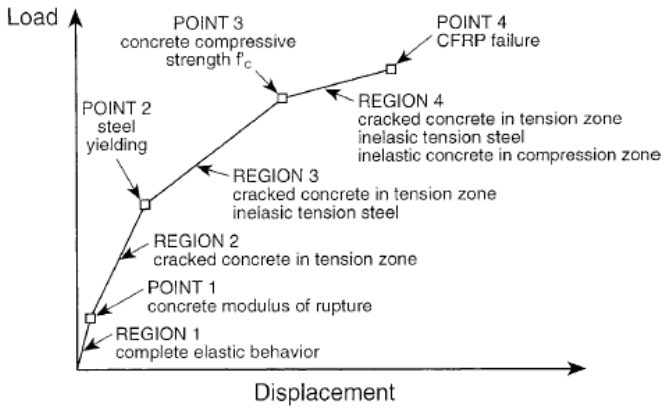

Figure 2.9: Load-displacement assumptions used in beam section analysis (Ross et al., 1999).

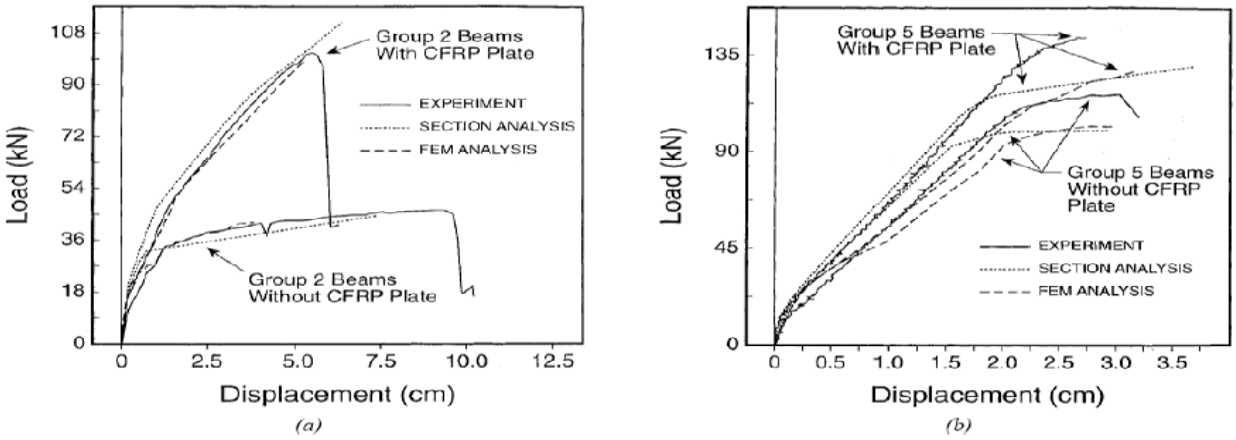

Figure 2.10: Comparison of load-deflection curves for (a) Lightly-reinforced RC beams; (2) Heavily-reinforced RC beams (Ross et al., 1999).

2.6 LOCAL FAILURE

Local failures are commonly referred to as concrete cover separation, plate-end debonding and intermediate (midspan) crack-induced debonding. In RC-strengthened beams, tensile forces develop in the bonded plate and are transferred to the original beam via interfacial shear and

normal stresses. Consequently, debonding failure may occur at plate-ends or cracks along the beam due to combination of high shear and normal interfacial stresses. A review of previous studies focusing on concrete cover separation, plate-end debonding, intermediate crack-induced debonding, and interfacial stresses across the adhesive layer are presented in this subsection.

2.6.1 Concrete Cover Separation

Shear failure of the concrete cover between the steel reinforcement and FRP laminates can lead to the separation of the FRP plate. In this case, debonding typically starts from the end of the plate where high interface shear stresses arise. Delamination from the anchorage zone occurs when the interface shear stress reaches a limiting value, which is defined as a function of concrete compressive strength. This value has been reported to be approximately 8 MPa for normal strength concrete (Triantafillou and Plevris, 1991).

An analytical formulation to predict the ultimate load of CFRP-plated beams due to concrete cover separation was presented by Ngujen et al. (2001). This model is based on the composite action of the RC beam and FRP plate. Whereas plate debonding results from high local bond stresses and peeling forces near the FRP plate ends in the adhesive interface, the critical stresses for ripping of concrete are at the flexural steel level after shear cracks have developed at the plate ends. The shear crack causes an eccentricity between the tensile forces in the FRP plate and in the steel bars, leading to the ripping out of the concrete cover. Based on experimental results, the authors divided the composite behaviour of the FRP-RC beam at ultimate load into three zones: (1) a "de-stressed" zone at the end of the plate where strains are approximately zero, (2) a "bond-development" zone where strains increase linearly, and (3) a "composite" zone where the plate acted compositely with the beam as illustrated in Figure 2.11. It was concluded that if the plate strain at the transition point between the "bond-development"

and "composite" zones was limited to a critical value (0.0017 in this case), ripping failures could be prevented. The axial strain in the plate at the transition point (ε_{pe}) is given as:

$$\varepsilon_{pe} = \frac{1}{E_c}\frac{M_e}{I_C}(d_p - x) \tag{2-1}$$

where:

M_e – applied bending moment at transition point

E_c – elastic modulus of concrete

I_c – cracked equivalent moment of inertia of composite beam

d_p – distance between the top of the beam to the centre of the plate

x – distance from the top of the beam to the neutral axis

The location of the transition point from the plate-end is determined by the bond development length (l_{dev}), which is determined by:

$$l_{dev} = c_m + \frac{d_p}{2} + \frac{4.61}{\lambda}, \qquad \lambda^2 = \frac{1}{E_p t_p}\frac{G_a G_c}{G_c t_a + G_a c_m} \tag{2-2}$$

where:

c_m – thickness of concrete cover

E – elastic modulus

G – shear modulus

t – thickness

Subscripts p, a, and c represent the FRP plate, adhesive layer, and concrete, respectively. The total bond length was found to be independent of the applied load, length of plate, and shear span. When provided a plate strain limit from simple bond tests, the two equations given above can be used to predict the failure load of the beam due to concrete cover separation.

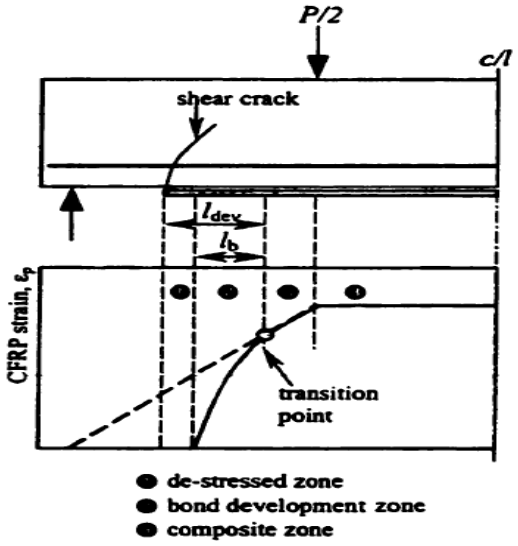

Figure 2.11: Composite model of concrete beam bonded with FRP plate (Ngujen et al., 2001).

Yang et al. (2003) modelled the behaviour of an FRP-strengthened RC beam by using a discrete crack based FE analysis. A mixed-mode linear-elastic fracture mechanics program was developed to automatically simulate multiple discrete crack propagation during the entire loading process, including the concrete cover separation and ultimate collapse of the structure. Four-node quadrilateral isoparametric elements and three-node constant strain elements were used to model the concrete, adhesive, and FRP plate. The internal steel reinforcement was modelled using two-node truss elements. Figure 2.12(a) illustrates loading at early stages where many uniformly spaced cracks initiate in the tension side of beam. The cracks found in the midspan grew quickly and migrated upward past the reinforcing steel, while new cracks simultaneously initiated between major cracks as shown in Figure 2.12(b). As the load continues to increase, a number of flexural cracks propagate close to the compression zone roughly in the direction towards the loading point and form flexural-shear cracks. The cracks initiated from the plate-end have now developed into major cracks with the greatest width. At the intersection between this crack and tension steel reinforcement, a new horizontal crack is initiated as shown in Figure

2.12(c). As this major crack continues to widen, the horizontal crack starts to propagate very quickly along the interface between the concrete cover and the tension steel reinforcement. Very little change occurs in the other cracks once the horizontal crack starts to propagate rapidly. The beam soon fails when the horizontal crack intersects with existing major flexural shear crack resulting in concrete cover separation failure, as shown in Figure 2.12(d). The predicted failure process was verified with experimental results published by He et al. (1995) and was found to be in good accord.

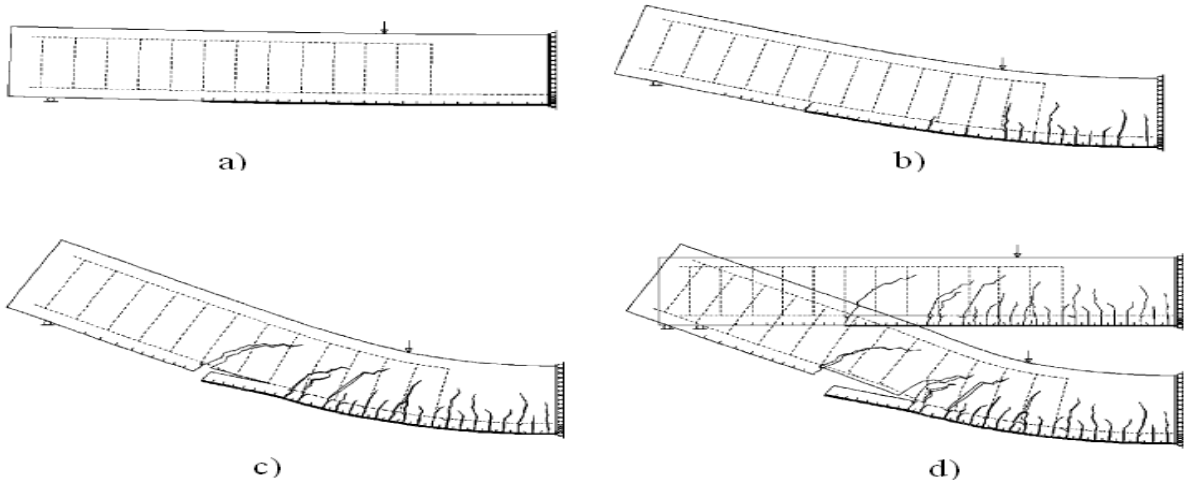

Figure 2.12: Plated beam displacement and cracking behaviour: (a) uniformly spaced cracks; (b) migration of major cracks and initiation of new cracks; (c) initiation of horizontal crack; (d) plate-end delamination (Yang et al., 2003).

2.5.2 Plate-End Debonding

The most frequent and studied type of failure is the delamination of FRP laminate and adjacent concrete cover due to normal and shear stress concentrations at the end of the bonded plate. When the FRP composite on the beam soffit is subjected to tensile forces, the adhesive layer is loaded in shear to provided shear connection between concrete and FRP. Therefore, the crack propagation will be similar to fracture mode II. The critical strain energy release rate for the interface (G_{IIC}) is given by Triantafillou and Plevris (1991) as:

$$G_{IIC} = \frac{kP^2}{b}\frac{\partial C}{\partial a} \tag{2-3}$$

where:

k – a constant

P – applied load

b – member's width

C – inverse of the gradient of the load-deflection curve

a – crack length

Fracture occurs when the value G_{IIC} is reached, and the load causing debonding can then be found.

A closed form analytical model to predict the distribution of shear and normal stress concentrations at the plate cutoff point was presented by Malek et al. (1998). The model assumes linear-elastic and isotropic behaviour of all materials, complete composite action between plate and concrete (i.e. no slip), and employs discrete crack propagation. The proposed method was verified by comparing with a finite element analysis using ABAQUS. Good agreement was found between the results for both the interfacial shear and normal stress, as shown in Figure 2.13.

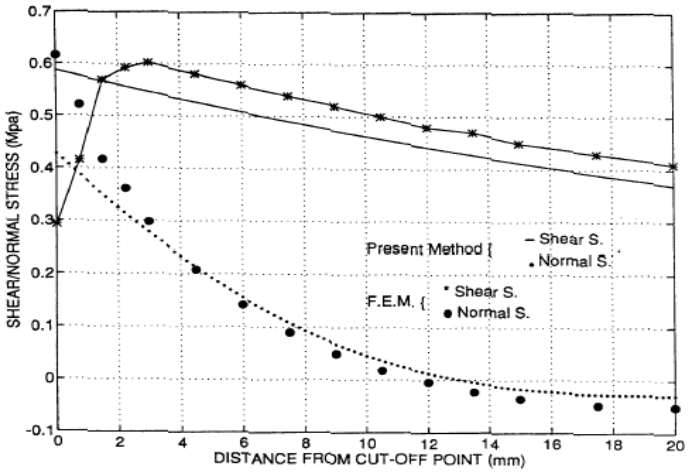

Figure 2.13: Comparison of the stresses around the cutoff point in a larger scale (Malek et al. 1998).

The applicability and reliability of existing analytical techniques to predict brittle plate debonding that occurs in RC beams strengthened with FRP laminates was critically assessed by Mukhopadhyaka and Swamy (2001). The authors reported that the analytical models proposed by other researchers such as Roberts et al. (1989), Roberts (1989), Arduni and Di Leo (1996), Taljesten (1997), Malek et al. (1998), are too complex for use in practical design, and produce inconsistent results when compared with all available experimental published results. These findings indicated an urgent need to take a fresh look and approach toward the problem of plate-end debonding. Whereas the majority of analytical models proposed by other researchers predicted shear and normal stress concentrations near the FRP plate ends, Mukhopadhyaka and Swamy (2001) present uses of interface shear stress, as later defined in Chapter 4, to predict plate debonding failures. The concept of the interface shear stress is based on a limiting value of shear stress between the concrete and FRP plates which becomes critical near the plate cut-off end as shown in Figure 2.14 and can be calculated from:

$$\tau = \frac{F_{P2} - F_{P1}}{(\Delta L) t_p w_p} \tag{2-4}$$

where:

F_p – plate force

$\Delta L = L_2 - L_1$

t_p – thickness of plate

w_p – width of plate

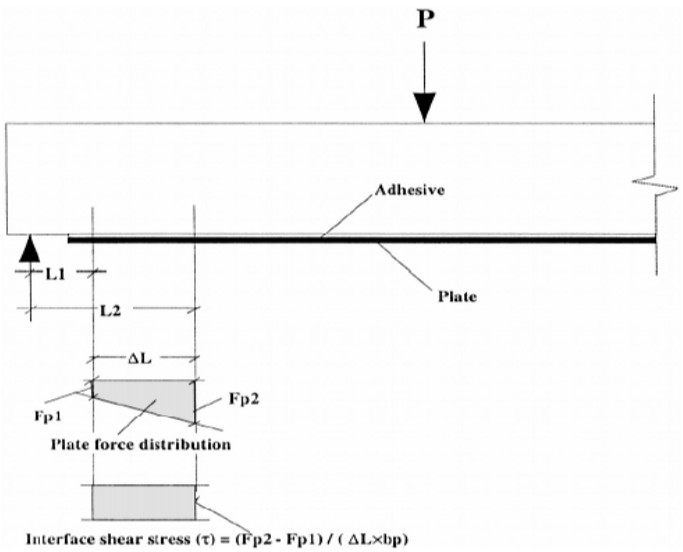

Figure 2.14: Interface shear stress between bonded plate and concrete (Mukhopadhyaka and Swamy, 2001).

An extensive review of all major publications in which FRP debonds at the cut-off point was conducted and it was found that the critical interface shear stress varied between 0.33 and 1.35 MPa for CFRP plates, and from 0.26 to 0.90 MPa for GFRP plates. The publications were further analyzed by the authors to investigate the effects of concrete strength, FRP stiffness, moment resistance capacity, and size of beam in relation to the interface shear stress. The concrete strength was found to have a minimal increase on the interface shear stress value as shown in Figure 2.15a. As the stiffness and relative moment contribution of the FRP plates increased, the interface shear stress also increased as shown in Figure 2.15b and c. It was reported that plate debonding is more likely to take place in beams with a depth to width ratio of 2.0 or more, or in beams with a shear span to depth ratio greater than or equal to 6.0. The authors stated that further research is required before this new design approach can be implemented.

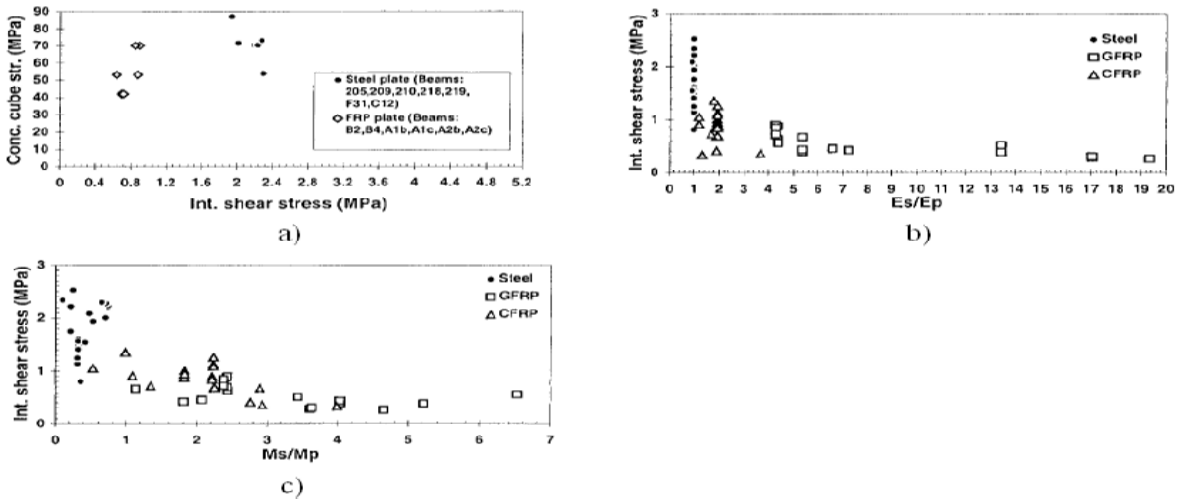

Figure 2.15: Interface shear stress plot vs: (a) Concrete strength; (b) FRP stiffness; (c) FRP moment resistance; (Mukhopadhyaka and Swamy, 2001).

An experimental program designed to study interfacial shear stress concentration at plate curtailment of FRP-RC beams was carried out by Maalej and Bian (2001). Specifically, this study looks at the relationship between CFRP plate thickness and the internal shear stress concentration at cut-off points, the failure modes of CFRP-strengthened beams, and the efficiency of the CFRP external reinforcing system. The experimental program included five rectangular beams where one beam, *beam 1*, was used as control and the other four, *beams 2 to 5*, were strengthened in flexure using one, two, three, and four layers of externally bonded CFRP. The beams were tested in four-point bending over a simple span with strain gauges installed on the longitudinal and transverse reinforcement. Two types of failure modes were observed in the CFRP-strengthened beams: CFRP tensile rupture (beam 2) and plate-end delamination starting at one of the CFRP cut-off points (beams 3, 4, 5). The load-deflection curves for beams 1 to 5 are shown in Figure 2.16. Despite having larger areas of CFRP external reinforcement Beams 4 and 5 did not exhibit larger strength gains than that for Beam 3. The beams with lesser number of CFRP layers displayed higher deflection capacities. This indicates that there exists an optimum

thickness of CFRP for which the ultimate load-carrying capacity of the beam becomes a maximum. This can be attributed to two competing effects that would influence ultimate load carrying capacity of the beam as the CFRP thickness increases. The first effect decreases the tensile load in the CFRP plate at failure due to the reduction in average CFRP stress at midspan. The second increases it as a result of increased area of CFRP. The reduction in load carrying capacity in beams 4 and 5 due to premature failure can be explained by the inability of thick FRP plates to maintain strain compatibility throughout their bonded length. At small loads there is an inherent tendency for the CFRP plate to deform while maintaining strain compatibility on the cross section. This tendency results in interfacial shear and normal stress concentrations at areas of discontinuities such as FRP cut-off points. This requirement to maintain cross-sectional strain compatibility becomes more stringent as the thickness of the FRP and/or the imposed deflection is increased due to high interfacial shear and normal stress concentration (Maalej and Bian, 2001). The authors suggest predicting interfacial shear and normal stress concentration as functions of displacement rather than loads in the future.

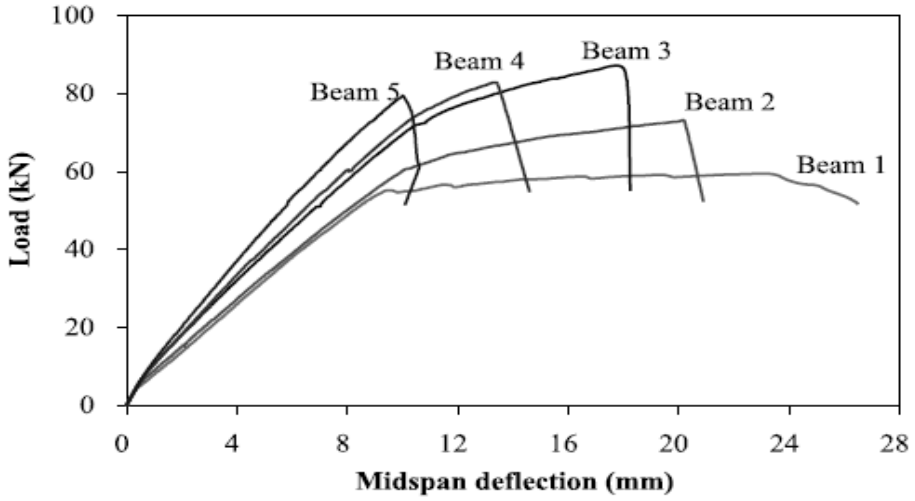

Figure 2.16: Summary of load-deflection curves (Maalej and Bian, 2001).

2.5.3 Intermediate Crack-Induced Debonding

Delamination can occur either at the end of an externally applied reinforcing plate or at the location of a crack in a concrete beam. While previous researchers have assumed delamination to start at the end of the bonded plate, flexural/shear cracks commonly found on the tensile side of the concrete beam tend to open and induce high interfacial shear stress under loading.

Sebastian (2001) drew attention to experimental data that revealed the existence of another critical debond mode found in concrete cover delamination: midspan debonding. Results from an experimental program out of Bristol University were reviewed in which several large-scale FRP-plated concrete beams were tested in four point bending. To initiate flexural cracks in the midspan region, a crack inducer in the form of a thin lubricated steel shell was placed vertically at the midspan section of the beam. Corrosion of the reinforcement was simulated by reducing in section all the longitudinal steel bars over a short length symmetric to the midspan. The data reveals that midspan debond action is triggered by high shear stresses transmitted from the plates to the concrete cover as shown in Figure 2.17. Initially, these stresses arise from tension stiffening in the cracked concrete and corrosion of the embedded steel. Soon after initiation, the midspan debond process is self-propagating before failure, as shown in Figure 2.18.

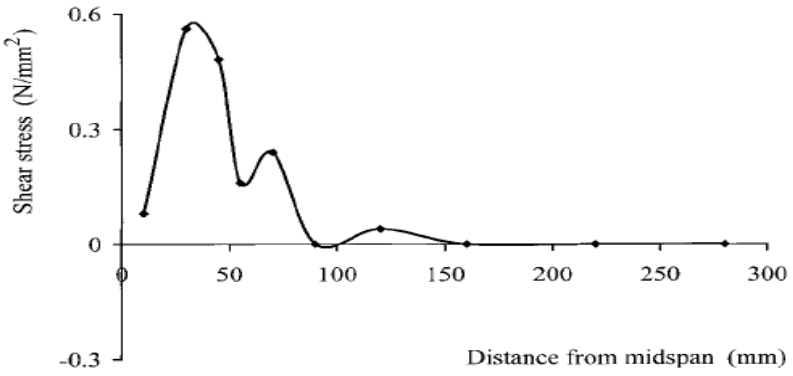

Figure 2.17: Shear bond stress the midspan (Sebastian, 2001).

a) b)

Figure 2.18: Debonding failure: (a) Inclined cracks and concrete fracture near midspan before failure; (b) Soffit of beam at midspan after failure; (Sebastian, 2001).

Leung (2001) performed an analysis on the delamination initiated at the bottom of a crack in a retrofitted RC beam. An analytical model was developed to simulate the interfacial stresses at the vicinity of the crack. The model was first developed to relate the bridging stress in a plate to the crack opening width. Then, fracture mechanics based equations are set up relate moment, crack length, and crack width. By solving these equations, the variation of maximum interfacial shear stress, τ_{max}, with the applied moment for various combinations of material and geometric parameters can be obtained. Predictions from the model were compared with finite element analysis and found to be in good agreement. The results indicate that delamination is favoured by large crack space, low adhesive thickness, low plate stiffeners, and small contact area between the plate and adhesive.

A study to investigate the debonding behaviour and failure mechanisms caused by multiple or distributed flexural cracks in FRP-strengthened RC beams was conducted by Niu and Wu (2005). To clarify how the debonding mechanism is affected by different types of crack distributions in concrete, a series of parameters such as crack spacing, local bond strength, initial interfacial stiffness, and interfacial fracture energy are varied to investigate the corresponding

effects on the interfacial debonding behaviour and load-carrying capacity. A nonlinear fracture mechanics-based FE model was developed to carry out the study. For simplicity, stirrups, which are used to ensure beams do not fail in shear, were not considered in the simulations. The model was comprised of a discrete crack model for concrete crack propagation and a bilinear bond-slip relationship with softening behaviour to represent FRP-concrete interfacial behaviour. In their finite element model, the final debonding failure occurs when debonding of the FRP plate passes through two flexural cracks with spacing equal to the effective bond length. It was found that the crack spacing had a significant effect on the debonding mechanism and the ultimate load capacity. If the FRP bond length is longer than the effective bond length, the ultimate load capacity is similar to that of the beam failure by debonding from only a single flexural crack. Figure 2.19 illustrates the reinforcement stresses for various crack spacing at the midspan. For the case of the crack spacing larger than the effective transfer length of the FRP sheets, the debonding mechanism and structural performance are similar to that of the case with a single localized crack. Once yielding occurs in the reinforcing bars, FRP stresses increase at a much higher rate until it becomes constant when interfacial debonding occurs. The large crack spacing facilitates the debonding propagation along the FRP-concrete interface allowing the stresses to remain constant until final debonding failure. For the beam with small crack spacing, a higher load carrying capacity is obtained due to stress redistribution in the FRP plate after cracking.

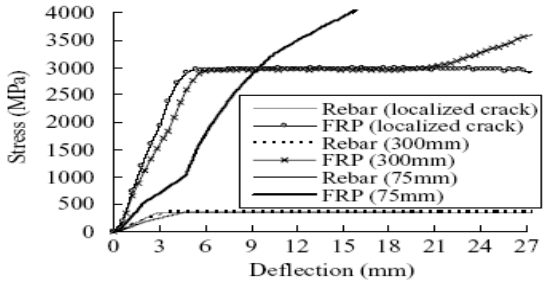

Figure 2.19: Reinforcement stresses vs. deflection for various crack spacing (Niu and Wu, 2005).

2.5.4 Diagonal Cracks

Kishi et al. (2005) developed a three-dimensional elasto-plastic finite element model to simulate the load-carrying capacity of FRP-RC beams failed in sheet plate-end debonding due to the opening of a critical diagonal crack (CDC). Interface elements were used to model geometrical discontinuities due opening of dominant cracks, slipping of rebar, and debonding of the FRP sheet. To investigate the effects of CDC on the load-carrying capacity a comparison between the response of the strengthened beam with and without a CDC was preformed. The results shown in Figure 2.20 clearly demonstrate that the presence of the CDC critically influence the debonding behaviour of the FRP sheet. In the case without considering CDC, the applied load increases linearly after rebar yielding and there is no tendency for the FRP sheet to debond until rupture. When including the CDC, it is clear that the opening of the crack limits the load-carrying capacity by prompting debonding failure. The authors suggest restraining the initiating and/or the widening of a CDC to improve the load-carrying capacity and ductility of RC beams.

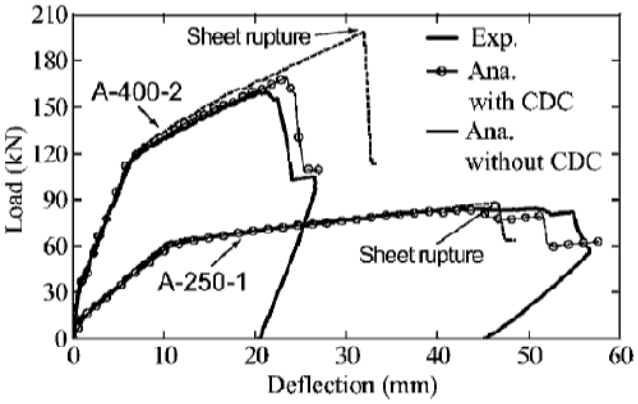

Figure 2.20: Load-deflection curves for analysis with and without CDC (Kishi et al., 2005).

An investigation into debonding mechanisms caused by diagonal macro-cracks in concrete was performed by Niu et al. (2006). Using interfacial bond behaviour observed through previously conducted experiments, a FE model was developed using the commercially available

program DIANA-8. The concrete beam was modeled with 3-node triangular and 4-node quadrilateral plane stress elements; the FRP was modeled using 2-node beam elements while the crack planes and FRP-interfaces were modeled using zero-thickness interface elements. A midspan flexural crack and two diagonal flexural-shear cracks were modeled using the discrete crack approach to simulate crack growth and discontinuity under three-point loading. A linear shear stress-slip relationship with softening behaviour is adopted to model the FRP-concrete interfacial behaviour. Since the primary emphasis of the study was to clarify debonding mechanisms caused by diagonal macro-cracking, shear retention was neglected once the crack widens. The authors investigated the effects of interfacial bond strength and revealed that this parameter substantially affects pre-cracking, post-cracking, and debonding initiation response until final failure. A set of four bond strength values, 0.5, 2, 8, and 16 MPa, were used to obtain the load-deflection curve found in Figure 2.21. The first two values, 0.5 and 2 MPa, represent low interfacial bond strengths which leads to premature crack opening, lower overall strengthen capacity, and low rates of stress transfer. This results in debonding from the midspan crack without the occurrence of the diagonal crack causing only mode II response. The use of higher interfacial bond strengths leads to more effective rehabilitation with greater load capacity and ductility, in addition to faster load transfer and activation of the diagonal crack induced debonding mode. The authors highlighted the fact that further increase of interfacial bond strength beyond a threshold does not result in any increase in ultimate load-carrying capacity, as seen in the use of 8 and 16 MPa levels. The effect of interfacial fracture energy variation on load-deflection response was investigated and it was found that low interfacial fracture energy makes it easier for debond initiation and propagation from the maximum moment region

(midspan) to the end of the FRP. Low interfacial fracture energy limits stress transfer and is thus unable to distributed effects of cracking resulting in very low efficiency use of the FRP.

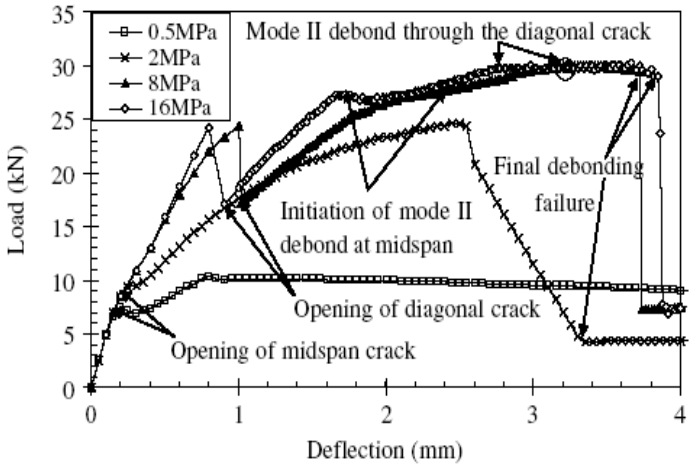

Figure 2.21: Effect of interfacial bond strength variation on load-deflection response (Niu et al., 2006).

2.5.5 Adhesive Layer

The determination of interfacial stresses has been researched in the last decade for beams bonded with either steel or FRP plates and several closed-form analytical solutions have been developed. In spite of the amount of analytical solutions presented over the years, there is a lack of FE studies to investigate interfacial stresses. Reviews of both numerical techniques are presented.

Analytical Studies

A review of existing solutions for predicting the shear and normal stress concentrations in the adhesive layer of plated-RC beams is presented. Despite disagreement over specific models, all these solutions are for linear elastic materials and employ the simplifying assumption that the adhesive layer is subject to shear and normal stresses that are constant across the thickness of the adhesive layer. In the solutions reviewed, two approaches have been implemented: deformation compatibility condition and staged analysis approach. A solution by Smith and Teng (2001) removes deficiencies found in these solutions and is discussed. Finally, a solution by Shen et al.

(2001) that models the non-uniform behaviour of the adhesive layer by employing a zero stress condition is presented.

Deformation compatibility condition can be used to determine interfacial stresses in the adhesive layer. Interfacial shear stresses are related to the difference between the longitudinal displacement at the base of the beams and at the top of the soffit plate. Interfacial normal stresses are related to vertical deformation compatibility between the beam and the bonded plate. This approach was adopted by Vilnay (1988), Liu and Zhu (1994), Taljsten (1997) and Malek et al. (1998). The main difference between the solutions for the interfacial shear stresses is in the selection of terms included for determining longitudinal displacements. For example, Liu and Zhu (1994) are the only authors to consider the effects of shear deformations of the beam, but they ignore the contribution in the plate and beam caused by interfacial normal stresses. The differences between the solutions for interfacial normal stresses are in the derivation of governing equations. Vilnay (1988) and Taljsten (1997) derived governing equations in terms of vertical displacement of the bonded plate whereas Liu and Zhu (1994) and Malek et al. (1998) derived the equations in terms of interfacial normal stress.

The staged analysis approach was adopted by Roberts (1989) and is commonly referred to when discussing shear and normal stress concentrations in the adhesive layer of plated-RC beams as it established a foundation on which future studies would follow. The solution presented by Roberts (1989) implemented general loading conditions during each of its three stages. In the first stage, the interfacial shear stress in the adhesive layer is determined and axial forces are produced at the end of each plate. Opposite axial forces are applied at the plate-ends in the second stage. At the end of stage two, non-zero moments and non-zero shear forces exist at each end of the plate. In the final stage, equal but opposite moments and shear forces are

applied at the ends of the plate. Final interfacial shear stresses are obtained by combining the results from stages 1 and 2, while the interfacial normal stresses are only given by stage 3 of the analysis as. From a physical point of view, interfacial stresses in the adhesive layer are inducted as the adhesive layer attempts to enforce deformation compatibility between the RC beam and the soffit plate which otherwise would deform without interaction (Smith and Teng, 2001). Thus, the deformation compatibility method, which embodies this physical aspect, is believed to be superior to the staged analysis approach.

All of the existing solutions reviewed include the bending deformations in the beam and the axial deformations in the bonded plate. However, the inability of existing solutions to include terms of which additional bending deformations in the bonded plate occur due to interfacial shear stresses prompted the need for a similar but more accurate solution as presented by Smith and Teng (2001). The model assumes linear elastic behaviour and invariant stresses across the adhesive layer. Shear deformations of the RC beam and soffit plate are neglected, as their effect is small and their inclusion couples the two governing equations (Smith and Teng, 2001). A parametric study comparing the predictions of Smith and Teng's solution with a FE analysis, preformed by Teng et al. (2002), of the mid-adhesive layer stresses demonstrated a reasonably close agreement. Details of the FE analysis are described in the following subsection. The adhesive layer thickness, adhesive elastic modulus, soffit plate thickness and soffit plate elastic modulus were varied one at a time to monitor their effect. Interfacial normal and shear stresses were obtained for four different adhesive layer thicknesses of 0.5, 1, 2, and 4 mm, as shown in Figure 2.22a and b. It can be seen that reducing the thickness of the adhesive layer leads to an increase in both normal and shear stresses. The locations of the peak normal and shear stresses were found to vary depending on the adhesive layer thickness. For the 1, 2, and 4

mm thick adhesive layers, the FE interfacial normal stress occurs near the plate-end, while the analytical peak stress occurs at the plate-end. As the adhesive layer is reduced, the FE peak normal stress moves towards the end of the plate. For the 0.5 mm thick layer, the FE peak normal stress is found at the end, as predicted by the analytical solution. A similar trend is observed for the case of interfacial shear stress. The peak FE shear stress occurs at a short distance from the end of the plate, rather than at the end of the plate by the analytical solution. This distance reduces with a reduction in adhesive layer thickness. The interfacial stresses were found to increase with a reduction in adhesive elastic modulus, plate thickness, and plate elastic modulus. This was expected as a stiff adhesive/plate takes up a larger share of the total load and this larger share has to be transferred from the beam via higher interfacial stresses. The locations of the FE peak normal and shear stresses did not vary with these parameters.

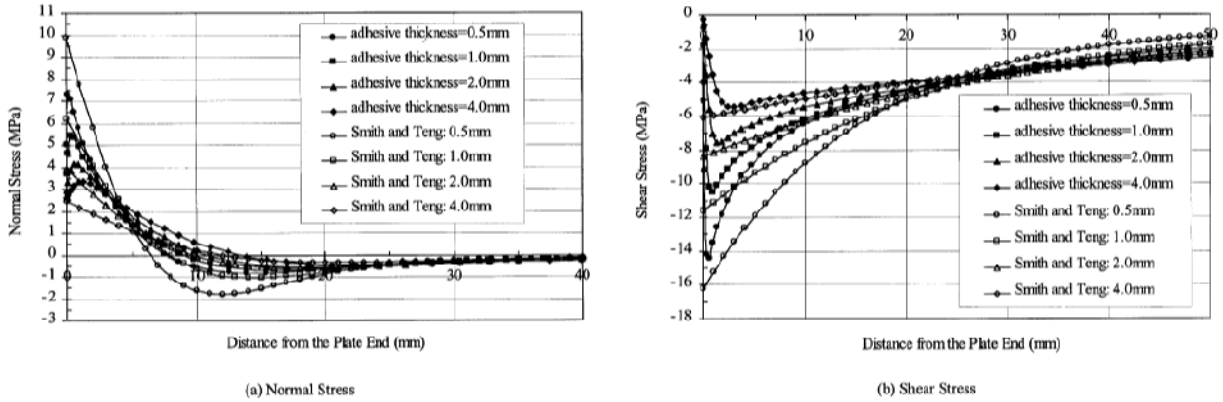

Figure 2.22: Effect of adhesive thickness: (a) normal stress; (b) shear stress (Teng et al., 2002).

Despite the advances of the analytical models over the last decade, all existing analytical solutions suffer from two important limitations. First, the predicted maximum interfacial shear stress occurs at the plate end, where the shear stress should be zero as shown in the FE analysis by Teng et al. (2002). This violates the free surface condition at the end of the adhesive layer. Second, the adhesive layer is modeled as shear and transverse springs, without any interaction

between the two. Consequently, the adhesive layer is assumed to be subject to uniform shear and transverse normal stresses. Rabinovich and Frostig (2000) were the first researchers to introduce an analytical solution where the adhesive layer is treated as an elastic medium with transverse normal stresses varying across the adhesive layer. However, two major drawbacks in this solution have prevented it from being implemented as a design rule. Unlike other solutions, explicit expressions are not available for the interfacial stresses, so results are not easily obtainable, which makes is difficult to be validated by other researchers. Second, the longitudinal stresses are ignored, so the shear stresses are still assumed to remain constant across the adhesive layer thickness. Shen et al. (2001) developed an alternative solution that removes the two deficiencies found in the Rabinovich and Frostig (2000) model by providing an explicit closed-form expression for interfacial stresses and the inclusion of non-zero longitudinal stresses in the adhesive layer. The analysis is applicable to simply supported beams and one-way slabs subject to a uniformly distributed load and bending moment. The validity of the Shen et al. (2001) stress analysis is established by comparison with the well-known solutions of Roberts and Haji-Kazemi (1989) and Smith and Teng (2000). Figure 2.23a shows that the peak interfacial shear stresses predicted by the present solution are almost identical for the both interfaces. However, a discrepancy exists near the free edge where the two existing solutions, Roberts and Haji-Kazemi (1989) and Smith and Teng (2000), predict increasing interfacial shear stress toward the free edge and the present solution reduces rapidly to zero to satisfy the free surface condition. The interfacial normal stresses shown in Figure 2.23b predicted by the present solution are different for the two interfaces, indicating that the distribution of the normal stress across the adhesive is non-uniform. Additionally, the concrete-adhesive interface appears to be the more critical interface for debonding failure.

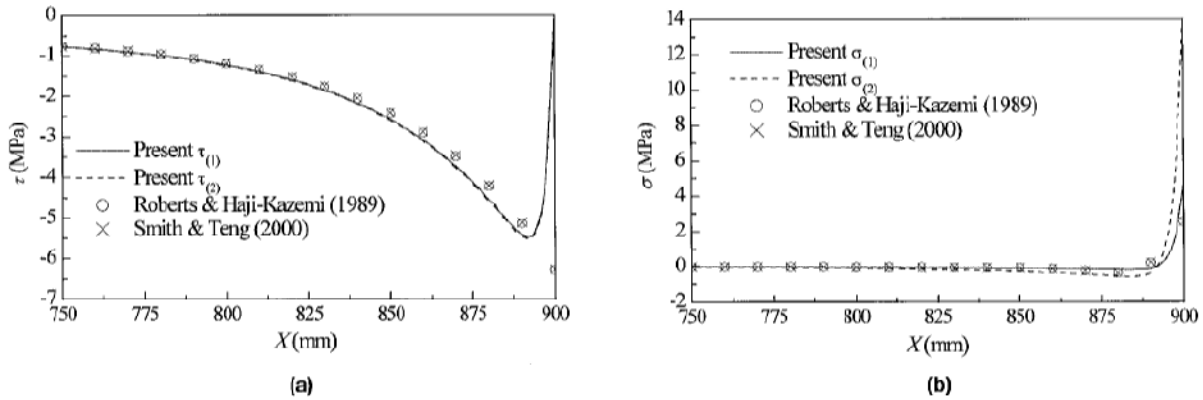

Figure 2.23: Comparison of interfacial stresses: (a) shear stress; (b) normal stress (Shen et al., 2001).

Finite Element Studies

There is a lack of detailed FE studies on the interfacial stresses in plated RC beams. This may be attributed to the existence of points of stress singularity found at the two end points of the adhesive layer, the concrete-adhesive (CA) interface and the plate-adhesive (PA) interface. At these points, stresses grow without bound with mesh refinement and require a very fine mesh for accurate determination of interfacial stresses. A brief discussion on stress singularity in a soffit-plated beam is now discussed.

A soffit-plated beam is composed of three components of different materials: the RC beam, adhesive layer and the soffit plate. Each pair of adjacent materials, such as the RC beams and adhesive layer can be considered to form a two-material wedge. According to the theory of elasticity, the point at the end of the interface in such a wedge is a point of stress singularity and stresses approach infinity towards the singular point (Hein and Erdogan, 1971). The rates at which stresses increase towards a singular point reflect the strength of singularity. The relationship between the magnitude of stresses (σ_i) and strength (λ) of singularity can be expressed as (Hein and Erdogan, 1971):

$$\sigma_i \infty \alpha r^{-\lambda} \tag{2-5}$$

where *r* is the distance from a singular point. This relationship shows that the stresses are infinite at the singular point and reduce exponentially away from this point. The strength of singularity is dependent on the elastic modulus (E_i), Poisson's ratio (υ_i) and geometric shape (θ_i) of a wedge for the materials. The case of a soffit-plated beam at CA interface are shown in Figure 2.24 with $\theta_1 = 90°$ and $\theta_2 = -180°$, where components 1 and 2 represent the adhesive layer and RC beam, respectively. A typical adhesive-concrete E_1/E_2 ratio is 0.1 and this leads to singularity strength of 0.3. The case of a soffit-plate beam at the PA interface nearer the end of the plate is shown in Figure 2.25 with $\theta_1 = \theta_2 = 90°$, where components 1 and 2 being the adhesive layer and plate, respectively. For a typical value of 0.01 for the E_1/E_2 ratio, a strength singularity 0.21 is obtained. Thus, the strength of singularity is higher at the end of the CA interface than at the PA interface.

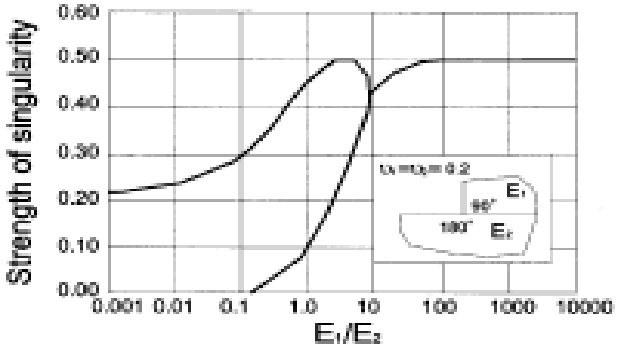

Figure 2.24: Strength singularity for two-material wedges: $\theta_1 = 90°$, $\theta_2 = -180°$ (Hein and Erodogan, 1971).

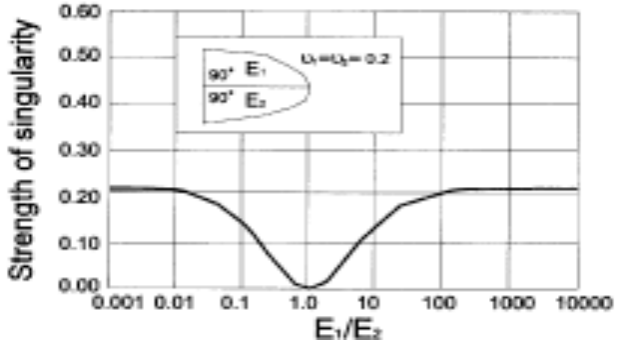

Figure 2.25: Strength singularity for two-material wedges: $\theta_1 = \theta_2 = 90°$ (Hein and Erodogan, 1971).

A FE analysis preformed by Teng et al. (2002), using the general-purpose program LUCAS, was used to analyze different mesh sizes at points of singular stresses. A four-node quadrilateral plane stress element was used to model the plated beam and a fine finite element mesh was employed to model the adhesive layer and the plate near the plate-end to obtain accurate interfacial stresses. Figure 2.26 shows an enlarged view of the mesh in the vicinity of the end plate, where *A* denotes the CA interface and *B* denotes the PA interface. Four different element heights of 0.8, 0.4, 0.2, and 0.1 mm are modeled across the adhesive layer and their corresponding variation of interfacial stresses are shown in Figure 2.27. The maximum CA interfacial stresses, which occur at the plate-end, are seen to grow with mesh refinement, which is characteristic of singular behaviour. The CA stresses from different mesh sizes converge at a distance of approximately 1 mm from the plate-end for the normal stress and 6 mm from the plate-end for the shear stress. No points of stress singularity were found to exist along the mid-adhesive (MA) layer. The PA interfacial normal stresses were found to increase with mesh refinement within 1 mm from the plate-end and 0.1 mm from the plate-end for the shear stress. A comparison of the CA and PA interfaces confirms that the stronger stress singularity exists at point A than at point B.

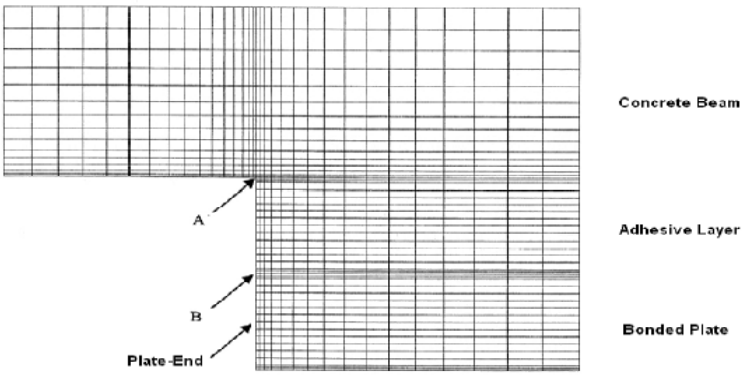

Figure 2.26: Detailed view of fine finite element mesh near the plate-end (Teng et al., 2002).

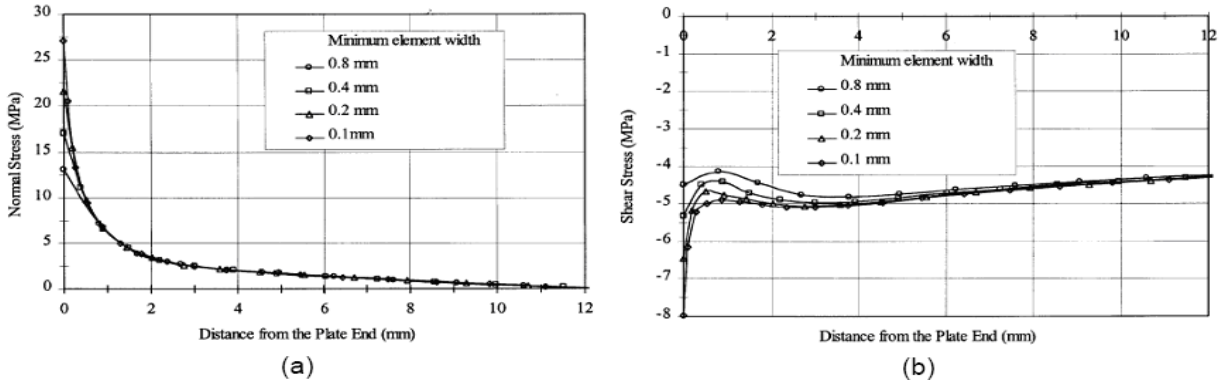

Figure 2.27: CA Interfacial stresses (a) Normal stresses; (b) Shear stresses (Teng et al., 2002).

2.6 BOND CHARACTERIZATION

Bond is a critical parameter in strengthening systems as it provides the shear transfer between concrete and FRP necessary for composite action. To attain a better understanding of the debonding phenomenon, researchers have studied bond characterization between the concrete and FRP materials. This section will review factors influencing bond strength, effect of employing perfect bond assumptions, a new FE modeling approach, and a review of analytical models to determine ultimate bond strength.

2.6.1 Factors Influencing Bond Strength

Yozhizawa et al. (1996) examined the effect of various bonding conditions on the bond strength between CFRP sheets and concrete. Bonding conditions such as surface preparation, types of CFRP sheets, and debonding area were assessed using double-face shear specimens. The effect of using a water jet or sander for surface preparation was investigated and it was found that surface treatment by water jet was superior in enhancing the bond strength as it removes layers of very fine particles that may inhibit the bond of epoxy and concrete. CFRP plates were found to have higher bond strength when employing plates with high tensile strength or elastic modulus. The bond strength also increased as more layers of CFRP laminates were applied.

Flexural tests involving full-scale beams were also conducted, and it was found that fracture of the concrete cover occurred rather than separation of the CFRP laminate from the concrete.

Chajes et al. (1996) investigated the effect of surface preparation on the shear bond strength of FRP plates. Three different procedures were used: (a) no surface preparation; (b) grinding with a stone wheel to give a smooth finish; and (c) mechanically abrading with a wire wheel. In their tests, bond strength was defined as the ultimate load that the bond can sustain divided by the bonded area. The results of the surface preparation tests showed that the failure was initiated due to the shearing of the concrete directly beneath the adhesive layer. Based on these test results, mechanical abrasion of the concrete surface was found to produce the highest bond strength. In the case of the concrete failure directly beneath the adhesive layer, the researchers concluded that the ultimate bond strength is proportional to the square root of the compressive strength of concrete.

Taljsten (1997) presented the result of pull out tests performed on concrete prisms onto which steel or CFRP plates have been bonded. The anchor length was defined as the minimum length of FRP/steel plate that contributes to the ultimate load capacity such that a longer bond would not add to the capacity. The criteria for the necessary anchor lengths for steel and FRP plates were presented as well as the critical strain level in the concrete at failure. The results showed that there is a specific anchor length for each material used. It was shown that the strain in the concrete was the governing factor in determining the interfacial bond failure. The observed failure occurs directly in the thin concrete layer under the adhesive. The load response of the bond was determined and the debonding process was related to the strain distribution in the FRP.

Bizindavyi and Neale (1999) investigated the shear conditions between FRP sheets and concrete. Strain gauges were used to determine the strain distribution in the FRP at different load

levels. From the strain data, the shear stress distribution along the bonded joint between concrete and FRP was determined. A uniform shear stress distribution along the bonded joint was assumed to determine the bond strength, which is the ultimate load divided by the bonded area. The values of the initial transfer lengths for GFRP/concrete and CFRP/concrete joints were estimated by defining the transfer length as the distance from the loaded end to the point on the joint where strain reaches zero.

An experimental investigation performed by Tripi et al. (2000) aimed to characterize the local and global deformations in tensile-loaded concrete prisms bonded with CFRP sheets. The main variables studied were the thickness of the adhesive layer and the modulus of the CFRP fibers. It was found that the local deformations are dependent on the thickness of the adhesive layer. Thicker layers transfer load between the cracked-concrete cover and CFRP over long transfer zones, which increases crack spacing and relative displacements. The modulus of the CFRP sheet significantly influenced the peak longitudinal strains at cracks, but had a negligible effect on relative displacements and crack spacing. Thus, it was suggested that the FRP sheet extensional stiffness (modulus x thickness) controls global behaviour while the epoxy shear stiffness (modulus / thickness) controls the local behaviour (Tripi et al., 2000). Since a stiff adhesive layer was found to increase global stiffness, the use of high modulus FRP laminates should be employed to enhance the stiffness of a cracked RC member. The authors observed that diagonal cracking affects load transfer near cracks along the beam. Thus, the concrete strength should be considered in the bond behaviour of external FRP reinforcement.

2.6.2 Perfect Bond Assumption

Arduini et al. (1997) developed analytical models to simulate the different failure mechanisms occurring in RC beams strengthened with FRP laminates. The maximum shear and normal

stresses are calculated from the Arduini and Nanni (1997) solution explained in Section 2.3 along with Table 2.1 to detect various failure mechanisms. The model was compared with RC beams strengthened with CFRP strips and sheets tested by the authors, and a commercial FE program based on a smeared crack approach. Beams strengthened with CFRP strips were analyzed with a two-dimensional mesh, while those with CFRP sheets were modeled in three-dimension. Both the analytical and FE numerical models assumed perfect bond. Load-deflection curves for the beams bonded with FRP strips are given in the Figure 2.28, along with the results obtained from analytical and numerical FE simulations. Beams A1 and A2 reached failure by crushing of concrete long after yielding of steel. Beams A3, A4, and A5 showed a brittle concrete shear failure. In these beams, a crack started from the end of the plate and propagated along the crack cover parallel to the longitudinal steel reinforcing bars. Beams A6 also experienced a brittle failure mechanism, however in this case delamination of the FRP plate from the concrete occurred. Although good accord was found between the curves, the analytical and numerical FE results yielded stiffer plots than those from the experimental program. This can be attributed to the existence of slippage at the concrete-FRP interface in both vertical and horizontal direction. Thus, perfect bond assumption was not justified.

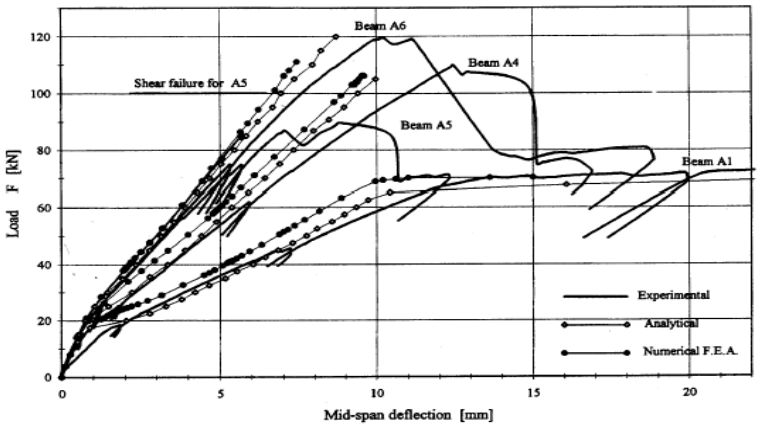

Figure 2.28: Load versus mid-span deflection for experimental, analytical, and numerical FE analysis results for beams reinforced with CFRP (Arduni et al., 1997).

A nonlinear FE layered model, developed by Nitereka and Neale (1999), was able to simulate the complete loading deformation response of RC beams strengthened with FRP laminates. Concrete is assumed to be nonlinear in compression, with post-cracking tension stiffening effects. The behaviour of the steel reinforcement is modeled as elastic-plastic while the FRP laminates are linear elastic using an equivalent elastic modulus from the classical lamination theory of composite structures. The steel reinforcing bars and composite laminates are smeared into the beam and are transformed into layers of equivalent area. Full bond between concrete and steel reinforcement is assumed, and bond-slip at the concrete-FRP interface is neglected. Shear deformations are neglected and equal displacements are imposed at the interfaces of adjacent layers to ensure interlayer compatibility. The FE analysis was validated using test results published by M'Bazaa (1995) and Chicoine (1997) as shown in Figure 2.29. The beam tested by M'Bazaa (1995) exhibited a concrete delamination failure mode at about 60% of the predicted ultimate load. This problem was eliminated in a specimen tested by Chicoine (1997) by applying U-shaped composite anchors at the end of the beam. This enabled the composite-reinforced beam to reach approximately 95% of its ultimate theoretical load. From the numerical analysis, it was concluded that tension stiffening effects provide a more continuous load-deflection response, and that the concrete cover should be divided into several layers such that the load transfer from the concrete to FRP can be represented realistically. It was also reported that the FRP strains measured experimentally greatly exceeds those predicted by the analysis, as shown in Figure 2.30. This was attributed to assumption made by the authors of a perfect bond between adjacent layers and suggests that slippage occurs at the concrete-FRP interface leading to eventual delamination. Hence, the perfect bond assumption used in numerical analysis is inappropriate

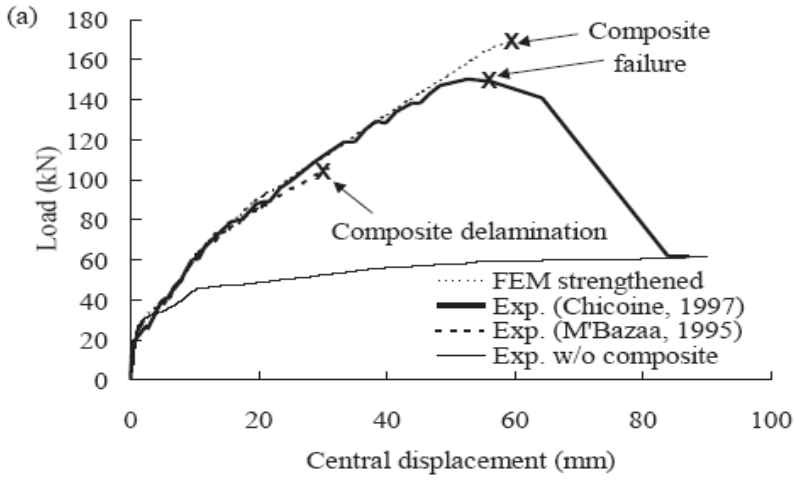

Figure 2.29: Predicted and experimental load-displacement curves for beams tested by M'Bazaa (1995) and Chicoine (1997); (Nitereka and Neale, 1999).

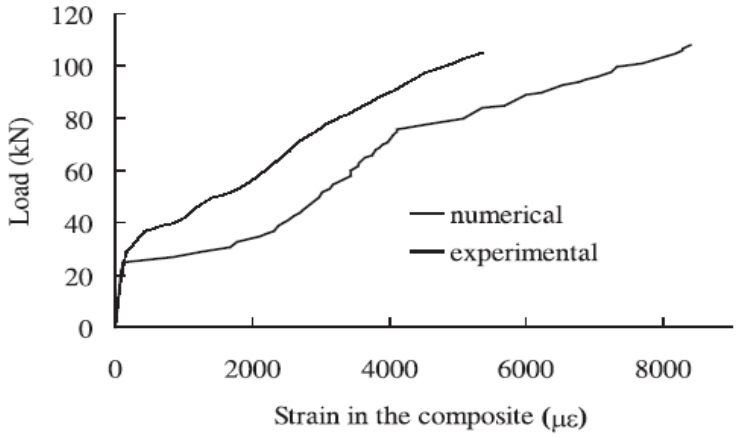

Figure 2.30: Predicted and experimental load-strains for composite reinforcement (Nitereka and Neale, 1999).

Wong and Vecchio (2003) preformed an investigation to consider the bond-slip behaviour at the FRP-RC beam interface in numerical modeling. A two-dimensional nonlinear FE program was formulated utilizing two constitutive relationships for bond interface: elastic-plastic and linear-elastic as shown in Figure 2.31. One-dimensional contact bond elements were used to represent a continuous connection between the concrete and FRP elements as shown in Figure 2.32. The nodes of these two adherents were connected by bond elements to allow relative displacement, or slip, to take place between concrete and FRP. The difference in

displacement between the concrete node and FRP node determines the nodal slip of the bond element. The bond stress is then calculated using the specified constitutive relationships. Finally, the force transferred by the bond element is found my multiplying the bond stress and the bonded surface area represented by the element.

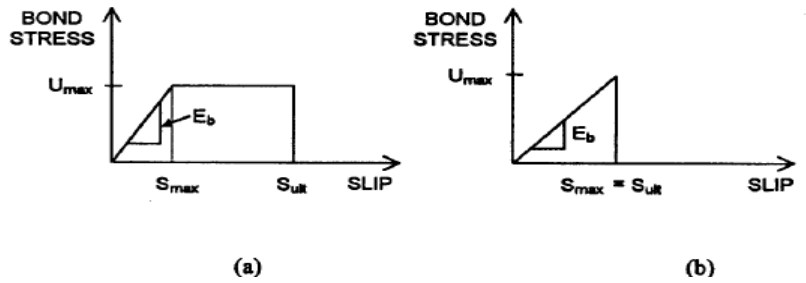

Figure 2.31: Constitutive relationship for bond interface: (a) elastic-plastic; and (b) linear elastic; (Wong and Vecchio, 2003)

Figure 2.32: One-dimensional contact element (Wong and Vecchio, 2003).

A nonlinear FE program developed by Vecchio and Bucci (1999), which assumes perfect bond, was compared with published experimental data. The first set of flexural specimens was modeled with RC beams strengthened with CFRP plates tested by Zarnic et al. (1999). Sudden failure was experienced in these specimens caused by delamination of the plates below the concentrated load. The load-deflection curves from the experimental results and numerical analyses are shown in Figure 2.33. The perfect bond condition (FE-P) overestimated the failure load by 19%, with a corresponding midspan deflection of 66% larger than the experimental value. The elastic-plastic bond law (FE-EP) provides values of ultimate load and deflection that

were 17 and 59% higher than the test data. The linear-elastic relationship (FE-LE) produces a reasonably accurate response, with a failure load of 111 kN; 5% lower than the test value.

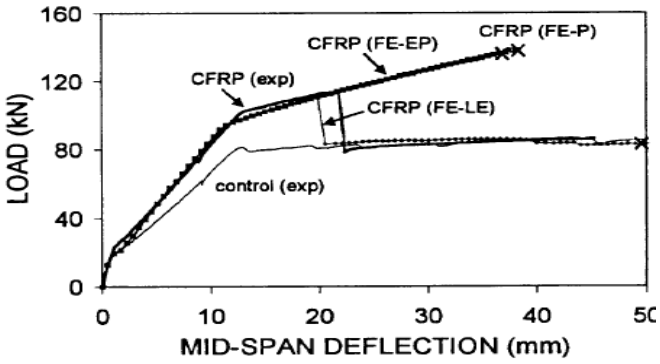

Figure 2.33: Load-deflection curves of Zarnic specimens (Wong and Vecchio, 2003).

A second set of specimens modeled numerically were the De Rose and Sheikh (1997) specimens, where shear failure was dominant. Figure 2.34 compares the numerical analyses with the experimental results. The perfect bond condition (FE-P) resulted in a higher post-yielding stiffness and greatly underestimated the deflection at failure by approximately 75%. The linear elastic bond model (FE-LE) also predicted an early failure of the beam and underestimated the deflection at failure by 65%. However, the beam modeled using the elastic-plastic bond law (FE-EP) failed in a shear-flexural mode at a load of 2465 kN – 2% lower than the actual result. It was concluded that the accuracy of the predictions depends on the constitutive relationships chosen for the analysis. The linear-elastic bond law was found to be most appropriate when the failure was dominated by sudden delamination of the FRP plate, which is expected to occur when the shear strength of the epoxy is low (Wong and Vecchio, 2003). In specimens employing stronger epoxies, the failure was predominately though the peeling of the concrete cover, which was critical due to its lower shear stress. These specimens compared well with experimental data when the elastic-plastic bond relationship was applied. The authors suggested that the cutoff of the maximum bond stress is a function of the concrete's modulus of rupture, the

maximum slip is a function of the shear modulus of the epoxy, and the existence of the plastic range in the bond law depends on the shear strength of the epoxy (Wong and Vecchio, 2003).

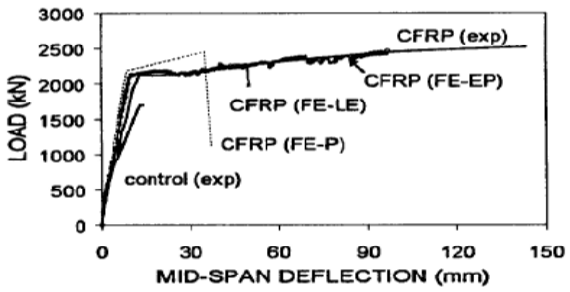

Figure 2.34 - Load-deflection curves for De Rose specimens (Wong and Vecchio, 2003).

2.6.3 Meso-Scale FE Approach

Lu et al. (2005) explored a numerical approach where the bond-slip curve at any point along the FRP-concrete interface can be obtained. The approach was motivated by the difficulty in obtaining accurate bond-slip curves directly from strain measurements in pull tests. It is based on the observation that debonding of FRP from concrete occurs within a thin layer of concrete 2 to 5 mm thick adjacent to the adhesive layer, unless the adhesive is rather weak. The numerical approach relies on the accurate modelling of concrete failure near the adhesive layer, which includes properly tracing the paths of cracks as deformation progresses. To simulate concrete failure within such a thin layer, a meso-scale FE approach is proposed in which a very fine mesh with element sizes being one order smaller than the thickness of the fracture layer of concrete are used in conjunction with a fixed angle crack model (FACM). To reduce computational effort, the three-dimensional FRP-to-concrete bonded joint was modelled as a plane stress problem using four-node isoparametric elements, with the effect of FRP-to-concrete width ratio being separately considered using a width ratio factor devised by Chen and Teng (2001):

$$\beta_w = \sqrt{\frac{2 - b_f / b_c}{1 + b_f / b_c}} \tag{2-6}$$

where:

b_f – width of FRP plate

b_c – width of concrete

The FE model was implemented into the general-purpose finite element package MSC.Marc as a user subroutine. Comparisons between the predictions of this model and results of 10 pull tests taken from studies by Wu et al. (2001), Ueda et al. (1999), Tan (2002), and Yuan et al. (2004) yielded a close agreement for all specimens. From the FE model, the local bond-slip curve of a point along the interface can be obtained by plotting the bond stress value at that point versus the slip of that point. The local bond stress distribution was calculated as:

$$\tau = \frac{d\sigma_f}{dx} t_f \tag{2-7}$$

where:

σ_f - axial stress in the FRP plate

t_f - thickness of the FRP plate

To obtain usable local bond stresses, a Fast Fourier Transform (FFT) smoothing procedure was implemented to process the large fluctuations curves as a result of interfacial cracks in the concrete. A FFT smoothing length of 5 to 20 mm was found to be suitable to filter out local 'noises' without a loss of the characteristics of the resulting bond-slip curve. A smoothing length of 10 mm was found to best represent the experimental data considered in terms of accurate prediction of the local bond-slip curve, as shown in Figure 2.35

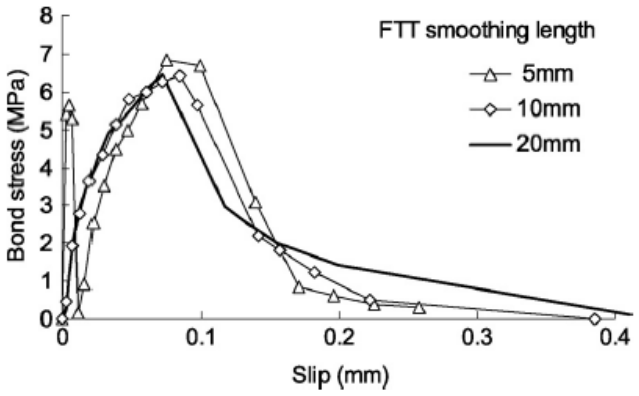

Figure 2.35: Local bond-slip curves from smoothed bonded stresses with various FFT smoothing lengths (Lu et al., 2005).

Baky et al. (2007) performed a FE study to investigate the FRP-concrete interfacial response of FRP-RC beams. The analysis was carried out using two different relations to study the interface: nonlinear and bilinear bond-slip laws derived by Lu et al. (2005). The results predicted using these two laws were compared to those based on the full-bond assumption. The authors reported that the predictions of the ultimate load carrying capacities using either law were virtually the same. This was attributed to the fact that both laws were characterized by the same interfacial fracture energy. When assuming full bond between the FRP and concrete, the numerical models were found to over-predict the experimental ultimate capacities of the strengthened beam, as summarized in Table 2.5.

Table 2.5: Comparison of different bond-slip assumptions with published experimental results (Baky et al., 2007).

		Numerical analysis					
		Nonlinear		Bilinear		Full-bond	
Beam set	Beam	Load (kN)	Num./Exp.	Load (kN)	Num./Exp.	Load (kN)	Num./Exp.
Ross et al. (1999)	B1	80.0	1.00	76.8	0.95	105.0	1.03
Chicoine (1997)	P_3	172.8	1.01	172.8	1.01	175.2	1.02
M'Bazaa (1995)	P_0	105.0	1.05	111.0	1.11	156.0	1.56
Kamińska and Kotynia (2000)	B-08/S	178.0	0.99	190.0	1.06	204.0	1.13
Brena et al. (2003)	A3	138.0	0.99	140.0	0.99	162.0	1.17
Brena et al. (2003)	A1	120.0	1.00	110.0	0.92	138.0	1.15

2.6.4 Ultimate Bond Strength

Chen and Teng (2001) critically reviewed and assessed existing bond strength models (empirical, fracture mechanics, and simple design models), by comparing them with experimental data gathered from literature. This enabled the identification of the deficiencies of the existing models and initiated a simple rational model based on fracture mechanics analysis and experimental observations. A linearly decreasing shear-slip model was incorporated as shown in Figure 2.36.

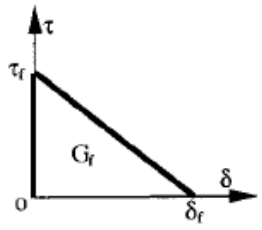

Figure 2.36: Shear-slip model for bonded concrete joints (Chen and Teng, 2001).

Review of the experimental data revealed that the width ratio of the bonded plate to the concrete member, b_f/b_c, has a significant effect on the ultimate bond strength. If the width of the bonded plate is smaller than that of the concrete member, the force transfers from the plate to the concrete leads to a non-uniform stress distribution across the width of the concrete member. A smaller b_f compared to b_c may result in a higher shear stress in the adhesive at failure, attributed to the contribution from the concrete outside the bond area. Regressional analysis of the test data reveals that the ultimate bond strength is linear to β_f in the form of equation (2-6). By taking into consideration the width ratio factor, the ultimate bond strength can be calculated as:

$$P_u = 0.427\beta_p\beta_L\sqrt{f_c'}b_pL_e \tag{2-8}$$

where:

P_u – ultimate bond strength

$L_e = \sqrt{\frac{E_p t_p}{\sqrt{f_c'}}}$ – effective bond length

E_p – Elastic modulus of FRP

t_p – thickness of FRP

b_p – width of FRP

f_c' - concrete compressive strength

$$\beta_L = \begin{cases} 1 & L \geq L_e \\ \sin\frac{\pi L}{2L_e} & L < L_e \end{cases}$$

Table 2.6 compares the proposed model with six other well-known models using the test data gathered. As shown, equation (2-8) produces an overall average value of 1.05 for the ratio of observed to predicted ultimate bond strength and a corresponding standard deviation of 0.18. A later study by Lu et al. (2005) critically reviewed existing bond strength models and concluded that among the 12 existing bond strength models reviewed the model proposed by Chen and Teng (2001) remains the most accurate.

Table 2.6: Measured to predicted bond strength ratios (Chen and Teng, 2001).

Source	**Average**	**Standard Deviation**	**Coefficient of Variation**
Hiroyuki and Wu (1997)	2.87	0.95	33%
Tanaka (1996)	2.92	1.65	56%
Van Germert (1980)	2.19	1.12	51%
Chaallal et al. (1998)	1.81	0.89	49%
Khalifa et al. (1998)	1.07	0.24	23%
Neubauer and Rostasy (1997)	0.82	0.15	18%
Chen and Teng (2001)	1.05	0.18	17%

3 NUMERICAL FORMULATIONS

3.1 INTRODUCTION

Reinforced concrete externally bonded with FRP is considered as a type of heterogeneous composite structure consisting of three major components: concrete, reinforcing steel, and FRP. The composite poses a highly nonlinear analysis challenge that involves complications such as extensive cracking, local effects, and failure modes. A general approach to model such a problem is to select a suitable numerical approach to treat the response of each component separately and then obtain their combined effects by imposing the condition of material continuity. Thus, a complete analysis includes selecting a suitable numerical method, modelling each material using appropriate laws, and modelling the interaction between the materials. The following provides a review of the formulations used in the analysis.

3.2 ANALYSIS APPROACH

For a structure with a given geometry, material properties, and boundary conditions, a structural analysis may be performed to investigate local effects such as internal forces or stresses, or global effects such as displacements/reactions. There are three common ways of analyzing a structure: empirically, analytically, and numerically. Empirical investigations make up the majority of data compiled on FRP-RC structures to date, exemplifying the need to develop more refined analysis tools to reduce the high cost and significant time required to conduct full-scale physical testing. Basic analytical solutions are feasible only for structures of relatively simple geometries and boundary conditions. Many practical engineering problems cannot be solved analytically due to the complexities of the structure. More complex analyses are carried out using numerical approaches by breaking down a structure (domain) into smaller pieces (sub-

domains). The three main numerical solution procedures are: finite difference method, boundary element method, and finite element method.

3.2.1 Finite Difference Method (FDM)

In the FDM, a structure is broken into nodal regions and the governing equations are replaced by finite difference equations. Once the set of equations are formed they are solved simultaneously to yield a solution. The disadvantages of the FDM are that it is difficult to apply the technique to structures with complicated geometries, boundary conditions, and/or problems of rapidly changing variables, such as stress concentration problems, since it is difficult to vary the size of the grid in a particular region. This method is most suitable for problems related to heat transfer and fluid low.

3.2.2 Boundary Element Method (BEM)

The BEM only forms elements on the boundary of the structure and uses the divergence theorem to determine the distribution of the variable within the closed boundary. Although it is computationally efficient, this method yields fully populated matrices and is difficult to use for nonlinear problems and structures composed of different materials and element types.

3.2.3 Finite Element Method (FEM)

The FEM breaks down the entire domain of a structure into pieces referred to as finite elements. A solution of the governing equations on each element is given based on appropriate theories applied to the elements (such as truss, beam, 2D or 3D continuum), and the combined solution from all the elements form the solution for the entire part. This method is especially proficient for complex structures composed of multiple structural components and different materials.

The FEM offers a powerful and general analytical tool for studying structural behavior of reinforced concrete structures. Cracking, tension stiffening, non-linear material properties,

interface behaviors, and other effects previously ignored or treated in a very approximate by other numerical methods can be modeled rationally using FEM. The reliability of the method is largely dependent on the accuracy with which the model simulates the actual behavior and geometrical characteristics of the prototype structure. Where simple analytical methods are not feasible for the solution of complex civil engineering problems, the FEM offers an effective, versatile, and reliable approach to handle such cases. Thus, the FEM is selected for this investigation.

3.3 FINITE ELEMENT PROCEDURE

Displacement-based finite element methods are commonly used in structural analysis and result in a system of equations relating unknown nodal displacements to specified forces by the structure stiffness matrix typically in the form:

$$R = KU \tag{3-1}$$

where:

R – external forces

K – element stiffness

U – displacement

Based on the computed displacements, stresses and strains are calculated. The equations involved are derived from appropriate structural theory and satisfy the following equations: equilibrium (relate stresses to applied forces), compatibility (strains to displacement), and constitutive (stresses to strains). Together, these relationships are used to form the displacement-based FEA equations in the matrix form:

$$\{R\} = [K]\{D\} \tag{3-2}$$

where:

{R} – global stiffness matrix

[K] – global stiffness matrix

{D} – load vector

The matrix equation is then solved for the displacement vector {D}. Solving the equations allows us to go directly from forces to displacements. Strains and stresses are then computed from the displacement results. Shape functions are used to describe displacements. They are created through the use of Lagrangian interpolation to perform the necessary function of relating local coordinate position to global coordinate position. For an eight-node solid element shown in Figure 3.1, eight shape functions are necessary to express the three directions of displacement as a function of the eight nodes. The eight shape functions defined in local element coordinate system are:

$$\begin{aligned} N_1 &= \frac{1}{8}(1-g)(1-h)(1-r) & N_5 &= \frac{1}{8}(1-g)(1-h)(1+r) \\ N_2 &= \frac{1}{8}(1+g)(1-h)(1-r) & N_6 &= \frac{1}{8}(1+g)(1-h)(1+r) \\ N_3 &= \frac{1}{8}(1+g)(1+h)(1-r) & N_7 &= \frac{1}{8}(1+g)(1+h)(1+r) \\ N_4 &= \frac{1}{8}(1-g)(1+h)(1-r) & N_8 &= \frac{1}{8}(1-g)(1+h)(1+r) \end{aligned} \tag{3-3}$$

where:

N_1 to N_8 – Lagrangian interpolation shape functions

g,h,r – local element coordinate system position

Displacements and coordinates are described through the use of shape functions as:

$$\begin{aligned} u &= \sum N_i u_i & x &= \sum N_i x_i \\ v &= \sum N_i v_i & y &= \sum N_i y_i \\ w &= \sum N_j w_j & z &= \sum N_j z_j \end{aligned} \tag{3-4}$$

where:

u, v, w – local displacement as a function of nodal displacements

x, y, z – global coordinates as a function of local position

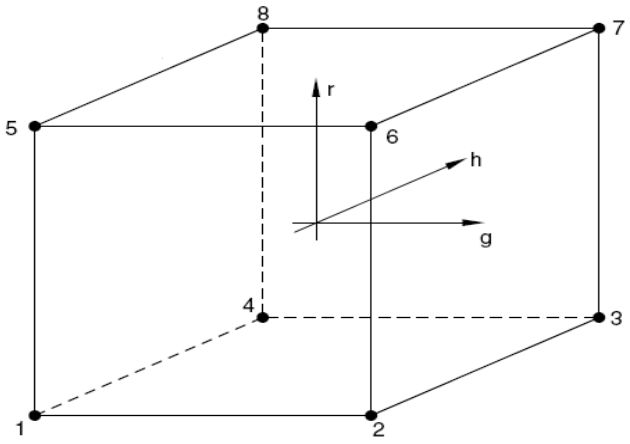

Figure 3.1: Eight-node solid brick element.

Once the displacements are calculated, they can be related to the strains within the element. The determination if strain requires partial differentiation of the displacement function with respect to the global coordinates. The global coordinate system must include the displacements that are calculated in the local coordinate system. Transformation from the local to global coordinate system is accomplished through the use derivation of the strain values:

$$\{\varepsilon\} = [B]\{q\} \tag{3-5}$$

where:

{ε} – element strain vector

[B] – strain-displacement matrix

{q} – global displacement vector

The principal of virtual work is then utilized to determine the element stiffness matrix in the form:

$$[K] = \int_{1}^{\Omega} [B]^T [C][B] d\Omega \tag{3-6}$$

where:

[K] – element stiffness matrix

[C] – material properties (constitutive) matrix

Ω – domain over which integration is preformed

For the analysis of nonlinear materials, such as concrete, the [C] and [B] matrix are not constant and must be evaluated for at the onset and growth of damage.

3.4 CONCRETE DAMAGE PLASTICITY MODEL

The model is a continuum, plasticity-based, damage model for concrete. It uses concepts of isotropic tensile and compressive plasticity to represent the inelastic behaviour of concrete. The model assumes that the two main failure mechanisms are tensile cracking and compressive crushing of the concrete material. Hardening variables are used to represent the extent of damage in concrete and stiffness degradation is quantified to characterize the uniaxial tensile and compressive stress-strain response under loading. The evolution of the yield (or failure) surface is also linked to failure mechanisms under tensile and compressive loading through the hardening variables. A non-associated plastic flow potential is adopted using the Drucker-Pager hyperbolic function to represent flow potential. To improve the convergence rate in the concrete softening and stiffness regimes, a viscoplastic regularization of the constitutive equations using a small viscosity parameter value is used. Detailed discussions of the different aspects of the constitutive model are described below.

3.4.1 Hardening Variables

Damage states in tension and compression are characterized independently by two hardening variables, $\tilde{\varepsilon}_t^{pl}$ and $\tilde{\varepsilon}_c^{pl}$, which are referred to as equivalent plastic strains in tension and compression, respectively. The evolution of the hardening variables is given by an expression of the form:

$$\tilde{\varepsilon}^{pl} = \begin{bmatrix} \tilde{\varepsilon}_t^{pl} \\ \tilde{\varepsilon}_c^{pl} \end{bmatrix} \tag{3-7}$$

where:

$\tilde{\varepsilon}_t^{pl} = \int_0^t \dot{\tilde{\varepsilon}}_t^{pl} dt$ - equivalent tensile plastic strain

$\tilde{\varepsilon}_c^{pl} = \int_0^t \dot{\tilde{\varepsilon}}_c^{pl} dt$ - equivalent compressive plastic strain

$\dot{\tilde{\varepsilon}}_t^{pl}, \dot{\tilde{\varepsilon}}_c^{pl}$ - equivalent tensile and compressive plastic strain rates, respectively

Under uniaxial loading conditions the effective tensile and compressive plastic strain rates are given, respectively, as:

$$\dot{\tilde{\varepsilon}}_t^{pl} = \dot{\varepsilon}_{11}^{pl} \text{ and } \dot{\tilde{\varepsilon}}_c^{pl} = -\dot{\varepsilon}_{11}^{pl}. \tag{3-8}$$

Micro-cracking and crushing in the concrete are represented by increasing values of the hardening variables. These variables control the degradation of the elastic stiffness and the evolution of the yield surface. They are also closely related to the dissipated fracture energy required to generate micro-cracks.

3.4.2 Damage and Stiffness Degradation

The modeling of crack initiation and propagation is one of the most important aspects in the failure analysis of concrete structures. The crack process in concrete is distinguished from cracking of other materials, such as metal and glass, in that it is not a sudden onset of new free surfaces but a continuous forming and connecting of microcracks. Typically, the formation of

microcracks is represented macroscopically as softening behavior of the material, which causes the localization and redistribution of strain in a structure. Whereas the behavior at the macroscopic level can be modeled by classical plasticity theory, the microcracking process in concrete causes stiffness degradation that is difficult to represent with classical plasticity. To overcome this, stiffness degradation is be modeled by defining a relationship between stresses and effective stresses, as in continuum damage mechanics. The Cauchy stress is used to relate effective stress through a damage degradation variable, d.

The damage variable replaces the usual 'hardening variable' in classical plasticity theory, and is similar to the latter in that it never decreases and increases if and only if plastic deformation takes place. The plastic-damage variable cannot increase beyond a limiting value and the attainment of this value at a point of the solid represents total damage, which can be interpreted as the formation of a macroscopic crack. Since the degradation of the elastic stiffness is significantly different between tension and compression, two independent uniaxial damage variables, d_t and d_c, are introduced as:

$$d_t = d_t(\tilde{\varepsilon}_t^{pl}, \theta, f_i) \qquad (0 \le d_t \le 1), \tag{3-9}$$

$$d_c = d_c(\tilde{\varepsilon}_c^{pl}, \theta, f_i) \qquad (0 \le d_c \le 1), \tag{3-10}$$

where:

$\tilde{\varepsilon}_t^{pl}$, $\tilde{\varepsilon}_c^{pl}$ - tensile and compressive plastic strain, respectively

θ - temperature

The stiffness degradation is isotropic and the damage variables can take values ranging from zero, for the undamaged material, to one, for the fully damaged material.

The stress-strain relations are governed by scalar damage elasticity:

$$\sigma = [D]^{el} : (\varepsilon - \varepsilon^{pl}) \tag{3-11}$$

where:

$[D]^{el} = (1-d)[D]_0^{el}$ - degraded elastic stiffness

$[D]_0^{el}$ - initial (undamaged) elastic stiffness

The effective stress is defined as:

$$\bar{\sigma}_{eff} \overset{def}{=} [D]_0^{el} : (\varepsilon - \varepsilon^{pl}). \tag{3-12}$$

The Cauchy stress is related to the effective stress through the scalar degradation relation:

$$\sigma = (1-d)\bar{\sigma}_{eff} \tag{3-13}$$

For any given cross-section of the material, the factor (1 - *d*) represents the ratio of the effective load-carrying area (i.e. overall area minus damaged area) to the overall section area. In the absence of damage (*d* = 0) the effective stress is equivalent to the Cauchy stress. However, when damage occurs, the effective stress is more representative than the Cauchy stress because it is the effective stress area that is resisting the external loads. Thus, it is more convenient to formulate the plasticity problem in terms of the effective stress.

The uniaxial tensile and compressive stress-strain response of concrete is characterized by damage plasticity as shown in Figure 3.2. Under uniaxial tension the stress-strain response follows a linear elastic relationship until the value of the failure stress, σ_{t0}, is reached. The failure stress corresponds to the onset of micro-cracking in the concrete material. Beyond the failure stress the formation of micro-cracks is represented macroscopically with a softening stress-strain response, which induces strain localization in the concrete structure. Under uniaxial compression the response is linear until the value of initial yield, σ_{c0}. In the plastic regime, the response is typically characterized by stress hardening followed by strain softening beyond the ultimate stress, σ_{cu}.

If E_0 is the initial (undamaged) elastic stiffness of the material, the stress-strain relations under uniaxial tension and compression loading are, respectively:

$$\sigma_t = (1 - d_t) E_0 (\varepsilon_t - \tilde{\varepsilon}_t^{pl}), \tag{3-14}$$

$$\sigma_c = (1 - d_c) E_0 (\varepsilon_c - \tilde{\varepsilon}_c^{pl}). \tag{3-15}$$

where:

subscripts *c* and *t* represent compression and tension, respectively

$\sigma_t = \sigma_t(\tilde{\varepsilon}_t^{pl}, \dot{\tilde{\varepsilon}}_t^{pl}, \theta)$

$\sigma_c = \sigma_c(\tilde{\varepsilon}_c^{pl}, \dot{\tilde{\varepsilon}}_c^{pl}, \theta)$

$\dot{\tilde{\varepsilon}}_t^{pl}, \dot{\tilde{\varepsilon}}_c^{pl}$ - equivalent plastic strain rates

$\tilde{\varepsilon}_t^{pl} = \int_0^t \dot{\tilde{\varepsilon}}_t^{pl} dt$ - equivalent tensile plastic strain

$\tilde{\varepsilon}_c^{pl} = \int_0^t \dot{\tilde{\varepsilon}}_c^{pl} dt$ - equivalent compressive plastic strain

Under uniaxial loading, cracks propagate in a direction transverse to the stress direction. The nucleation and propagation of cracks therefore results in a reduction of the available load-carrying area, which in turn leads to an increase in the effective stress. This reduction of load-carrying area is similar to the vanishing of cohesion in geomaterials. As it is well know, concrete and geomaterials eventually exhibit strain-softening leading to a complete loss of strength. In this regard, concrete resembles cohesive soils and may be classified as materials with cohesion. The eventual loss of strength may be thought of as the vanishing of the cohesion. With that, we define the 'effective' uniaxial cohesion stresses, $\bar{\sigma}_{eff(t)}$ and $\bar{\sigma}_{eff(c)}$, which are used to determine the size of the yield (or failure) surface, as:

$$\bar{\sigma}_{eff\,(t)} = \frac{\sigma_t}{(1-d_t)} = E_0(\varepsilon_t - \tilde{\varepsilon}_t^{pl}), \tag{3-16}$$

$$\bar{\sigma}_{eff\,(c)} = \frac{\sigma_c}{(1-d_c)} = E_0(\varepsilon_c - \tilde{\varepsilon}_c^{pl}). \tag{3-17}$$

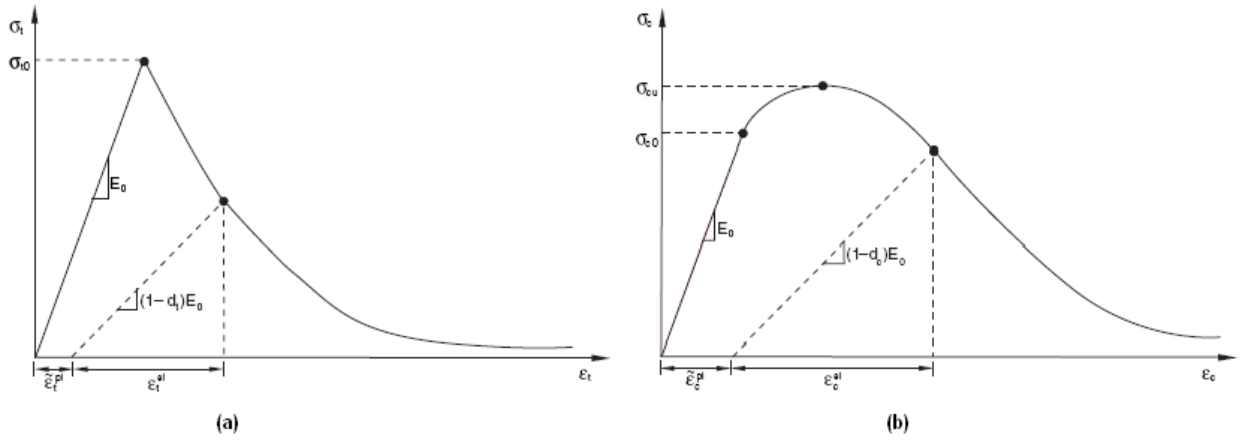

Figure 3.2: Response of concrete to uniaxial loading in (a) tension and (b) compression.

3.4.3 Yield Function

The plastic-damage concrete model uses a yield function proposed by Lubliner et al. (1989) and incorporates the modifications proposed by Lee and Fenves (1998) to account for different evolution of strength under tension and compression. The evolution of the yield (or failure) surface is controlled by two hardening variables, $\bar{\varepsilon}_t^{pl}$ and $\bar{\varepsilon}_c^{pl}$, linked to failure mechanisms under tension and compression, respectively.

In terms of effective stresses, the yield function takes the form:

$$F\left(\bar{\sigma}, \bar{\varepsilon}^{pl}\right) = \frac{1}{1-\alpha}\left[\bar{q} - 3\alpha\bar{p} + \beta\left(\bar{\varepsilon}^{pl}\right)\left\langle\hat{\bar{\sigma}}_{\max}\right\rangle - \gamma\left\langle-\hat{\bar{\sigma}}_{\max}\right\rangle\right] - \bar{\sigma}_c\left(\bar{\varepsilon}_c^{pl}\right) \le 0 \tag{3-18}$$

where:

$\bar{p} = -\frac{1}{3}\bar{\sigma} : \mathrm{I}$ - effective hydrostatic pressure

$\bar{q} = \sqrt{\frac{3}{2}\bar{\mathrm{S}} : \bar{\mathrm{S}}}$ - Mises equivalent effective stress

$\bar{S} = \bar{p}I + \bar{\sigma}$ - deviatoric part of effective stress tensor $\bar{\sigma}$

$\bar{\sigma}_t, \bar{\sigma}_c$ - effective tensile and compressive cohesion stresses, respectively

$\hat{\bar{\sigma}}_{max}$ - maximum principle effective stress

$$\beta\left(\bar{\varepsilon}^{pl}\right) = \frac{\bar{\sigma}_c\left(\tilde{\varepsilon}_c^{pl}\right)}{\bar{\sigma}_t\left(\tilde{\varepsilon}_t^{pl}\right)}\left(1-\alpha\right) - \left(1+\alpha\right),$$

α - dimensionless material constant, $0.08 \le \alpha \le 0.12$ (Lubliner et al., 1989)

$\gamma = \dfrac{3(1-K_c)}{2K_c - 1}$ - dimensionless material constant

$K_c = \bar{q}_{(TM)} / \bar{q}_{(CM)}$; $0.5 \le K_c \le 1.0$ (as shown in Figure 3.3)

$\bar{q}_{(TM)}$ - ratio of second stress invariant on tensile meridian

$\bar{q}_{(CM)}$ - ratio of second stress invariant on compressive meridian

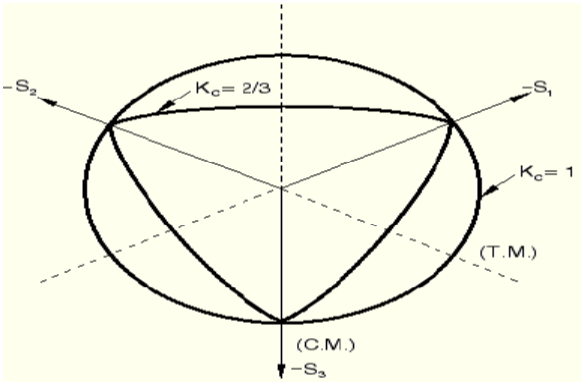

Figure 3.3: Yield surfaces in the deviatoric plane, corresponding to different values of K_c (Abaqus Theory Manual, 2007).

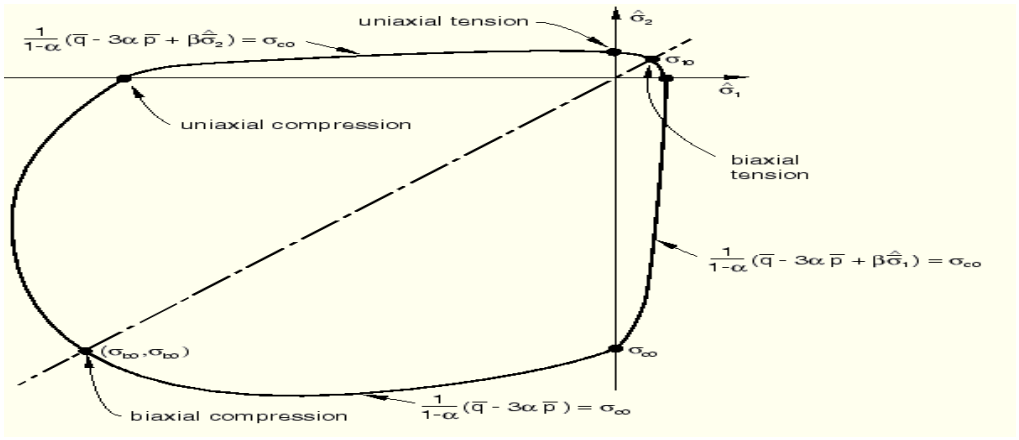

Figure 3.4: Yield surface in plane stress (Abaqus Theory Manual, 2007).

3.4.4 Flow Rule

The plastic-damage model assumes non-associated potential flow,

$$\dot{\varepsilon}^{pl} = \dot{\lambda}\frac{\partial G(\bar{\sigma})}{\partial \bar{\sigma}}. \tag{3-19}$$

The flow potential, G, chosen for this model is the Drucker-Prager hyperbolic function:

$$G = \sqrt{(\text{ə}\,\sigma_{to}\tan\psi)^2 + \bar{q}^2} - \bar{p}\tan\psi, \tag{3-20}$$

where:

ψ - dilation angle measured in the p-q plane at high confining pressure

σ_{to} - uniaxial tensile stress at failure

ə - eccentricity,

The parameter eccentricity, ə, defines the rate at which the function approaches the asymptote (the flow potential tends to a straight line as the eccentricity tends to zero). This flow potential, which is continuous and smooth, ensures that the flow direction is defined uniquely. The function asymptotically approaches the liner Drucker-Prager flow potential at high confining pressure stress and intersects the hydrostatic pressure axis at 90˚. Because plastic flow is

nonassociated, the use of the plastic-damage concrete model requires the solution of nonsymmetric equations.

3.4.5 Viscoplastic Regularization

Material models exhibiting softening behavior and stiffness degradation often lead to severe convergence difficulties in implicit analysis programs. To overcome these convergence difficulties a viscoplastic regularization of the constitutive equations is adopted to permit stresses to be outside of the yield surface. The stress-strain relation of the viscoplastic model is given as:

$$\sigma = (1 - d_v)\mathrm{D}_0^{el} : (\varepsilon - \varepsilon_v^{pl}) \tag{3-21}$$

where:

$\dot{\varepsilon}_v^{pl} = \frac{1}{\mu}(\varepsilon^{pl} - \varepsilon_v^{pl})$ - viscoplastic strain rate tensor

$\dot{d}_v = \frac{1}{\mu}(d - d_v)$ - viscous stiffness degradation rate variable

μ - viscosity parameter

ε^{pl} - plastic strain

d_v - viscous stiffness degradation variable

d - degradation variable

3.5 CLASSICAL METAL PLASTICITY

A classical metal plasticity model is used for the nonlinear material effects of steel reinforcement cast in concrete. Incremental theory is used in the plasticity model to relate load, deformation and stress nonlinearity once yielding has occurred. For an arbitrary load history, the final state of stress and deformation can be determined by accounting for the history of stress and strain. The history is taken into account by formations that relate increments of stress to increments of strain.

The model utilizes a von Mises yield criterion, associated plastic flow rule, and isotropic hardening.

Increments of strain consist of recoverable (elastic) and non-recoverable (plastic) components. In its integrated form, strain in expressed as:

$$\varepsilon = \varepsilon^{el} + \varepsilon^{pl} \tag{3-22}$$

where:

ε - total strain

ε^{el} - elastic strain

ε^{pl} - inelastic (plastic) strain

The elastic strain component is linear, isotropic, and written in terms of two dependent material properties: bulk modulus, K, and shear modulus, G, defined as:

$$K = \frac{E}{3(1-2v)} \tag{3-23}$$

$$G = \frac{E}{2(1+v)} \tag{3-24}$$

where:

E – Young's Modulus

G – Shear Modulus

v – Poisson's ratio

3.5.1 Yield Criterion

The initiation of plastic deformation commences when the material reaches the von Mises (effective) stress, expressed as:

$$F = \sigma_e \tag{3-25}$$

where:

F – yield function

σ_e - von Mises (effective) stress

$$\sigma_e = \frac{1}{\sqrt{2}}\left[(\sigma_x - \sigma_y)^2 + (\sigma_y - \sigma_z)^2 + (\sigma_z - \sigma_x)^2 + 6(\tau_{xy}^2 + \tau_{yz}^2 + \tau_{xz}^2)\right]^{1/2}$$

$\sigma_x, \sigma_y, \sigma_z$ - normal stresses in x, y, z direction, respectively

τ_x, τ_y, τ_z - shear stresses in x, y, z direction, respectively

The stress state is represented as the sum of a hydrostatic and deviatoric state. A hydrostatic state produces no changes of shape and a deviatoric state produces no change of volume. Deviatoric shear stress are the same as actual shear stress, while deviatoric normal stresses are actual normal stresses minus the mean normal stress, σ_m, defined as:

$$\{s_N\} = \begin{Bmatrix} s_x \\ s_y \\ s_z \end{Bmatrix} = \begin{Bmatrix} \sigma_x - \sigma_m \\ \sigma_y - \sigma_m \\ \sigma_z - \sigma_m \end{Bmatrix} = \frac{1}{3}\begin{Bmatrix} 2\sigma_x - \sigma_y - \sigma_z \\ 2\sigma_y - \sigma_x - \sigma_z \\ 2\sigma_z - \sigma_y - \sigma_x \end{Bmatrix} \tag{3-26}$$

$$\{s_\tau\} = \begin{Bmatrix} s_{xy} \\ s_{yz} \\ s_{zx} \end{Bmatrix} = \begin{Bmatrix} \tau_{xy} \\ \tau_{yz} \\ \tau_{zx} \end{Bmatrix} \tag{3-27}$$

where:

$\sigma_m = \dfrac{\sigma_x - \sigma_y - \sigma_z}{3}$ - mean normal stress

s_N - normal deviatoric stress

s_τ - shear deviatoric stress

In terms of deviatoric stress, σ_e has the form:

$$\sigma_e = \sqrt{\frac{3}{2}}\left[s_x^2 + s_y^2 + s_z + 6(s_{xy}^2 + s_{yz}^2 + s_{xz}^2)\right]^{1/2} \tag{3-28}$$

3.5.2 Flow Rule

The flow rule relates the state of stress, $\{\sigma\}$, to size increments of plastic strain, $\{d\varepsilon^p\}$, when an increment of plastic flow occurs. The flow rule is stated in terms of a function Q, which has units of stress and is referred to as a *plastic potential*. Plastic strain increments are given by:

$$\{d\varepsilon^p\} = \left\{\frac{\partial Q}{\partial \sigma}\right\} d\lambda \tag{3-29}$$

where:

$d\lambda$ - scalar plastic multiplier

If Q=F, the flow rule is referred to as *associated* and *non-associated* otherwise. Associated rules are commonly used for ductile metals, whereas non-associated rules are better suited to soil and granular materials. Thus, the von Mises theory adopts associate plasticity.

The plastic multiplier has the form:

$$d\lambda = [P_\lambda]\{d\varepsilon\} \tag{3-30}$$

where P_λ is the row matrix and can be expressed as:

$$[P_\lambda] = \frac{\left\{\frac{\partial F}{\partial \sigma}\right\}^T [E]}{\left\{\frac{\partial F}{\partial \sigma}\right\}^T [E]\left\{\frac{\partial F}{\partial \sigma}\right\} + H_p} \tag{3-31}$$

where H_p is the strain-hardening parameter expressed as:

$$H_p = \frac{E_t}{1 - \frac{E_t}{E}} \tag{3-32}$$

where:

E_t - tangent (plastic) modulus

$$\left\{\frac{\partial F}{\partial Q}\right\} = \frac{3}{\sigma_e}\left(\frac{1}{2}\begin{Bmatrix} s_N \\ 0 \end{Bmatrix} + \begin{Bmatrix} 0 \\ s_\tau \end{Bmatrix}\right) \tag{3-33}$$

3.5.3 Hardening Rule

The hardening rule describes how the yield criterion is modified by straining beyond initial yield. The model adopts isotropic hardening and is represented by plastic work per unit volume, W_p, which describes growth of the yield surface expressed as:

$$W_p = \int \{\sigma\}^T \{d\varepsilon^p\} \tag{3-34}$$

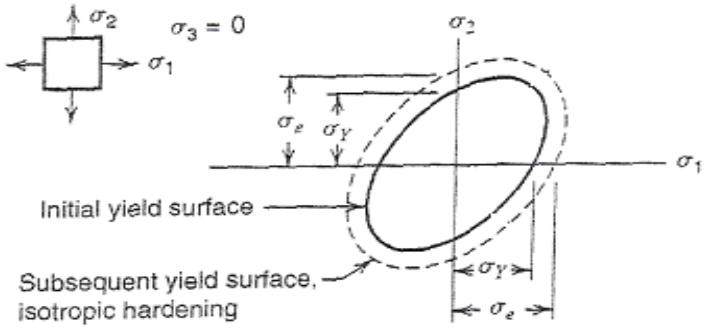

Figure 3.5: Isotropic hardening case for plane stress with nonzero principle stresses σ_1 and σ_2 (Cook et al., 2002).

3.5.4 Element Stiffness Matrix

The element formulation stiffness matrix using classical plasticity theory is then defined as:

$$[K] = \int [B]^T [E_{ep}][B] dV \tag{3-35}$$

where:

$[K]$ – plasticity stiffness matrix

$[B]$ – strain-displacement matrix

$[E_{ep}]$ – elastic-plastic matrix

When yielding has yet to appear, the elastic-plastic matrix is simply set the initial elastic modulus of the material $[E]$, such as:

$$[E_{ep}] = [E]. \tag{3-36}$$

When yielding has occurred, the matrix is expressed as:

$$[E_{ep}] = [E]\left([I] - \left\{\frac{\partial Q}{\partial \sigma}\right\}[P_{\lambda}]\right) \tag{3-37}$$

where:

$[I]$ – unit matrix.

3.6 TRACTION-SEPARATION FOR BONDED INTERFACES

Interface elements are used to model the bond mechanism between concrete and rebar, and FRP and concrete. The modeling of progressive damage and failure of the interface elements are defined in terms of traction-separation as shown in Figure 3.6. The model describes initial loading, initiation of damage, and propagation of damage leading to eventual failure at the bonded interface.

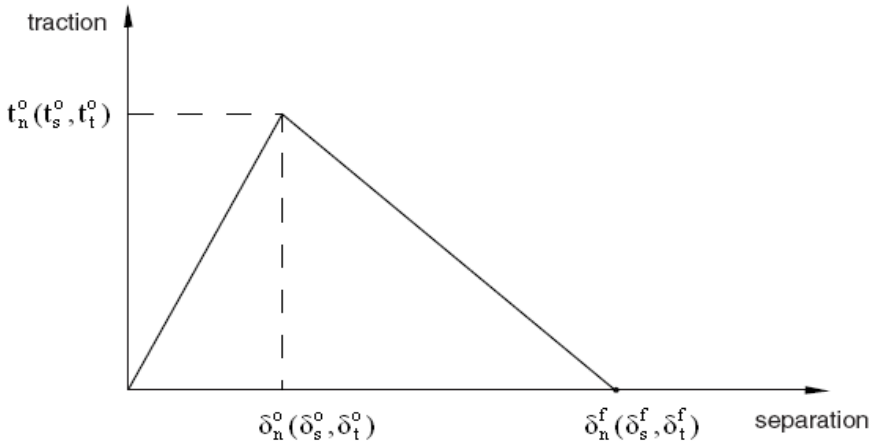

Figure 3.6: Traction-separation response (Abaqus Analysis User's Manual, 2007).

3.6.1 Initial Loading

The behavior of the interface prior to initiation of damage is described as linear-elastic in terms of a penalty stiffness that degrades under tensile and/or shear loading. The elastic behavior is written in terms of an elastic constitutive matrix that relates the nominal stresses to the nominal strains across the interface. The nominal stresses are the force components divided by the original area at each integration point, while the nominal strains are the separations divided by the original thickness at each integration point.

The nominal traction stress vector, $\boldsymbol{t}$, consists of two components in two-dimensional problems: t_n, t_s, which represent the normal and shear traction, respectively. The corresponding separations are denoted by δ_n and δ_s. The elastic behavior is then expressed as:

$$t = \begin{Bmatrix} t_n \\ t_s \end{Bmatrix} = \begin{bmatrix} K_{nn} & K_{ns} \\ K_{ns} & K_{ss} \end{bmatrix} \begin{Bmatrix} \varepsilon_n \\ \varepsilon_s \end{Bmatrix} \tag{3-38}$$

$$\varepsilon_n = \frac{\delta_n}{T_0}, \varepsilon_s = \frac{\delta_s}{T_0} \tag{3-39}$$

where:

$\varepsilon_n, \varepsilon_s$ - normal and shear strain, respectively

T_0 - original thickness of interface element

3.6.2 Initiation of Damage

Damage initiation refers to the beginning of degradation of the response of a material point. The process of degradation is assumed to initiate when the maximum nominal stress ratio reaches a value of one, and represented as:

$$\max\left\{\frac{\langle t_n \rangle}{t_n^0}, \frac{t_s}{t_s^0}\right\} = 1 \tag{3-40}$$

where:

t_n^0, t_s^0 - peak values of normal and shear traction, respectively

3.6.3 Damage Evolution

The damage evolution law describes the rate at which the material stiffness is degraded once the corresponding initiation criterion is reached. There are two components to the definition of the evolution of damage: effective displacement and damage variable. The first component involves specifying either the effective displacement at complete failure, δ_m^f, relative to the effective displacement at the initiation of damage, δ_m^0; or the energy dissipated due to failure, G^C, as shown in Figure 3.7. An effective displacement is introduced to describe the evolution of damage under a combination of normal and shear deformation across the interface as:

$$\delta_m = \sqrt{\langle \delta_n \rangle^2 + \delta_s^2}. \tag{3-41}$$

The second component is the specification of the evolution of the damage variable, *d*, between the initiation of damage and final failure. The scalar damage variable represents the overall damage in the material as it evolves from 0 (undamaged) to 1 (fully-damaged). The evolution of the damage law is characterized using a linear softening law proposed by Camanho and Davila (2002), defined as:

$$d = \frac{\delta_m^f (\delta_m^{\max} - \delta_m^0)}{\delta_m^{\max} (\delta_m^f - \delta_m^0)} \tag{3-42}$$

where:

$\delta_m^{\max}$ - maximum value of the effective displacement attained during the loading history

δ_m^0 - effective displacement at initiation of damage

δ_m^f - effective displacement at complete failure

The stress components of the traction-separation model are affected by the damage according to:

$$\begin{aligned} t_n &= (1-d)\bar{t}_n \\ t_s &= (1-d)\bar{t}_s \end{aligned} \tag{3-43}$$

where:

$\bar{t}_n, \bar{t}_s$ - normal and shear stress components predicted by the elastic traction-separation behaviour for the current strains without damage

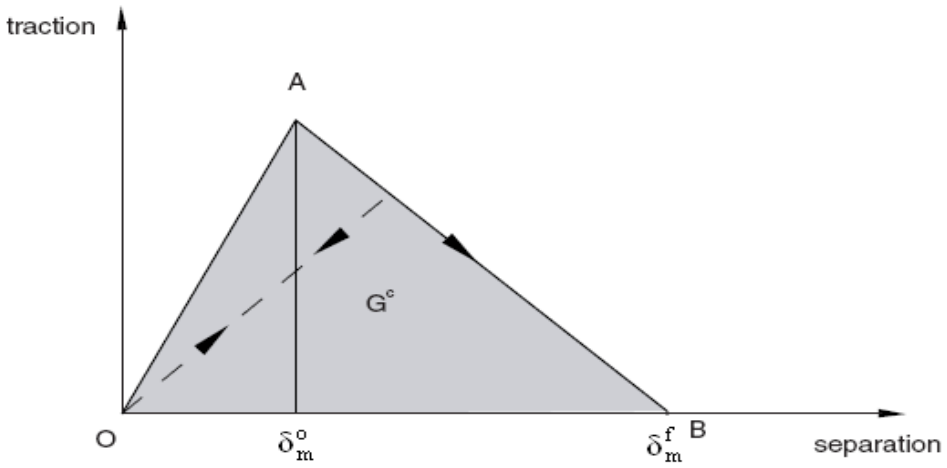

Figure 3.7: Linear damage evolution (Abaqus Analysis User's Manual, 2007).

3.7 ELEMENTS

The structural member is modeled as a mesh of finite elements. A wide range of elements are available in ABAQUS. Among these, continuum elements are the most comprehensive as they can be used in almost any linear/nonlinear stress-displacement and crack propagation analysis. Both two- and three-dimensional (2D and 3D) continuum elements are available however, 2D continuum elements can adequately investigate the behavior of the beams in this research. The 2D elements can be either triangular (3 or 6 nodes) or quadrilateral (4 or 8 nodes). Since, reinforcement cannot be modeled with triangular elements quadrilateral elements were opted for in this investigation.

Continuum elements are provided with first-order (linear) and second-order (quadratic) interpolation and careful consideration must be decided as to which is more appropriate for the application. First-order elements use linear interpolation to obtain displacements at nodes, whereas second-order elements use quadratic interpolation to obtain displacements at nodes. ABAQUS offers two integration options for the number of Gauss points required to integrate the polynomial terms in an element's stiffness matrix: "full" and "reduced". Fully-integrated linear and quadratic elements use two and three integration points in each direction as shown in Figure 3.8, respectively.

Figure 3.8: Integration points in fully-integrated, two-dimensional, quadrilateral elements (Abaqus User's Manual, 2007).

In the analysis of flexural members, fully-integrated linear elements suffer from a phenomenon referred to as 'shear locking' that has been found to produce inaccurate results. Since first-order elements use linear interpolation to obtain nodal displacements, the edges of these elements are unable to curve under bending resulting in shear rather than bending deformation as shown in Figure 3.9(a). Shear locking is not a problem for quadratic elements since their edges are able to curve through the use of quadratic interpolation as shown in Figure 3.9(b).

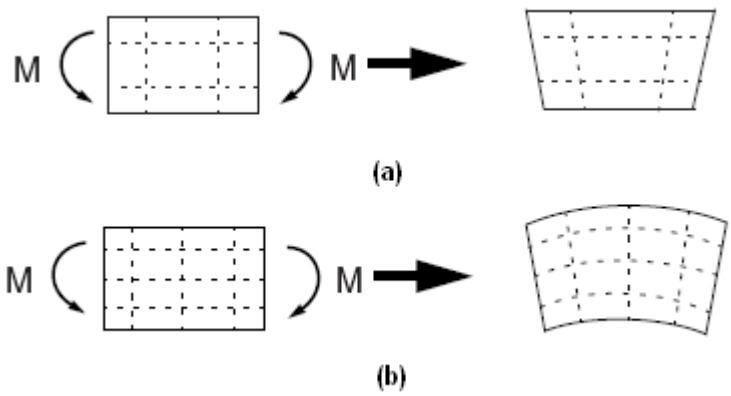

Figure 3.9: Deformation of fully-integrated: (a) linear element, (b) quadratic element subjected to bending moment, M (Abaqus User's Manual, 2007).

To overcome shear locking for linear elements and reduce overall computational effort, ABAQUS offers reduced-integration elements, which use one fewer integration point in each direction than the fully integrated elements as shown in Figure 3.10. On the surface, this appears to be a poor approximation, but it has proven to offer significant advantages. First, the reduced integration elements are located at points that provide optimal stresses and strains; the so-called Barlow points (Barlow, 1976). A second advantage is that the reduced integration points decrease the computation effort and storage requirements. The disadvantage is that the reduced integration procedure can admit deformation modes that cause no straining at the integration points. These zero-energy modes make the element rank-deficient and cause an occurrence known as 'hour glassing,' where the zero energy mode starts propagating through the mesh, leading to inaccurate solutions. This problem is particularly severe in first-order elements by making the elements too flexible. Figure 3.11 considers a linear reduced-integration element subject to pure bending. Neither of the dotted visualization lines has changed in length, and the angle between them is also unchanged, which means that all components of stress at the element's single integration point are zero. Thus, this bending mode of deformation produces a zero-energy mode since no strain energy is generated by this element distortion. The element is

unable to resist this type of deformation because it does not contain stiffness in this mode. To overcome this, a small amount of artificial 'hourglass stiffness' is introduced in first-order reduced-integration elements to limit the propagation of the hourglass mode. This stiffness is more effective at limiting hourglass modes when more elements are introduced in the model. Thus, linear reduced elements have been found to provide acceptable results as long as a reasonably fine mesh is used. While it is generally recommended to use the highest-order elements available should be used to obtain accurate results, first-order reduced-integration elements are selected in this analysis for their ability to support severe distortion and proven success when used in plasticity models, such as the Concrete Damage Plasticity model employed in the analysis. Linear reduced-integration elements are very tolerant of distortion when a fine mesh is employed, and have been found to be the best choice in where geometric nonlinearities exist (Abaqus Theory Manual, 2007). As the solution approaches the limit load in plasticity applications, most plasticity models tend toward hyperbolic behaviour (diverge exponentially). This allows discontinuities to occur in the solution (such as the slip line solutions of classical perfect plasticity theory which are plots of the characteristic lines of velocity discontinuities in the hyperbolic equations of the problem). If the finite element solution is to exhibit accuracy, these discontinuities in the gradient field of the solution should be reasonably well modeled. With a fixed mesh that does not use special elements that admit discontinuities in their formulation, this suggests that the lowest-order elements (linear) are likely to be the most successful because, for a given number of nodes, they provide the most locations at which some component of the gradient of the solution can be discontinuous (the element edges). This argument is hardly rigorous, but it holds true that first-order elements tend to be preferred for such cases and are thus adopted for this research.

Figure 3.10: Integration points in two-dimensional elements with reduced integration (Abaqus User's Manual, 2007).

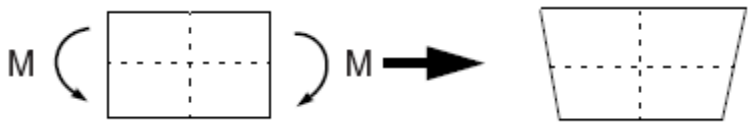

Figure 3.11: Deformation of linear reduced-integration element subject to bending moment, M (Abaqus User's Manual, 2007).

4 MODELLING APPROACH

A CFRP-strengthened RC beam subjected for four-point loading tested by Brena et al. (2003) was analyzed using the commercial finite element program ABAQUS Version 6.7-2. The constitutive modelling, analysis approach, verification of the finite element model, and special modeling considerations and modifications are outlined in this chapter.

4.1 CONSTITUTIVE MODELS

The constitutive relationships for the concrete, steel, and FRP are entered through the ABAQUS formulations, as described in detail in Chapter 3.0. The following covers the material models employed to describe each component.

4.1.1 Concrete

The compressive stress-strain behavior of concrete is simulated using a uniaxial nonlinear constitutive model proposed by Hogenstad (1950). This model is attractive due to its relative simplicity as well as its accuracy for concrete with strengths up to 60MPa (MacGregor and Bartlett, 2000). It consists of an ascending quadratic stress-strain curve followed by a linear descending branch as shown in Figure 4.1. The peak concrete stress is defined as f_c'', and the strain corresponding to the maximum stress is ε_{c0}. The peak compressive stress used in the model is the product of a constant, *k*, and the compressive stress determined from the concrete cylinder tests, f_c'. The constant, *k*, is defined as the ratio of the compressive stress as determined from compression concrete cylinders tests to the maximum compressive stress reached in the concrete in the actual member, and is commonly found to be 0.9 (Hognestad et al., 1955). The model then follows a linearly descending branch with increasing strain until the maximum usable strain in the concrete is reached, ε_{cu}. The stress corresponding to the maximum concrete strain is assumed to be equal to 85 percent of the peak stress with a limiting strain of

0.0035. The stress-strain relations derived from the Hogenstad model are then incorporated into the concrete damage plasticity formulation as described in Section 3.4. The equations that describe the behaviour of concrete in compression for different regions of the stress-strain diagram are defined as:

$$f_c = f_c''\left[\frac{2\varepsilon_c}{\varepsilon_{c0}} - \left(\frac{\varepsilon_c}{\varepsilon_{c0}}\right)^2\right] \qquad \text{for } 0 \le \varepsilon_c \le \varepsilon_{c0} \tag{4-1}$$

$$f_c = f_c''\left[1 - 0.15\left(\frac{\varepsilon_c - \varepsilon_{c0}}{\varepsilon_{cu} - \varepsilon_{c0}}\right)\right] \qquad \text{for } \varepsilon_{c0} \le \varepsilon_c \le \varepsilon_{cu} \tag{4-2}$$

$$\varepsilon_{c0} = \frac{2f_c''}{E_c} \qquad f_c'' = 0.9f_c' \tag{4-3}$$

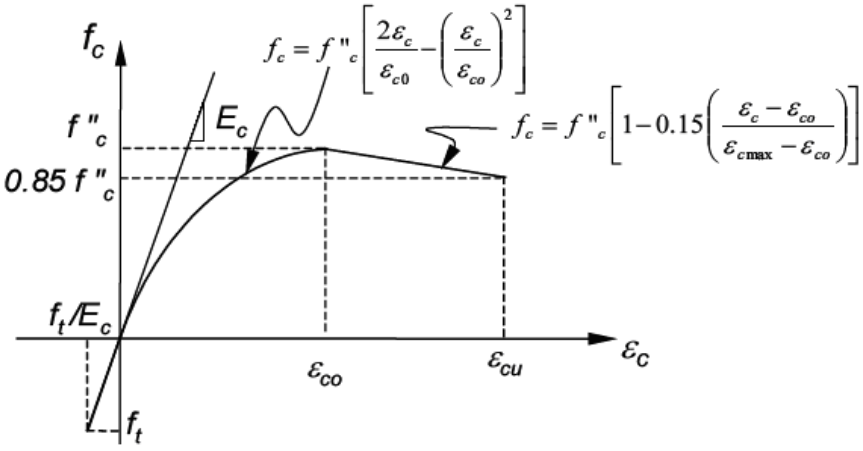

Figure 4.1: Constitutive model for compressive concrete.

The tensile behavior of concrete is assumed to exhibit a linear elastic behaviour until the ultimate tensile stress, f_t', is reached. Beyond this point, a linear softening branch commonly referred to as 'tension-stiffening' is adopted. This assumes that the concrete between the cracks still carries a certain amount of stress and has been studied by many investigators (Scanlon and Murray, 1974; Lin and Scordelis, 1975, Link et al. 1989). Rather than characterizing the tensile

behaviour in terms of a stress-strain response, a stress-displacement response is adopted using Hillerborg's (1976) fracture energy proposal. Hillerborg (1976) defines the energy required to open a unit of area of crack, G_f^c, as a material parameter using brittle fracture concepts. Under tension, a concrete specimen will crack across some section. After it has been pulled apart sufficiently for most of the stress to be removed, its length will be determined primarily by the opening at the crack. The model adopted to simulate the tensile behaviour is illustrated in Figure 4.2 and defined as:

$$f_t' = 0.62\sqrt{f_c'}$$

$$u_o = f_t' / E_0' \tag{4-4}$$

$$u_{ot} = 2G_f^c \Big/ f_t^{'}$$

where:

f_t' - ultimate tensile strength

u_o - corresponding crack width at ultimate tensile strength

u_{ot} - ultimate crack width corresponding to zero stress

E_c - initial elastic modulus

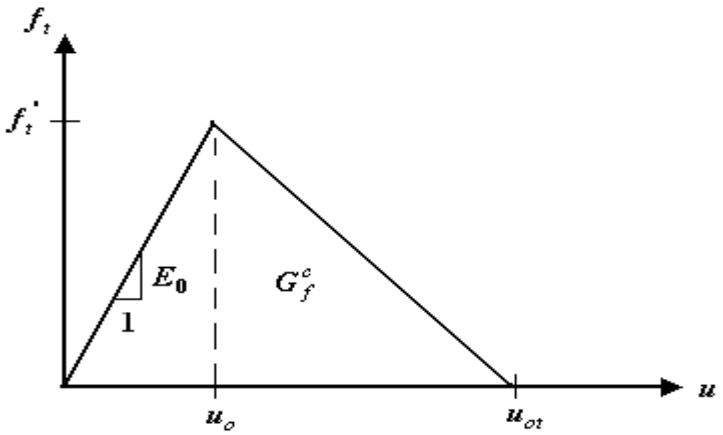

Figure 4.2: Constitutive model for tensile concrete.

4.1.2 Reinforcing Steel

The stress-strain relationship for reinforcing steel with a well-defined yield point was idealized using three linear segments. The elastic modulus for the initial slope in the stress-strain curve, E_s, was assumed to be 200 MPa. After reaching the yield strain, ε_y, the slope of the stress-strain curve was assumed to equal to zero until the strain corresponding to initiation of strain hardening, ε_{sh}, was reached. The strain-hardening behavior of the reinforcement was modeled using a- positive slope beginning at ε_{sh}, as shown in Figure 4.3. The strain-hardening slope, E_{sh}, was assumed to be equal to 5% of the initial elastic modulus. The reinforcing steel is modeled with use of the classical metal plasticity model outlined in Section 3.5.

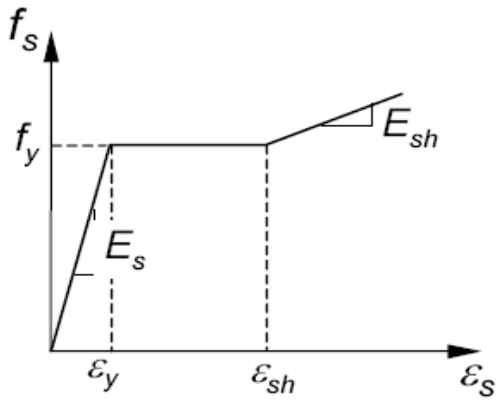

Figure 4.3: Idealized stress-strain relationship for reinforcing steel.

4.1.3 Fiber Reinforced Polymer Composites

The uniaxial behaviour of the FRP composites used in this study are assumed to be linear-elastic until failure with no post peak or ductile behaviour. Failure in these materials is reached when the strain, ε_{pu}, corresponding to failure reaches its rupture stress, f_{pu}, as shown in Figure 4.4. Since the FRP is used primarily to carry tensile forces, it has stiffness in only one direction (along the fibres), thus no lateral and shear resistance is observed. Based on the experimental

data of Brena et al. (2003) the FRP was noted to have E_p, f_{pu}, and ε_{pu} values of 230GPa, 3800MPa, and 0.015, respectively.

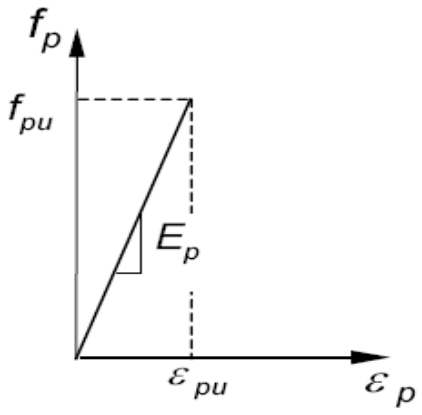

Figure 4.4: Idealized stress-strain relationship for FRP composites.

4.2 ANALYSIS MODEL

The modelling approaches considered and then ultimately selected in the investigation are outlined in this section using the finite element method.

4.2.1 Discretization of Structure

The structural member is broken down into finite elements to model the composite beam. Since more than one type of material and interfaces are considered in the analysis, different types of finite elements are required to discretize the structure. The concrete is modeled using continuum elements; the reinforcing steel and FRP materials are modeled using beam elements; and the rebar-concrete and FRP-concrete interfaces are modeled using cohesive/interface elements, as represented in Figure 4.5. Linear reduced-integration continuum elements are employed throughout the analysis with a fine mesh for their ability to withstand severe distortion in plasticity and crack propagation applications, as explained in Section 3.8. Furthermore, since cohesive elements can only be defined as linear elements in ABAQUS, it was convenient that the surrounding elements are also first-order. Otherwise the computationally expensive "tie

constraints" would have had to be assigned at all cohesive-concrete interfaces to ensure mesh compatibility. Tie constraints are used to fuse together regions with dissimilar meshes and/or geometry, and significantly increase computational effort since master and slave surface definitions are required, as explained in Section 3.7.1. Plane strain condition was assumed throughout the analysis, as covered in Section 4.2.3.

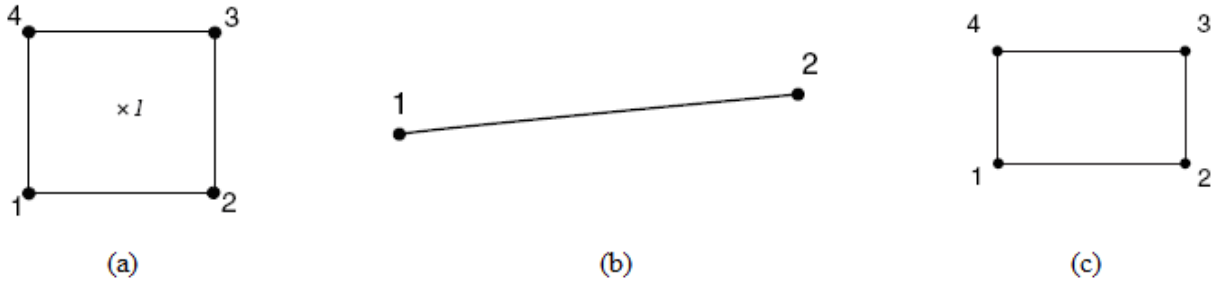

Figure 4.5: Analysis elements - (a) linear reduced-integration; (b) two-node linear beam; (c) cohesive/interface.

4.2.2 Boundary Conditions

Due to symmetry, only half of beam was modeled in two-dimensions. Load was applied in the form of an imposed displacement at the top face of the specimen. A displacement-controlled load was selected for the analysis to capture the response of the beam beyond its peak load. A pin-support was used to restrain the beam in the vertical direction. Figure 4.6 illustrates the boundary conditions employed in the study.

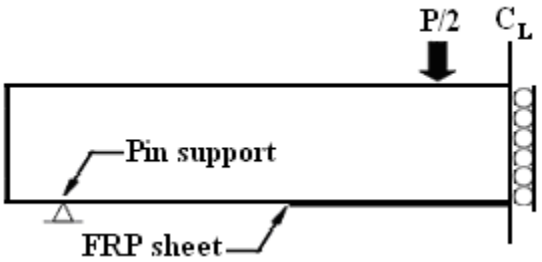

Figure 4.6: Boundary conditions.

4.2.3 State of Stress

Anderson (1994) pointed out that the condition at a crack tip is "neither plane stress nor plane strain, but three-dimensional." This can be more clearly explained by considering the plastic zone that surrounds the crack tip using the principles of linear elastic fracture mechanics (LEFM).

LEFM was originally developed to describe crack growth and fracture under essentially elastic conditions. In this case, plasticity is confined to a very small region surrounding the crack tip. However, such conditions are met only for fracture of high strength metallic materials and for fracture of intrinsically brittle materials like ceramics, glasses, and rocks (Janssen et al., 2006). According to the linear elastic stress field solution some stress components tend to infinity in the vicinity of the crack tip. However real materials, such as concrete, cannot support the theoretically infinite stresses, so that upon loading the crack tip region deforms plastically and the equivalent stress remains close to the material yield limit. This means that there is always a region around the crack tip, where plastic deformations occur. The near crack tip plastic region is commonly referred to as the *plastic zone* and the size and shape of the plastic zone is affected by the state of stress: plane stress or plane strain. Figure 4.7(a) provides a good illustration of such effects. An explanation of this occurrence can be further explained by considering a section through a plate in the plane of a crack as shown in Figure 4.7(b). With no strain hardening, the material within the plastic zone should be able to flow freely and contract in the thickness direction. However, this adjacent (and surrounding) elastic material cannot contract to the same extent. This phenomenon is referred to as *plastic constraint* and leads to tensile stresses in the thickness direction on the plastic zone boundary as shown in Figure 4.7(b). Moreover, it creates a tri-axial stress condition which, when unrelieved by deformation, would

correspond to plane strain. For these reasons, it is of interest to investigate the state of stress in the crack tip region for the specimen.

Simple calculation of the stress state distribution for a certain plate thickness is not possible (Janssen et al., 2006). However, there are *empirical* rules for estimating whether the condition is predominantly plane stress or plane strain (Janssen et al., 2006):

1. Full plane stress may be expected if the calculated size of the plane stress plastic zone (i.e. $2r_y$ in Irwin's analysis) is of the order of plate thickness.
2. Predominately plane strain may be expected when the calculated size of the plane stress plastic zone, $2r_y$ (the approximate value at the plate surfaces), is no larger than one-tenth of the plate thickness.

Such an analysis was performed and it was found that *plain strain* conditions prevail, as found in the appendix.

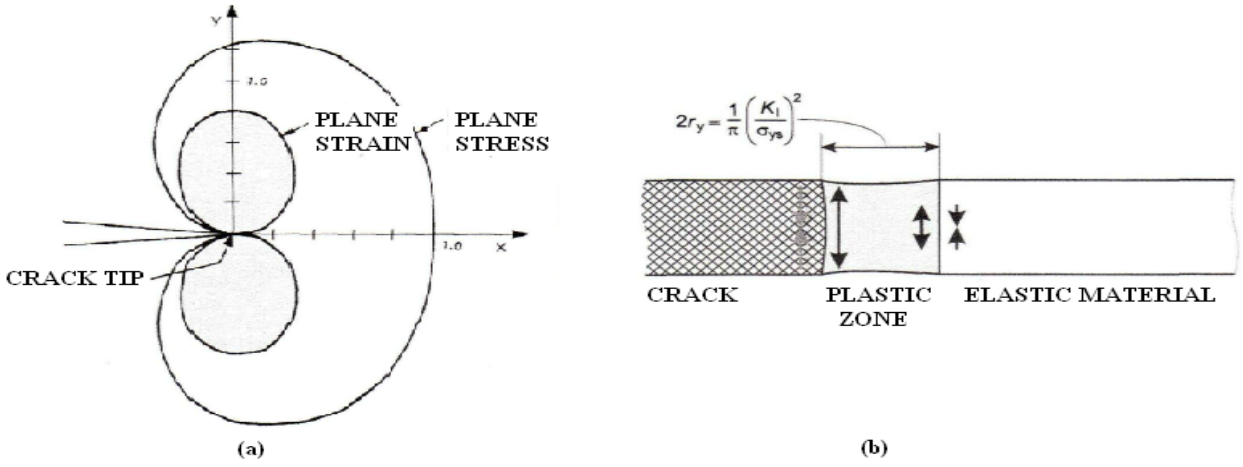

Figure 4.7: (a) Dimensionless plastic zone shapes; (b) Schematic sketch in the crack plane (Janssen et al., 2006).

4.2.4 Composite Modeling

A general approach to model the composite behaviour of the FRP-RC beam is to select suitable constitutive models to represent each material component separately and then obtain their

combined effects by properly modeling the interaction between the materials. The following outlines the methods and techniques applied to best simulate composite behaviour for the reinforcing steel, FRP, and FRP-concrete interface.

Steel Reinforcement Modeling

To account for the effect of the steel reinforcement in the finite element analysis, three modeling techniques have been commonly employed: embedded, smeared, and discrete definitions. The embedded reinforcing technique was first proposed by Phillips and Zienkiewcz (1976). With this approach, the reinforcing layer is aligned with one of the local isoparametric element coordinate axis. Generally, the reinforcing bar is considered to be an axial member built into the concrete element in such a way that its displacements are compatible with those of surrounding concrete elements. The advantage of the embedded model is that it allows independent choice of the concrete mesh. The disadvantage is that the additional nodes required for the reinforcement increase the total number of degrees of freedom (DOF) and the computation effort. Thus, this approach was not selected for the investigation.

In the smeared reinforcing model, the reinforcements are assumed to be distributed uniformly over the element. Perfect bond between the concrete and reinforcement is assumed and the constitutive relations can be derived from the composite theory. The advantage of the smeared model is that it can be used very efficiently for representing uniformly distributed reinforcement. The disadvantage is that it cannot accurately capture bond degradation with applied loading and is not very effective handling cases when the rebar is sparsely located in the concrete member. As a result, this approach was not selected for the analysis because of the perfect bond assumption between the concrete and steel. Some researchers have employed this

assumption, as noted in Chapter 2.0, even though this is not the case in reality, especially during large inelastic deformations, as expected in this study.

The discrete reinforcing model was first suggested by Ngo and Scordelis (1967) and later modified by Nilson (1968). In this model, a one-dimensional bar element is superimposed on a two-dimensional element. This model has the advantage of representing different material properties more precisely that the previous two approaches. The disadvantages are that the finite element mesh patterns are restricted by the location of the reinforcement and it is numerically less efficient that the other models. However, since the contribution of the reinforcing steel is a crucial component in the overall response of the composite beam, the discrete reinforcing model was selected in the analysis as it best represents the rebar properties and interaction of the rebar with the surrounding concrete. It also enables direct calculation of the forces within the rebar, which will be needed for the interpretation of the results.

Thus, the reinforcing steel is modeled as one-dimensional beam elements discretely defined and superimposed onto the 'host' concrete element through the use of stringer elements in the ABAQUS library. This essentially means that the concrete mechanical properties were negligible in these areas as these elements were completely filled with reinforcing steel. The stringer element allows the definition of the beam element to be defined with a circular cross-section to represents that of the rebar. The main rebar (compressive and tensile) were surrounded by interface elements to consider slippage between rebar and concrete as shown in Figure 4.9. Preliminary analyses revealed that the global response of the beam is better represented when slippage of the rebar is considered in the model. This is attributed to the fact that a bond transfer mechanism is created when the concrete bears on the lugs of the deformed bars as shown in Figure 4.10. The action of the lugs against concrete produces incline cracks at

relatively low bond stresses. To simulate this interaction, the relationship between bonding stress, τ_b, and relative displacement, S, was defined according to the CEB-FIB model code (CEB-FIB, 1993), as shown in Figure 4.11. On the other hand, stirrups were modeled assuming perfect bond between the steel and concrete. This was considered to be an acceptable assumption to reduce computation effort since the beam is loaded in flexure and not expected to fail in shear.

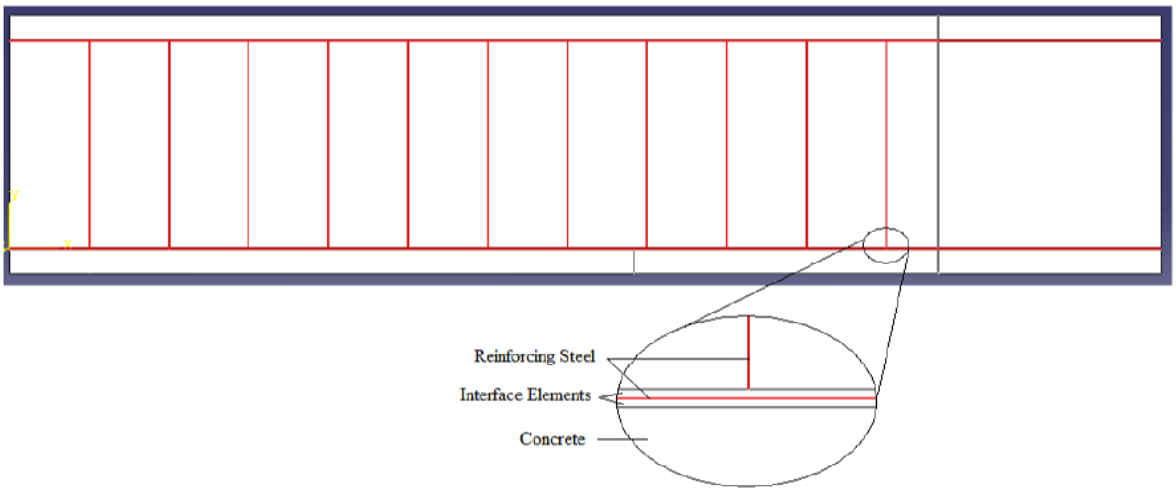

Figure 4.9: Snapshot of rebar-concrete interface modeling.

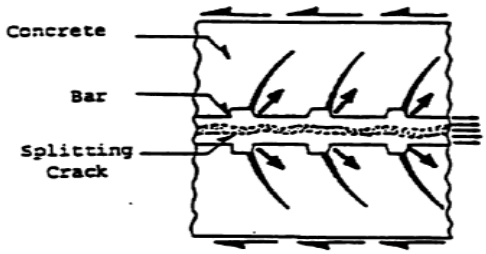

Figure 4.10: Incline cracks at steel lugs (Soroushian et al., 1991).

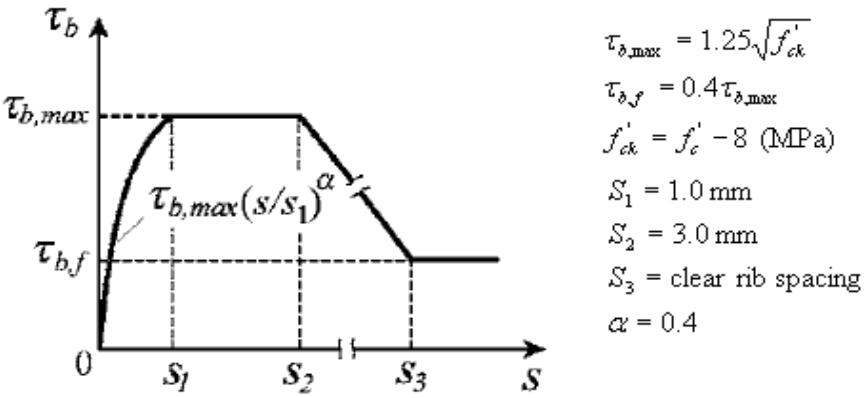

Figure 4.11: Stress-relative displacement relations for rebar slippage (CEB-FIB, 1993).

FRP Composite Modeling

The FRP composites are modeled as singly defined beam elements attached to the concrete specimen through interface elements. The FRP and interface layers are modeled as a single part attached to the concrete substrate through the use of "tie constraints". A tie constraint essentially unites two regions with dissimilar geometries and/or meshes together so that there is no relative motion between them. They are incorporated in the model since the FRP, and therefore the interface debonding elements, do not span the same length as the concrete specimen. Additionally, the interface debonding elements requires a more refined mesh than the concrete substrate for adequate modeling of interfacial crack propagation as later noted in Chapters 5 and 6. With this technique, each of the nodes on the refined mesh has the same displacement as the point on the coarse mesh to which it is closest. A schematic representation of FRP, interface, and concrete attachment is shown in Figure 4.12. At each end of the interface element, the interaction between the two nodes is represented by two springs: the shear spring with stiffness, k_s^{int}, and the normal (tension-compression) spring with stiffness, k_n^{int}.

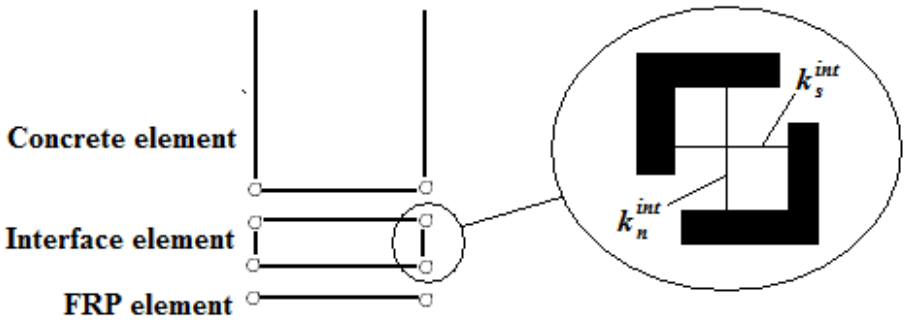

Figure 4.12: Schematic representation of FRP-concrete interface connection.

FRP-Concrete Interface Modeling

The interface between the FRP and concrete plays a critical role in providing stress transfer from the concrete to the FRP. In this study, the FPR-concrete interface refers to a thin layer of the

adhesive and adjacent concrete within which the relative deformation between FRP and concrete mainly happens, as revealed by experimental studies (Yuan et al., 2004). Section 2.6 outlined the importance of considering the FRP-concrete interface in numerical studies, and as a result the interface is incorporated in this research. Various bond stress-slip relationships for the FRP-concrete interface have been proposed. Despite past research efforts, a common consensus of a single model has not been achieved mainly due to the many factors which influence the bond behaviour, such as the concrete strength, FRP thickness and stiffness, relative stiffness of FRP and steel reinforcement, epoxy thickness, and mechanical properties of the resin. Among the proposed relationships, numerous researches (Homan, Sato, Nanni, Lee, and Wong and Vecchio) have employed either linear-elastic or elastic-plastic models for the FRP-concrete interface despite numerous experimental studies showing that stress deformation relationship of the interface is nonlinear (Chajes et al., 1995, 1996; Biziindavyi and Neale, 1999; dai et al., 2005; Yao et al., 2005). The stress deformation relationship is generally referred to as bond-slip law in literature since the deformation of interface is mainly the relative displacement (slip) between the FRP and the concrete beam. Generally, this nonlinear relationship consists of two stages: an initially elastic stage in which the interfacial stress increases with the slip until it reaches a maximum value, and a softening stage in which the interfacial stress decreases with slip. Existing solutions of FRP debonding fail to consider this softening stage of the interface and therefore, are limited to elastic analysis and cannot be used to simulate debonding growth (Wang, 2006). By considering a nonlinear bond-slip law, it is possible to model the whole debonding process of FRP-concrete interface as demonstrated recently by Yuan et al. (2004).

A simplified bilinear bond curve with softening behaviour was employed to simulate the real FRP-concrete bond behaviour, as shown in Figure 4.13. The bond-slip relationship is

idealized with a well defined yield stress, τ_{max}, and corresponding slip, S_0. The elastic modulus for the initial slope, K_0, is defined as:

$$K_0 = \frac{K_a K_c}{K_a + K_c} \tag{4-5}$$

where:

$K_a = G_a / t_a$

$K_c = G_c / t_c$

G_a, G_c - shear modulus of adhesive and concrete, respectively

t_a, t_c - thickness of adhesive and concrete, respectively

The thickness of the concrete, t_c, is the effective thickness of concrete whose deformation forms part of the interfacial slip. Lu et al. (2005) investigated its effect and found that a thickness of 5mm provides the best prediction of the bond-slip curve. Thus, the thickness of concrete was assumed to equal 5mm throughout the study. When τ_{max} is achieved, the stress transfer decreases linearly to zero. The area under the curve is defined as the interfacial fracture energy, G^c. This model is capable of simulating the bond behaviour regardless of whether debonding occurs within the concrete substrate or within the adhesive layer. The difference only lies in the choice of parameters: local bond strength, initial stiffness, and fracture energy, which are each individually investigated in Section 5.0.

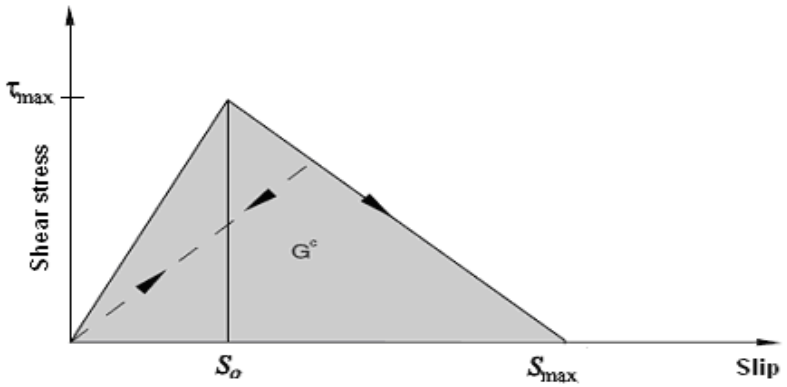

Figure 4.13: FRP-concrete interface model definition.

4.3 MODEL VERIFICATION

Brena et al. (2003) performed an experimental investigation to study the response of a FRP-RC strengthened beam subjected to IC debonding failure. To simulate this type of failure, the beam was fabricated with a crack initiator in the form of a piece of sheet metal positioned under one of the point loads to provide a fixed location of the first flexural crack. The sheet metal extended the entire width of the beam and was 6.35mm deep. The beam was 200 mm wide, 350 mm deep, and 2890 mm deep as shown in Figure 4.14. Since this is one of the most comprehensive studies preformed on IC debonding, which it a primary focus of the investigation, it is appropriate that the model be validated against their results. The following analyses were performed to validate the model: reduction from three-dimensional to two-dimensional finite element representation, calibration of individual material models, and composite beam response.

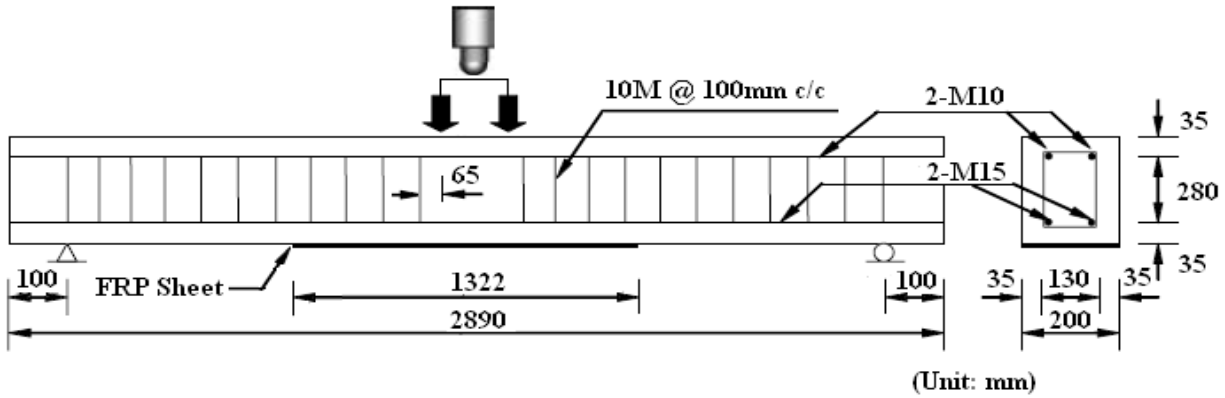

Figure 4.14: Dimensions of calibration model.

4.3.1 3-D to 2-D Finite Element Reduction

Both two-dimensional (2-D) and three-dimensional (3-D) finite element representations have been used by previous researchers to model bonded FRP-concrete specimens. As 3-D models can be computationally demanding, a 2-D model can be an attractive alternative. However, to confirm the validity of the reduction, a comparison between the two models was preformed.

The numerical model was initially modeled three dimensionally. One quarter of the RC beam was modeled with respect to the two symmetrical axes. Figure 4.15 shows a schematic representation of the model. In this model, reinforcing steel and FRP sheet were modeled using eight-node solid elements and concrete was modeled using eight-node and/or six-node solid elements. Stirrups were modeled using as assuming a perfect bond between the concrete and steel. To limit the stress concentration occurring in the concrete elements around the loading and supporting points, elastic steel plates 50 x 100 x 25 mm in dimension were introduced into the numerical analysis and were modeled using eight-node solid elements. Geometrical discontinuities due to opening of dominant cracks, slipping of rebar, and debonding of FRP sheet were taken into account with the discrete crack approach, as noted in Section 4.2, and illustrated in Figure 4.15. Mesh sensitivity was investigated and it was found that a fine mesh of 654, 681 elements was required to obtain convergence and demonstrated in Figure A4.1 of the appendix.

The beam was then reduced to two-dimensions with the same constitutive relations employed as in the three-dimensional model. Only half of the beam was modeled due to symmetry. Mesh sensitivity was investigated and it revealed that a fine mesh of 47,554 elements was required to obtain convergence, as shown in Figure A4.2 of the appendix. Figure 4.16 compares the load-deflection responses of the two- and three-dimensional models. The results from the comparison clearly show that reducing the 3-D model to 2-D can be safely employed

without compromising the integrity of the results. From a computational standpoint, the 2-D model proved to far superior and was selected for the remainder of the analysis.

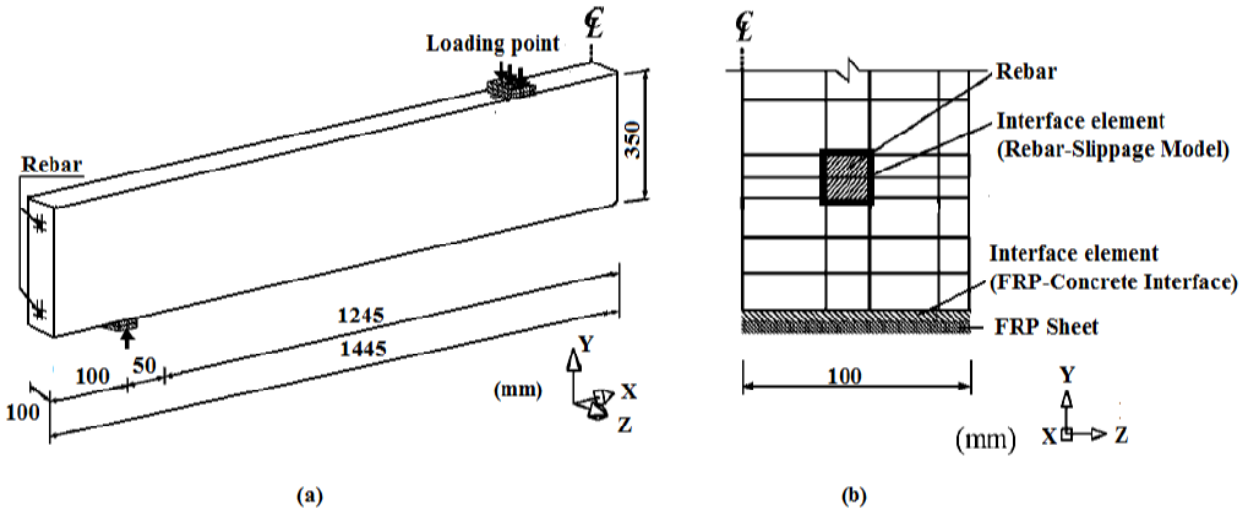

Figure 4.15: Schematic representation of 3-D model (a) Doubly symmetric beam; (b) Cross section around rebar.

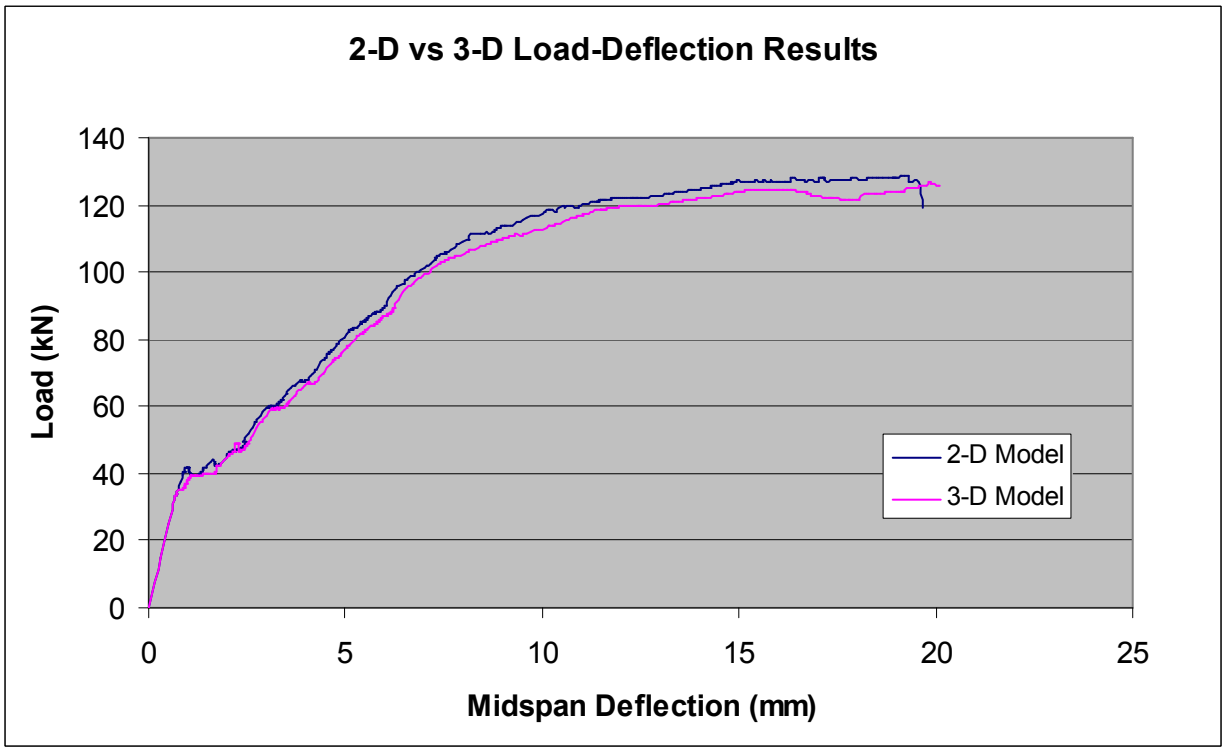

Figure 4.16: Comparison between 2-D and 3-D load-deflection results.

4.3.2 Calibration Results

To validate the finite element model, the numerical results from each material constituent as well as the global response of the composite beam were compared with the results reported by Brena et al. (2003).

Material Modeling

The material properties were numerically tested in accordance with CSA testing procedures to calibrate the yield parameters of the materials. The compressive strength, tensile strength, and elastic modulus of concrete in the calibration model were 35MPa, 3.5MPa, and 26.5GPa, respectively. Details of the material calibration models can be found in the Appendix. Figure 4.17 and 4.18 compare the results of the numerical simulation and experimental data for concrete and reinforcing steel, respectively. Good correlation between the results indicates that the material data entered in the analysis was properly input.

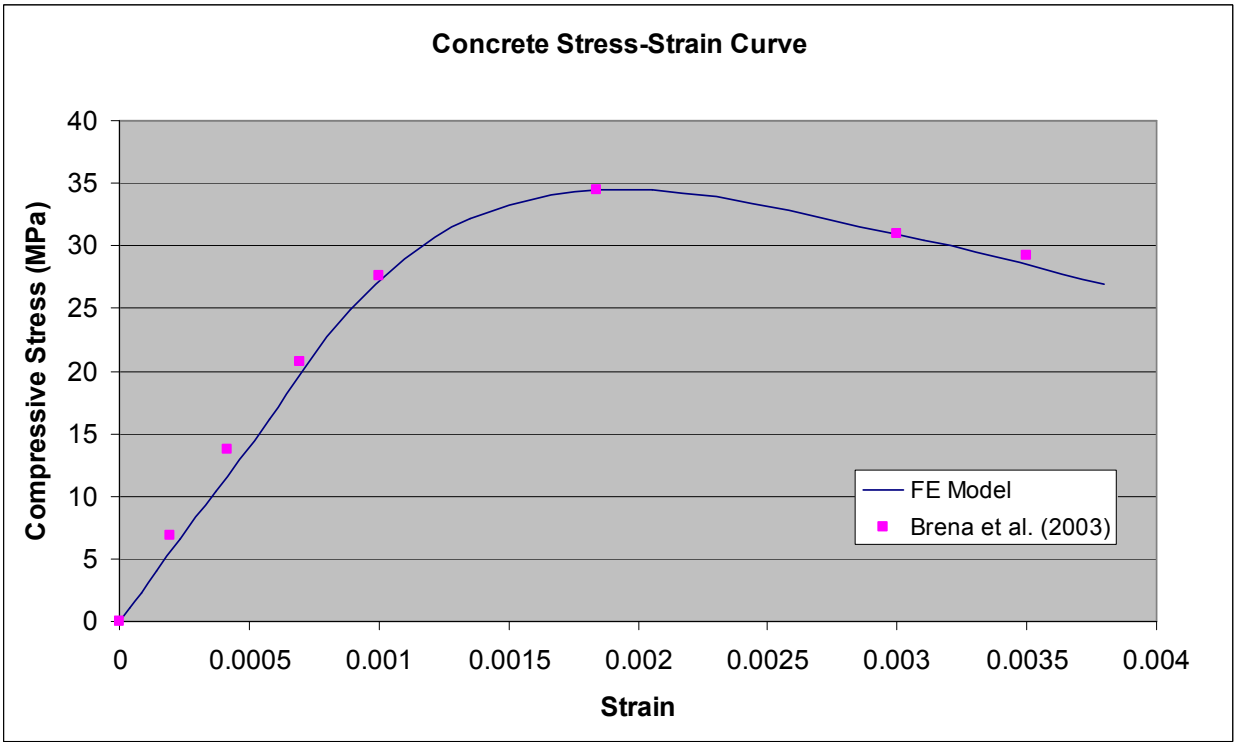

Figure 4.17: Concrete compressive stress-strain material model validation.

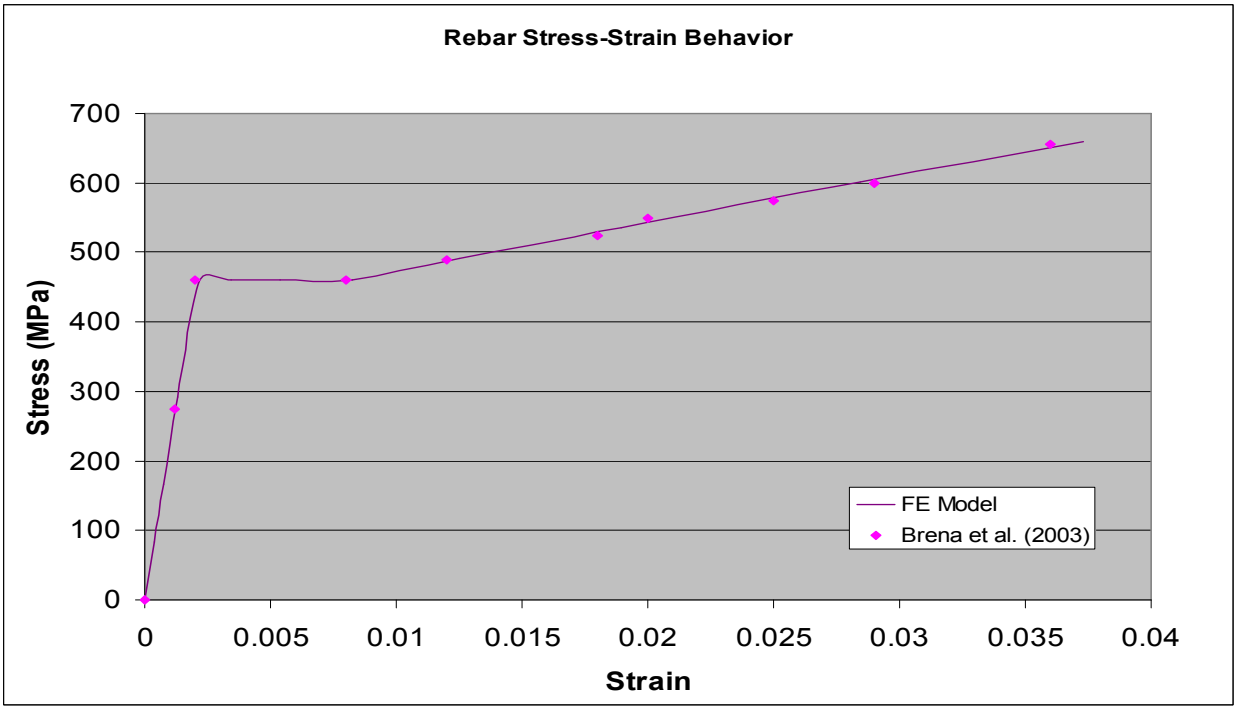

Figure 4.18: Reinforcing steel material validation.

Composite Beam Modeling

The FRP-RC beam was compared to with the experimental results in terms of load-midspan deflection, load-reinforcing steel strain, and load-CFRP strain, as demonstrated in Figures 4.19-4.21, respectively. The model contains 47,554 elements comprised of: 1922 beam (B21), 6871 cohesive (COH2D4), and 38,761 linear reduced-integration (CPR4R) elements. Good correlations between the numerical and experimental results were found indicating that the model is suitable for the remainder of the analysis.

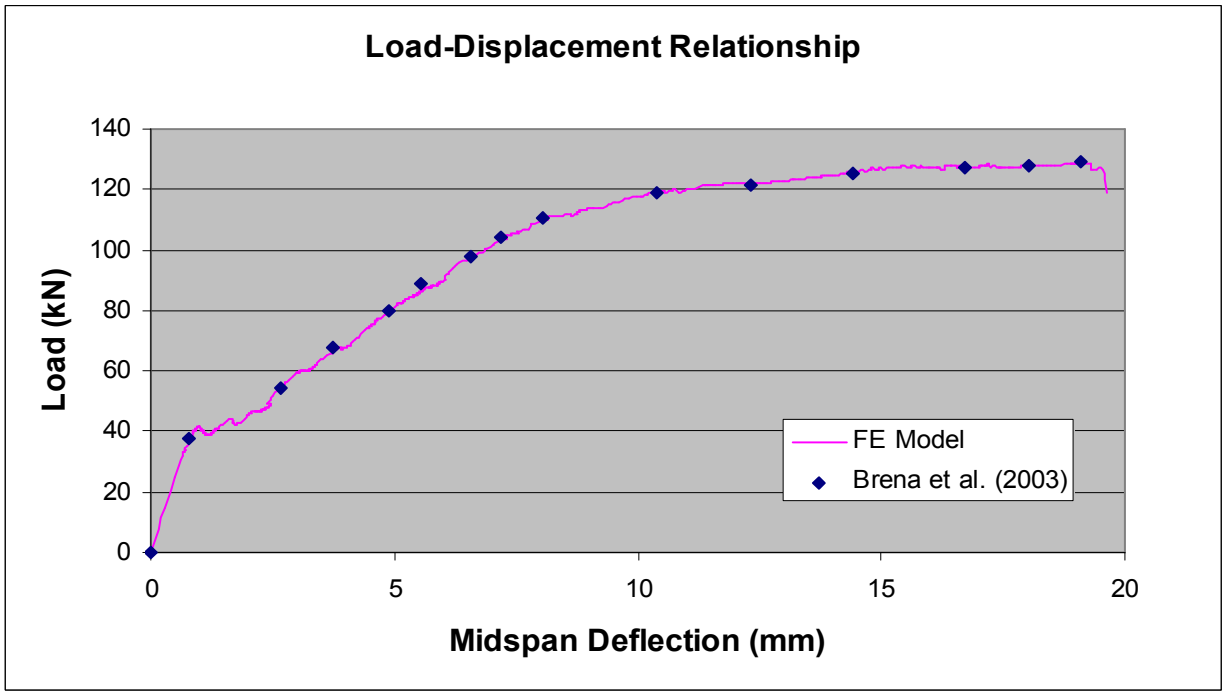

Figure 4.19: Load-deflection model calibration.

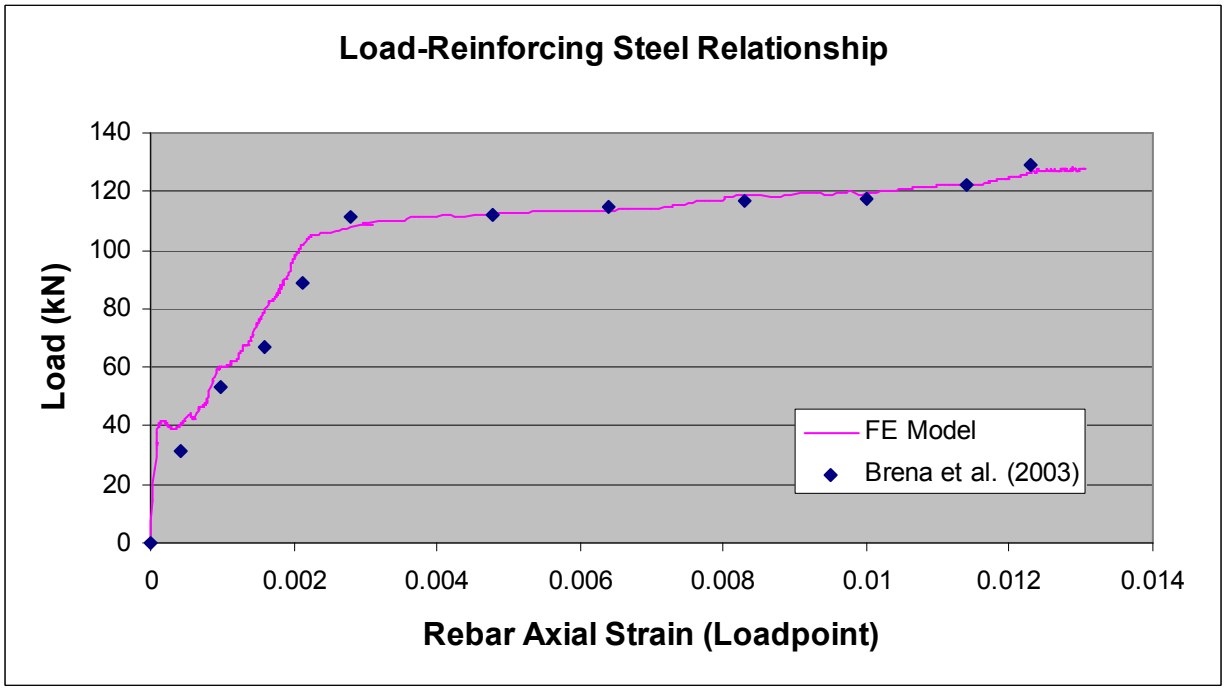

Figure 4.20: Load-reinforcing steel strain for model calibration.

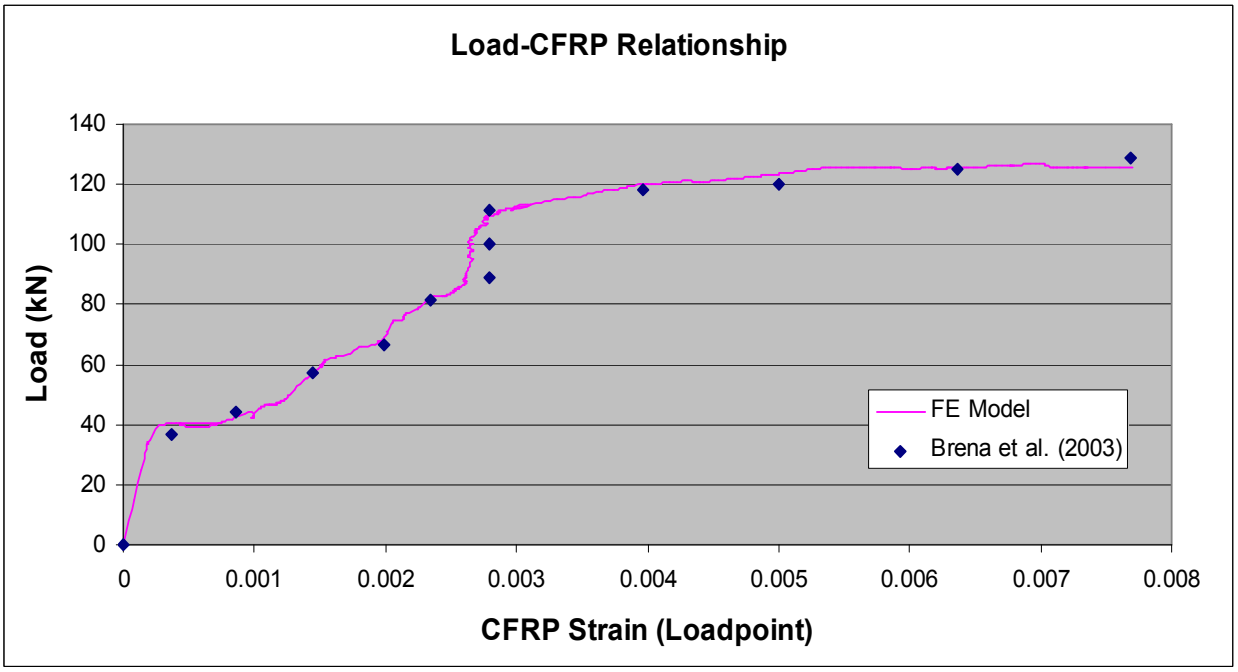

Figure 4.21: Load-CFRP plate strain for model calibration.

4.4 SPECIAL CONSIDERATIONS AND MODIFICATIONS

In the chapters that follow, modifications are made to the calibrated specimen tested by Brena et al. (2003) to investigate numerically how the structural behaviour and debonding mechanisms of FRP-RC strengthened beams are influenced by various intermediate cracks which occur under external loading. As a result, modeling techniques, geometric characteristics, and material properties are modified to carry out the parametric analyses. All revisions to the model are discussed in detailed below.

4.4.1 Concrete Cracking and Interfacial Models

The focus of this investigation is to characterize the debonding behaviour and failure mechanisms caused by cracks which occur from an intermediate crack in the concrete beam. Generally, there are two approaches to simulate fracture process in finite element modeling: a continuum approach and a discrete approach. The continuum approach treats fracture as the end process of localization and accumulation of damage in continuum, without creating a real

discontinuity in the material. The discrete crack approach models a crack discretely as a geometrical entity. The continuum approach, commonly referred as the 'smeared crack approach', has been widely used in finite element applications and was chosen to calibrate the specimen tested by Brena et al. (2003) due to its simplicity and accuracy in representing overall cracking. The continuum approach can efficiently capture the first spreading of micro-cracking in localized regions, such as pre-existing notches, but for increasing levels of damage the model in unable to trace individual macro-cracks because it tends to spread the crack motion over a region of a structure rather than at localized points. This can be overcome if the characteristic dimensions of finite elements are chosen small enough from the beginning of the analysis to accurately resolve the evolving damage zone. This was shown in a study by Lu et al. (2005) where the authors proposed the so-called 'mesoscale FE approach' using the smeared crack approach, as noted in Section 2.6. However, for real-life structures such as beams, the computation costs become excessive and impractical. Thus, the continuum approach was not selected to model dominant cracks in the investigation for its inability to efficiently capture the initiation, propagation and trace exact crack patterns in the beam. Alternatively, the discrete crack approach was selected to simulate the cracking behaviour in the model.

Geometrical discontinuities due to opening of dominant cracks, slipping of rebar, and debonding of the FRP sheet where taken into account with the discrete crack approach. This approach has been modeled using a cohesive zone model (CZM) implemented in the analysis using zero-thickness interface elements, as covered in Section 3.6. By applying appropriate stress-relative displacement or stress-relative energy models to the interface elements, discontinuous failure can be simulated. In this study, three stress-relative displacement models called: discrete cracking, bond-slip, and FRP sheet debonding models are adopted.

The discrete cracking model simulates fracture within the RC beam by predefining possible flexural and shear cracks in the model, depending on the focus of the analysis. Figure 4.22 demonstrates the definition of predefined cracks in the discrete crack model, where possible flexural and shear cracks are divided into two zones: traction-free and cohesive crack. A traction free crack physically represents a 'notch' that would be set in the concrete beam at the time of casting to ensure that cracking initiates at a predefined location. No forces are transferred along this zone and cracks surfaces are completely separated. The forces in cohesive crack surfaces follow a predefined response whereby a linear softening curve is employed to model mode I tension softening of concrete. The cohesive crack, preceding the formation of a real crack, is assumed to initiate if tensile stresses attain the tensile strength of concrete, f_t, whereas the real crack is formed when the energy required to create a unit area of crack is achieved. The area below the curve represents the fracture energy, G_f^c. Unloading and reloading behaviours are modeled by a secant path, which means following a straight line back to the origin upon unloading the stress. After cracking, no shear stress is assumed to be transferred along the crack surface. The concrete had a tensile strength of 3.5 MPa, fracture energy of 100 N/m, and elastic modulus of 26.5GPa.

In the locations other that where discrete cracks are prescribed in advance, the nonlinear behaviour of concrete is modeled by the concrete damage plasticity model, as covered in Section 3.4. To ensure that cracking does not occur in locations other than where the predefined cracks are set, the compressive and tensile material models were defined without limitation of strain capacity, as shown in Figure 4.23. The concrete damage plasticity model employed in the analysis is a smeared crack model; meaning that the model does not physically generate macro-cracks and cracks are indirectly accounted for by the way their presence affects the stress and

material stiffness. The crack process in concrete is not a sudden onset of new free surfaces but a continuous forming and connecting of micro-cracks. Micro-cracking and crushing in the concrete are represented by increasing values of the hardening variables. These variables control the degradation of the elastic stiffness and the evolution of the yield surface. They are also closely related to the dissipated fracture energy required to generate micro-cracks. Typically, the formation of micro-cracks is represented macroscopically as softening behavior of the material, which causes the localization and redistribution of strain in a structure. One way to remove the effects of cracking is to modify the compressive hardening and tensile softening of the material model. Cracking leads to softening behaviour of the material, so if any post-yield softening is removed from the model, the effects of cracking could be avoided in the material thereby only permitting cracking to occur within the predefined locations.

The model used to simulate the rebar-concrete interface has not changed from the calibration model and all properties of the interface remain constant throughout the study. Details can be found in Section 4.2.4.

The FRP-concrete interface model remains the same as the model described in Section 4.2.4. However, the properties making up the model such as interfacial stiffness, bond strength, and fracture energy are parametrically investigated and thus are changed throughout the course of the investigation. Details of the parametric themes can be found in Chapters 5.0 and 6.0. A snapshot of the discrete crack modeling is shown in Figure 4.24.

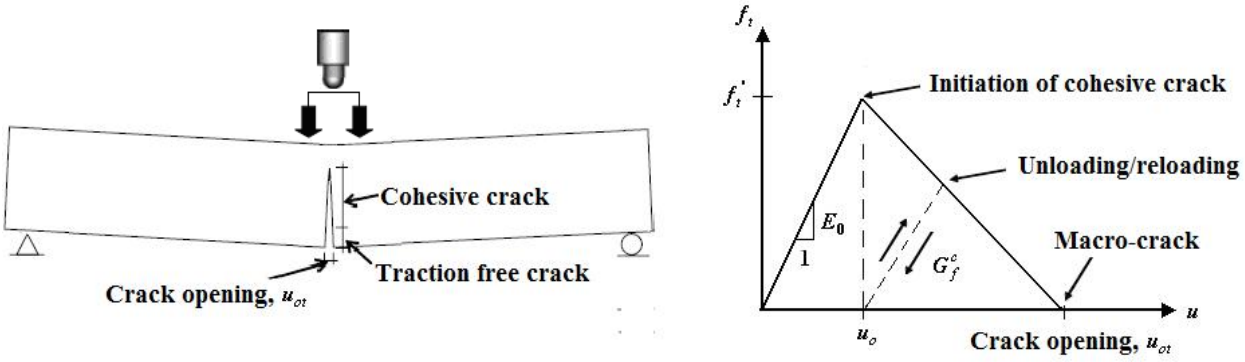

Figure 4.22: Stress-relative displacement relationship of discrete cracking model.

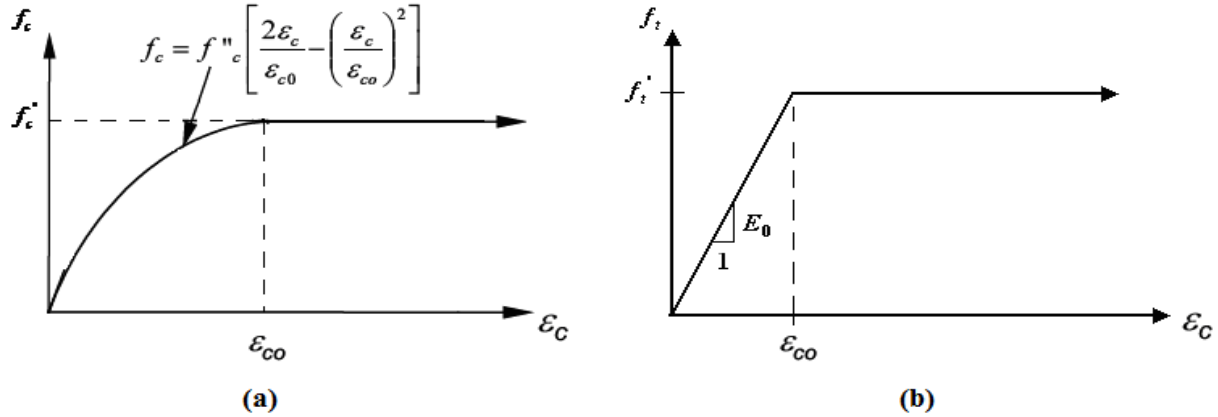

Figure 4.23: Strain hardening behaviour of concrete in (a) compression; (b) tension.

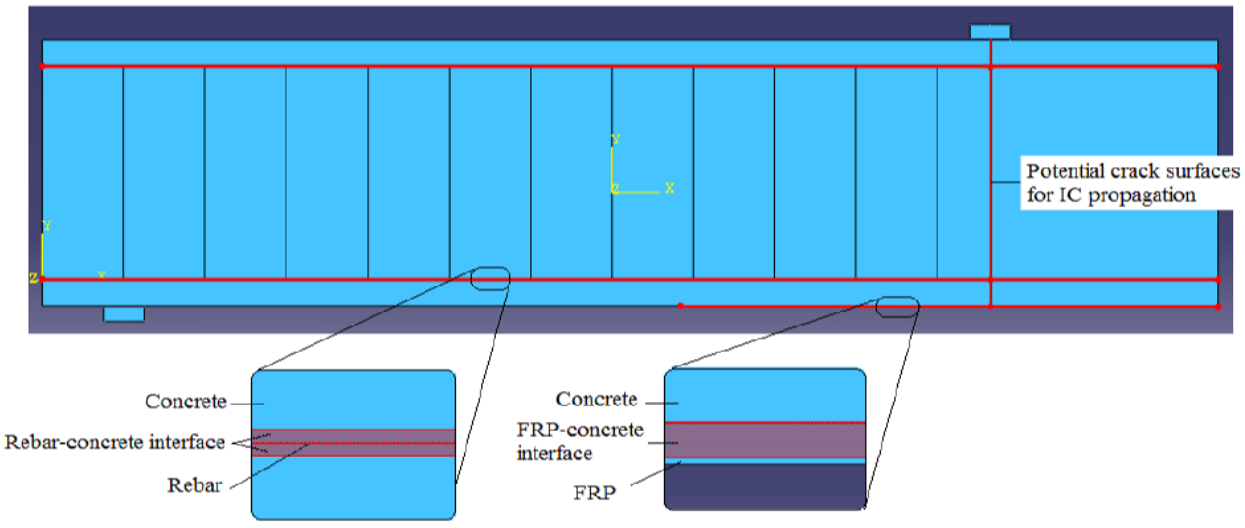

Figure 4.24: Snapshot of discrete crack approach.

4.4.3 Geometric Modifications

The length of the FRP laminate was increased from 1322mm to 2200mm to investigate how debonding initiates and propagates from an intermediate crack towards the support. For simplicity, stirrups, which are used to ensure the beams would not fail in shear, are not considered in the following simulations. To ensure that the removal of stirrups does not result in premature failure of the model due to shear, an investigation into the effect of stirrup removal was performed to study how its removal would influence the outcome of the results. The analysis was evaluated based on load-deflection response, crack growth, and strains in the shear span. Figure 4.25 illustrates that there is virtually no difference in the response of the beam in terms of load-deflection behaviour, with the exception shown at around the midspan deflection of 14mm. The model without the stirrups experiences a drop in load earlier than the model with the stirrups. This can be explained by inspecting the crack formation under loading as shown in Figures 4.26 and 4.27, with and without stirrups, respectively. It appears as if the model containing the stirrups restricts the formation of a dominant crack developing in the shear span, whereas the model without the stirrups allows the crack to migrate towards the load point with less resistance. However, in the analysis that follows, such a crack would not be able to develop since the discrete crack model is employed, thereby not allowing the development of cracks in-between predefined locations. Thus, the removal of the stirrups is not considered to influence outcome of the results and are removed from the model for simplicity. Moreover, other than in locations where two the discrepancies in the fracture was found, the strains in the shear span were found to be nearly identical, as shown in Figure A4.7 and A4.8 of the appendix. A schematic representation of the analysis model after the modifications is shown in Figure 4.28.

It should be noted that in the present analysis, no attempt is made to consider the application of FRP composites to a pre-damaged RC structure. While in practice, many cracks will have already formed with some spacing before the application of FRP composites, a clear explanation on how these cracks may affect the bond characteristics between concrete and FRP and ultimately influence the mode of failure is unavailable (Niu et al., 2007). Without established empirical evidence on this topic, any finite element model created to carry out such an analysis can potentially be contradicted. Thus, a virgin RC beam strengthened with FRP sheets was used to investigate the research themes in subsequent chapters.

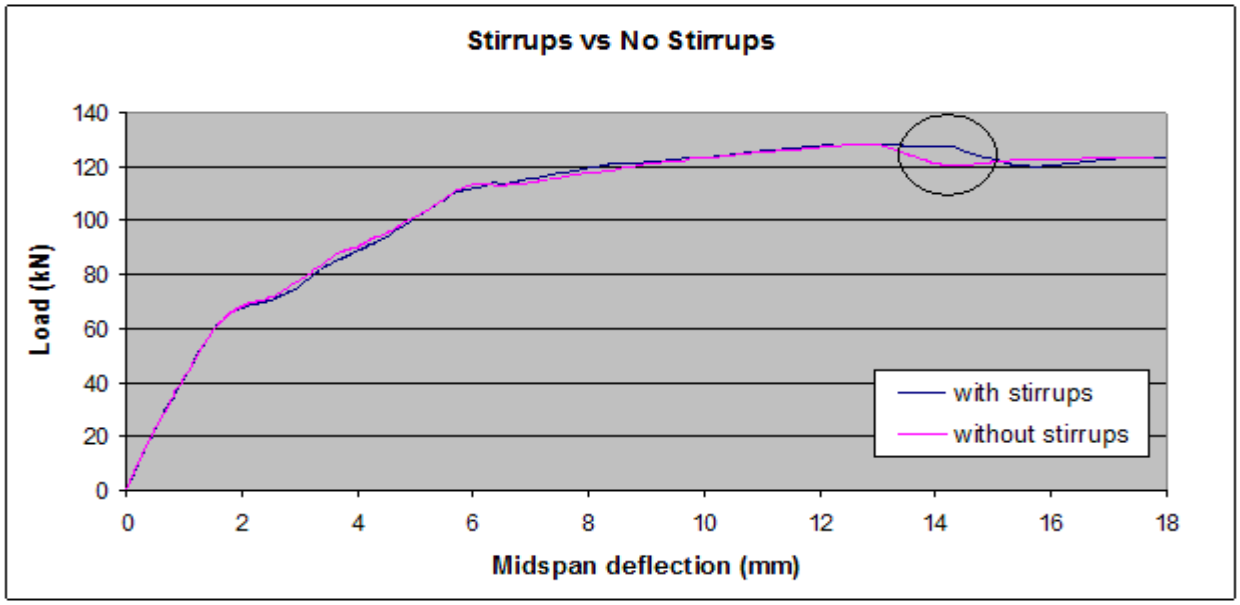

Figure 4.25: Effect of stirrups on load-deflection response of model.

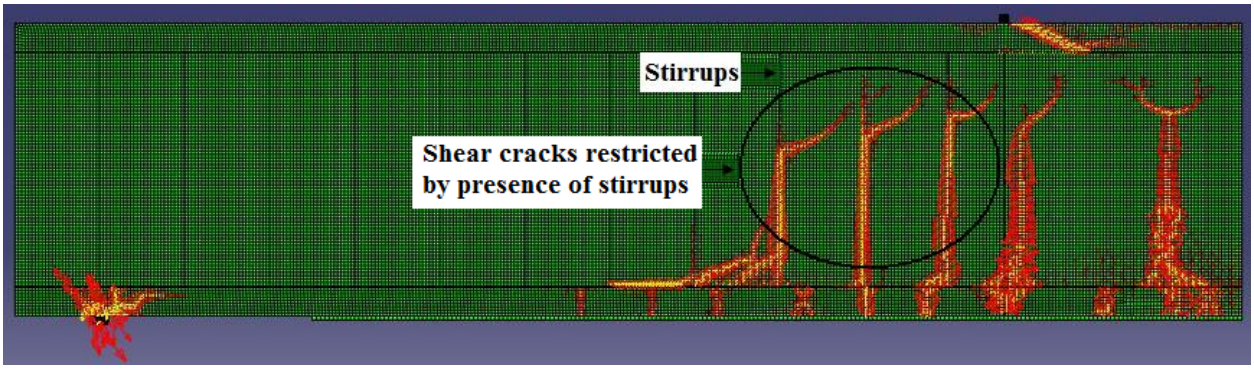

Figure 4.26: Crack formation in model with stirrups.

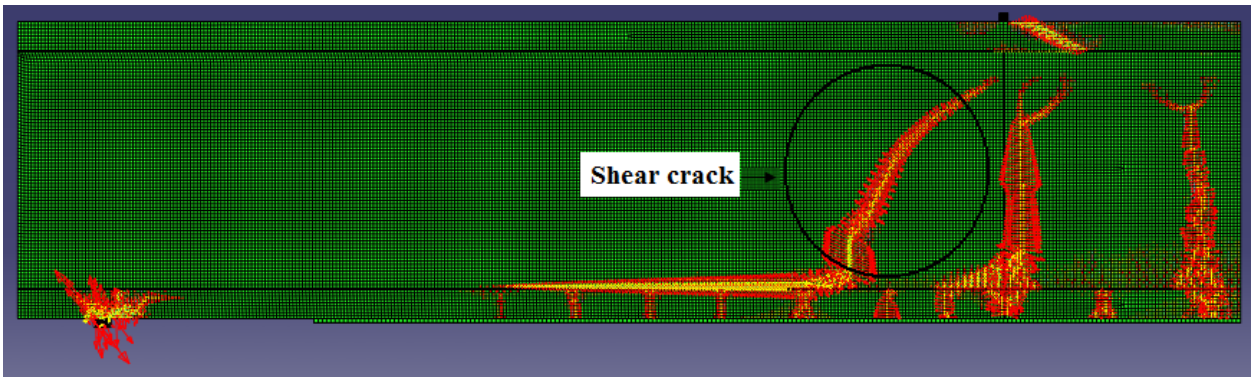

Figure 4.27: Crack formation in model without stirrups.

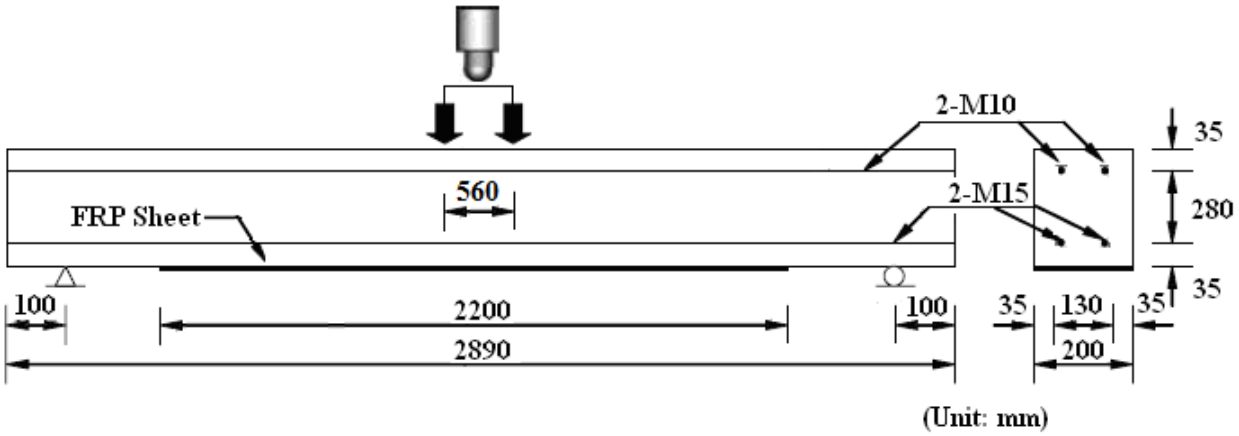

Figure 4.28: Schematic representation of analysis model.

4.5 DEBONDING ANALYSIS

Since the focus of this investigation is to study how different fracture modes affect the debonding mechanism in FRP strengthened RC beams, a debonding model unique to each type of crack considered needs to be implemented in the analysis. The following outlines the different fracture failures modes, and the models used in the debonding analysis when considering a dominant flexural and shear crack.

4.5.1 Common Fracture Behaviours

A crack is viewed as a plane separation boarded inside the material by a tip (Miannay, 1998). Irwin (1957) demonstrated that there are three kinematically independent motions of the upper

and lower surfaces of the crack relative to each other. These three motions are schematically represented in Figure 4.29. The type of crack that initiates under loading will influence the behaviour under which the FRP debonds from the concrete substrate. Chapter 5.0 considers only mode II fracture behaviour, whereas Chapter 6.0 considers mixed-mode failure, as explained in the subsequent sections.

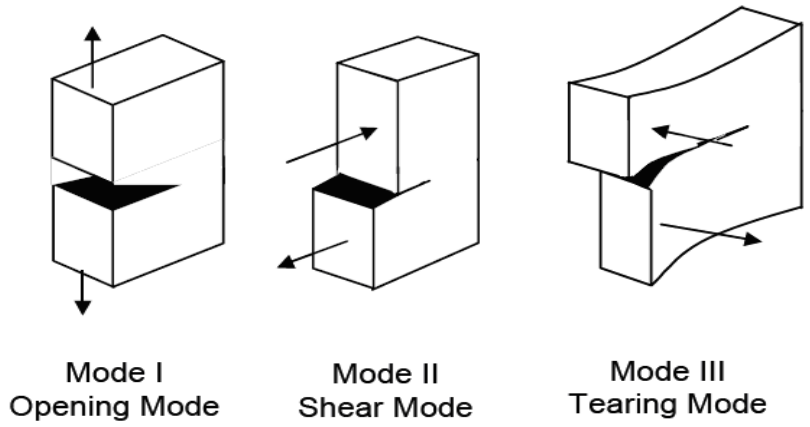

Figure 4.29: Schematic representation of three modes of failure.

4.5.2 Intermediate Flexural Cracks

Vertical flexural cracks usually yield local regions of high shear stress concentration at the FRP-concrete interface. The flexural crack introduces local flexibility at the crack locations and is modeled as a discrete crack entity that propagates when a critical stress criteria is met as covered in Section 3.7.3 and illustrated in Figure 4.30. It should be pointed out that interfacial normal (peel) stress also exits at IC locations. It is not shown in the figure and not considered Chapter 5.0 because it is generally accepted that the debonding of the FRP resembles mode II fracture behaviour as the adhesive layer transfers shear stresses from the concrete to the FRP. However, in strict sense (microscopic), any interface if naturally mixed-mode and the stress state within the interface is very complicated (Hutchinson and Suo, 1992). Only the debonding behaviour within the adhesive layer may be like mode II fracture behaviour, whereas the general debonding within

the adjacent concrete layer may be associated with a concrete mode I fracture and mode II shearing fracture behaviour. However, the latest research on this topic has shown that it is acceptable to ignore the mode I fracture behaviour since it has a negligible effect on the overall debonding process. The works that has lead to this assumption are briefly outlined below:

- According to Rabinovitch and Frostig (2001), the concrete beam and FRP plate are in contact at the vicinity of the flexural crack. This suggests that the normal interface stress is compressive at this location, and therefore, doesn't affect the debonding of the FRP-concrete interface if friction is neglected. This is different from the normal stress at the FRP plate end, which is tensile and plays a critical role in the plate-end debonding.
- Existing solutions proposed by Smith and Teng (2001) show that the normal stress has little effect on the derivation of shear stress.
- By using a displacement discontinuity model, Wu et al. (2002) found that there exists a linear correlation between mode I concrete and a mode II interfacial fracture energy values for a given shearing fracture energy introduced on the crack surface. This means that the overall debonding behaviour can be regarded as a mode II for intermediate cracks.

Thus, it is considered to be an acceptable assumption that the IC debonding is treated as a mode II fracture.

The debonding analysis is investigated through the non-linear fracture mechanics approach proposed by Lu et al. (2005) and is shown in Figure 4.31. This is one of the most accurate bond stress-slip models that can be incorporated into a finite element analysis. Its validity has been proven by numerous researchers (Lu et al., 2005; Baky et al., 2007; Ebead and Neale, 2007) and has been found to be superior to other proposed models, as covered in Section

2.6. Under external load, interfacial shear stress is developed along the FRP-concrete interface. Initially, the applied load is small and the interfacial stress, τ, is less than, τ_{max}, and therefore the interface is in its elastic stage. Due to the crack tip opening displacement introduced by the discrete crack, a finite slip, *S,* between the FRP plate and the concrete beam exists at the location of the crack. A stress concentration is introduced by this slip at the vicinity of the discrete crack. This stage ends when the interfacial stress reaches τ_{max}, or when the slip reaches S_0. If we keep on increasing the load, the slip at the location of the flexural crack becomes greater than S_0 representing the onset of micro-cracking. As slip continues to increase at the location of the crack, the interfacial shear stresses reduces to zero and full debonding initiates and grows along the FRP-concrete interface. The slip, *S*, at the interface is given by:

$$S = u_p - u_c \tag{4-6}$$

where: u_p - horizontal displacement of the FRP

u_c - horizontal displacement of the concrete

The formulations for the nonlinear shear stress-slip relation are defined as:

$$\tau = \begin{cases} \tau_{\max}\sqrt{\dfrac{S}{S_0}} & \text{if } S \le S_0 \\ \tau_{\max}\exp\left[-\alpha\left(\dfrac{S}{S_0}-1\right)\right] & \text{if } S > S_0 \end{cases} \tag{4-7}$$

where:

$S_0 = 0.0195\beta_w f_t$

$\tau_{\max} = 1.5\beta_w f_t$ - maximum interfacial shear stress

$\alpha = \dfrac{1}{\dfrac{G_f}{\tau_{\max} S_o} - \dfrac{2}{3}}$ - coefficient

$G_f = 0.308\beta_w^2\sqrt{f_t}$ - interfacial fracture energy

$\beta_w = \sqrt{\left(2.25 - \frac{b_f}{b_c}\right) \Big/ \left(1.25 + \frac{b_f}{b_c}\right)}$ - FRP width factor

It should be noted that the FRP-concrete interface can be viewed as a large-scale fracture process zone (cohesive zone) and the nonlinear bond-slip relationship essentially is the cohesive law of this zone. Therefore, by using a nonlinear bond-slip law in the finite element model, the debonding process is basically approached through a non-linear fracture mechanics method (Wang, 2006). The locally damaged materials forming a narrow band of localized deformation may be modeled by interface elements, which represent major physical variables. Linear-elastic fracture mechanics ignores the microscopic details and discloses little of what happens within the damage zone (Wang, 2006). This non-linear approach unifies the crack initiation and growth into one model and is commonly referred to as the cohesive zone model pioneered by Dugdale (1960) and Barenblatt (1962).

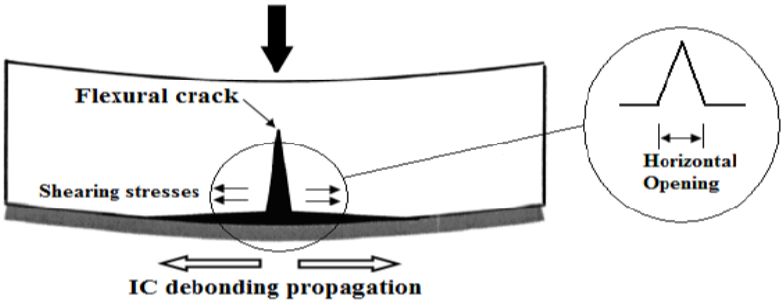

Figure 4.30: Intermediate crack debonding mechanism.

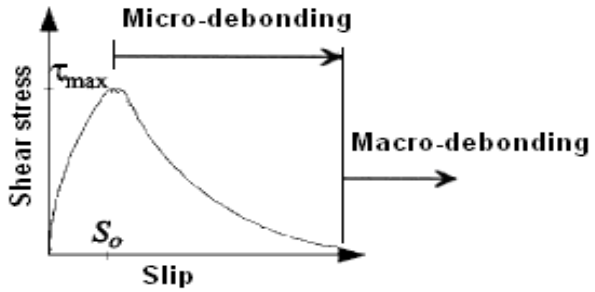

Figure 4.31: Bond stress-slip model for FRP-concrete interface.

4.5.3 Intermediate Diagonal/Shear Crack

In a FRP-RC strengthened beam, a diagonal flexural-shear or shear crack may develop under applied load within the span of the specimen. Opening of a major shear crack may induce high normal and shear stresses near the toe of the crack. These stresses are attributed to the horizontal and vertical displacements between two sides of the crack as shown in Figure 4.32. FRP debonding failure may occur under a crack of this nature and propagate to the plate end. This failure mode may be regarded as FRP debonding in mixed model fracture behaviour (i.e. mode I and mode II) due to the presence of both shearing and opening displacement along the FRP/concrete interface as shown in Figure 4.32. Whereas it is commonly acceptable to consider a flexural crack as a mode II dominated fracture behaviour, accurate modeling of the interface subjected to a shear crack must take into consideration a mixed debonding mode. Thus, two models are considered in Chapter 6.0 of this investigation in an attempt to consider both normal and shear stress-slip relationship at the interface.

The shear stress-slip model employed in this model was previously covered in Section 4.5.3. The interfacial normal stress-slip relationship is shown in Figure 4.33. When the FRP-concrete interface is loaded in compression, the normal stress is assumed to behave in a linear-elastic fashion. The scheme of unloading and reloading, as described previously, follows a secant path. It should be noticed that no account is taken of the coupling effect between mode I and mode II behaviour other than the assumption that no shear transfer occurs along the interface once the magnitude of peeling (i.e. normal) stress attains the level of tensile strength, f_t, or enters the softening branch. Thus loss of shear transfer capacity can occur if either mode II fracture energy, G_f^{int}, is met, or if the normal tensile strength, f_t, is attained. Due to the lack of data, and to provide simplicity in the initial investigation, deterioration effects of cracks on bond

properties are not considered in this model, beyond their effect on debond initiation and propagation.

The slip, *S*, at the interface is given by:

$$S = u_n^p - u_n^c \tag{4-8}$$

where: u_n^p - normal displacement of the FRP

u_n^c - normal displacement of the concrete

The formulations for the nonlinear shear stress-slip relation are defined as:

$$\delta = \begin{cases} f_t \dfrac{S}{S_0} & \text{if } S \le S_0 \\ f_t \dfrac{S_{\max} - S}{S_{\max} - S_0} & \text{if } S_0 < S \le S_{\max} \\ 0 & S_{\max} > S \end{cases} \tag{4-9}$$

where:

$S_0 = \dfrac{f_t}{k_n^{\text{int}}}$ - slip corresponding to initiation of interface softening

$S_{\max} = \dfrac{2G_f^c}{f_t}$ - maximum interfacial slip

G_f^c - concrete fracture energy

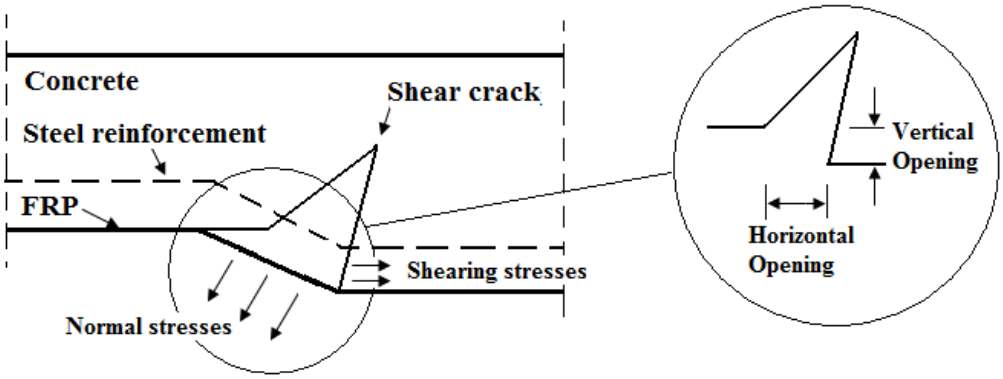

Figure 4.32: Schematic representation of stresses created from a flexural/shear crack.

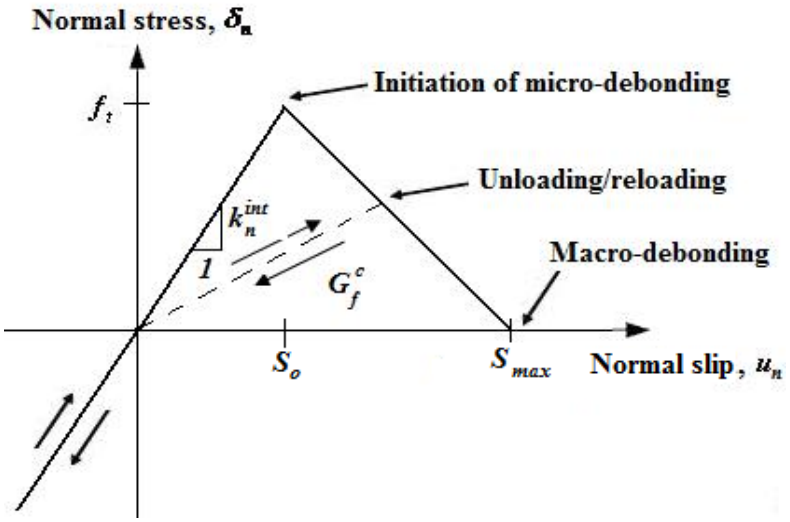

Figure 4.33: Schematic representation of interfacial normal stress-displacement relationship.

5 FRP DEBONDING UNDER MULTIPLE FLEXURAL CRACKS

5.1 INTRODUCTION

When loading is applied to a FRP-RC strengthened beam, a number of flexural or flexural/shear cracks form along the span. As mentioned in Chapter 2.0, empirical studies have shown that FRP debonding may initiate from the bottom of an intermediate crack (IC) near the middle of the span, where the bending moment and hence force in the FRP is high, as shown in Figure 5.1. With an increase in load, the debonded zone grows and propagates towards the free-end of the plate, leading to ultimate debonding failure of the strengthened structure. In recent years, debonding failure and the presence of multiple cracks has started to attract attention in the research community. In fact, FRP debonding failure under the presence of multiple cracks is now being considered in design recommendations, such as CEB-FIB (2001). However, the proposed model has not yet been verified experimentally.

One of the advantages of finite-element models is their ability to capture quantities that are virtually impossible to measure experimentally, such as stress/slip concentrations and distributions along the FRP-concrete interface. In addition, they provide insight into effects of micro- and macro-cracking on the interfacial behaviour and they allow us to better obtain results which may vary significantly from researcher to researcher, such as FRP strain. Most of the reported FRP strains are measured from electrical resistance strain gauges placed on the outside surface of the FRP plate, normally within the constant or high moment regions. Due to the induced stress concentrations on the externally bonded plates due to flexural cracking, these reported strains could vary significantly, even if they are placed very close together. The variation of the reported debonding strain value could also be due to the time at which the strain

was measured. In some cases, researchers report the strain at the initiation of debonding and others just before IC debonding failure, a difference that could be as much as 230% (Yao et al., 2004). Due to the wide variation in reported strains, some have tried back-calculation of the debonding strains using strain compatibility and equilibrium and the measured values for the applied load; however the results of this exercise were inconclusive (Yao et al., 2004).

Another commonly accepted method of studying IC debonding by researchers and industrial practitioners is to apply a direct shear test on the composite beam, as illustrated in Figure 5.2. This test involves pulling a FRP plate bonded to a concrete prism along the direction of its length to determine the bond capacity of the strengthened specimen. Due to the shear lag phenomenon, the bond capacity approaches a plateau value with increasing bond length. By performing the direct shear test on members with different bond lengths, it is possible to determine the maximum bond capacity and FRP strain for a given width and thickness of the FRP plate. While this test may be frequently employed, an empirical study preformed by Teng et al. (2002) proves otherwise, as mentioned in Section 2.5. The results indicate that debonding models with parameters derived from the direct shear test significantly underestimate the maximum FRP strain in the strengthened beam (Teng et al., 2002). These findings may be attributed to the presence of multiple secondary cracks along the beam as the opening of cracks along the beam act to reduce relative sliding between concrete and FRP, and may lessen the rate of softening along the interface. The discrepancy between commonly accepted practices and empirical evidence is just one example of why further investigations into the mechanism that trigger FRP debonding from IC are needed in an attempt to improve the efficiency of rehabilitation projects in civil engineering applications.

This chapter is mainly focused on the debonding behaviour and failure mechanisms caused by different types of flexural crack distributions in FRP-strengthened RC beams. Parameters such as crack spacing, local bond strength, interfacial stiffness, and interfacial fracture energy are investigated in a detailed parametric study to gain a clearer understanding of how these properties influence debonding mechanisms and strengthening effects. The findings of this investigation will be of interest to researchers and engineers looking to apply FRP composites in civil engineering applications, and may provide some implications for future design codes.

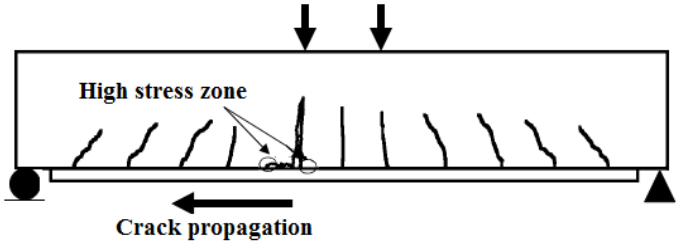

Figure 5.1: Intermediate crack induced debonding.

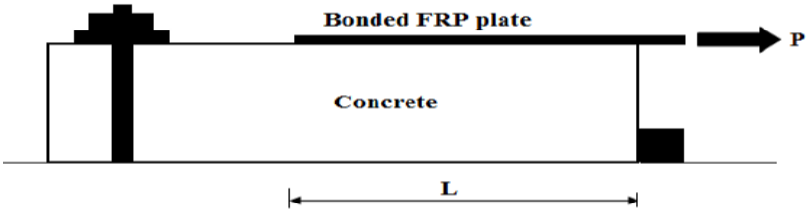

Figure 5.2: Set-up for the direct shear test.

5.2 STRUCTURAL MODEL AND SPECIAL CONSIDERATIONS

The finite element model includes single or multiple flexural cracks (FC) at a spacing x_c from the applied load to enable an investigation into the debonding initiation, propagation, and strengthening effects from intermediate cracks, as well an investigation of interfacial parameters. Due to symmetry, only half of the beam was modelled. A representation of the model with predefined flexural cracks is shown in Figure 5.3, where the dark vertical lines represent flexural

cracks. A snapshot of each finite element model for each specific crack orientation can be found in the Appendix; Figures A5.11-5.16. Detailed description of the modeling techniques used in this analysis can be found in Chapter 4.0.

Intermediated crack-induced debonding is a common failure mode in composites beams that exhibit flexural behaviour. FRP-plated regular RC beams will typically exhibit flexural behaviour when the shear span-to-depth (a/d) ratio is approximately 2.5 or greater. Since the model has a shear span of 3.05, it is expected to simulate such behaviour.

A general check on the mesh density was investigated prior to the start of the analysis since the original model tested described in Section 4.0 was altered with the increase in FRP length, removal of steel stirrups, and modifications made to the concrete compressive and tensile material models. Figure 5.4 shows the results of the load-deflection response using six levels of mesh refinement for the case of a single discrete crack located under the load point. It can be seen that the structural performance is overestimated with the use of the coarse mesh, while refining the mesh leads to convergence of response. While it appears that the convergence is achieved by employing a fine structured mesh of element size 5mm by 5mm, a closer inspection of the results in terms of interfacial shear stress versus midspan deflection proves otherwise. Figure 5.5 demonstrates that the fine meshes employing element sizes of 5mm by 5mm and 4mm by 4mm overestimate the interfacial shear stress response of the specimen, where as mesh convergence is ultimately obtained with the use of a finer mesh size of 3.5mm by 3.5mm. Previous researchers (Niu and Wu, 2005; Niu et al., 2006) that have preformed FRP-RC debonding investigations overlooked the effect interfacial shear stress when selecting their mesh for the analysis. Ignoring this parameter may lead to inaccurate results at the interface as the coarser meshes appear to be incapable of converging prior to macro-debonding. The finer mesh

containing 51,354 elements seems to be able to accurately capture the complicated fracture behaviour involving concrete cracking and interfacial debonding. This model contains 51,354 elements comprised of: 1925 beam (B21), 2840 cohesive (COH2D4), and 46,589 linear reduced-integration (CPR4R) elements.

Another general check was performed for the model employing the smallest crack spacing (i.e. x_c = 50 mm). This model represents a case in which convergence problems may arise if an incorrect mesh density is assigned as the debonding behaviour will become very complicated due to the existence of more closely spaced cracks. Figures A5.6 and A5.7 of appendix demonstrate the convergence of the mesh when employing the refined mesh of element size 3.5 mm by 3.5 mm in terms of load-deflection and interfacial shear stress-deflection, respectively. The analyses preformed to investigate mesh density suggest that the refined mesh of element sizes 3.5 mm by 3.5 mm is suitable for the all analyses that follow in this chapter, independent on the spacing in-between the predefined cracks. Snapshots of all the mesh densities employed in the analysis can be found in the Appendix; Figures A5.1-5.8.

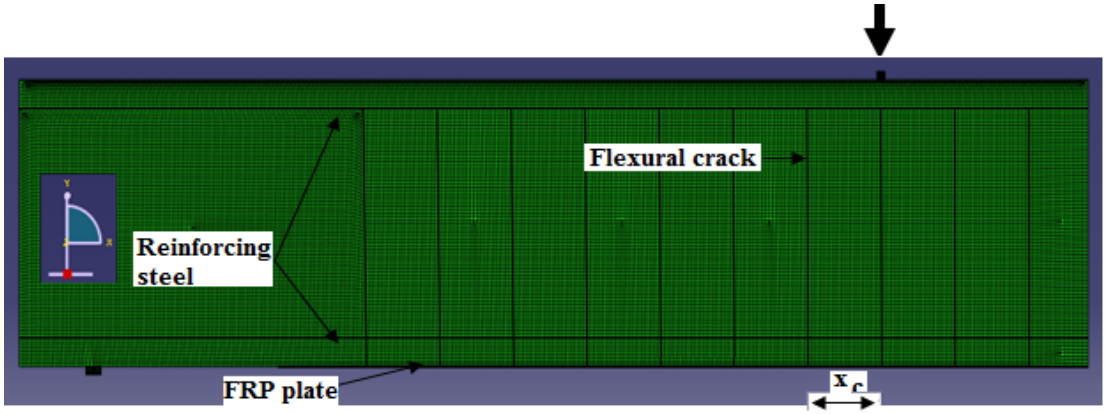

Figure 5.3: Structural model for FRP-strengthened RC-beam.

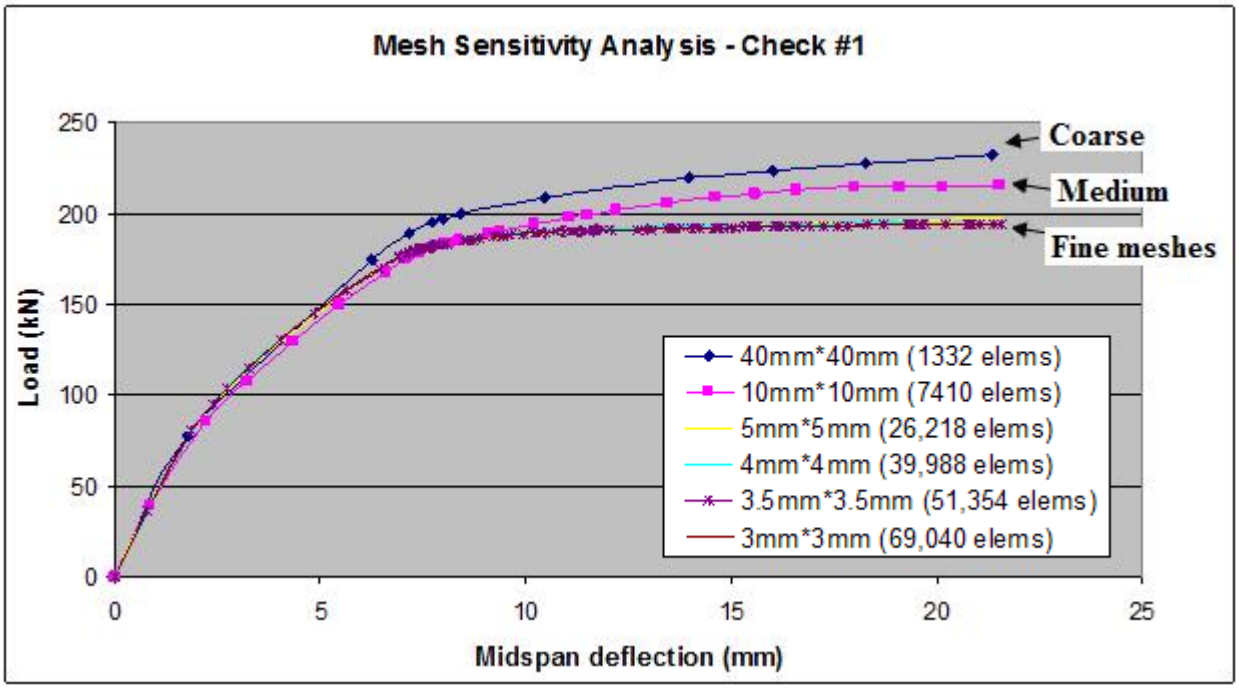

Figure 5.4: Effect of mesh refinement in terms of load versus deflection (single localized crack).

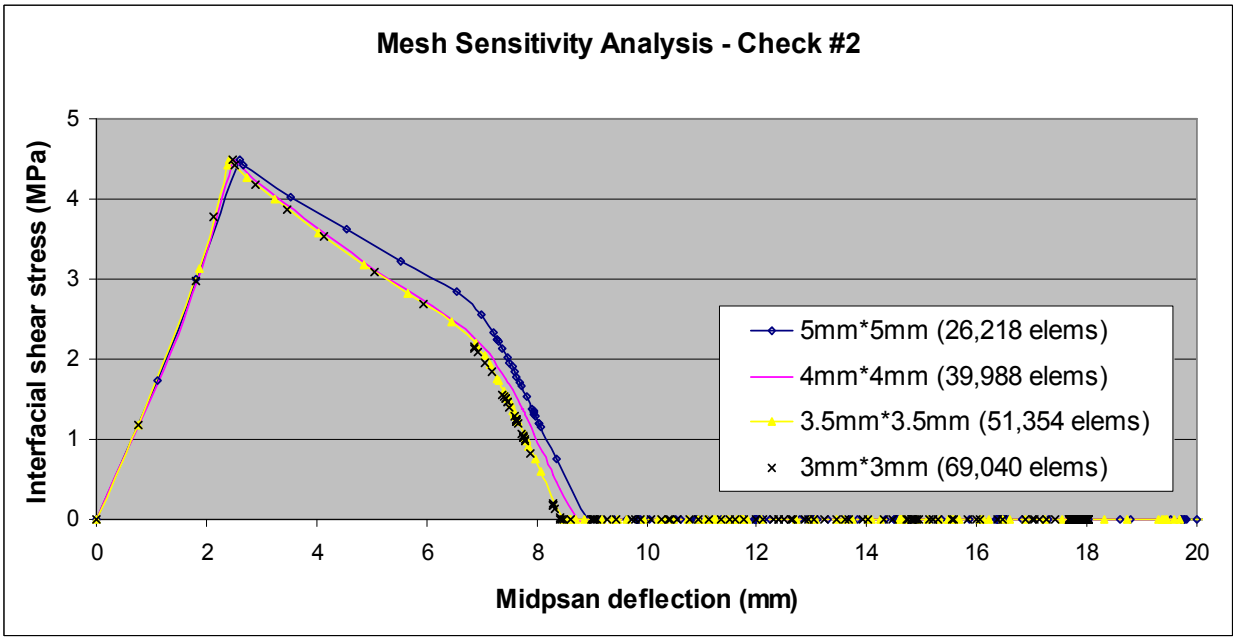

Figure 5.5: Effect of mesh refinement in terms of interfacial shear stress versus deflection (single localized crack).

5.3 OVERVIEW OF PARAMETRIC ANALYSIS

The crack distribution in RC beams depends on many factors such as diameter of rebar, depth of concrete cover, FRP reinforcing stiffness, and concrete properties. According to Yoshizawa and Wu (1999), crack spacing and crack width were significantly smaller for both tensile and flexural RC members when CFRP sheets were bonded. Average crack spacing was only slightly affected by those factors and remained at about 100mm for RC tension specimens and 70mm for flexural RC specimens (Yoshizawa and Wu, 1999). In the first portion of the analysis, the cracking spacing, $x_{c,}$ is varied throughout the model to observe the how the spacing between cracks affects the debonding mechanisms of the FRP-RC strengthened beam. This is followed by a series of parametric analyses to investigate interfacial properties such as interfacial stiffness, bond strength, and fracture energy with an average crack spacing of 100mm c/c. Table 5.1 summarizes the main parameters investigated in the numerical study.

Table 5.1: List of parameters used in investigation.

Parametric study	**Crack spacing (mm)**	**Interfacial shear stiffness k_s^{int} (MPa/mm)**	**Interfacial bond strength τ_b (MPa)**	**Interfacial fracture energy G_f^{int} (N/mm)**
I	Localized crack 280 125 100 75 50	160	4.5	0.5
II	100	50 160 500	4.5	0.5
III	100	160	1.5 4.5 12	0.5
IV	100	160	4.5	0.2 0.5 1.0

5.4 NUMERICAL SIMULATIONS AND DISCUSSION: EFFECT OF CRACK SPACING

In this portion of the analysis, the aforementioned concrete mode I fracture behaviour, shown in Figure 4.22, is introduced into the interface elements to model failure. By fixing the interfacial fracture energy at G_f^{int} = 0.5 N/mm, interfacial bond strength τ_b^{int} = 4.5 MPa, and interfacial stiffness k_b^{int} = 160 MPa/mm, the effects of six crack spaces: single localized crack, 50 mm, 75 mm, 100 mm, 125 mm and 280 mm are studied. Its effects are evaluated in terms of load-deflection, interfacial shear stress, and FRP and rebar strain throughout the analysis.

5.4.1 Single Localized Crack

Before performing the analysis, the location of the first crack needs to be chosen. For a beam subjected to a concentrated load, the first flexural crack, referred to as Crack 1, is assumed to occur immediately under the applied load as shown in Figure A5.11. Prior to the initiation of flexural cracking, there is no slip and therefore no shear stress at the FRP-concrete interface. The interfacial shear stress increases with load until micro-debonding initiates at a midspan deflection of 2.4 mm, as shown in Figure 5.6. At this point, the micro-cracking occurs in the weaker concrete layer of the interface and high bond stresses develop near the toe of Crack 1 creating sliding between the concrete and the FRP plate. The strain in the plate is no longer equal to the strain in the adjacent concrete and the difference is defined as slip strain. This point is illustrated in Figure 5.7 as the stress concentration at the toe of Crack 1 reaches its maximum value of 4.5MPa. As we move along the interface away from Crack 1, note that the stress concentrations have not yet reached the maximum stress capacity of 4.5 MPa. This is implies that the interface away from Crack 1 is still in its elastic stage (i.e. micro-debonding has not initiated). Micro-debonding at Crack 1 initiates because of the stress development at the interface. In order to accommodate the stress development at Crack 1, the FRP plate requires infinite strains across the

crack, which is not possible. As a result, Crack 1 tends to open causing a shift of the maximum interfacial values of bond stresses from the load point in two opposite directions: towards the support and the midspan. This shift may be attributed to the increase in loading which forced the interfacial shear stresses to exceed the interfacial shear capacity of the interface and form a horizontal crack that begins to propagate along the interface.

The shift is clearly captured in Figure 5.7 at a midspan deflection of 6.6mm, which represents the yielding at the reinforcing steel. At this point, the stress concentration at Crack 1 has decrease from 4.5 to 2.26MPa, implying that the interface adjacent to the crack is softening. Once the yielding occurs in the reinforcing steel, the FRP strain increases at a much higher rate as shown in Figure 5.7. This sudden increase can be attributed to the fact that the FRP is now required to restrain the opening of the flexural crack as loading further increases.

As the slip at Crack 1 further increases, the debonding crack is forced to propagate along the interface. The first sign of macro-debonding of the interface is found to initiate at Crack 1 at a midspan deflection of 8.5mm. This point is also captured in Figure 5.7 where the stress concentration has decreased to zero at Crack 1. The strain in the reinforcing steel and FRP plate continue to increase to restrain the opening of Crack 1. The effective shear transfer length required to attain the ultimate load-carrying capacity, as mentioned in Chapter 4.0, may be regarded as about 140mm.

With further load, the slip at the crack continues to increases and the debonding crack propagates along the interface in two directions: towards the midspan and plate-end. To demonstrate the debonding propagation along the interface, Figure 5.8 captures the interfacial shear stress distribution at three loading phases: 12.5, 15, and 20mm midspan deflections. For the case of midspan deflection of 12.5mm, the FRP plate has debonded form the concrete

substrate between the locations of 155 and 460 mm from the midspan, with its peak interfacial shear stress concentrations of 4.5 MPa at 80 and 535 mm from the midspan. These peak locations represent the shifting of the maximum values of bond stresses towards the midspan and plate end, respectively, as well as the changing locations at which micro-debonding initiates. An increase in the debonded region is found at the midspan deflection of 15 mm, where the FRP has completely debonded from the concrete at the locations of 145 to 535 mm from the midspan, with peak stress concentrations of 4.5 MPa at locations of 55 and 610 mm. This trend continues for the case of the midspan deflection of 20 mm, where the debonded region of the FRP continues to increase now from 125 to 715 mm from the midspan, and peak stress concentrations at locations of 35 and 810 mm. The debonded region continues to grow until the FRP completely debonds from the concrete substrate towards the plate-end at a midspan deflection of 27.4 mm. Table 5.2 summarizes the critical values in the analysis.

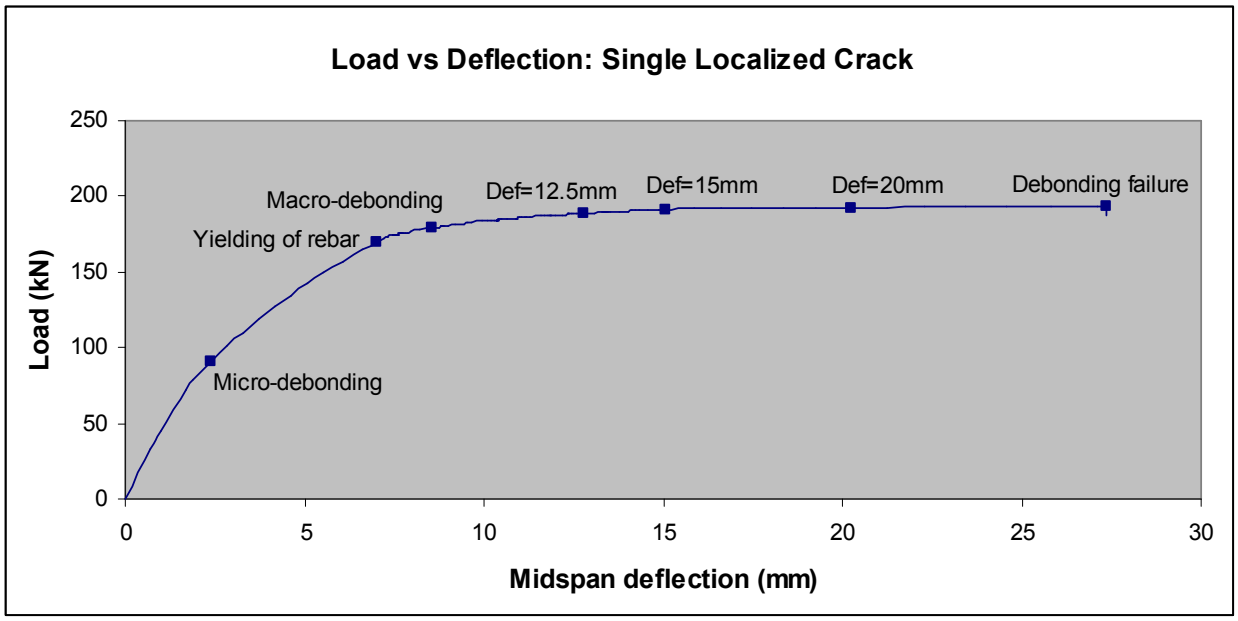

Figure 5.6: Load versus deflection for single localized crack.

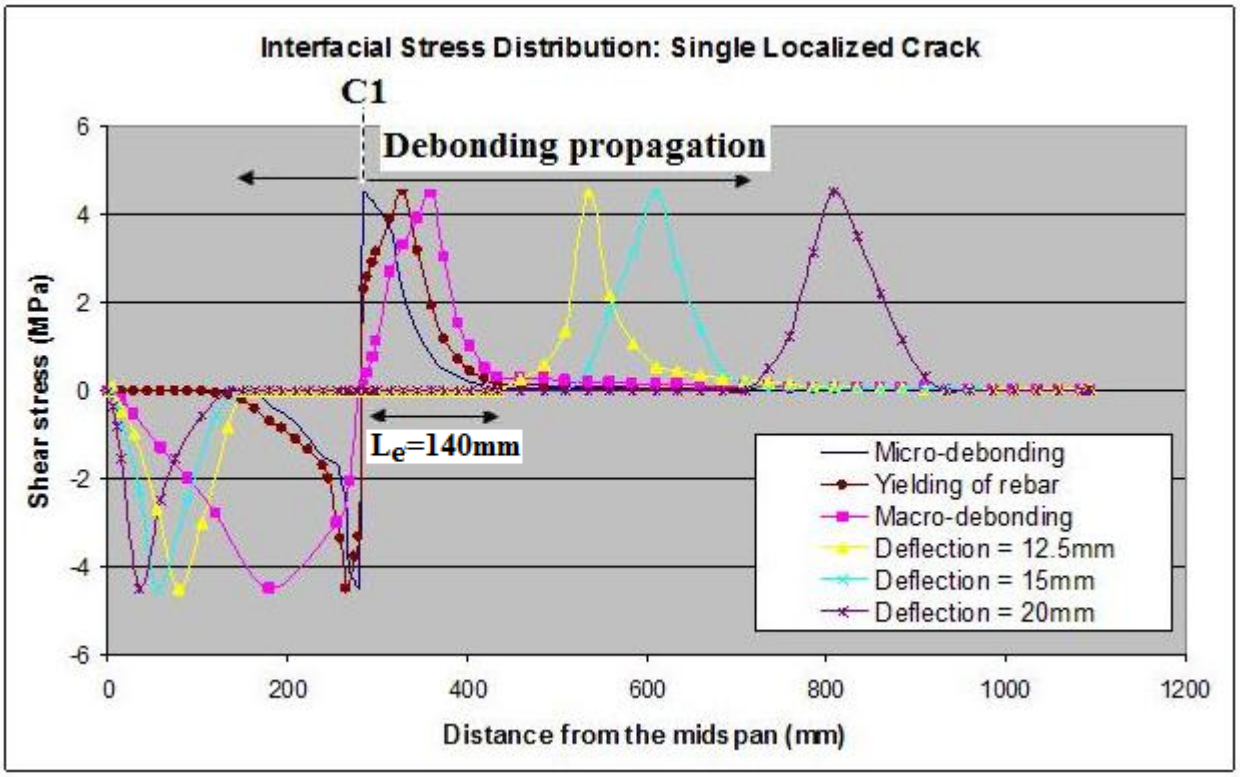

Figure 5.7: Interfacial stress distribution for the case of a single localized crack.

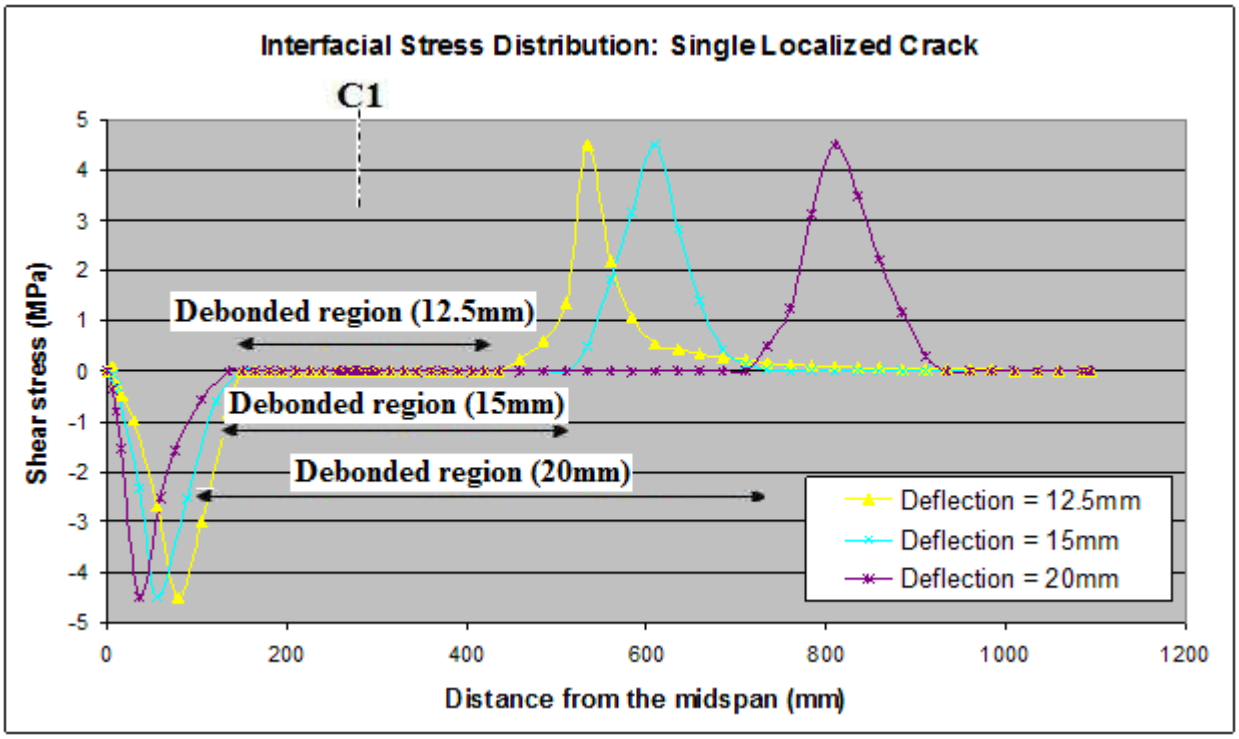

Figure 5.8: Debonded regions for single localized crack.

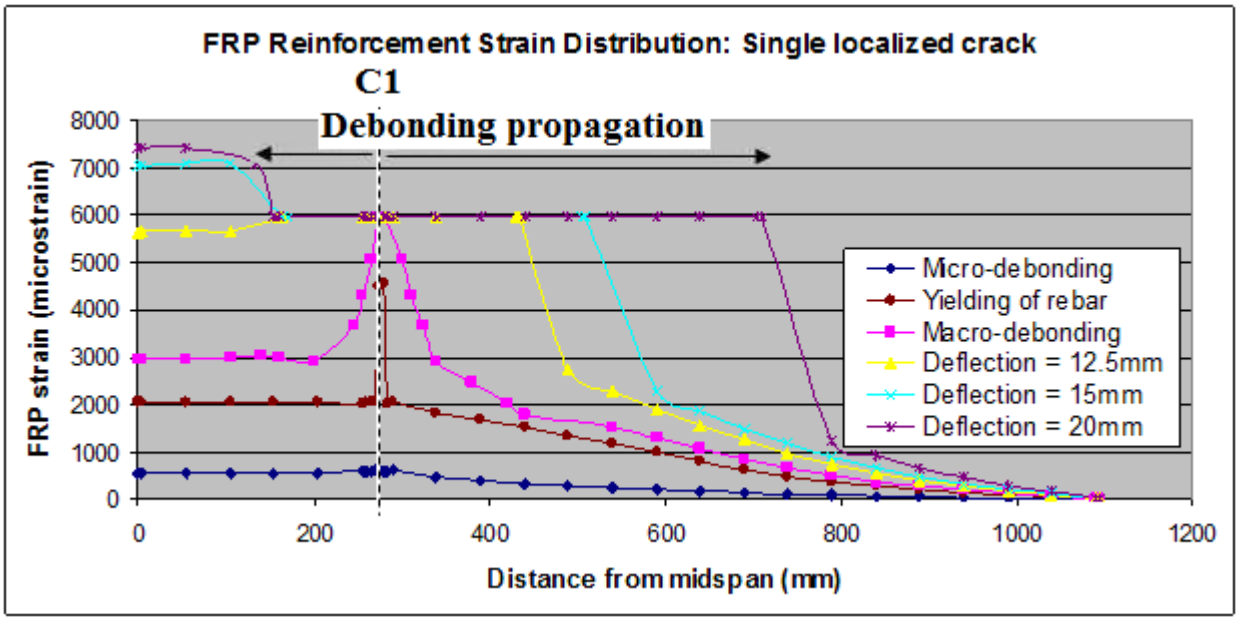

Figure 5.9: FRP reinforcement strain distribution for a single localized crack.

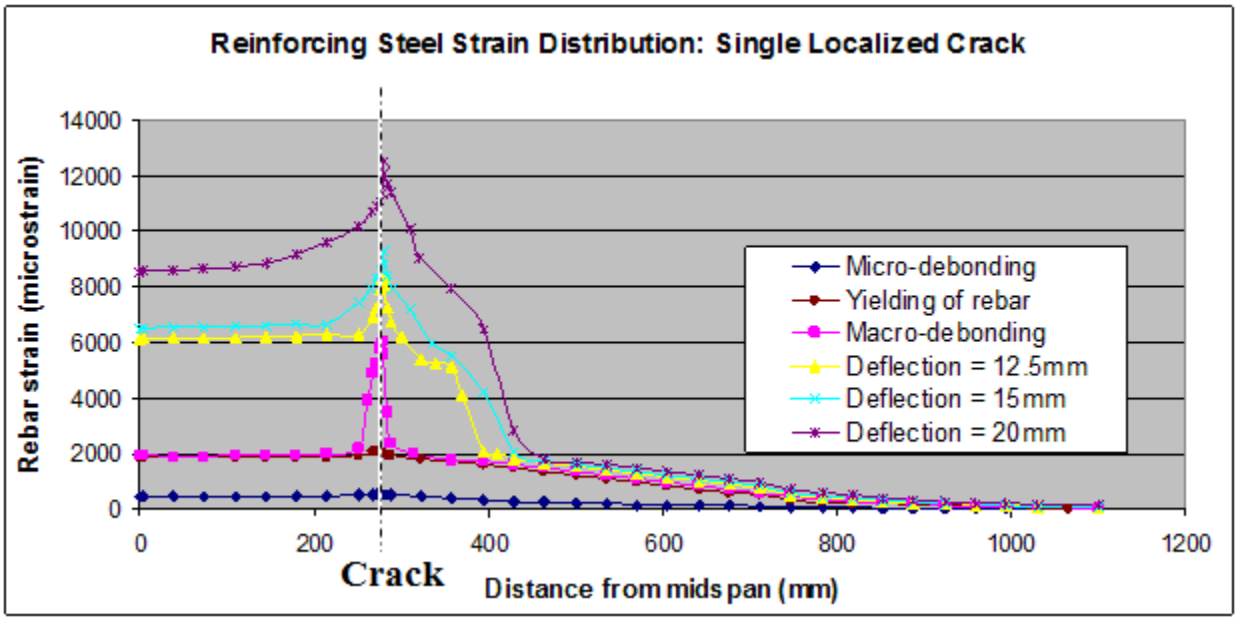

Figure 5.10: Steel reinforcement strain distribution for a single localized crack.

5.4.2 Crack Spacing: x_c = 280 mm

To study the effect of crack spacing in the composite beam, flexural cracks were predefined in the model spaced at 280 mm as shown in Figure A5.16. The first flexural crack, referred to as

Crack 1, is assumed to occur at the midspan and the second flexural crack, Crack 2, occurs under the load point located 280mm from Crack 1, and so on as shown in Figure A5.16. A total of four flexural cracks were arranged in the model. Prior to the initiation of flexural cracking, there is no slip and therefore no shear stress at the FRP-concrete interface. The interfacial shear stress increases with load until micro-debonding initiates at Crack 2 at a midspan deflection of 2.8mm as shown in Figures 5.11 and 5.12. At this point, the micro-cracking occurs in the weaker concrete layer of the interface and high bond stresses develop near the toe of Crack 2 creating sliding between the concrete and the FRP plate. The strain in the plate is no longer equal to the strain in the adjacent concrete and the difference is defined as slip strain. It was expected that micro-debonding would initiate at Crack 2 since this flexural crack is located in the maximum moment region and also experiences the highest shearing force of the four predefined cracks. This point is illustrated in Figure 5.12 as the stress concentration at the toe of Crack 2 reaches its maximum value of 4.5MPa. It can be seen that the occurrence of a new crack adjacent to Crack2 affects the interfacial shear stress distribution of the beam since there is a change in slip direction, i.e. there now exists a negative slip. As a result, there is a change in direction in bond stress between subsequent cracks in order to maintain equilibrium. This was not the case for the single localized crack in Figure 5.7, where there was no change in direction of bond stress. The region between Cracks 1 and 2 is located in the constant moment region of the beam. To maintain equilibrium in this region, there exists a point of zero slip at the midpoint between the two cracks, as opposed to the region between Cracks 2-3 and Cracks 3-4 that lie in a varying moment region and the point of zero slip that moves toward the subsequent cracks as slip increases, as shown in Figure 5.12. Note that at the initiation of micro-debonding at Crack 2, the other three cracks are still in their elastic stage as shown in Figure 5.11 as they have not yet

reached their peak interfacial shear strength values of 4.5MPa. As Crack 2 tends to open, it causes a shift of the maximum interfacial values of bond stresses from the load point in two opposite directions: towards the support and the midspan. This shift may be attributed to the increase in loading which forced the interfacial shear stresses to exceed the interfacial shear capacity of the interface and form a horizontal crack that begins to propagate along the interface.

The shift is captured in Figure 5.12 at the point of yielding of the reinforcing steel where the stress concentration at Crack 2 has decreased from 4.5MPa at the onset of micro-debonding to 2.82MPa, at a midspan deflection of 6.9mm. This drop in stress concentration illustrates the increase in slip as well as the softening of the interface at Crack 2. Similar behaviour was also found between Cracks 1-2, 2-3, and 3-4. However at this point, the region between Crack 4 to the plate-end (PE) is still in its elastic stage. This can be attributed to Crack 4 experiencing the lowest bending moment of predefined cracks since it is located the furthest from the load point. The reinforcing steel has only yielded at Cracks 1 and 2. This can be attributed to Cracks 1 and 2 being located in the maximum moment regions. Once the yielding occurs in the reinforcing bars at Cracks 1 and 2, FRP strain increases at a much higher rate as shown in Figure 5.31. This sudden increase can be attributed to the fact that the FRP is now required to restrain the opening of the flexural crack as loading further increases. It should be noted that between Cracks 1 and 2 there still exists the point of zero slip at the midpoint between the two cracks, similar to the case during the initiation of micro-debonding. However, in the varying moment region the point of zero slip between Cracks 2-3 slightly shifts towards Crack 2. This may indicate the gradual opening of Crack 3 and hence reducing the slip to the left face of Crack 2.

As the slip at Crack 2 further increases, the debonding crack is forced to propagate along the interface. The first sign of macro-debonding of the interface is found to initiate at Crack 2 at

a midspan deflection of 9.0 mm. This point is captured in Figure 5.12 where the stress concentration has decreased to zero. At this point, the regions between Cracks 1-2 and 3-4 are experiencing softening of the interface, where Crack 4-PE is still in its elastic stage. The strain in the reinforcing steel and FRP plate continue to increase to restrain the opening of Crack 2. The effective shear transfer length required to attain the ultimate load-carrying capacity, as mentioned in Chapter 4.0, may be regarded as about 145mm as shown in Figure 5.12. It should be noted that between Cracks 1 and 2 there still exists the point of zero slip at the midpoint between the two cracks, similar to the case during the initiation of micro-debonding and rebar yielding. However, the in the varying moment region the point of zero slip between Cracks 2-3 slightly shifts towards Crack 2 and between Cracks 3-4 the point of zero slip also shifts to the left towards Crack 3. This may indicate the gradual opening of Cracks 3 and 4, thereby reducing the slip to the left sides of Cracks 2 and 3, respectively. This also indicates that the debonding cracks to the right of Cracks 2 and 3 propagate towards the support whereas the debonding cracks propagating from the left of Cracks 3 and 4 moves towards the applied load.

As loading is further applied, slip at the interface increases and the debonding crack propagates along the beam. To demonstrate the debonding propagation along the interface, Figure 5.12 captures the interfacial shear stress distribution at the midspan deflection of 20mm. At this point, the FRP plate has debonded form the concrete substrate in two locations: between 0 to 80mm and 200 to 670 mm from the midspan. More specifically the FRP composite has completely debonded from the concrete substrate between Cracks 2-3, and partially between Cracks 1-2 and 3-4. Even though the FRP plate has partially debonded between Cracks 1-2, the point of zero slip at the midpoint between the two cracks is still intact. However, the in the varying moment region the point of zero slip between Cracks 2-3 has now shifted towards Crack

3 indicating that as enough slip increases to initiate macro-debonding, the debonding crack that was propagating from Crack 3 towards the applied load cannot propagate any further as it is restricted by the debonding crack propagating from Crack 2 towards the support. The debonding cracks now propagate in only one direction: towards the support. This may also indicate the debonding crack initiated to the left of Crack 3 has closed up. The interface between Cracks 3-PE is no longer in its elastic stage as micro-debonding has been initiated and it is the softening phase of the interface. The debonded region continues to grow until the FRP completely debonds from right of Crack 2 towards the plate-end at a midspan deflection of 25.6mm. To maintain equilibrium, the point of zero slip in the constant moment region always occurs at midpoint between two cracks, as opposed to a varying moment region where the point of zero slip moves toward the next crack as slip increases. Therefore, the debonding cracks in constant moment regions will propagate in both directions and will not close up like those in the varying moment regions. Table 5.2 summarizes all critical values of the analysis.

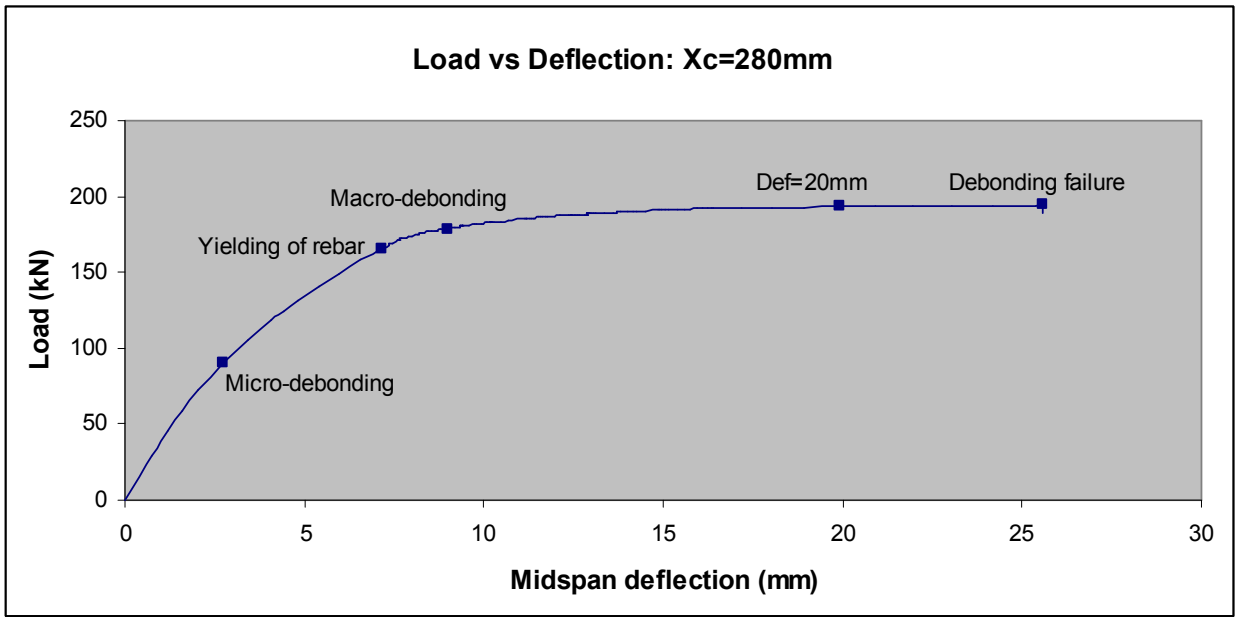

Figure 5.11: Load versus deflection for the crack spacing x_c = 280mm.

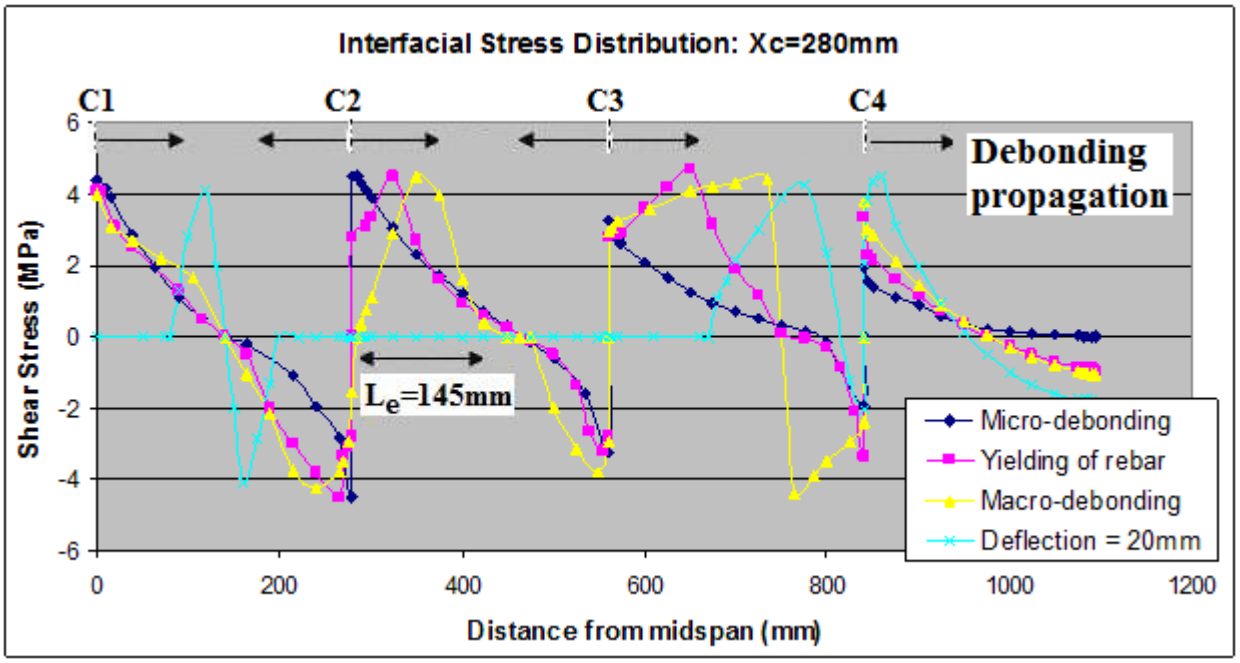

Figure 5.12: Interfacial stress distribution for the crack spacing x_c = 280mm.

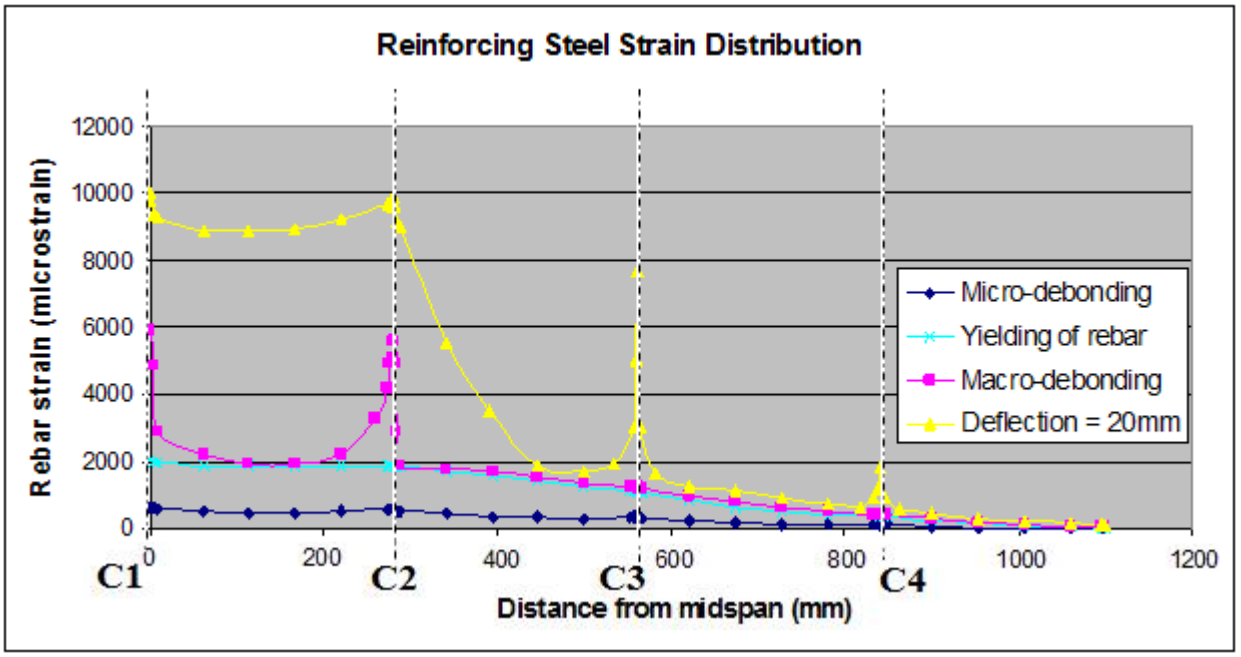

Figure 5.13: Steel reinforcement strain distribution for the crack spacing x_c = 280mm.

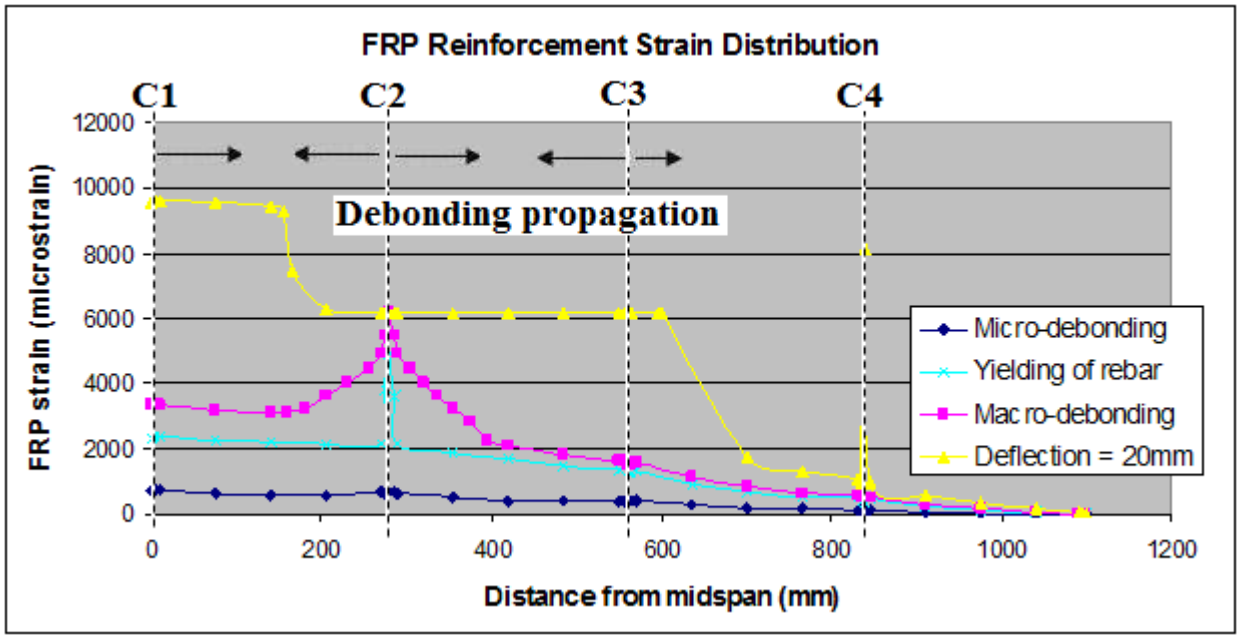

Figure 5.14: FRP reinforcement strain distribution for the crack spacing x_c = 280mm.

5.4.3 Crack Spacing: x_c = 125 mm

To study the effect of crack spacing, flexural cracks were predefined in the model spaced at 125mm as shown in Figure A5.15. The first flexural crack, referred to as Crack 1, is assumed to occur 30 mm from the midspan, and the subsequent crack (Crack 2) is located 125 mm from Crack 1. Crack 3 is predefined 125 mm from Crack 2 and is located directly beneath the load point. A total of eight flexural cracks are arranged in the model. Prior to the initiation of flexural cracking, there is no slip and therefore to shear stress at the interface. The interfacial shear stress increases with deflection until micro-debonding initiates at Crack 3 at a midspan deflection of 3.4 as shown in Figures 5.15 and 5.16. At this point, the micro-cracking occurs in the weaker concrete layer of the interface and high bond stresses develop near the toe of Crack 3 creating sliding between the concrete and FRP plate. The strain in the plate is no longer equal to the strain in the adjacent concrete and the difference is defined as slip strain. It was expected that micro-debonding would initiate at Crack 3 since this flexural crack is located in the

maximum moment region and also experiences the highest shearing force of the eight predefined cracks. This point is illustrated in Figure 5.16 as the stress concentration at the toe of Crack 3 reaches its maximum value of 4.5MPa. The occurrence of a crack adjacent to Crack 3 was found to influence the interfacial shear stress distribution of the beam by creating a change in slip direction. Consequently, there is also a change in direction of bond stress between subsequent cracks in order to maintain equilibrium. Cracks 1-3 lie in the constant moment region of the beam and in a case similar to that of the cracks spaced at 280mm centre-on-centre, a point of zero-slip exists at the midpoint between the cracks. Note that at the initiation of micro-debonding at Cracks 3, all other flexural cracks are still in their elastic stage as shown in Figure 5.16, as they have not yet reached their peak interfacial shear capacity of 4.5MPa. As Crack 3 tends to open, it causes a shift of the maximum interfacial values of bond stresses from the load point in two directions: towards the support and the midspan. This shift may be attributed to the increase in loading which forced the interfacial shear stresses to exceed the shear capacity of the interface and form a horizontal crack that begins to propagate along the length of the beam.

The shift is captured in Figure 5.16 at the point of yielding of reinforcing steel where the stress concentration at Crack 3 has decreased from 4.5MPa at the onset of micro-debonding (at a deflection of 3.4mm) to 2.93MPa, at a midspan deflection of 7.8mm. This drop in stress concentration illustrates the increase in slip as well as softening of the interface at Crack 3. Similar behaviour was also found between Cracks 1-2, 2-3, 3-4, 4-5, and 5-6. Whereas, Cracks 6-7, 7-8, and 8-PE are still in their elastic stage. The reinforcing steel has yielded at this point only at Cracks 1, 2 and 3 as evidenced in Figure 5.17. This can be attributed to Cracks 1, 2 and 3 being located in the maximum moment regions. Once the yielding occurs in the reinforcing bars at Cracks 1-3, FRP strain increases at a much higher rate as shown in Figure (FRP). This sudden

increase can be attributed to the fact that the FRP is now required to restrain the opening of the flexural crack as loading further increases. It should be noted that between Cracks 1-3 there still exists the point of zero slip at the midpoint between the two cracks, similar to the case during the initiation of micro-debonding. However, in the varying moment region the point of zero slip did not change from its position at the onset of micro-debonding, except between Cracks 3-4. In this region, the point of zero slip slightly shifted toward Crack 4, i.e. towards the support, indicating the gradual opening of Crack 4 and that the debonding crack initiating from Crack 3 is restricted by the debonding propagation from Crack 4 towards the applied load.

As the slip at Crack 3 continues to increase, the debonding crack is forced to propagate along the interface. Macro-debonding at the interface is found to initiate at Crack 3 at a midspan deflection of 10.1mm. This point in captured in Figure 5.16 where the stress concentration had decreased to zero. At this point, the regions between Cracks 1-2, 2-3, 4-5, 5-6 and 6-7 are experiencing softening of the interface, whereas Cracks 7-8 and 8-PE are still in their elastic stage. The strain in the reinforcing steel continues to increase with loading and sudden increases in strain are found at the predefined crack locations, as shown in Figure 5.17. A similar trend was also found in Figure 5.18 where the FRP strain suddenly increases at crack location. This may be attributed to the reinforcement being required to restrain the opening of the flexural cracks. As shown in Figure 5.16, macro-debonding is first formed under the applied load, but due to the fact that the crack spacing is smaller than the observed effective transfer length of about 140mm, the debonding propagation encounters resistance from the opposite direction near the location of the adjacent cracks. This leads to an increased equivalent transfer length that can be captured by the FRP strain distribution in Figure 5.18 of 190mm. It should be noted that between Cracks 1-2 and 2-3 there still exists the point of zero slip at the midpoint between the

two cracks, similar to the case during the initiation of micro-debonding and rebar yielding. However, in the varying moment region the point of zero slip between Cracks 3-4, 4-5, and 5-6 shift slightly towards the applied load, whereas it shifts toward the support between Cracks 6-7.

As loading is further increased, slip at the interface continues to grow and the debonding crack propagates along the beam. The interfacial shear stress distribution along the interface is captured at a midspan deflection of 20mm in Figure 5.16. At this point, the FRP plate has completely debonded from the concrete substrate from the location of 160 to 575mm from the midspan. More specifically, the plate is no longer attached from Crack 2 to 5, and halfway between Crack 5 to 6. The point of zero slip is between Cracks 1-2 is still intact whereas it has moved towards the support in the varying moment region between Cracks 5 to 8. The unison in which the debonding crack is propagating along the interface suggests that complete debonding is not far away as the crack is restricted to propagate in only one direction: towards the support. The debonded region continues to grow until the FRP has completely debonded from the right of Crack 3 to the plate-end at a midspan deflection of 24.9mm. Table 5.2 summarizes the critical values in the analysis.

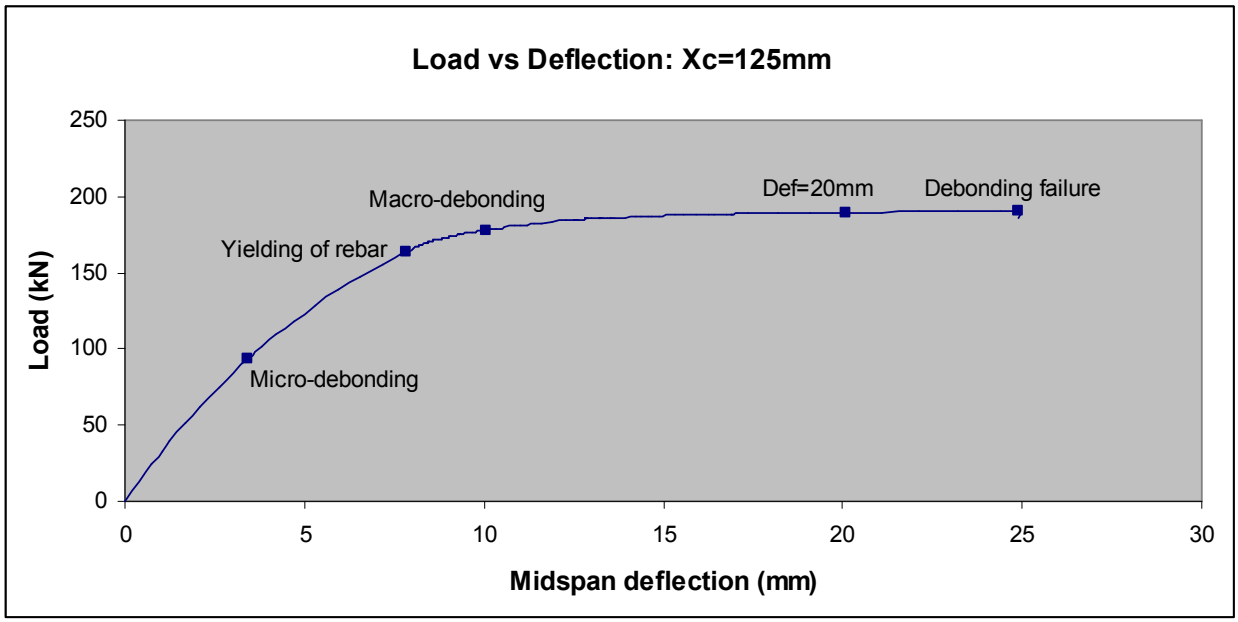

Figure 5.15: Load-deflection response for the crack spacing x_c = 125mm.

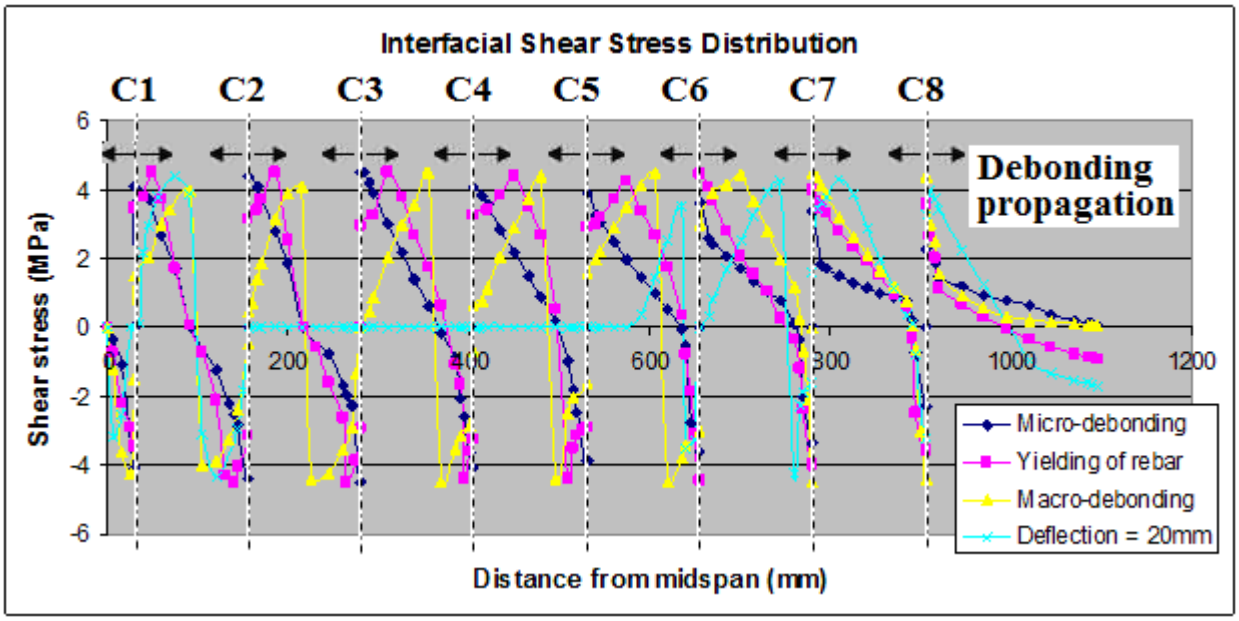

Figure 5.16: Interfacial stress distribution for the crack spacing x_c = 125mm.

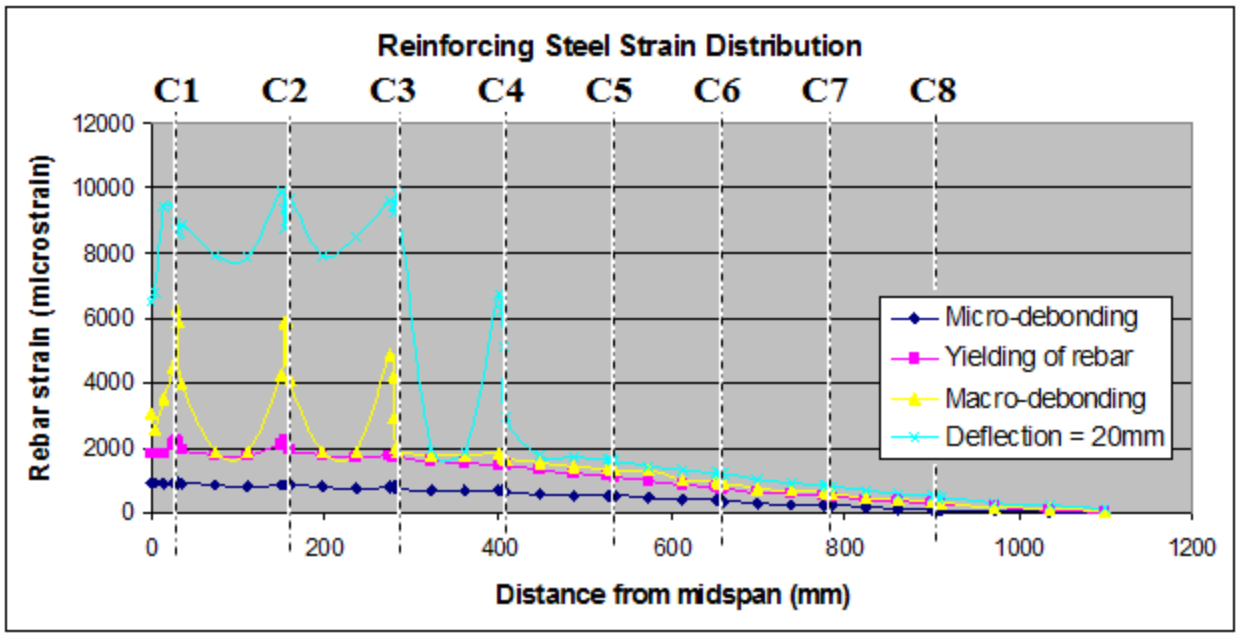

Figure 5.17: Steel reinforcement strain distribution for the crack spacing x_c = 125mm.

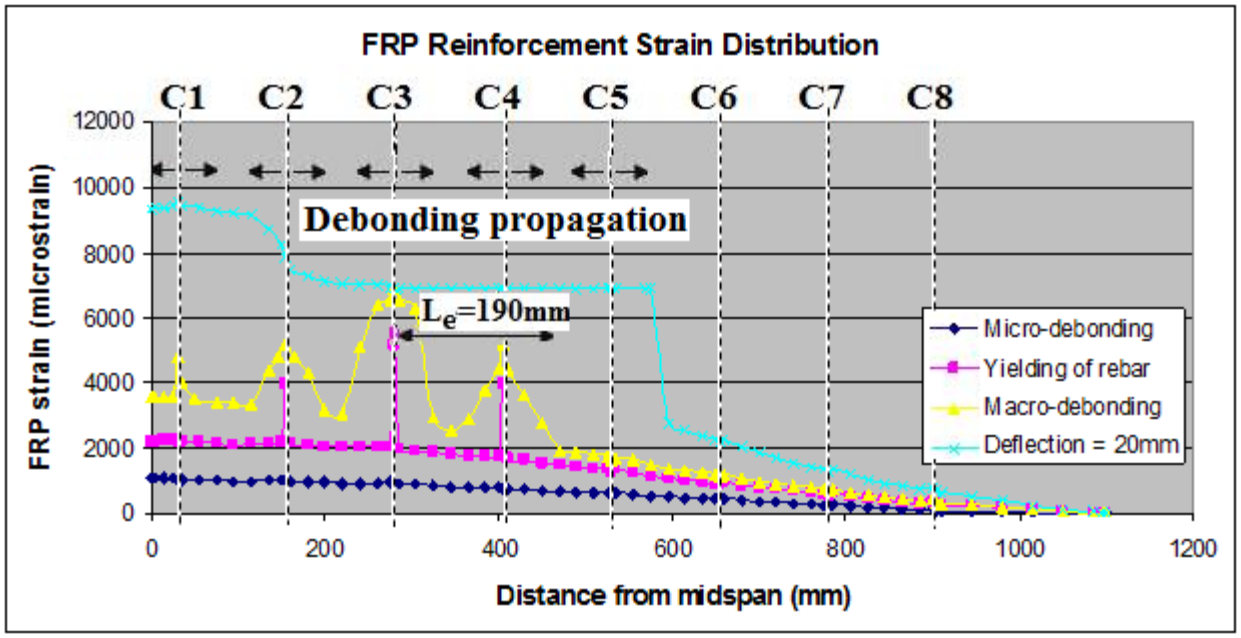

Figure 5.18: FRP reinforcement strain distribution for the crack spacing x_c = 125mm.

5.4.4 Crack Spacing: x_c = 100 mm

The flexural cracks in this portion of the investigation were spaced at 100mm as shown in Figure A5.14. The first flexural crack referred to as Crack 1, is predefined at 80mm from the midspan

with each subsequent crack spaced at 100mm centre-on-centre. Crack 3 lies directly beneath the applied load. A total of 10 flexural cracks are arranged in the model. Prior to the initiation of flexural cracking, there is no slip and therefore no shear stress at the FRP-concrete interface. Once flexural cracking initiates, the interfacial shear stress increases with load until micro-debonding initiates at Crack 3 at a midspan deflection of 4.5mm, as shown in Figure 5.19 and 5.20. At this point, the micro-cracking occurs in the weaker concrete layer of the interface and high bond stresses develop near the toe of Crack 3 creating sliding between the concrete and FRP plate. The strain in the plate is no longer equal to the strain in the adjacent concrete and the difference is defined as slip strain. It was expected that micro-debonding would initiate at Crack 3 since this flexural crack is located in the maximum region and also experiences the highest shearing force of the four predefined cracks. This point is illustrated in Figure 5.20 as the stress concentration at the toe of Crack 3 reaches it maximum value of 4.5MPa. The occurrence of closely spaced flexural cracks appears to affect the interfacial shear stress distribution of the beam by changing the direction of slip and consequently bond stress to maintain equilibrium. The regions between Cracks 1-3 are located in the constant moment region, and there exists a point of zero slip at the midpoint between subsequent cracks. The remaining cracks lie in the varying moment region where the point of zero slip seems to move towards the support along the interface. At the initiation of micro-debonding at Crack 3, the other nine cracks in the model are still in their elastic stage as shown in Figure 5.20. As Crack 3 tends to open, it causes a shift of the maximum interfacial values of bond stresses from the load point in two opposite directions: towards the support and the midspan. This shift may be attributed to the increase in loading which forced the interfacial shear stresses to exceed the interfacial shear capacity of the interface and form a horizontal crack that begins to propagate along the interface.

At the point of yielding of the steel reinforcement, Figure 5.20 shows the shifting of maximum interfacial shear stress from the toe of Crack 3 towards the support. Rebar yielding occurs at a midspan deflection of 8.1mm. At this point, the region between Cracks 1-2, 2-3, 3-4, 4-5, 5-6 and 6-7 also experience a shift in the locations of maximum interfacial shear stress indicating that the interface located at these areas are also experiencing softening of the interface. Whereas the interfacial shear stress continues to increase with changing position at cracks 7, 8, 9, and 10 suggesting that the interface is still in its elastic stage as shown in Figure 5.20. The reinforcing steel at this loading stage was found to yield only at Cracks 1, 2 and 3. This can be attributed to Cracks 1-3 being located in the maximum moment region. Once yielding occurs in the reinforcing bars at Cracks 1-3, FRP strain increases at a much higher rate as shown in Figure (FRP). This sudden increase can be attributed to the fact that the FRP is now required to restrain the opening of the flexural crack as loading further increases. It should be noted that between Cracks 1-3 there exists the point of zero slip at the midpoint between the two cracks, similar to the case during the initiation of micro-debonding. However, in the varying moment region the point of zero slip between Cracks 3-4, 4-5, 5-6, and 6-7 was found to move to the right, i.e. towards the support. This indicates that the uncracked concrete segment is gradually slipping towards the adjacent cracks situated closer to the support and hence reducing the slip on the left face of the crack. The point of zero slip between Cracks 7-8, 8-9 and 9-10 did not change in position from the onset of micro-debonding.

As the slip at Crack 3 continues to increase, the debonding crack is forced to propagate along the interface. The first sign of macro-debonding of the interface is found to initiate at Crack 3 and 4 at a midspan deflection of 10.3mm. This loading stage is captured in Figure (INT) where the stress concentration has reduced to zero. At this stage, the interfaces at Cracks 1, 2, 5,

6, 7 and 8 are softening whereas the interfaces at Cracks 9 and 10 are still in their elastic stage. The strain in the reinforcing steel and FRP plate continue to increase to restrain the opening of Cracks 1-4. Due to the fact that the crack spacing is smaller than the effective transfer length at about 140mm, the debonding propagation encounters resistance from the opposite direction near the adjacent crack. This leads to an increased equivalent transfer length that can be captured by examining the FRP strain distribution in Figure 5.21. Here, it is shown that the effective transfer length is approximately 215mm to the left of the load point. It should be noted that between Cracks 1-2 and 2-3 there still exists the point of zero slip at the midpoint between the adjacent cracks, similar to the case during the initiation of micro-debonding and rebar yielding. However, in the varying moment region the point of zero slip between Cracks 3-4, 4-5, 5-6 and 6-7 have shifted right of the cracks towards the applied load. This suggests the debonding crack propagating towards the support is being restricted by the debonding cracks propagating towards the applied load. This may explain the abrupt increase in the load-deflection response in Figure 5.19 at around this point (def=10.25mm). No change for the position of zero slip was found between Cracks 7-8, 8-9, and 9-10.

With increased loading, the slippage at the interface continues to grow eventually leading to the debonding crack to propagate along the composite. Figure 5.20 illustrates the debonding propagation at the midspan deflection of 20mm. At this moment, the FRP plate had debonded from the concrete substrate from 180 to 610mm from the midspan, or from Crack 2 to the halfway point between Cracks 6 and 7. The point of zero slip is found to still be located at the midpoint between Cracks 1-2. On the other hand, between Cracks 6-7, 7-8, 8-9, and 9-10, the point of zero slip has shifted right, i.e. towards the support. This may indicate that the debonding crack initiated from the left of the cracks (i.e. propagating towards the applied load) has closed

up. The reinforcing steel strain at Cracks 1-5 continue to increase at a more rapid rate as shown in Figure 5.22. This may be attributed to the fact that the rebar is required to solely restrain the opening of the flexural cracks as the FRP plate has completely debonded at this point. The debonded region continues to grow until the FRP completely debonds from the right of Crack 3 towards the plate-end at a midspan deflection of 24.0mm. A summary of critical values in that analysis can be found in Table 5.2.

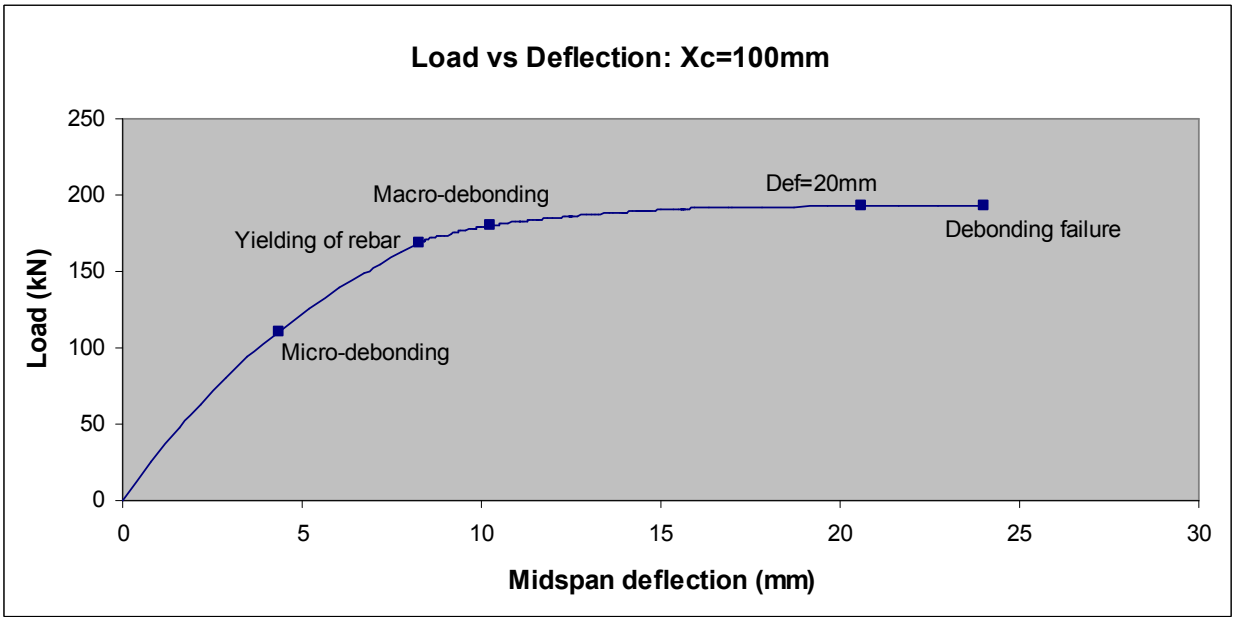

Figure 5.19: Load-deflection response for the crack spacing x_c = 100mm.

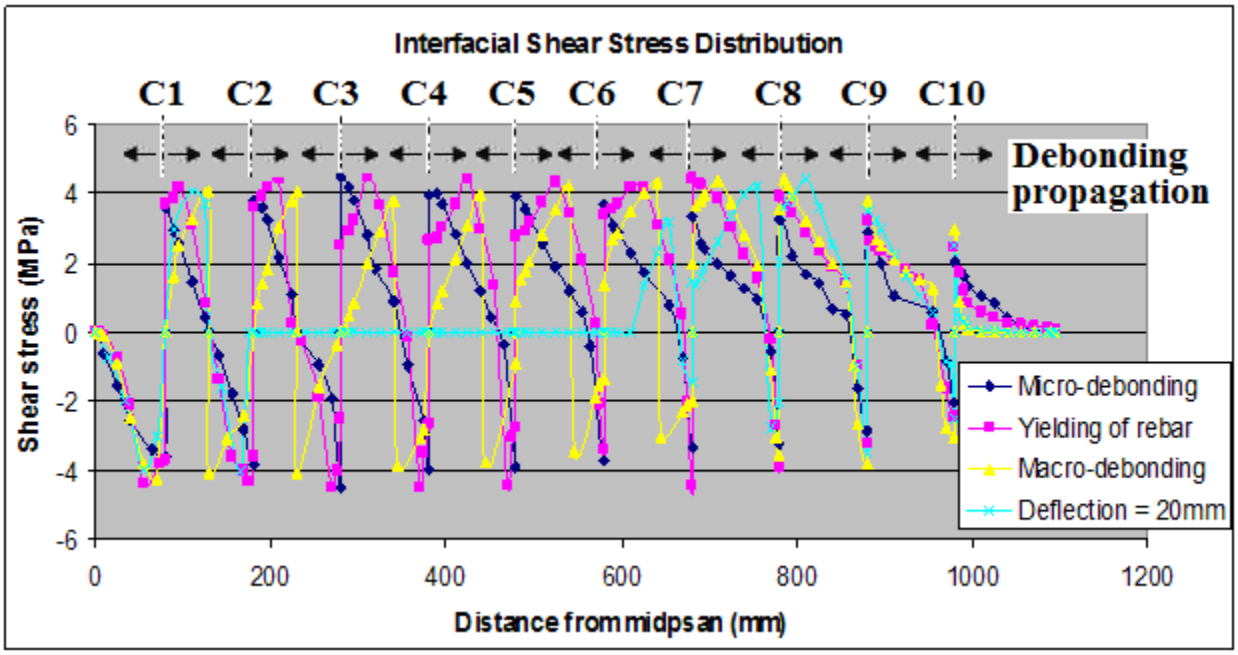

Figure 5.20: Interfacial stress distribution for the crack spacing x_c = 100mm.

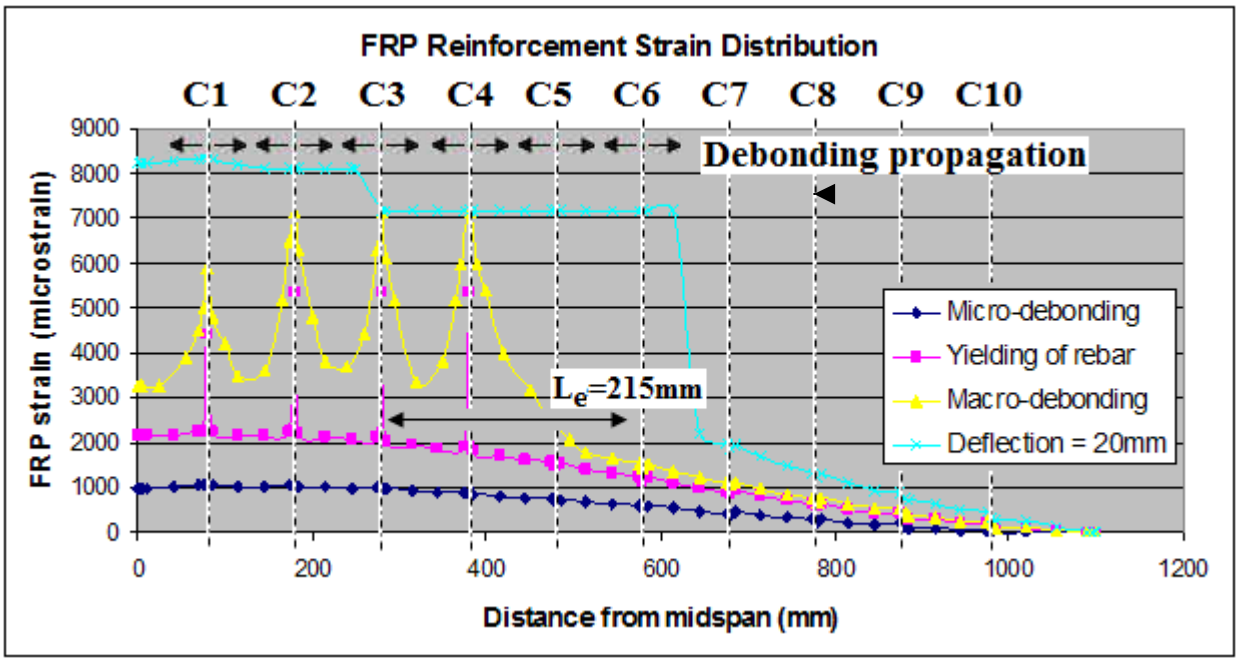

Figure 5.21: FRP reinforcement strain distribution for the crack spacing x_c = 100mm.

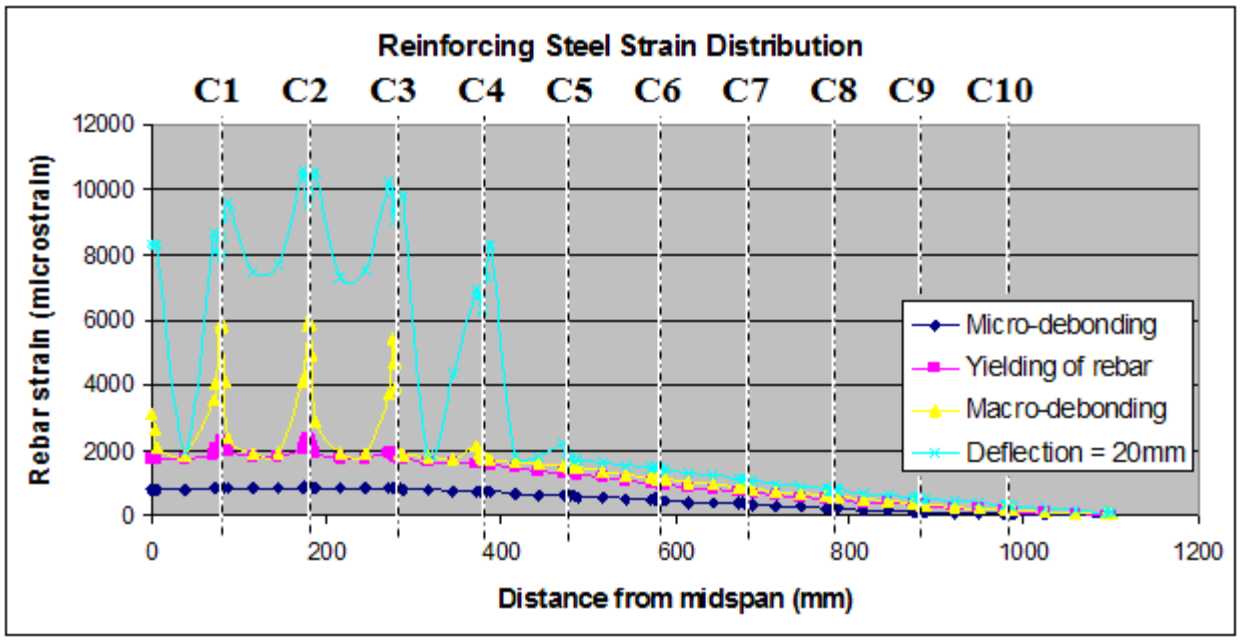

Figure 5.22: Steel reinforcement strain distribution for the crack spacing x_c = 100mm.

5.4.5 Crack Spacing: x_c = 75 mm

The flexural cracks were spaced at a 75mm c/c as shown in Figure A5.13. The first flexural crack, referred to as Crack 1, is predefined at 55mm from the midspan with each subsequent crack spaced at 75mm centre-on-centre. Crack 4 lies directly beneath the applied load. A total of 14 flexural cracks are arranged in the model. Prior to the initiation of flexural cracking, there is no slip and therefore no shear stress at the FRP-concrete interface. Once flexural cracking initiates, the interfacial shear stress increases with deflection until micro-debonding initiates at Crack 4 at a midspan deflection of 5.7mm, as shown in Figures 5.23 and 5.24. At this point, micro-cracking occurs in the weaker concrete layer of the interface and high bond stresses develop near the toe of Crack 4 creating sliding between the concrete and the FRP plate. The strain in the plate is no longer equal to the strain in the adjacent concrete and the difference is defined as slip strain. It was expected that micro-debonding would initiate at Crack 4 since this flexural crack is located in the maximum moment region and also experiences the highest

shearing force of the 14 predefined cracks. This point is illustrated in Figure 5.24 as the stress concentration at the toe of Crack 4 reaches is maximum value of 4.5MPa. The occurrence of closely spaced flexural cracks affects the interfacial shear stress distribution of the beam by changing the direction of slip and consequently the bond stress to maintain equilibrium. The regions between Cracks 1-4 are located in the constant moment region and there exists a point of zero slip at the midpoint between subsequent cracks. The other cracks lie in the varying moment region where the point of zero slip seems to move to the right of each crack (i.e. towards the support) along the interface with load. At the initiation of micro-debonding at Crack 4, the other 13 flexural cracks in the model are still in their elastic stage as shown in Figure 5.24. As Crack 4 tends to open, it causes a shift of the maximum interfacial values of bond stresses from the load point in two directions: towards the support and the applied load. The shift may be attributed to the increase in loading which forced the interfacial shear stresses to exceed the interfacial shear capacity of the interface and form a horizontal crack that begins to propagate along the interface.

This shift is captured in Figure 5.24 at the point of yielding of the reinforcing steel where the peak interfacial stress concentration has shifted right of the crack in the direction of the support at a midspan deflection of 8.5mm. This change in stress concentration suggests that the interface is softening as its shear strength capacity was reaches and now the interface is yielding. Similar behaviour of the interface was found between Cracks 3-4, 4-5, 5-6, 6-7, 7-8, 8-9, and 9-10. On the other hand, the interface between Cracks 1-2, 2-3, 10-11, 12-13, and 13-14 are still in their elastic stage. The reinforcing steel has yielded at Cracks 1-4 at this point. This can be attributed to the fact that all four of these cracks are located in the contact moment region near the midspan and experience the greatest bending moment of in the beam. Once yielding occurs in the reinforcing at Cracks 1-4, the FRP strain increases at a much higher rate as shown in

Figure 5.25. This sudden increase in the FRP strain can be attributed to the fact that the FRP is now required to restrain the opening of the flexural crack since the rebar has yielded and loading continues to increase. The interface between Cracks 1-2, 2-3, and 3-4 still have the point of zero slip positioned at the midpoint between the adjacent cracks, similar to the case at the initiation of micro-debonding. However in the varying moment region, the point of zero slip between remains in relatively the same position between all crack interfaces indicating the debonding crack initiating from the left of the crack (i.e. towards the applied load) is constrained by the debonding crack propagating to the right of the crack (i.e. towards the support).

Macro-debonding initiates at Crack 4 with a midspan deflection of 10.8mm. This point is clearly captured in Figure 5.24 where the stress concentration has decreased to zero. No sign of macro-debonding was found until the reinforcing steel has yielded. At this moment, Cracks 3 and 5 are also very close to macro-debonding suggesting the existence of extremely high stress concentration near the load point with the cracks spaced so closely together. The interface between Cracks 1-2, 2-3, 5-6, 6-7, 7-8, 8-9, 9-10 and 10-11 are experiencing softening of the interface whereas between Cracks 11-12, 12-13, and 13-14 are still in their elastic stage. Since the crack spacing is nearly half of the observed effective transfer length of 140mm, the debonding crack encounters resistance from the opposite direction near the adjacent crack. This leads to an increased equivalent transfer length that can be identified by considering the FRP strain distribution. Figure 5.25 finds that the increased transfer length is approximately 245mm to the left of the load point. The interfaces between the cracks in the constant moment region are still found to have the point of zero slip located at the midpoint between the subsequent cracks. However, in the varying moment region the point of zero slip has shifted right of the crack (i.e. towards the support) at the interfaces between Cracks 4-5, 5-6, 6-7, 7-8, 8-9, and 10-11. No

change in the position of the point of zero slip was observed at interfaces between Cracks 9-10, 11-12, 12-13, and 13-14.

As the slip at the crack further increases, the debonding crack propagates along the beam. To demonstrate the debonding propagation along the interface, Figure 5.27 captures the interfacial shear stress distribution at three loading phases: 12.5, 15, and 20mm midspan deflections. For the case of midspan deflection of 12.5mm, the FRP plate has debonded form the concrete substrate between the locations of 205 and 325mm from the midspan. These peak locations represent the shifting of the maximum values of bond stresses towards the midspan and plate end, respectively, as well as the point at which micro-debonding initiates followed by the softening regime of the interface, as represented in Figure 4.15. An increase in the debonded region is found at the midspan deflection of 15mm, where the FRP has completely debonded from the concrete at the locations of 190 to 400 mm from the midspan. This trend continues for the case of the midspan deflection of 20mm, where the debonded region of the FRP continues to increase now from 125 to 595 mm from the midspan. The debonded region continues to grow until the FRP completely debonds from the concrete substrate towards the plate-end at a midspan deflection of 22.6mm. A summary of all critical values in the analysis can be found in Table 5.2.

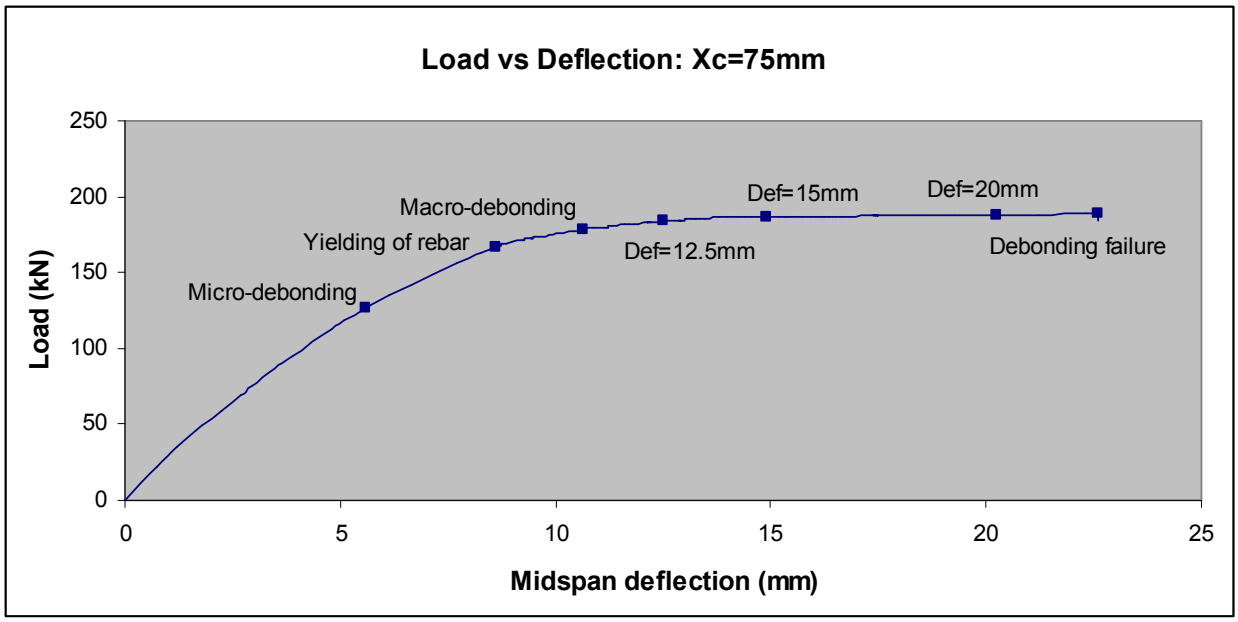

Figure 5.23: Load versus deflection for the crack spacing x_c = 75mm.

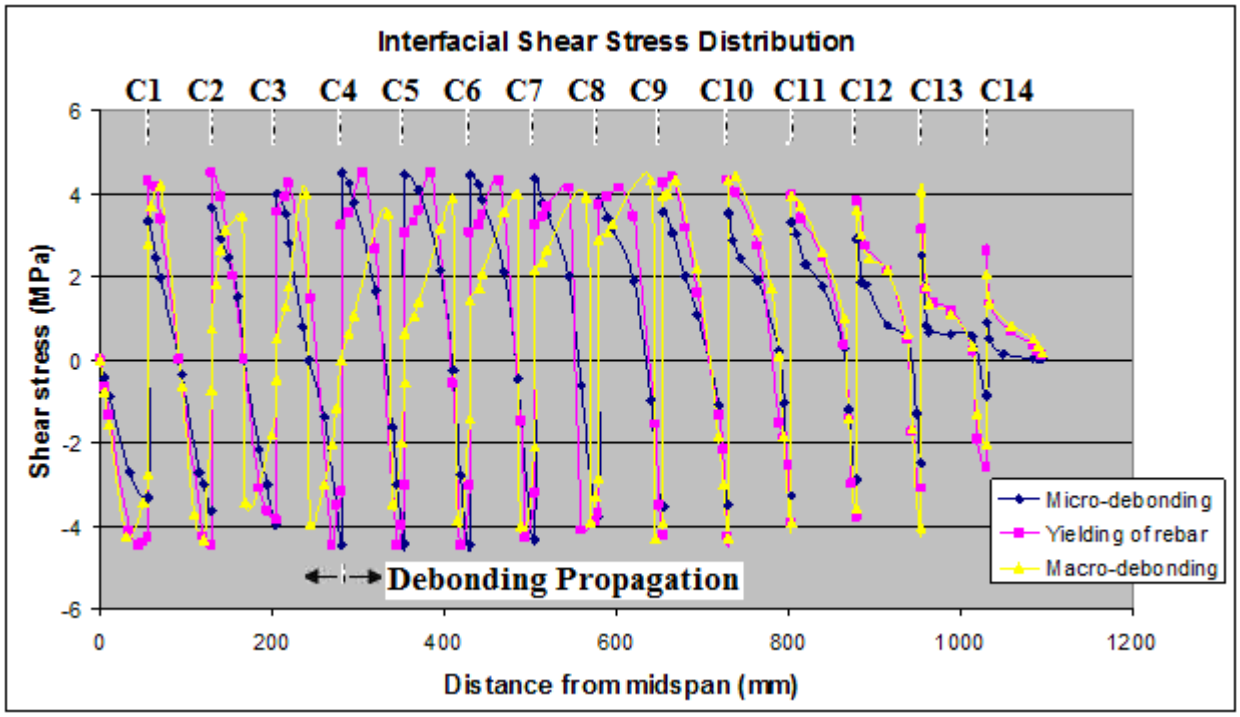

Figure 5.24: Interfacial stress distribution for the crack spacing x_c = 75mm.

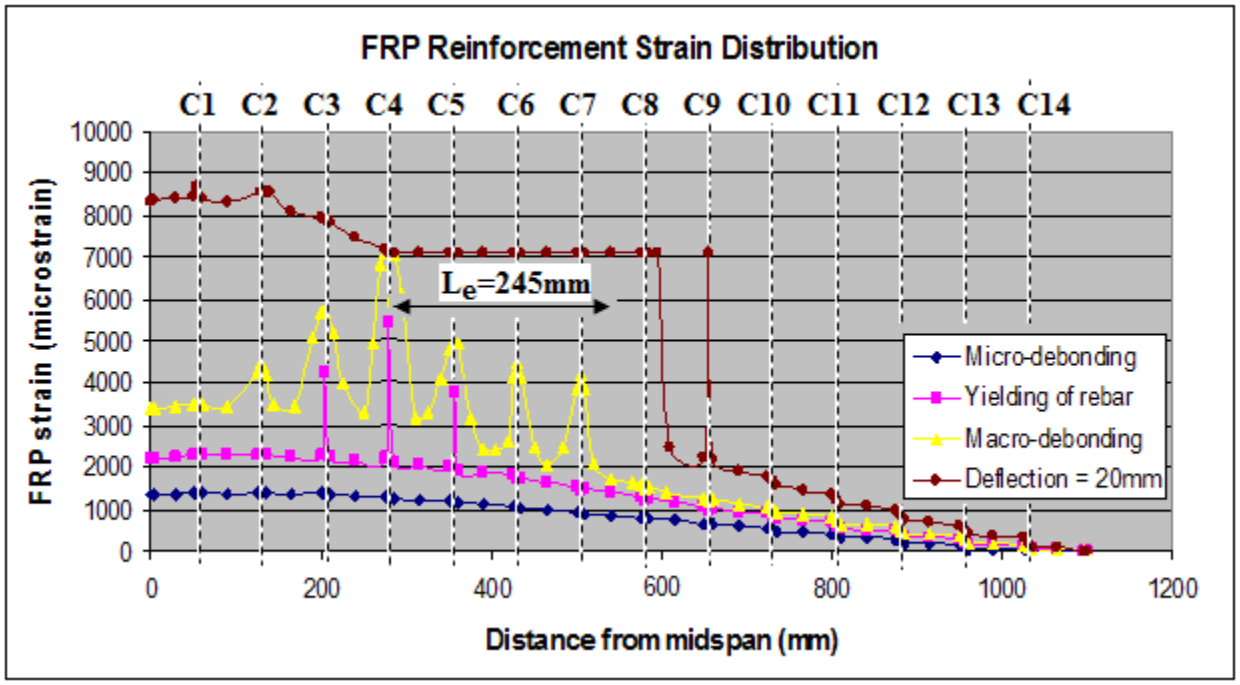

Figure 5.25: FRP reinforcement strain distribution for the crack spacing x_c = 75mm.

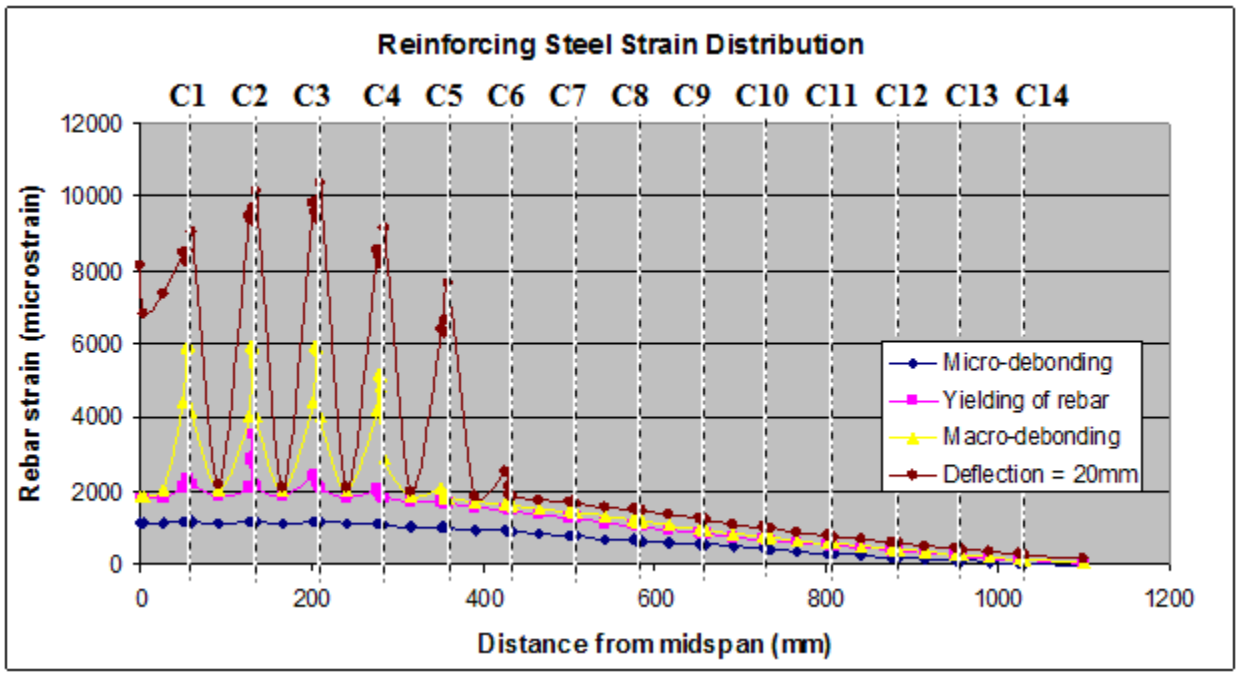

Figure 5.26: Steel reinforcement strain distribution for the crack spacing x_c = 75mm.

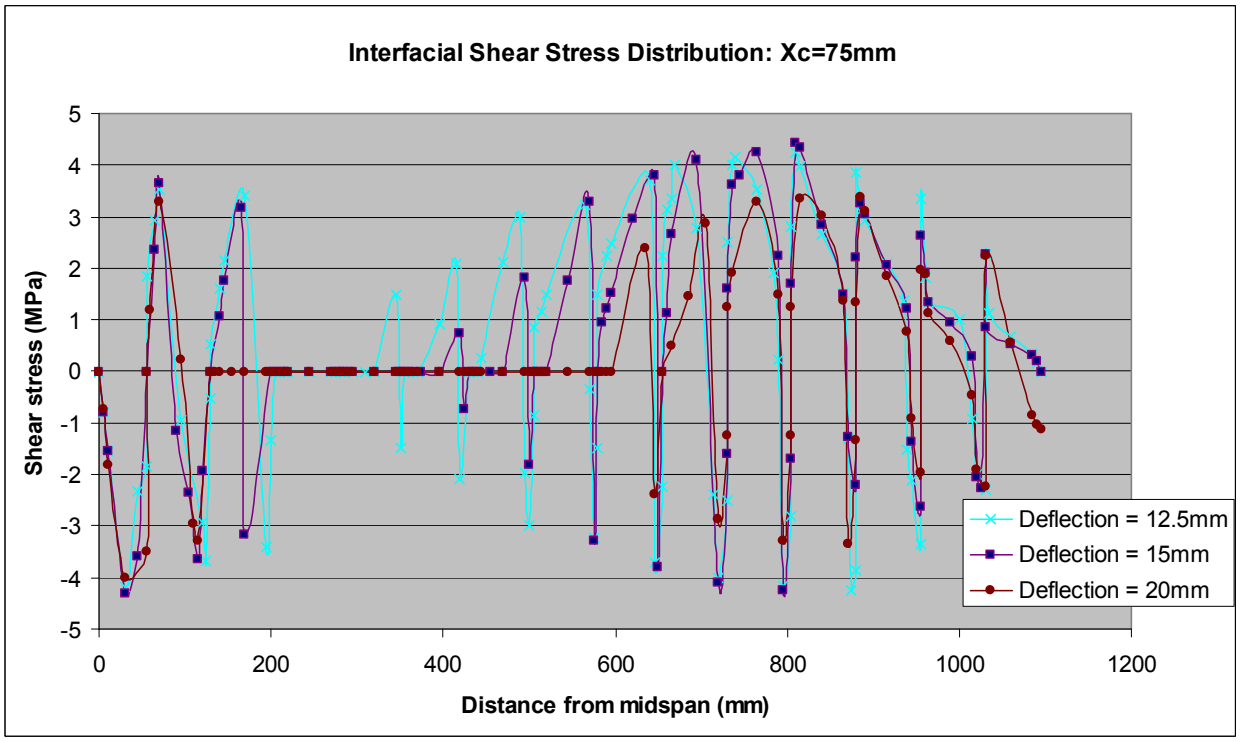

Figure 5.27: Interfacial stress distribution for various loading stages (x_c = 75mm).

5.4.6 Crack Spacing: x_c = 50 mm

The first flexural crack, referred to as Crack 1, is positioned 30mm from the midspan with each subsequent crack spaced at 50mm centre-on-centre, as shown in Figure A5.12. Crack 6 lies directly beneath the applied load. A total of 21 flexural cracks are arranged in the model. Prior to the initiation of flexural cracking, there is no slip and therefore no shear stress at the FRP-concrete interface. Once flexural cracking initiates, the interfacial shear stress increases elastically with load until micro-debonding initiates at Crack 6 at a midspan deflection at 6.1mm, as shown in Figure 5.28 and 5.29. At this point, micro-cracking occurs in the weaker concrete layer of the interface and high bond stresses develop near the toe at Crack 6 creating sliding between the concrete and the FRP plate. The strain in the plate is no longer equal to the strain in the adjacent concrete and the difference is defined as slip strain. It was expected that micro-debonding would initiate at Crack 6 since this flexural crack is located in the maximum moment

region and also experiences the highest shearing force of the four predefined cracks. This point is illustrated in Figure 5.29 at the stress concentration at the toe of Crack 6 reaches it maximum value of 4.5MPa. The existence of the closely spaced flexural cracks influences the interfacial shear stress distribution of the beam by changing the direction of slip, and consequently bond stress to maintain equilibrium. The interfaces between Cracks 1-6 are located in the constant moment region and a point of zero slip is found at the midpoint between adjacent cracks. The other cracks are positioned in the varying moment region of the beam and it is found that the point of zero slip is not positioned at the halfway point between adjacent cracks. The general trend between the cracks in this region is that the zero slip is located closest to the crack positioned nearest to the support as shown in Figure 5.29. This may be attributed to the differences in the opening of the flexural crack. The cracks located closer to the applied load will release tensile stresses and transfer high local interfacial shear stresses to the FRP plate sooner than the crack located closer to the support. Micro-debonding initiates simultaneously at Cracks 6 and 7, whereas the other 19 cracks are still in their elastic stage. As Crack 6 tends to open, it causes a shift of the maximum interface bond stress from the load point in two directions: towards the support and the midspan. This shift may be attributed to the increase in loading which forced the interfacial shear stresses to exceed the interfacial shear capacity of the interface and form a horizontal crack that begins to propagate along the interface.

Yielding of the steel reinforcement occurs at a midspan deflection of 8.9mm. At this moment, a shifting of the maximum interfacial shear stress is seen from the toe of Crack 6 move towards the support. The interfaces between Cracks 5-6, 6-7, 7-8, 8-9, 9-10, 10-11, 11-12 and 12-13 are experiencing a shift in the locations maximum interfacial shear stress suggesting that the interface located in these areas are softening. The interfaces between Cracks 1-2, 2-3, 3-4, 4-

5, 13-14, 14-15, 15-16, 16-17, 17-18, 18-19, 19-20 and 20-21 are still in their elastic stages as their peak interfacial shear capacity at the toe of the flexural crack has not been reached yet. The reinforcing steel was found to have yielded at Cracks 1-6 at this point as shown in Figure 5.32. This can be attributed to Cracks 1 – 6 being located in the maximum moment regions. Once the yielding occurs in the reinforcing bars at these cracks, the FRP strains increase at a much higher rate as shown in Figure 5.31. This sudden increase can be attributed to the fact that the FRP is now required to restrain the opening of the flexural cracks as loading further increases. It should be noted that between Cracks 1-6 there still exists a point of zero slip at the midpoint between the two cracks, similar to the case during the initiation of micro-debonding. However in the varying moment region the point of zero slip did not change positions from the initiation of micro-debonding, except at the interfaces between Cracks 12-13, 13-14, 14-15 and 15-16 where it shifts right of the crack, i.e. toward the support. This indicates that the un-cracked concrete segment is gradually slipping towards the adjacent crack situated closer to the support and hence reducing the slip on the left face of the crack.

As the loading further increases, the slip at the interface adjacent to Crack 6 grows and eventually initiates macro-debonding at a midspan deflection of 12.0mm. This point is captured in Figure 5.30 where the stress concentration has reduced to zero. Macro-debonding at cracks 5-9 initiate simultaneously. This is a rare occurrence in comparison to the other crack spaced models, where macro-debonding was found to previously occur only under the applied load and the subsequent cracks would debond as loading further increased. This may be attributed to the high local interfacial bond stresses that exist between the FRP-concrete interface and inadequate spacing between cracks to restrain the tensile stresses released by these flexural cracks and transferred to the FRP plate. The interfaces at Cracks 1-5 and 9-16 are all softening whereas the

interfaces at Cracks 17-21 are still in their elastic stage. The strain in the reinforcing steel and FRP plate continue to increase to restrain the opening of Cracks 5-12. Due to the fact that the crack spacing is smaller than the effective observed effective transfer length of about 140mm, the debonding propagation encounters resistance from the opposite direction near the adjacent crack. This leads to an increased equivalent transfer length that can be captured by considering the FRP strain distribution in Figure 5.31. Here it is shown that the effective transfer length is approximately 330mm to the left of the load point. Debonding failure occurred at a midspan deflection of 21.5mm.

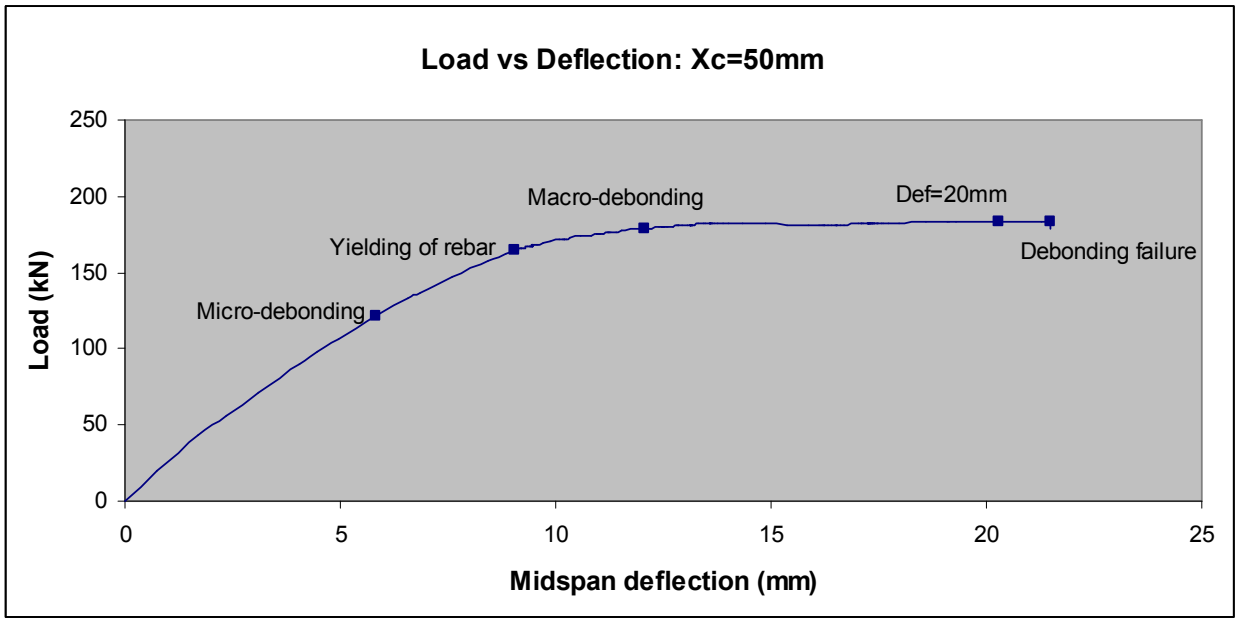

Figure 5.28: Load-deflection response for crack spacing x_c = 50mm.

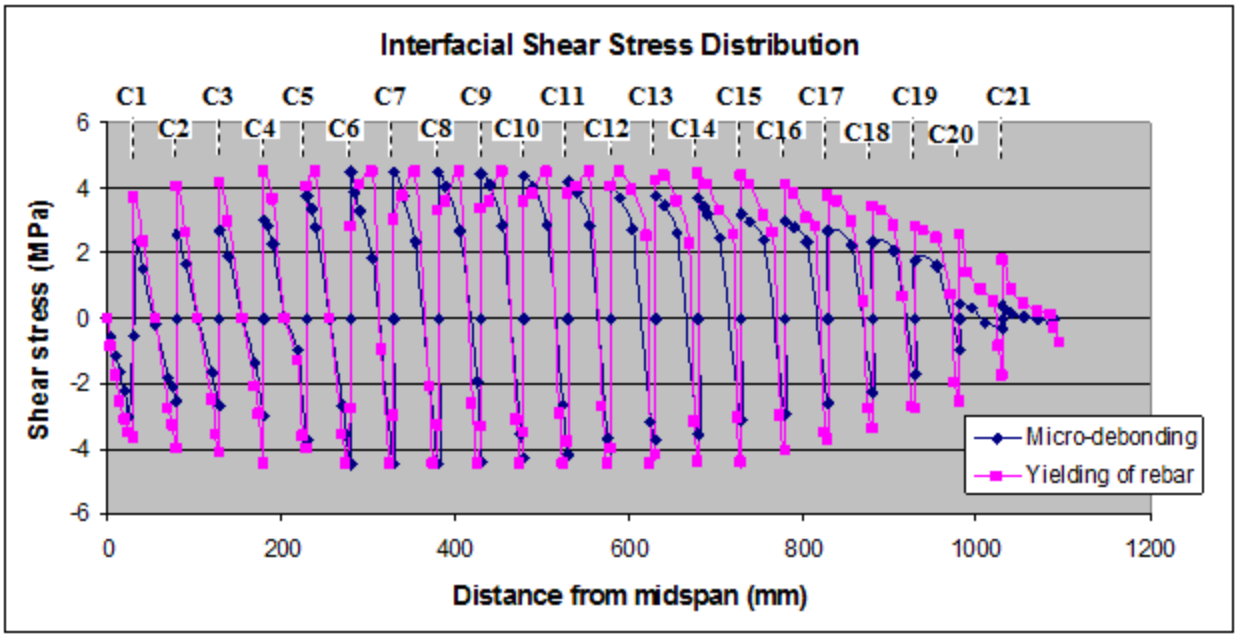

Figure 5.29: Interfacial shear stress distribution crack spacing x_c = 50mm.

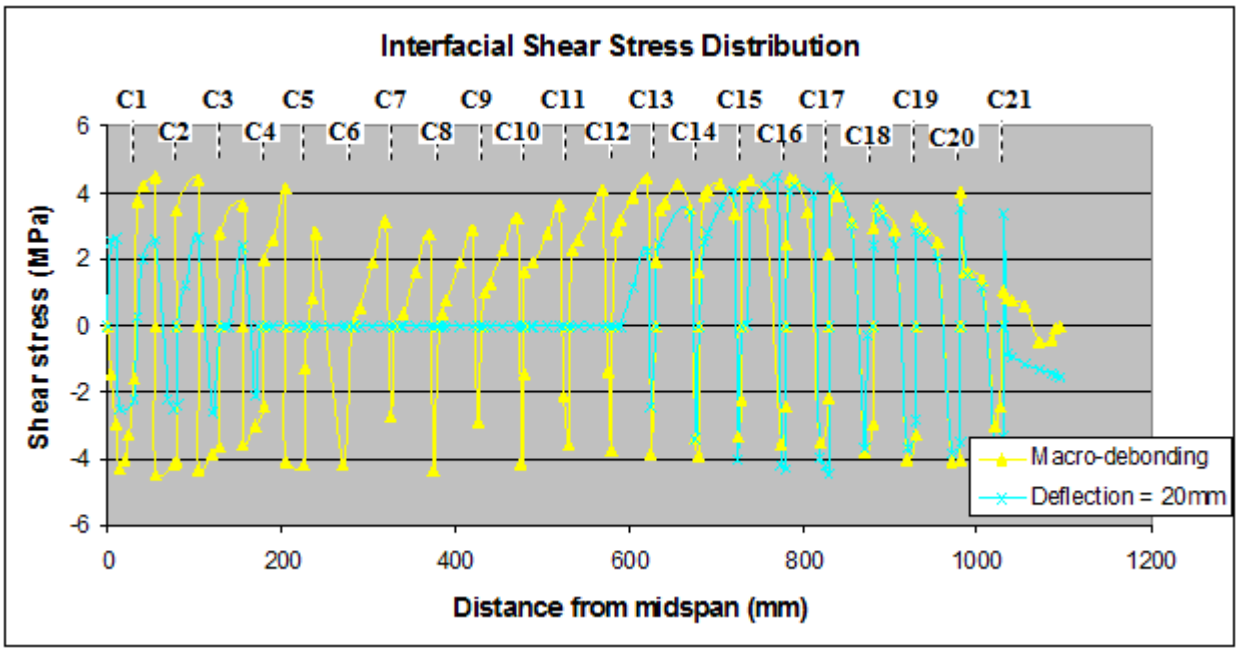

Figure 5.30: Interfacial shear stress distribution crack spacing x_c = 50mm.

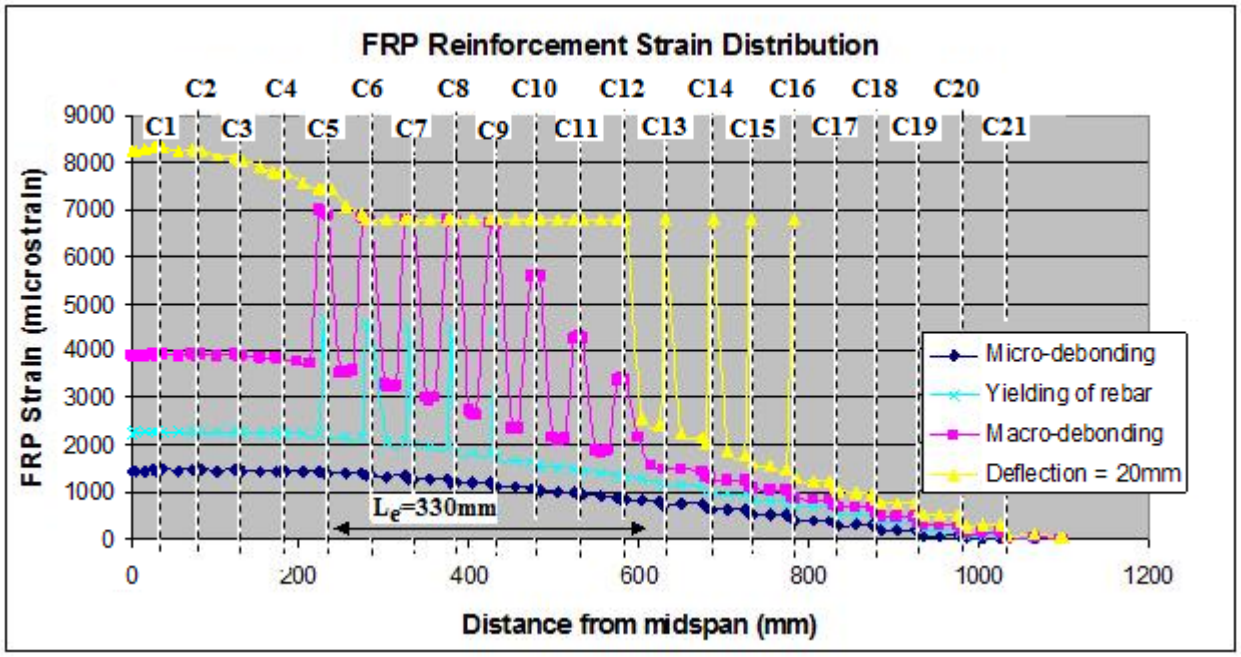

Figure 5.31: FRP strain distribution for crack spacing x_c = 50mm.

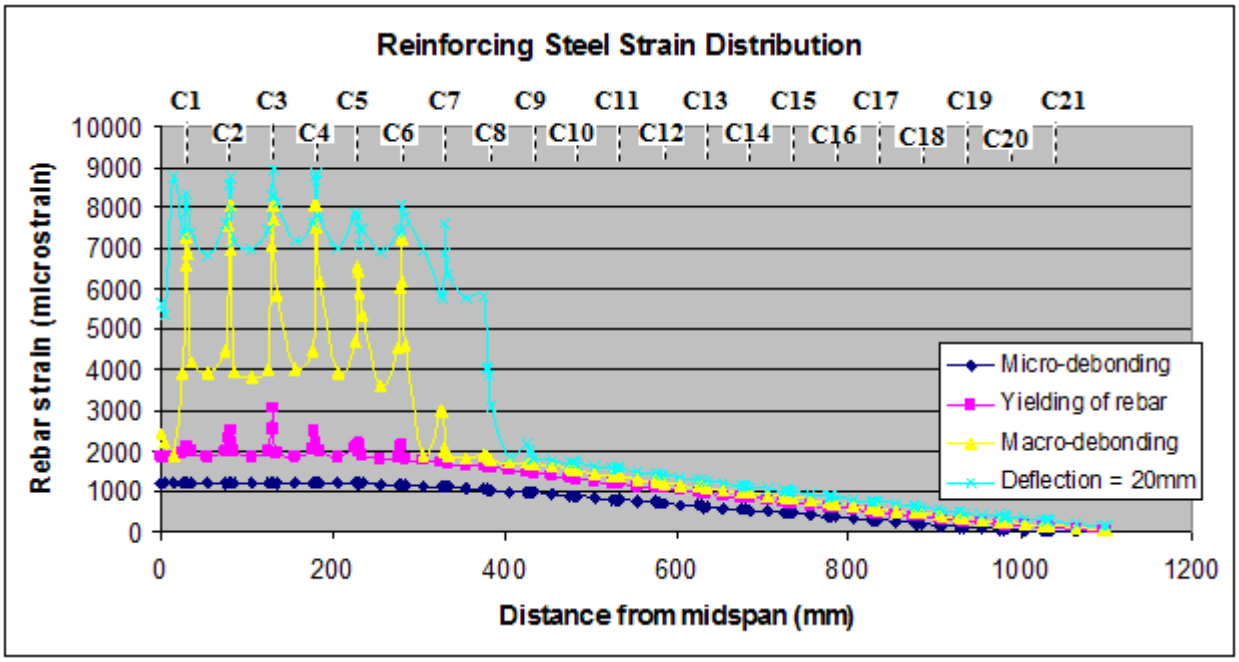

Figure 5.32: Reinforcing steel strain distribution for crack spacing x_c = 50mm.

5.4.7 Trends

In this section, a parametric analysis was presented that investigated the effect of crack spacing on debonding mechanisms and strengthening effect of FRP strengthened RC beams. The following trends were found:

1. The general trend in the load-deflection response is described with reference to Figure 5.33. In this figure, three distinct regions were observed: A, B, and C. Each region is represented quantitatively with a slope that depends on the flexural stiffness of the strengthened specimen. The first region in the load-deflection response, region A, ends at the load-corresponding to concrete cracking and can be calculated by using gross cross-sectional properties of the specimen. The second region, region B, is bounded by the load corresponding to cracking and the yield load and the slope is controlled by the amount of reinforcement on the cross section. Finally, the yield load and the maximum load of the strengthened specimens bounded the third region, region C, is governed by the contribution of the FRP plate in the strengthening scheme.
2. No evidence of debonding of the FRP plate was found until yielding of the rebar had occurred in all models.
3. Once macro-debonding would initiate, the debonding crack would propagate towards the end of the FRP sheet and the load would remain relatively constant until the final debonding failure.
4. The displacements at the toe of flexural crack create stress concentrations at the interface of the FRP plate and beam, leading to the development of localized interface cracks that propagate under the effect of the load. If distributed cracks are located along the

interface they will join adjacent flexural cracks, resulting in delamination of the FRP system.

5. The shear stress is both additive and subtractive on either side of each flexural crack due to equilibrium of forces. The value will be a maximum in high moment regions where the crack opening displacement has the greatest magnitude.
6. To maintain equilibrium in the constant moment region, a point of zero slip always occurs at the mid-distance between two cracks, as opposed to a varying moment region where the point of zero slip moves toward the next crack as slip increases. Therefore, debonding in constant moment regions will propagate in both directions and will not close up like those in varying moment regions.
7. The existence of a secondary crack adjacent to the crack positioned under the load-point appeared to have an effect on the debonding mechanisms. Table 5.2 lists the deflection values at the onset of micro-debonding, rebar yielding, and micro-debonding. The results suggest that the existence of the multiple cracks prolong the initiation of micro-debonding, rebar yielding, and macro-debonding. This is substantiated by inspecting the deflection values of the respective crack spacing set-ups. In all cases, debonding and yielding are found to occur at an earlier loading stage in models with larger crack spacing. This may be attributed to the *abrasion effect* along the interface. When a flexural crack opens under loading, longitudinal displacements at the bottom of the beam will increase. Due to the abrasion effect, the residual shear stress at any point along the debonded zone decreases with interfacial relative sliding. As a result, the relative displacement in the debonded zone is reduced and the interfacial shear stress will increase. In other words, the presence of cracks will reduce the initiation of micro-

debonding and rate of interfacial softening. Consequently, the maximum force in the FRP was found to increase with a decrease in crack spacing. The increase in FRP magnitudes demonstrates the effectiveness of FRP rehabilitation in delaying debonding and crack propagation. However, while some researchers have reported increases in ultimate load when crack spacing is reduced, such a phenomenon was not found occur in this study. The existence of more closely spaced flexural or shear/flexural cracks in the model greatly reduces the rigidity of the structure. Subsequent to the initiation of macro-debonding, the debonding propagation was found to be increased in models with smaller crack spacing, evidenced by the lower deflection values obtained before debonding failure. The results of this study are believed to be more representative of that encountered in practice in comparison than that reported by previous researchers. Past researchers (Niu and Wu, 2005; Niu et al., 2006) have investigated the effects of IC debonding by employing very high initial stiffness values to the interface. Other researchers (Wong and Vecchio, 2003; and Wu and Yin, 2003, Kishi et al., 2005) reported to lower the local bond strength to bring the FE results into closer agreement with test results. These researchers artificially adjusted the bond-slip relationships of these interface elements based only on empirical evidence. Such adjustments do not lead to a generally valid FE model for such debonding failures.

8. Table lists the strain values in the FPR plate at the initiation of micro-debonding and rebar yielding. The strain in the FRP plate increases with a decrease in cracking spacing (i.e. highest FRP strain for x_c=50mm model and is the lowest for the single crack spaced models). This may also be attributed to the abrasion effect as more energy is required for

the debonding to propagate through the cracks, which prolongs debonding and yielding initiation.

9. The presence of an FRP strengthening material bonded to the tension face of a RC beam will restrict but not prevent the opening of an intermediate flexural or shear crack due to applied loading.
10. Figure 5.34 demonstrates the effects of crack spacing on the load-deflection behaviour of the FRP-strengthened beam. It can be seen that the stiffness of the strengthened beam decreases with the decrease of crack spacing. Single localized crack and large crack spacing give almost the same ultimate load, which is lower than that of small crack spacing.

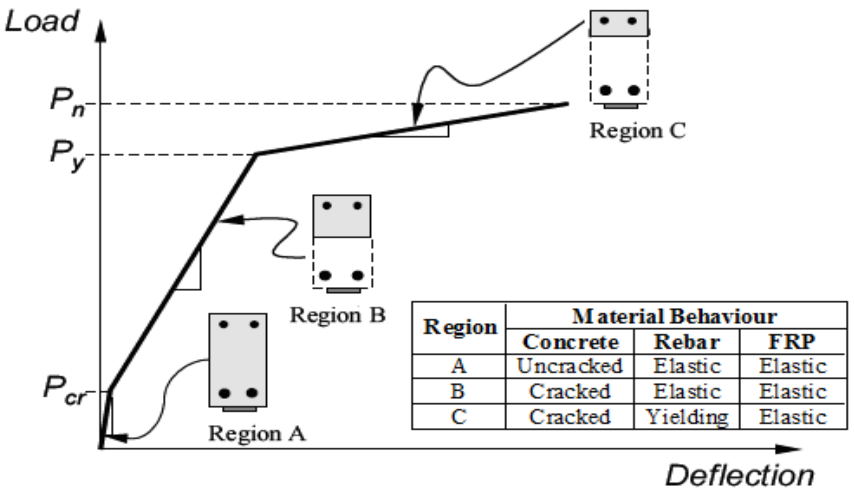

Region	Material Behaviour		
	Concrete	Rebar	FRP
A	Uncracked	Elastic	Elastic
B	Cracked	Elastic	Elastic
C	Cracked	Yielding	Elastic

Figure 5.33: Qualitative representation of the load-deflection response for FRP-RC beam.

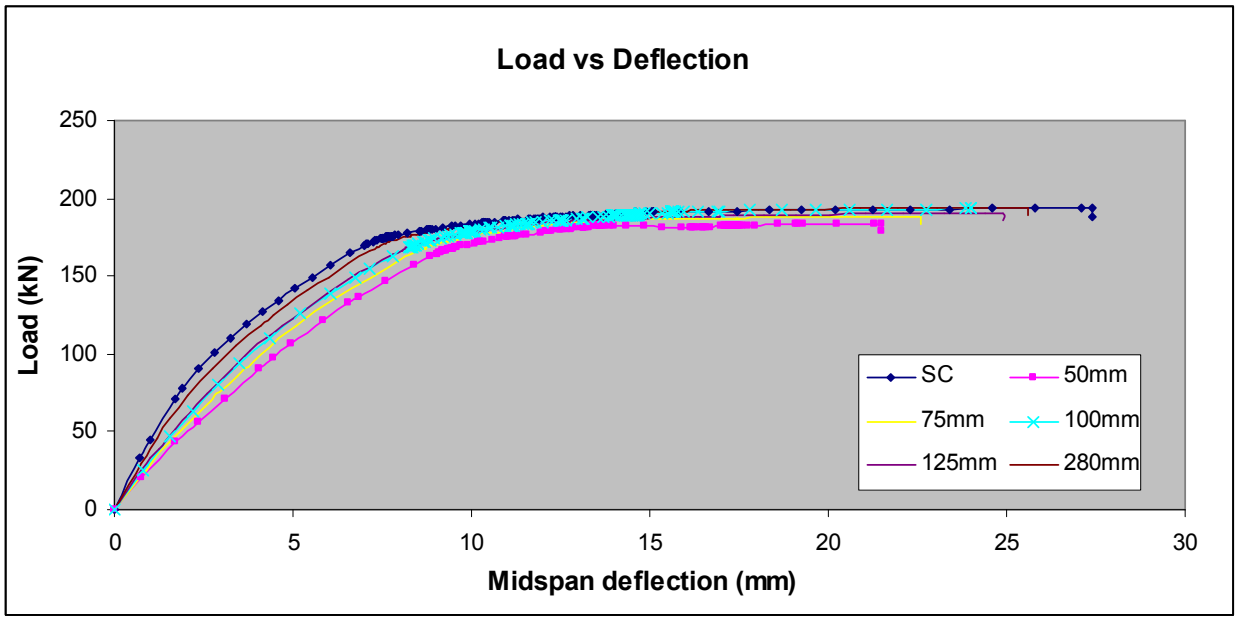

Figure 5.34: Comparison of load-deflection response of crack spaced models.

Table 5.2: Summary of effect of crack spacing analysis.

x_c	Init. of micro-debonding		Yield load		Init. of macro-debonding		Ultimate load		FRP strain (micro strain)			Mode of failure
(mm)	P (kN)	Δ (mm)	P (kN)	Δ (mm)	P (kN)	Δ (mm)	P (kN)	Δ (mm)	$*\varepsilon_m$	$*\varepsilon_y$	$*\varepsilon_{ult}$	
SC	90.4	2.4	176.7	6.9	184.9	8.5	193.9	27.4	603.9	4500	5950	IC
280	90.8	2.7	165.7	7.1	178.9	9.0	194.3	25.6	664.4	4950	6188	IC
125	94.0	3.4	163.8	7.8	178.0	10.1	190.6	24.9	897.7	5135	6924	IC
100	110.7	4.5	168.5	8.1	179.8	10.3	193.5	24.0	971.7	5360	7153	IC
75	126.8	5.7	167.0	8.5	178.2	10.8	188.6	22.6	1286	5399	7104	IC
50	121.7	6.1	164.2	8.9	178.2	12.0	183.8	21.5	1368	4580	6826	IC

$*\varepsilon_m$, ε_y, ε_{ult} – FRP strain at the initiation of micro-debonding, yield load, and ultimate load, respectively.

5.5 EFFECT OF INTERFACIAL STIFFNESS

Interfacial stiffness is directly related to the properties of the adhesive in contact with the concrete and the initial layer of the concrete substrate. It has a direct influence on the load transfer efficiency between the concrete substrate and the FRP, and is as a critical component in ensuring composite action between the two materials. For this reason, an effort was made to investigate its effect on the debonding behaviour and strengthening effect when subjected to

multiple distributed cracks. Yoshizawa et al (2000) performed single and double lap shear tests on interfacial stiffness and found that it is varied between 30 to 300MPa/mm with a commonly seen value of 160MPa/mm. By fixing the crack spacing at x_c=100mm, local bond strength at τ_b= 4.5MPa, and interfacial fracture energy at G_f^{int}=0.5N/mm, the effect of interfacial stiffness is studied by varying it for three cases: k_s=50, 160, and 500 MPa/mm. These cases represent low, average, and high stiffness materials that may be employed in practice. It was evaluated based on its response to: load versus deflection, interfacial shear stress versus midspan deflection, FRP strain distribution, rebar strain distribution, and interfacial shear stress distribution.

Figure 5.35 shows the load versus midspan deflection for the parametric analysis. While no difference is observed for the various values of initial stiffness prior to the yield load, the figure clearly demonstrates its effect immediately after. Complete debonding was found to occur at a midspan deflection of 11.7, 24.0, and 29.7mm for stiffness values of 50, 160, and 500MPa/mm, respectively. These findings suggest that a low value of interfacial stiffness results in a low rate of load transfer and a low level of structural stiffness after cracking. Moreover, the low rate of stress transfer forces the concrete to initially carry a higher level of load resulting in earlier formation and opening of the flexural cracks, which then causes premature initiation of debonding along the interface in comparison to higher stiffness interfaces. Yield and ultimate load were found to be increased in the higher stiffness model as well, as a load ratio of 1.24 was achieved, in comparison to 1.09 for the low stiffness model.

Figure 5.36 captures the interfacial shear stress versus midspan deflection at the flexural crack located directly beneath the applied load. The figure suggests that higher stiffness facilitates the initiation of micro-debonding, whereas lower interfacial stiffness prolongs it. Micro-debonding initiates at a midspan deflection of 5.4, 4.5, and 3.3mm for stiffness values of

50, 160, and 500MPa/mm, respectively. This may be attributed to lower stiffness interfaces reducing the rate of stress transfer at the interface and not utilizing the FRP material efficiently in the early loading stages. This is supported by comparing the strain development in the FRP plate at the midspan deflection of 4.5mm in Figure 5.37.

Yielding of the rebar then follows at 7.4, 8.1, and 8.5mm for stiffness values of 50, 160, and 500MPa/mm, respectively. Internal rebar was found to yield first in the low stiffness model, indicating that it was required to contribute more to the load carrying capacity than the high stiffness values due to the low transfer rate at the interface. On the other hand, the rebar in the highest stiffness interface was the last to yield in the loading sequence. This is attributed to the superior transfer of stresses at the interface when higher stiffness values are employed. It is also seen that higher stiffness prolongs mode II macro-debonding, suggesting that a stiffer interface reduces the rate of softening. This can be attributed to the fact that additional work is required for the debonding to propagate beyond the crack. Macro-debonding was found to initiate at midspan deflections of 8.5, 10.3, and 15.3mm, respectively for the values studied.

Low interfacial stiffness was found to influence the development of strain of the internal rebar. Figure 5.38 presents the strain of the rebar at the midspan deflection of 4.45mm for all stiffness models. At this point, the strain development in the low interfacial stiffness model is considerably greater than that of the higher stiffness models. This may be attributed to the low stress transfer rate between concrete and FRP plate which in turn yields a high strain distribution in the internal rebar. The internal rebar is required to contribute more to the load carrying capacity of the structure as the transfer of stresses at the interface is minimal. The low rate of transfer at this point is exemplified in Figure 5.37, where it can be clearly shown the model employing the low interfacial stiffness model is not utilizing the FPR plate to the same extent as

the higher stiffness values. However, as loading further increases, there appears to be no significant difference in rebar strain at a midspan deflection of 10.3mm, as shown in Figure 5.39. This may be attributed to the contribution of the FRP plate to the load-carrying capacity of the structure at this point. Figure 5.40 illustrates the strain in the FRP plate also at a midspan deflection of 10.3mm. It can be seen that for the low initial stiffness model, the strain in FRP plate is drawing closer to the higher stiffness models after yielding of the internal rebar has occurred. Unfortunately, the debonding of the FRP plate in the lower stiffness model at this loading stage prevented the confirmation of this development, as shown in Figure 5.40. Nonetheless, the findings do indicate that the interfacial stiffness may not influence the contribution of the FRP plate in later stages of loading provided the transferring of stresses from the concrete to FRP sheets is ensured; it may only delay it.

Figure 5.41 illustrates the interfacial shear stress distribution along the FRP-concrete interface at a midspan deflection of 10.3mm. In the case of the low stiffness model, the FRP plate has debonded from Crack 2 to 9 and is propagating in mode II fracture behaviour towards the plate-end. Whereas the 160MPa/mm is just beginning to macro-debond and the 500MPa/mm model still has its interface intact. The low interfacial stiffness model was found to debond at a premature loading stage due to its inability to obstruct the formation of micro-cracking and its inability to utilize the FRP plate to its full potential.

Interfacial stiffness is thus seen to affect yield and ultimate load, stress transfer, structural stiffness, initiation of micro- and macro-debonding, as well as overall efficiency of the strengthening system.

Table 5.3: Response of models for different interfacial shear stress models.

k_s^{int}	Init. of micro-debonding		Yield load		Init. of macro-debonding		Ultimate Load		LR*
(MPa/mm)	P (kN)	Δ (mm)	P (kN)	Δ (mm)	P (kN)	Δ (mm)	P (kN)	Δ (mm)	
50	120.4	5.4	151.6	7.4	162.2	8.5	183.9	23.8	1.09
160	110.7	4.5	168.5	8.1	179.8	10.3	193.5	24.0	1.15
500	95.2	3.3	175.9	8.5	203.1	15.3	208.1	25.6	1.24

*LR - Load ratio defined as maximum applied load resisted by specimen divided by yield load for control specimen.

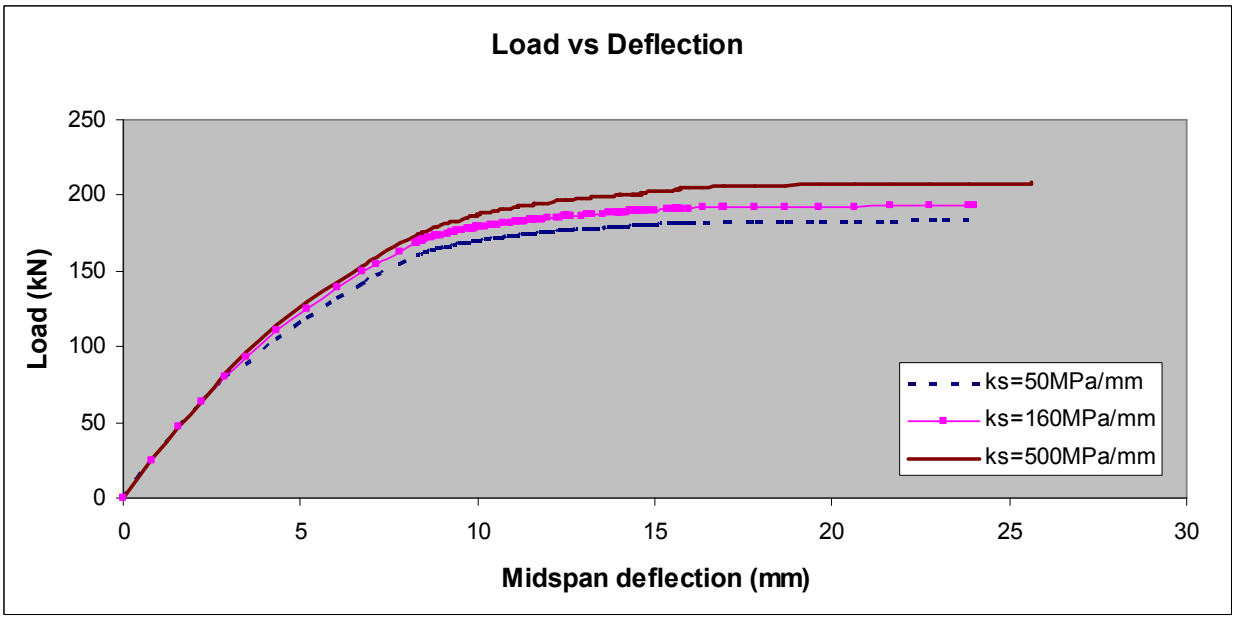

Figure 5.35: Effect of interfacial stiffness on load versus deflection response (x_c = 100mm).

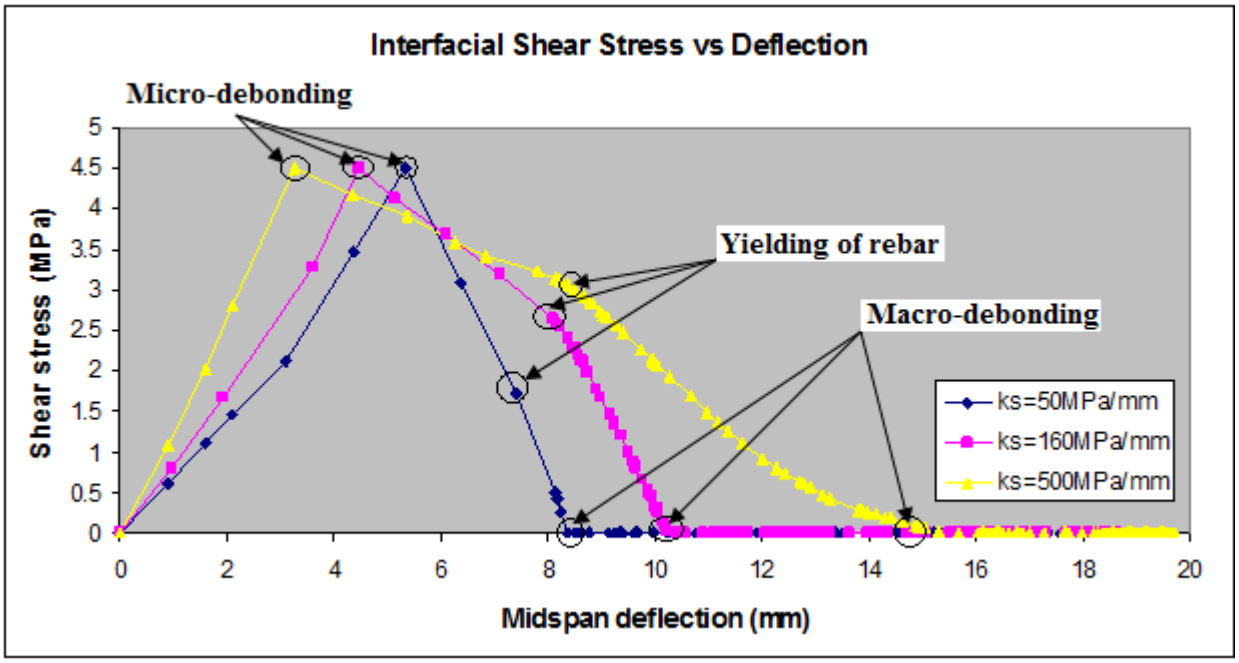

Figure 5.36: Effect of initial interfacial stiffness on interfacial shear stress versus deflection (x_c = 100mm, Crack 4).

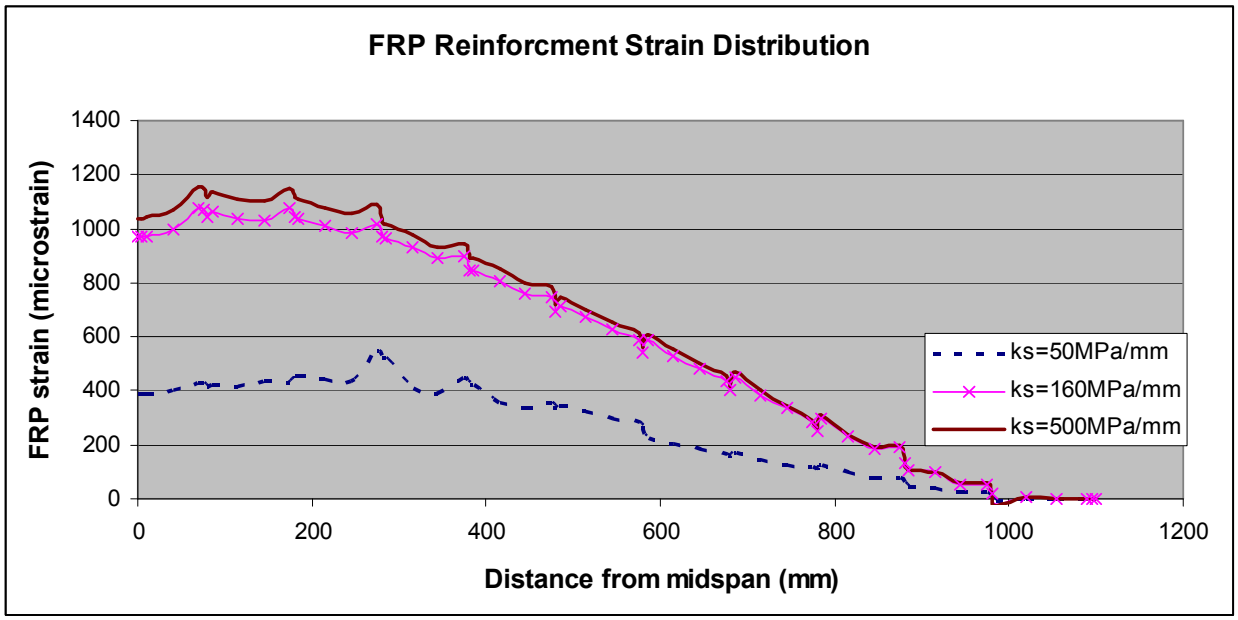

Figure 5.37: Effect of interfacial stiffness on FRP reinforcement distribution (x_c = 100mm, deflection=4.45mm).

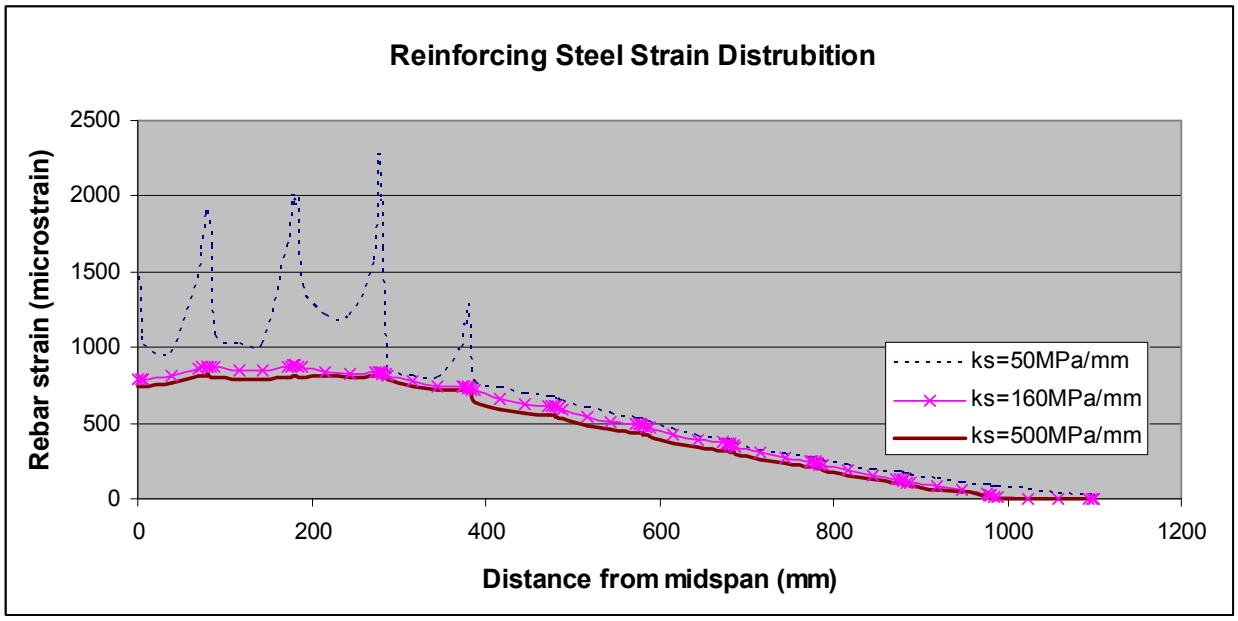

Figure 5.38: Effect of interfacial stiffness on steel reinforcement distribution (x_c = 100mm, deflection=4.45mm).

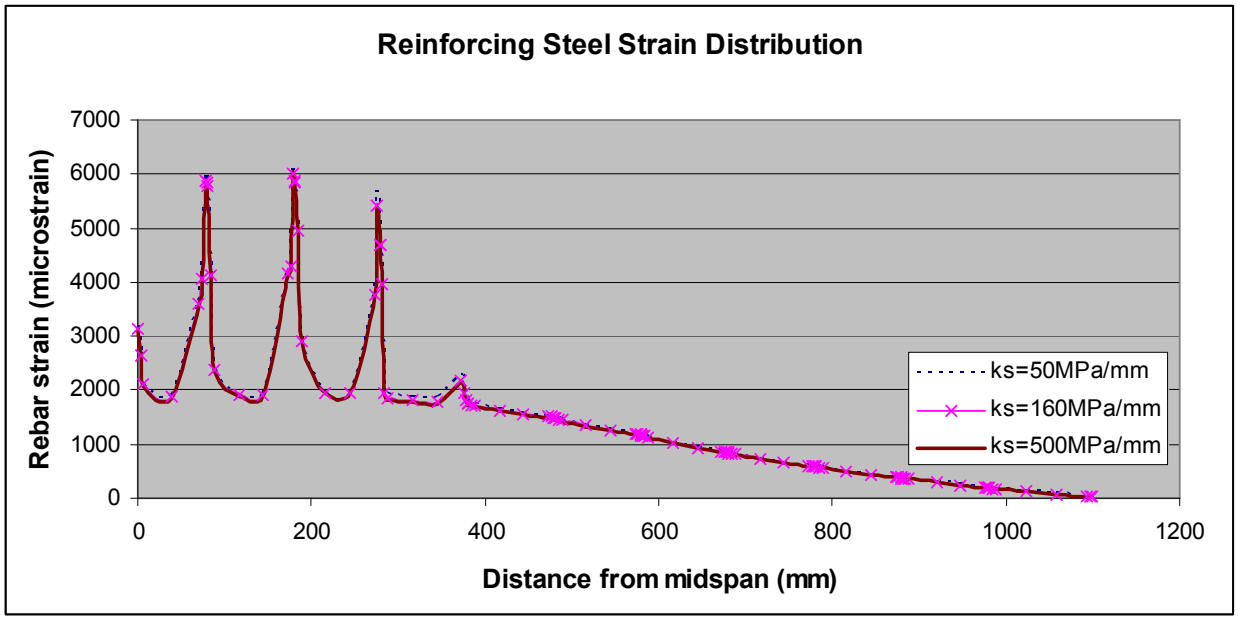

Figure 5.39: Effect of interfacial stiffness on steel reinforcement distribution (x_c = 100mm, deflection=10.2mm).

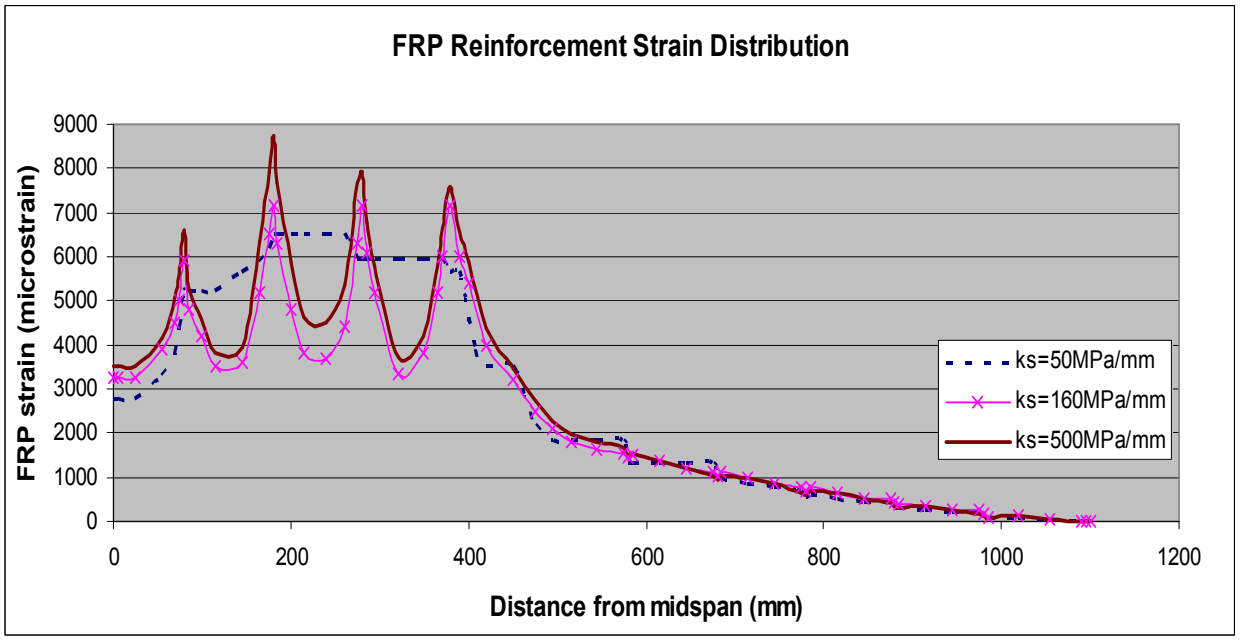

Figure 5.40: Effect of interfacial stiffness on FRP reinforcement distribution (x_c = 100mm, deflection=10.3mm).

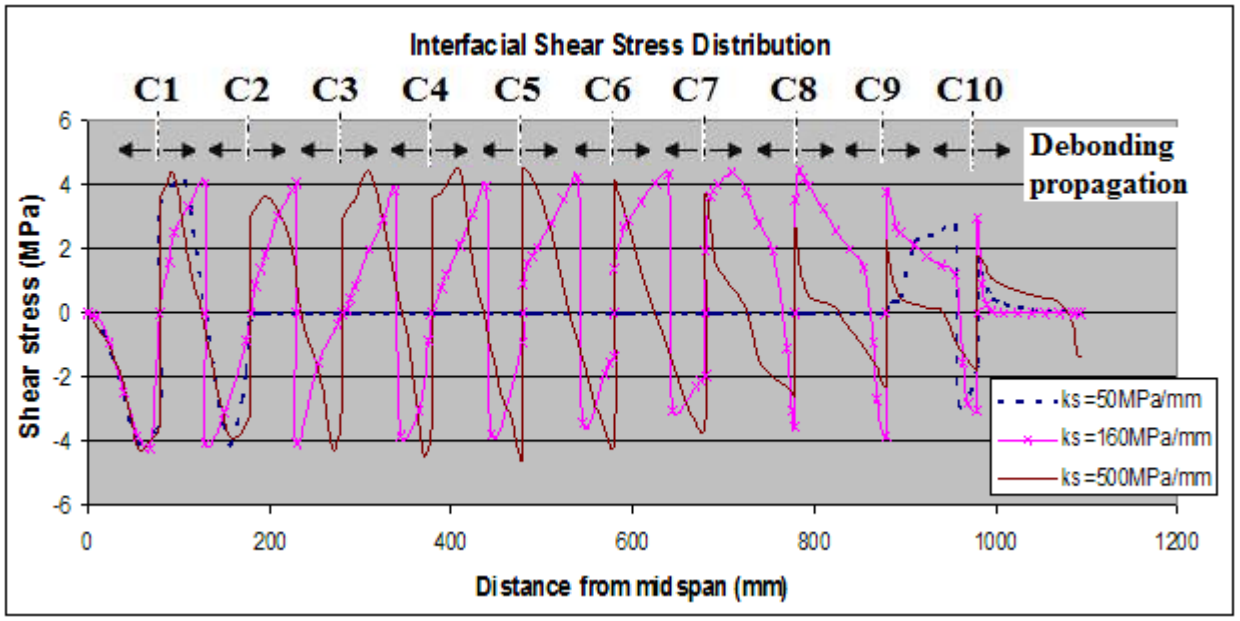

Figure 5.41: Effect of interfacial stiffness on interfacial shear stress distribution (x_c = 100mm, deflection=10.3mm).

5.6 EFFECT OF LOCAL BOND STRENGTH

The effectiveness of a FRP strengthened material bonded to the tension side of a flexural member is highly dependent on the bond stresses between the adherents and the member. Bond stresses are generated along the interface due to changes of internal moments along the length of the beam, and through the transfer of forces at plate-ends and/or across intermediate cracks (Neubauer and Rostasy, 1999). The bond transfer mechanism depends on the shear stiffness of the adhesive layer and the effective shear stiffness of an undetermined thickness of a concrete layer that transfers the force in the FRP into the concrete substrate. Since the distribution of bond stresses are often disrupted by flexural and shear cracks that develop within the interface an effort was made to investigate the effect of local bond strength on the debonding behaviour and strengthening effect when subjected to distributed flexural cracks. By fixing the initial interfacial stiffness at k_s=160MPa/mm and the interfacial fracture energy at G_f^{int}=0.5N/mm, the effect of local bond strength is studied by varying it for three cases: τ_b = 1.5, 4.5, 12MPa. It was evaluated based on its response to: load versus deflection, interfacial shear stress versus deflection, FRP strain distribution, reinforcement strain distribution, and interfacial shear stress distribution.

As shown in Figure 5.42, the higher bond strength (i.e. 12MPa) model provides a higher yield load than the two lower bond strength models. This may be attributed to the higher bond strength model being capable of delaying the initiation of micro-debonding and thereby transferring more stress to the FRP sheet, as shown in Figure 5.43. However, once the rebar yields in the high bond strength model, the load-deflection response beings to converge with the 4.5MPa bond strength model and both models are found to yield the same ultimate load. A possible explanation as to why the higher bond strength model does not enhance the strength

capacity at ultimate load may be attributed to the initiation of macro-debonding that occurs immediately after rebar yielding, as shown in Figure 5.43. The lower bond strength model of 1.5MPa was found to yield a lower yield load than the higher strength models. This may be attributed to less stress being transferred to the FRP sheets as shown in Figure 5.44, resulting in a less efficient strengthening system.

Figure 5.43 illustrates the interfacial shear stress versus midspan deflection at the flexural crack located directly beneath the applied load. The figure suggests that the lower bond strength facilitates early micro-debonding, whereas high bond strength may prolong the initiation of micro-debonding. Micro-debonding initiates at a midspan deflection of 1.7, 3.6, and 9.1mm for bond strengths of 1.5, 4.5, and 12MPa, respectively. Yielding of the rebar then follows at midspan deflections of 5.9, 8.1, and 9.2mm, respectively. Rebar was found to yield first in the low bond strength model. This may be attributed to the high strain distribution in the internal rebar found throughout loading, as shown in Figure 5.45. When a low bond strength between the concrete and FRP is employed the rebar is forced to contribute more to the load-carrying capacity of the structure in comparison to when higher bond strengths are achieved. This is attributed to the less stress being transferred from the RC beam to the FRP plate as shown in Figure 5.44. Figure 5.43 also suggests the high bond strength induces early macro-debonding, which in turn may reduce the structural ductility. Macro-debonding was found to initiate at midspan deflections of 23.1, 10.3, and 9.5mm, respectively. The low bond strength model debonds much later that the other two models mainly because of the low stress transfer rate between concrete and FRP sheets. On the other hand, the higher bond strength model rapidly transfers stress between the concrete and FRP, which in turn increases the yield load.

Figure 5.46 illustrates the interfacial shear stress distribution along the FRP plate at the midspan deflection of 20mm. In the case of the bond strength model, the FRP plate is still attached to the concrete substrate. This can be attributed to the low transfer of stress rate between the two materials, as previously mentioned. But with further increase in bond strength (i.e. 12MPa), the debonding crack propagating in the varying moment region was found to only propagate in one direction: towards the support; rather than in two directions (i.e. towards the applied load and support). This suggests the debonding crack which, typically propagates towards the applied load, encounters enough resistance from the adjacent crack to cause it to close up. This may be responsible for the abrupt termination of the FRP plate as the debonding crack is able to propagate in unison towards the support.

Interfacial bond strength is thus seen to affect yield load, initiation of micro- and macro-debonding, rebar yielding, stress transfer rate along the interface, and high bond strength may reduce the structural ductility.

Table 5.4: Response of models for local bond strength models.

τ_b	**Init. of micro-debonding**		**Yield load**		**Init. of macro-debonding**	
(MPa)	**P (kN)**	**Δ (mm)**	**P (kN)**	**Δ (mm)**	**P (kN)**	**Δ (mm)**
1.5	47.4	1.7	136.0	5.9	192.2	23.1
4.5	110.7	4.5	168.5	8.1	179.8	10.3
12	187.0	9.1	187.7	9.2	189.3	9.5

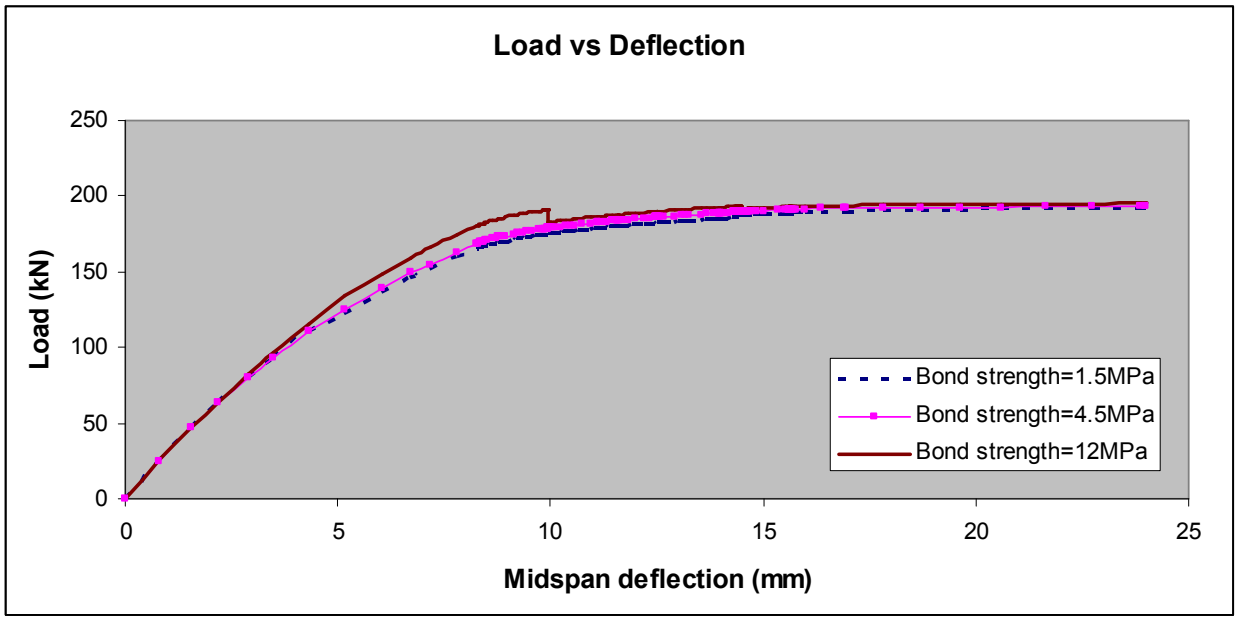

Figure 5.42: Effect of local bond strength on load versus deflection response (x_c = 100mm).

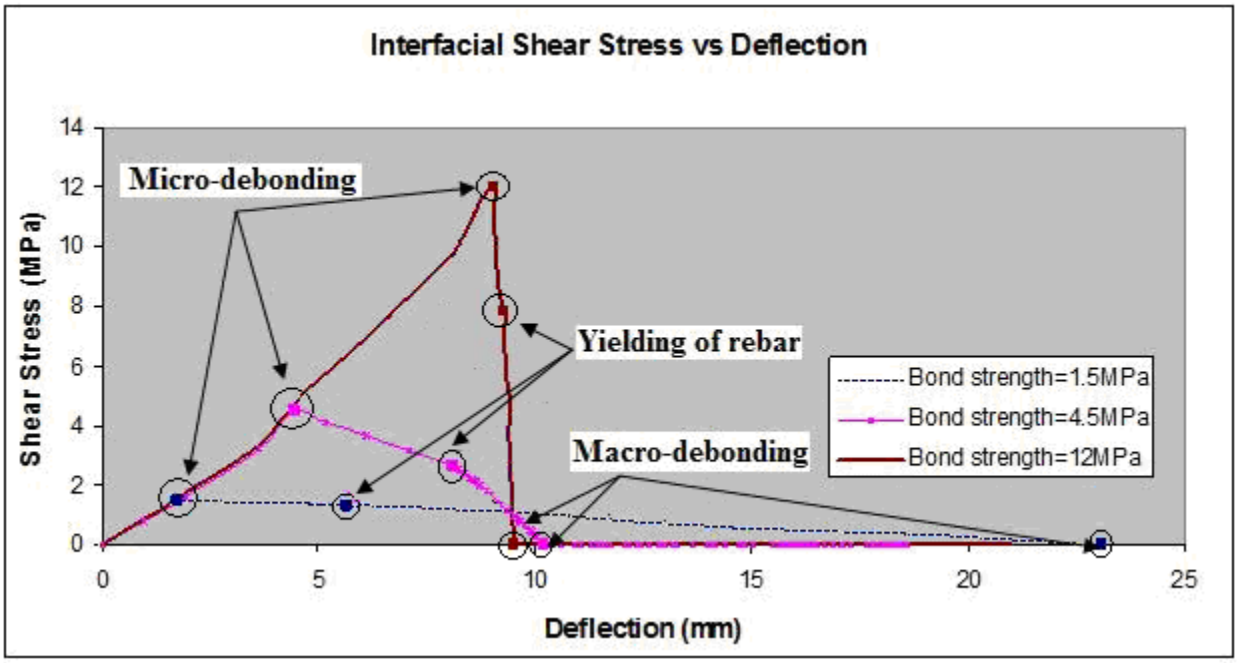

Figure 5.43: Effect of local bond strength on interfacial shear stress versus deflection (x_c = 100mm, Crack 4).

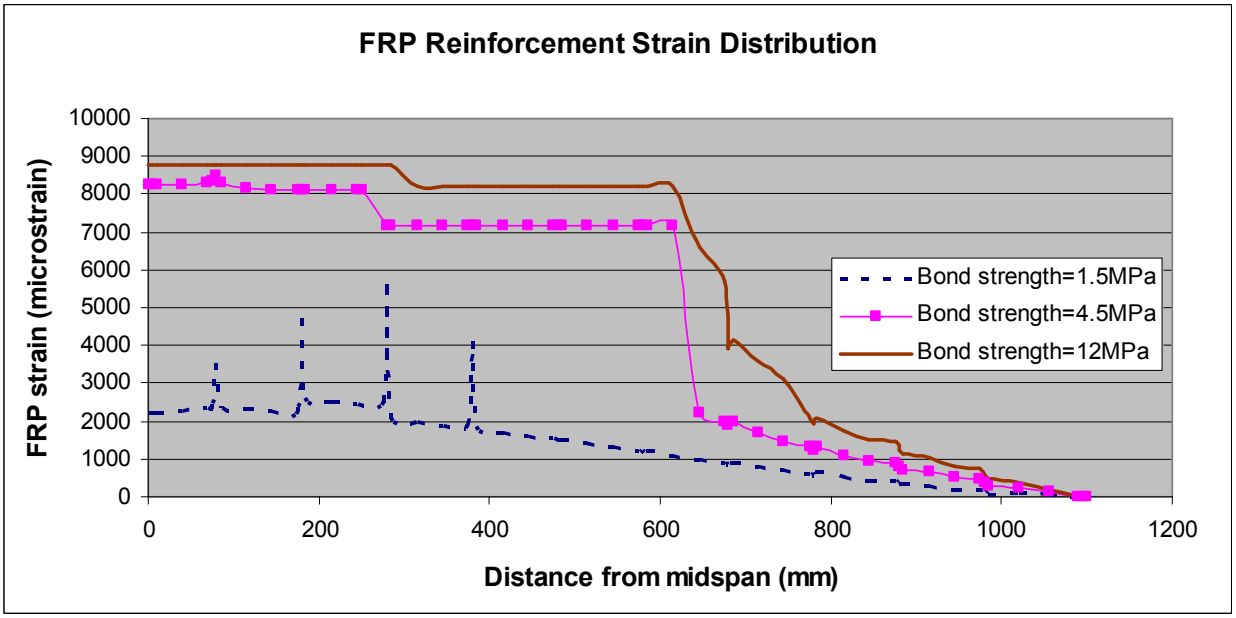

Figure 5.44: Effect of local bond strength on FRP reinforcement distribution (x_c = 100mm, deflection=20mm).

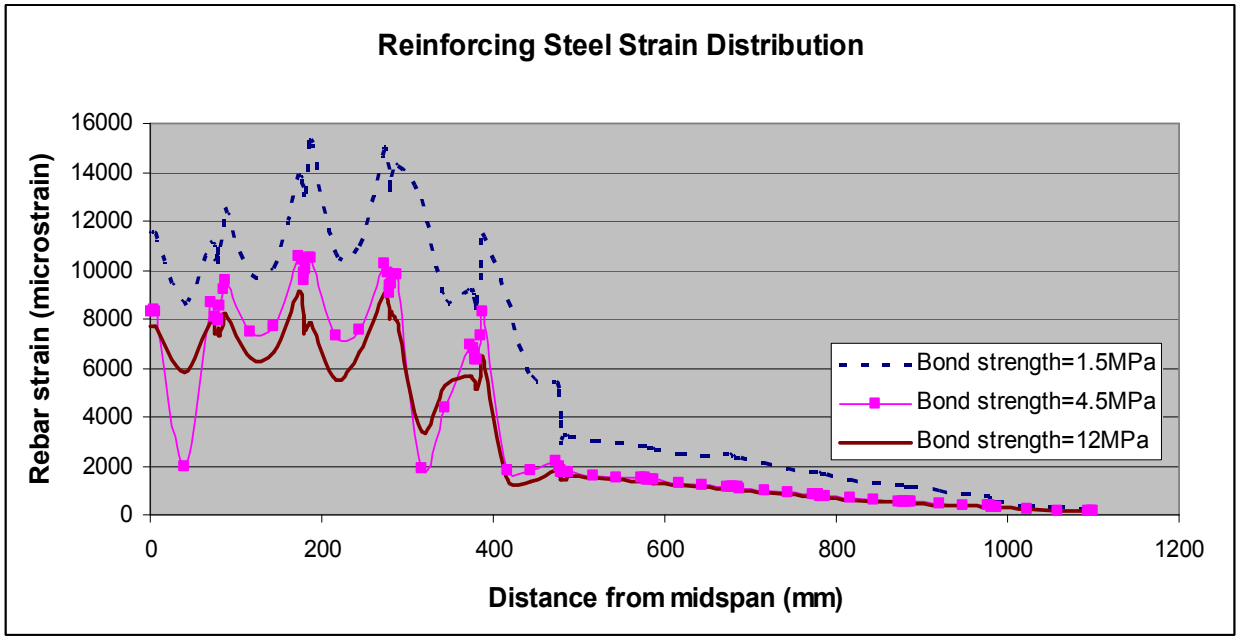

Figure 5.45: Effect of local bond strength on steel reinforcement distribution (x_c = 100mm, deflection=20mm).

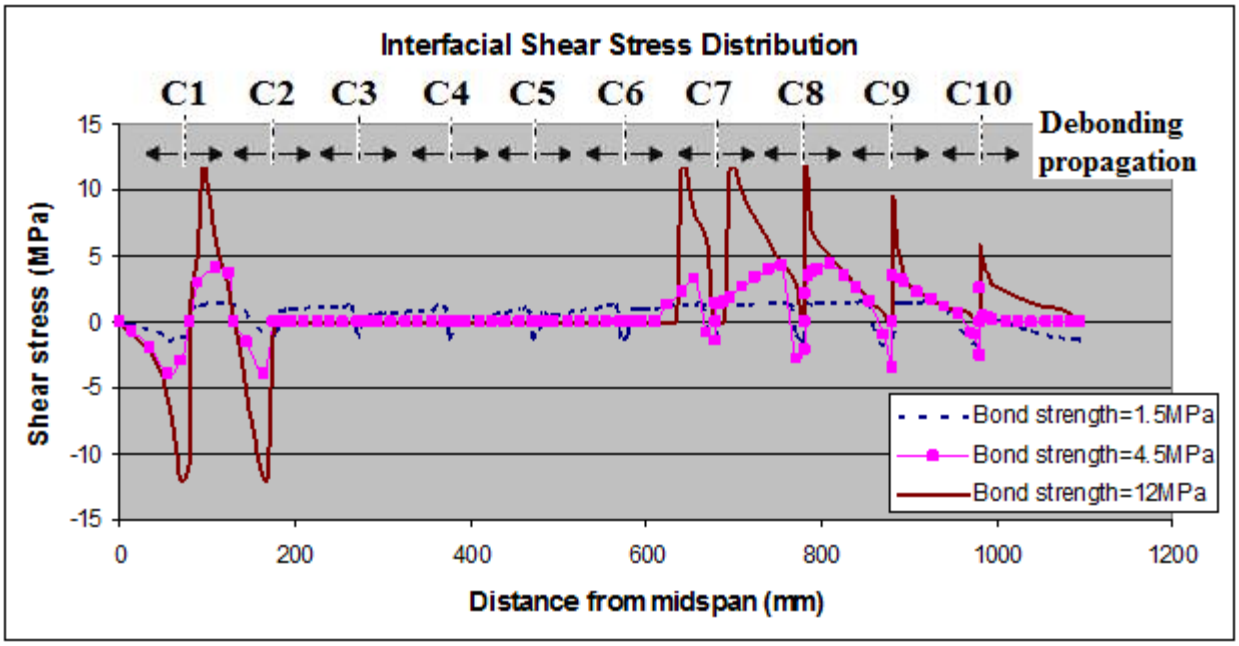

Figure 5.46: Effect of local bond strength on interfacial shear stress distribution (x_c = 100mm, deflection=20mm).

5.7 EFFECT OF INTERFACIAL FRACTURE ENERGY

Interfacial fracture energy, G_f^{int}, is a material property of the FRP-concrete interface and is defined as the energy required to produce a unit area of crack (Hillerborg, 1985). Fracture energy takes into account the external work of the load applied to a specimen, as well as the self-weight of the specimen, in order to fracture a specific ligament area. Interfacial fracture energy has been shown by Niu and Wu (2005) to influence the strengthening effect of FRP-RC specimens as more external energy (i.e. load) is required to cause debonding propagation when higher interfacial fracture energy interfaces are employed. However, the authors preformed the analysis by investigating its effect with unrealistically high energy values that would typically not be encountered in practice. Thus, to add on the previous work, interfacial fracture energy is investigated in this portion of the analysis utilizing commonly found energy values in engineering applications. By fixing the crack spacing at x_c=100mm, local bond strength at τ_b=

4.5MPa, and interfacial stiffness at k_s=160MPa/mm, the effect of interfacial fracture energy is then studied by varying it for three cases: G_f^{int}=0.2, 0.5, and 1.0N/mm. Its effect was evaluated based on its response to: load versus deflection, interfacial shear stress versus midspan deflection, rebar yielding, interfacial shear stress distribution, and FRP strain distribution.

Figure 5.47 shows the load versus midspan deflection for the parametric analysis. The figure clearly shows that the load carrying capacity and ultimate load increase with interfacial fracture energy. Complete debonding was found to occur at a midspan deflection of 18.7, 24.0, and 31.5mm for fracture energy values of 0.2, 0.5, and 1.0N/mm, respectively. This can be attributed to the fact that large interfacial fracture energy yields a large shear transfer length, and thus more external work is required to create the interfacial debonding as shown in Figure 5.48. A summary of details of the analysis is listed in Table.

Figure 5.48 illustrates the interfacial shear stress versus midspan deflection at the flexural crack located directly beneath the applied load (i.e. Crack 4). The figure indicates that interfacial fracture energy does not influence the initiation of micro-cracking at the interface as all the analyses revealed micro-debonding to occur at a midspan deflection of approximately 4.5mm ± 0.2mm. However, following the initiation of micro-debonding interfacial fracture energy was found to impact the softening behaviour of the interface, or more specifically the initiation of macro-debonding. Macro-debonding was found to initiate at 6.02, 10.2, and 16.2mm, respectively. As shown in the figure, an increase in fracture energy yields an increase in shear transfer length. This can be attributed to more external work being required to create the interfacial debonding. For the case of low interfacial fracture energy, FRP debonding was found to initiate prior to the yielding of the internal steel reinforcement. This is typically an unfavourable occurrence in composite action and should be avoided in practice as this indicates

the strengthening system was not utilized to its desired potential in comparison to the higher energy models, as shown in Figure 5.48.

Figure 5.49 illustrates the interfacial shear stress distribution along the FRP-concrete interface at a midspan deflection of 10.3mm. In the case of the low interfacial fracture energy at this point, the FRP has debonded near the toe of Cracks 1-6, as shown in Figure 5.50. It is interesting to note that in the varying moment region (i.e. Cracks 4-10), the debonding crack is only propagating in one direction: towards the support. This indicates that the debonding crack initiating from the left of the cracks (i.e. propagating towards the applied load) has closed up. This may be attributed to the fact that less external work is required to restrict crack propagation when lower interfacial fracture energy makes up the interface. In comparison Figure 5.49 demonstrates the interfacial shear stress along the interface when higher fracture energies are employed. The figure clearly indicates the difference between lower and higher energy values, as the interface is intact for the most part when higher energy exists and each flexural crack is generating debonding cracks in two directions: towards the load and support. When a debonding crack propagating along the interface is restricted by an opposing crack propagating towards it, the load-carrying capacity of the system is found to increase as more external work (i.e. load) is required to overcome the obstruction of the opposing crack. This may be an explanation as to why the lower interfacial fracture energy model yielded a lower ultimate load and achieved a load ratio of only 1.08, in comparison load ratio of 1.20 of the higher energy models as shown in Figure 5.47.

Figure 5.51 illustrates the FRP strain distributions along the interface for all energy values at compete debonding. The figure exemplifies how higher interfacial fracture energy interfaces contribute to the utilizing the full potential of the strengthening system as the strain the

FRP is noticeably greater when interfaces with higher interfacial energies are employed. The ratio of maximum FRP strain at complete debonding for the 0.5 to 0.2N/mm and 1.0 to 0.2N/mm interfaces are 1.48 and 2.16, respectively. This is attributed to the lower shear transfer length that exists when employing low energy interfaces, as the FRP plate debonds before it can maximize its strengthening potential. Since the higher energy interfaces delay the onset of macro-debonding, as previously shown in Figure 5.48, the FRP plate was able to contribute more to the strengthening system as revealed in the significantly higher strain profile and load-carrying capacity.

Interfacial fracture energy was not found to influence to onset of micro-debonding along the interface. It was found to affect the yield load, initiation of macro-debonding, direction of crack propagation, reinforcement strain development with load, and overall efficiency of the rehabilitation system.

Table 5.5: Response of models for different interfacial fracture energy models.

G_f^{int}	**Init. of micro-debonding**		**Yield load**		**Init. of macro-debonding**		**Ultimate Load**		**LR***
(N/mm)	**P (kN)**	**Δ (mm)**	**P (kN)**	**Δ (mm)**	**P (kN)**	**Δ (mm)**	**P (kN)**	**Δ (mm)**	
0.2	110.5	4.5	148.1	6.6	139.1	6.02	182.8	18.7	1.08
0.5	110.7	4.5	168.5	8.1	179.8	10.3	193.5	24.0	1.15
1.0	110.4	4.5	173.3	8.4	199.3	16.2	202.3	31.5	1.20

*LR - Load ratio defined as maximum applied load resisted by specimen divided by yield load for control specimen.

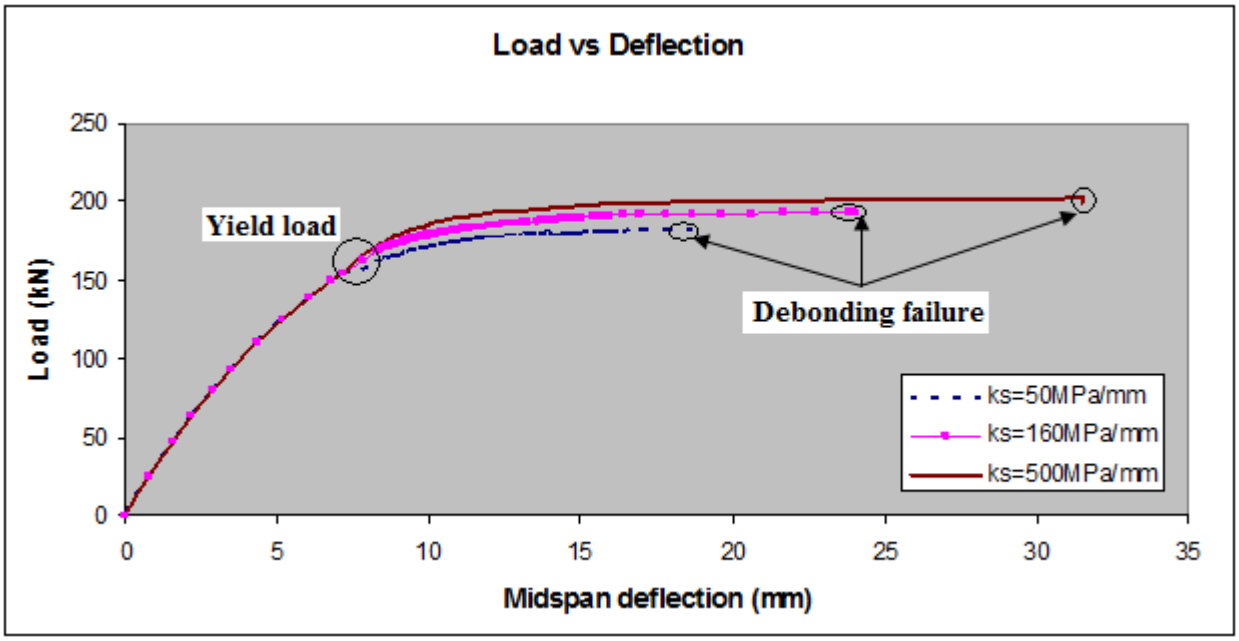

Figure 5.47: Effect of interfacial fracture energy on load versus deflection response (x_c = 100mm).

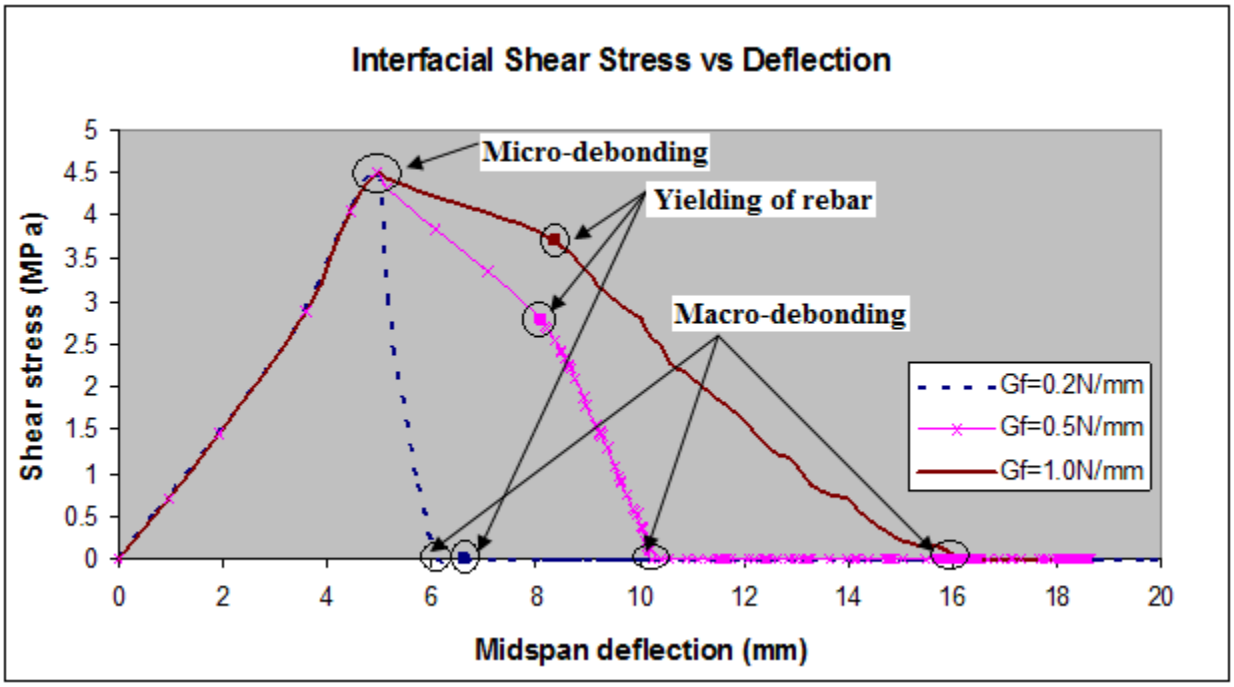

Figure 5.48: Effect of interfacial fracture energy on interfacial shear stress versus deflection (x_c = 100mm, Crack 4).

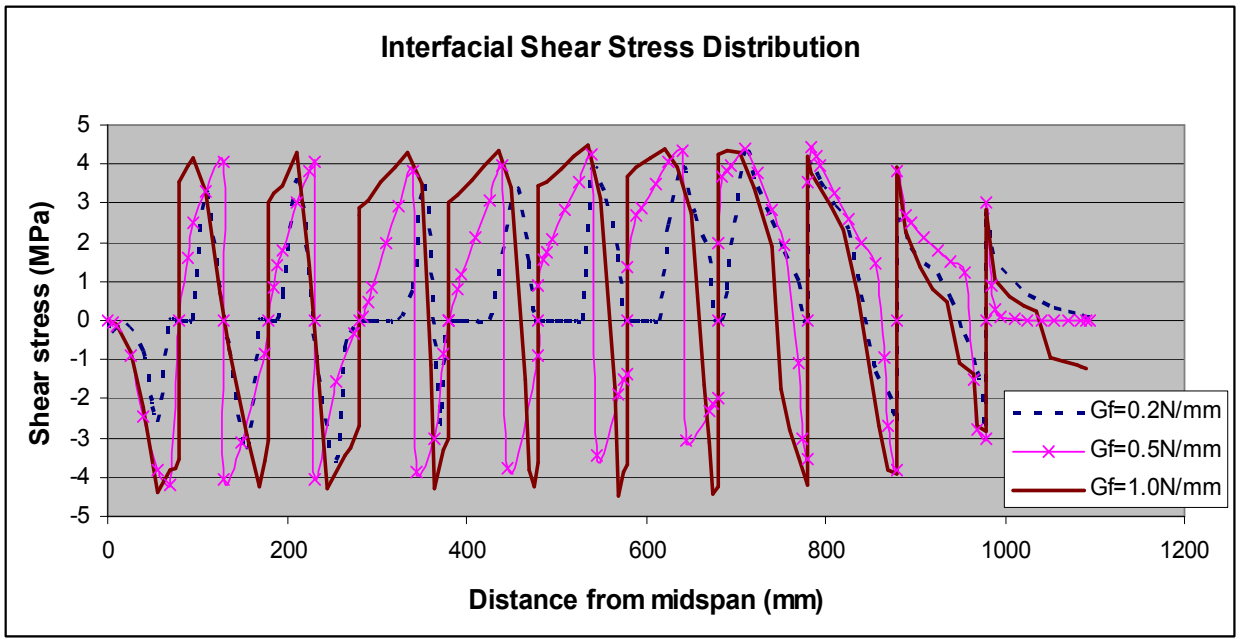

Figure 5.49: Effect of interfacial fracture energy interfacial shear stress distribution (x_c = 100mm, deflection=10.2mm).

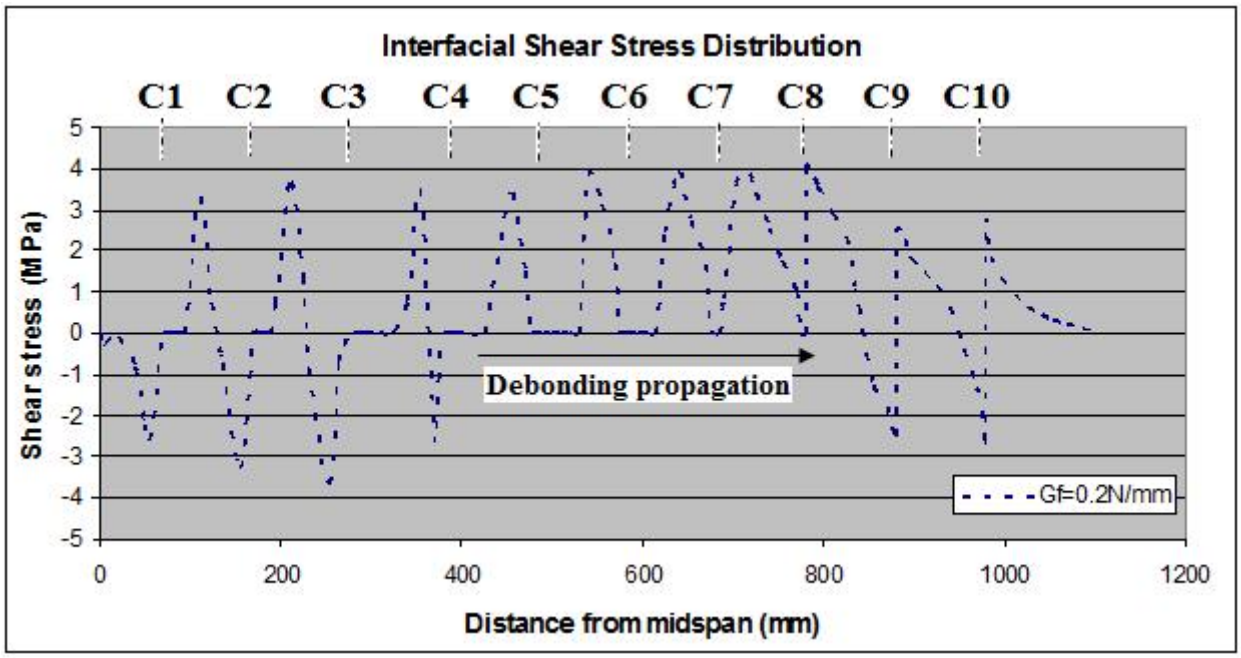

Figure 5.50: Effect of interfacial fracture energy interfacial shear stress distribution (x_c = 100mm, deflection=10.2mm, G_f^{int} =0.2N/mm).

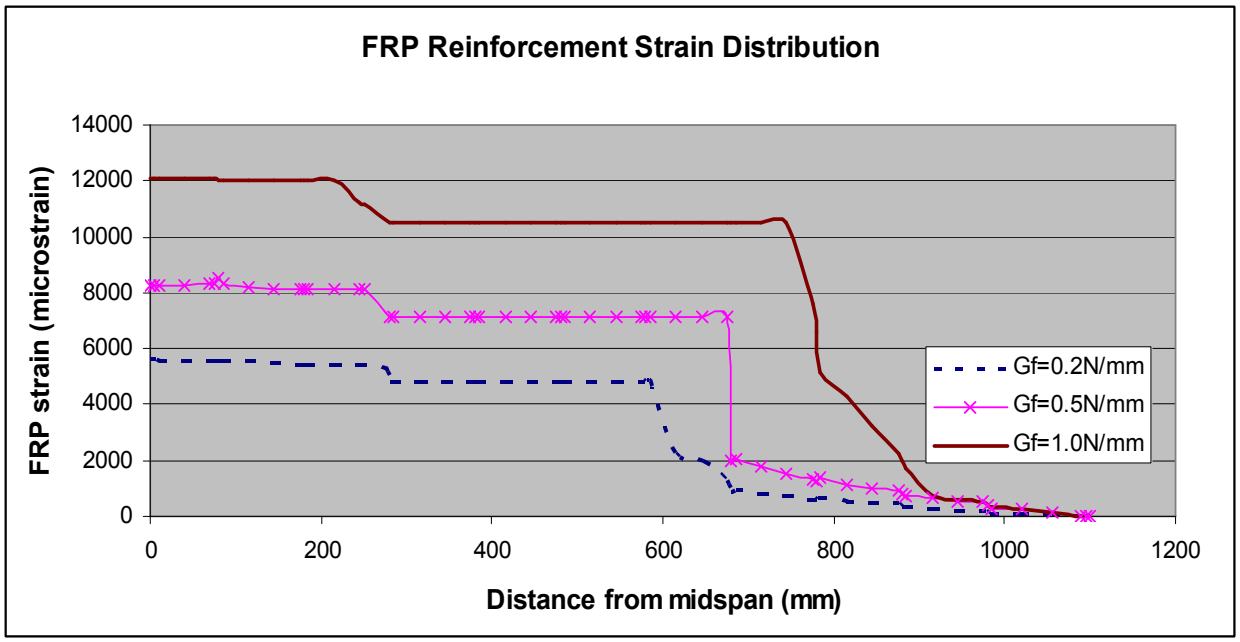

Figure 5.51: Effect of interfacial fracture energy on FRP reinforcement distribution (x_c = 100mm, at complete debonding of each specimen).

5.8 SUMMARY

In this chapter, to investigate flexural crack-induced debonding in the FRP strengthened RC members, a finite element model was developed to characterize the debonding behaviour and failure mechanisms caused by multiple or distributed flexural cracks. These characteristics are very important in the development of an efficient strengthening and rehabilitation system. To clarify how the debonding mechanisms are affected by different crack configurations, a series of parameters such as crack spacing, interfacial shear stiffness, local bond strength, and interfacial fracture energy are varied to investigate the corresponding effects on debonding and load-carrying capacity.

The flexural crack spacing was found to significantly affect the structural stiffness, debonding mechanisms, load-carrying capacity and efficiency of the reinforcement materials. Structural stiffness was found to decrease with crack spacing, contrary to previously reported numerical investigations. However, the initiation of micro- and macro-debonding, as well as

yield load was prolonged as crack spacing was decreased. This is believed to be attributed to the abrasion effect and increased shear transfer length along the interface as more energy is required for debonding to propagate through the closely spaced cracks. However, subsequent to the initiation of macro-debonding, the closely spaced cracks were found to quicken the debonding propagation as the debonding crack would join adjacent flexural cracks, resulting in delamination of the FRP system.

The stiffness of the FRP-concrete interface was found to influence the load-carrying capacity and the strain development in reinforcement materials caused by varying initiation of micro- and macro-debonding. A higher interfacial stiffness increases the rate of stress transfer at the interface and will result in a higher yield and ultimate load of the strengthened structure. Low interfacial stiffness was found to have the opposite effect.

The effectiveness of a FRP strengthening material bonded to the tension side of a flexural member is highly dependent on the bond stresses between the adherents and the member. The local bond strength may only affect the structural behaviour prior to the initiation of macro-debonding and no effect on the ultimate load-carrying capacity. Low bond strength facilitates micro-debonding and thus was not found to increase the yield load. At the other extreme, high bond strength may accelerate the initiation of macro-debonding and be unfavorable in increasing the ductility of the structure.

The interfacial fracture energy plays a critical role in the rehabilitation system. While it was not found to influence the onset of micro-debonding, an increase in fracture energy resulted in higher efficiency of the FRP material by increasing yield and ultimate load.

This chapter provides insight into the failure mechanisms caused by different types of flexural crack distributions and properties along the interface. Very limited research can be

found to date on such a topic, and the findings reported herein may be of interest to researchers and design engineers looking to successfully apply FRP products in civil engineering applications.

6 NUMERICAL INVESTIGATION OF MIXED-MODE DEBONDING

6.1 INTRODUCTION

In a FRP-RC strengthened concrete beam, a major shear/diagonal crack may appear along the span and tend to open with an increase in applied load. The opening of such a crack introduces both vertical and horizontal displacements between two sides of the crack, as shown in Figure 6.1, and interfacial debonding failure may initiate from the shear crack and propagate towards the plate-end. This failure mode can be regarded as mixed-mode debonding due to the presence of both opening (mode I) and shearing (mode II) displacement along the interface. In practice, FRP debonding from the end of an intermediate flexural and/or shear crack is sometimes unavoidable and more dominant despite careful surface preparation and good bond between FRP composites and concrete. However, very limited research can be found concerning such debonding failures, and the how the properties of the interface influence the debonding mechanisms.

The main objective of the present study is to present a clear understanding of how the initiation and propagation of debonding is influenced by the distribution of mixed-mode debonding and the interfacial properties. The findings of this study will be of interest to researchers and engineers looking to apply FRP composites in civil engineering applications, and may provide some implications for future design codes.

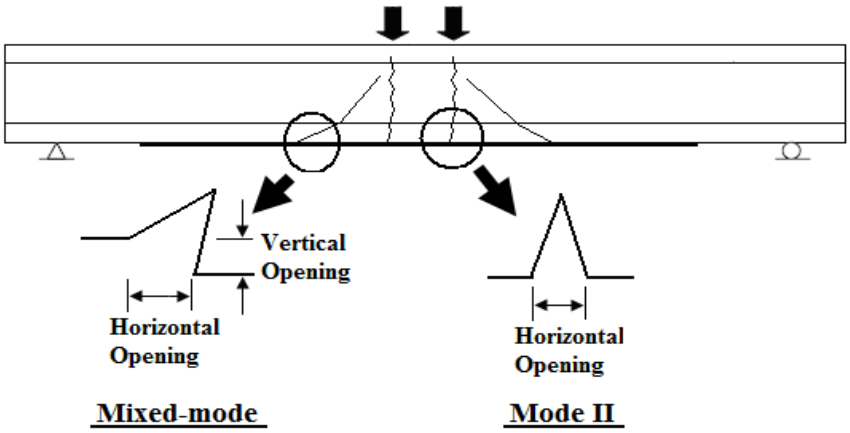

Figure 6.1: Schematic of simplified crack patterns for potential debonding failures.

6.2 STRUCTURAL MODEL AND SPECIAL CONSIDERATIONS

The finite element model includes of two flexural cracks (FC) and two shear/diagonal cracks (DC) to enable an investigation of debond initiation and growth from the cracks, as well as an assessment of which one governs in the initiation and development of final debonding failure. Due to symmetry, only half of the beam was modeled. A snapshot of the model is shown in Figure 6.2. A detailed description of the modeling techniques can be found in Chapter 4.0.

Mesh density was investigated prior to the start of the analysis since the calibrated model described in Chapter 4.0 was altered with the increase in FRP length, removal of steel stirrups, and modifications made to the concrete compressive and tensile material models. Figure 6.3 shows the results of the load-deflection response using five levels of mesh refinement for the model shown in Figure 6.2. It can be seen that the structural performance is overestimated with the use of the coarse mesh, while refining the mesh leads to convergence of response. While it appears that the convergence is achieved by employing a fine mesh of 26,904 elements, a closer inspection of the results in terms of interfacial shear stress versus midspan deflection proves otherwise. Figure 6.4 demonstrates that the fine meshes employing 26,904 and 40,138 elements overestimate the interfacial shear stress response of the specimen, where as mesh convergence is

ultimately obtained with the use of a finer mesh made up of 51,473 elements. Previous researchers (Niu and Wu, 2005; Niu et al., 2006) that have preformed FRP-RC debonding investigations overlooked the effect interfacial shear stress when selecting their mesh for the analysis. Ignoring this parameter may lead to inaccurate results at the interface as the coarser meshes appear to be incapable of converging prior to macro-debonding. The finer mesh containing 51,473 elements seems to be able to accurately capture the complicated fracture behaviour involving concrete cracking and interfacial debonding. This model contains 51,473 elements comprised of: 1925 beam (B21), 3189 cohesive (COH2D4), and 46,359 linear reduced-integration (CPR4R) elements.

A general check on the validity of the model can be made through an assessment of the interface stress conditions at the ends of the cracks represented at both sides of the flexural crack by P1 and P2, and both sides of the diagonal (shear) crack by P3 and P4 as shown in Figure 6.2. It can be seen from Figure 6.5 and 6.6 that the interfacial normal stress level is very small and the fracture behaviour is dominated by mode II fracture at the FC. However, at both ends of ends of the DC the interfacial normal stress occurs in opposite directions (i.e. tensile at P3 and compressive at P4). The high peeling stress at P3 is responsible for causing the loss of shear transfer capacity. Due to the existence of interfacial normal stresses, the debonding behaviour from the end of DC is not only related to the mode II component but also the mode I component, as previously suggested in Section 4.5.3. Neglecting either of them could result in a misleading results as overall strengthening performance may be overestimated if a pure mode II debonding behaviour is assumed without considering mode I peeling behaviour induced at the toe of the DC.

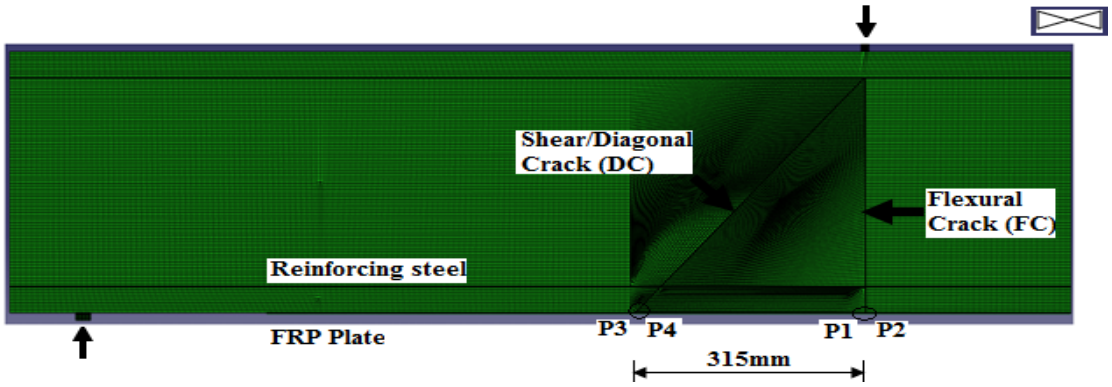

Figure 6.2: Snapshot of analysis mixed-mode debonding model.

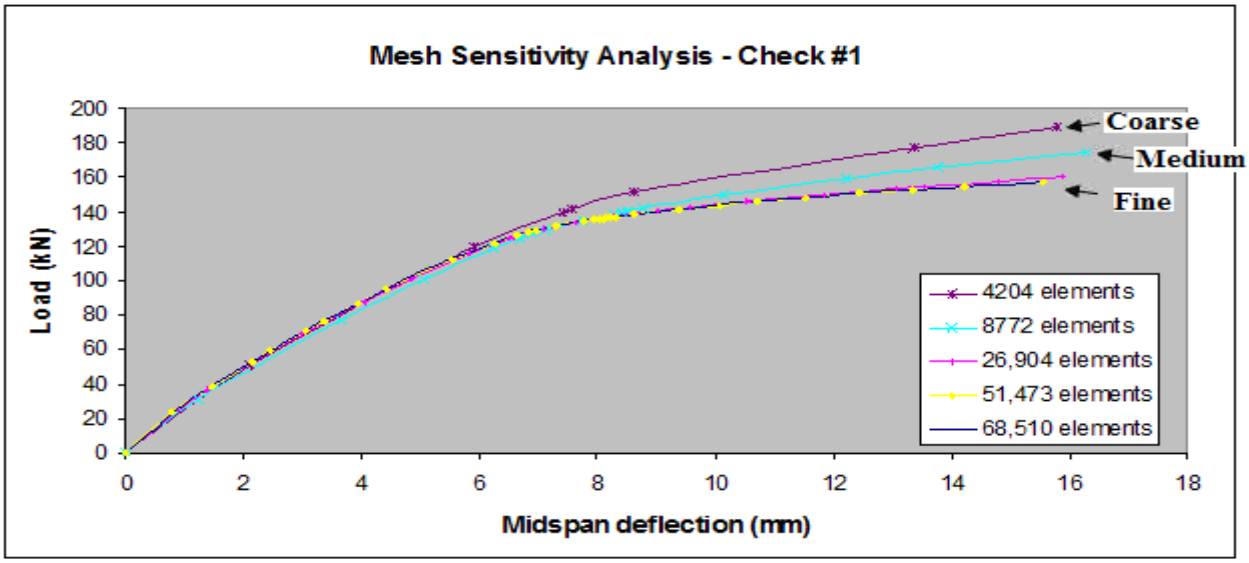

Figure 6.3: Effect of mesh refinement in terms of load versus deflection.

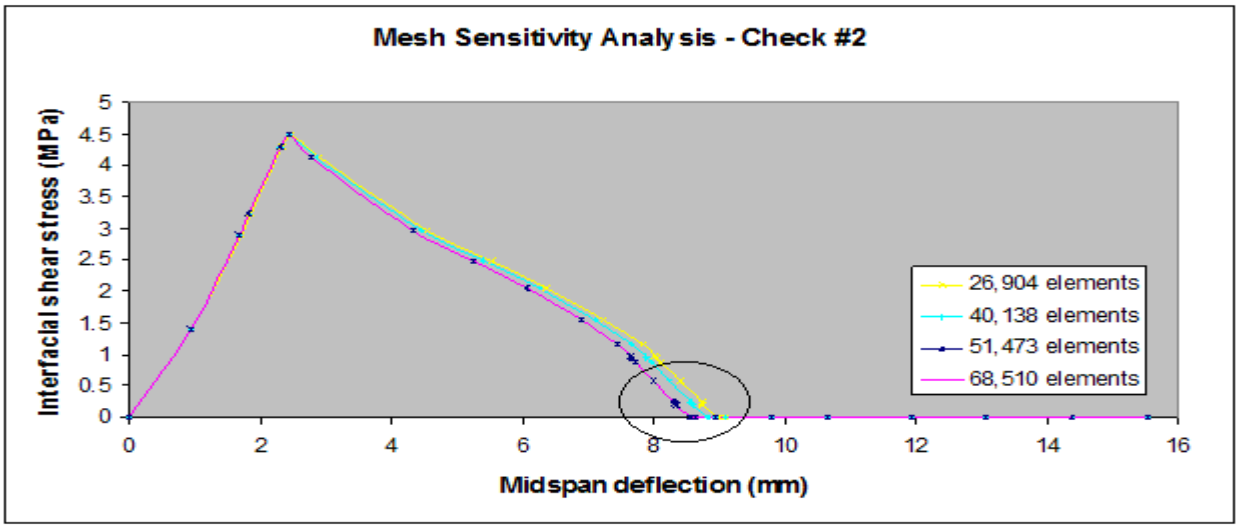

Figure 6.4: Effect of mesh refinement in terms of interfacial shear stress versus deflection (at flexural crack).

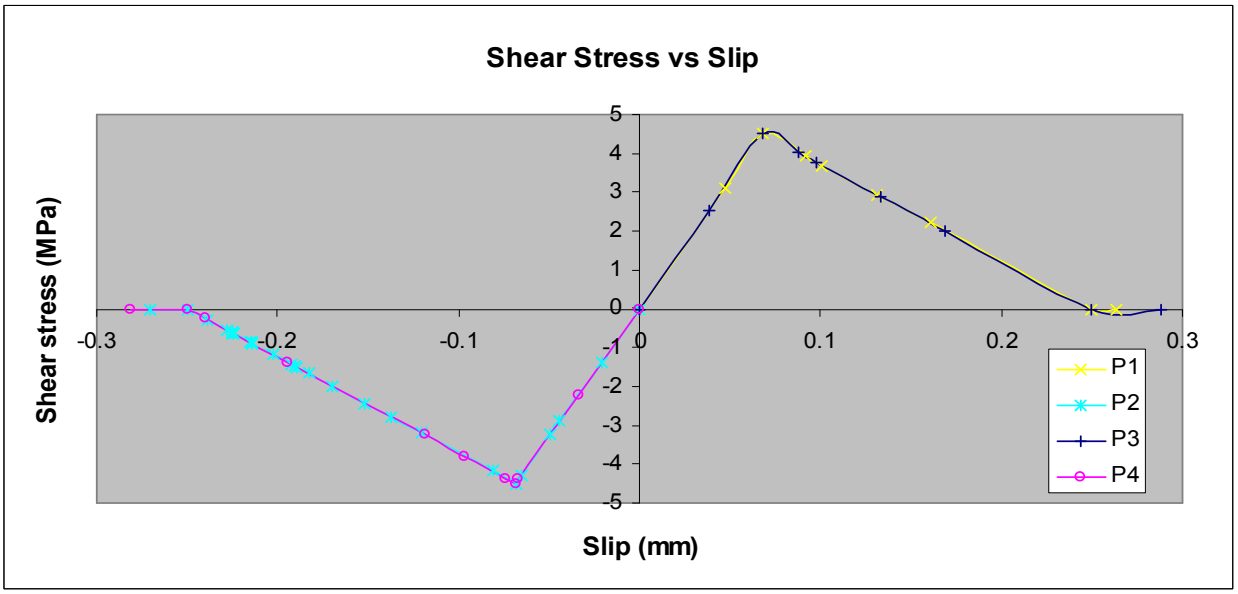

Figure 6.5: Interface shear stress concentration at ends of crack.

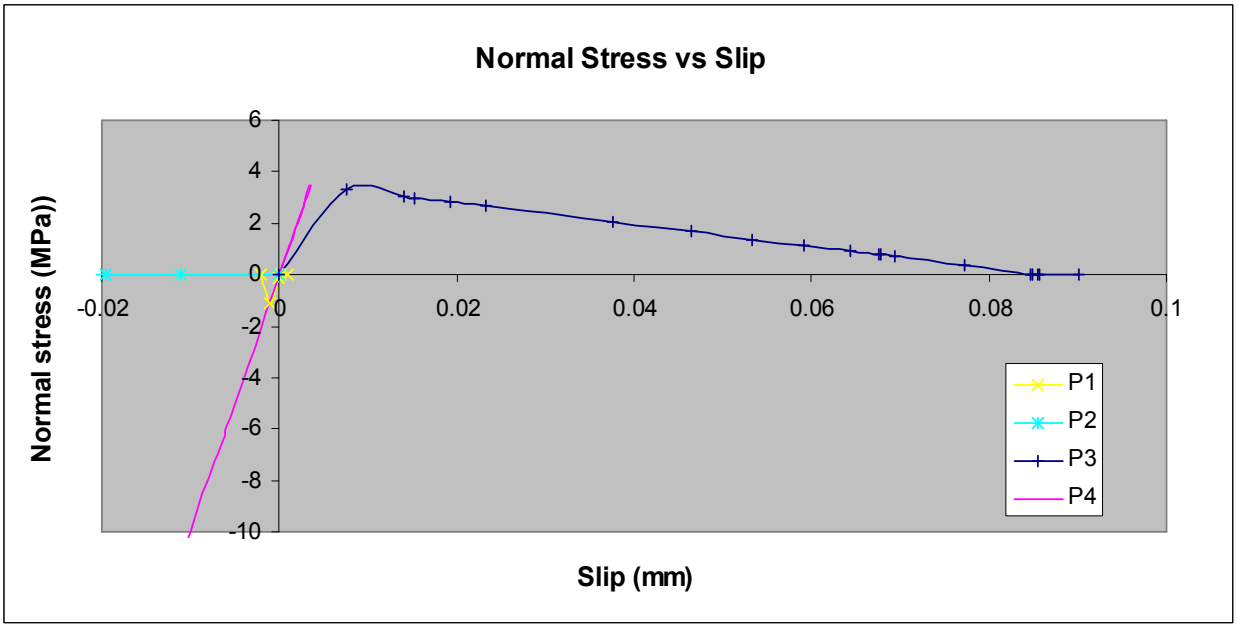

Figure 6.6: Interface normal stress concentration at ends of crack.

6.3 NUMERICAL SIMULATIONS AND DISCUSSIONS

The following outlines the parametric study to access the debonding mechanisms and strengthening effects of a FRP-RC beam associated with interfacial parameters such as shear

stiffness, bond strength, fracture energy, and normal stiffness. A list of parameters and the variation considered in the current investigation are shown in Table 6.1.

Table 6.1: List of parameters used in investigation.

Parametric study	**Interfacial shear stiffness k_s^{int} (MPa/mm)**	**Interfacial bond strength τ_b (MPa)**	**Interfacial fracture energy G_f^{int} (N/mm)**	**Interfacial normal stiffness k_n^{int} (MPa/mm)**
I	50 160 500	4.5	0.5	1000
II	160	1.5 4.5 10	0.5	1000
III	160	4.5	0.3 0.5 1.0	1000
IV	160	4.5	0.5	500 1000 1500

6.3.2 Control Model

The control model is based on typical values of interfacial parameters identified by experimental data, as mentioned in Chapter 4.0. The interfacial properties in the reference model are: k_s^{int}=160MPa/mm, τ_b=4.5MPa, G_f^{int}=0.5N/mm, and k_n^{int}=1000MPa/mm. Figure 6.7 illustrates the load-deflection response of the control model. Debonding of the FRP plate was found to initiate from the FC in mode II fashion at a midspan deflection of 7.9mm. Debonding at the shear crack follows shortly after a midspan deflection of 8.3mm due to mode I opening at the toe of the crack. Debonding failure was dominated by mode II fracture behaviour, initiating from the FC and propagating towards the plate-end. Figures 6.8-6.11 illustrates the interfacial shear stress, interfacial normal stress, rebar strain, and FRP strain distribution along the interface, respectively, at deflection values of 1.7, 6.0 and 8.5mm. These deflection values are consistent throughout the analysis as they are selected in an attempt to capture the critical points in all

analyses, such as the initiation of micro-debonding, softening of the interface, and the initiation/propagation of macro-debonding along the interface, while maintaining a standard by which all models can be fairly judged. The results from the control data are further discussed in subsequent sections.

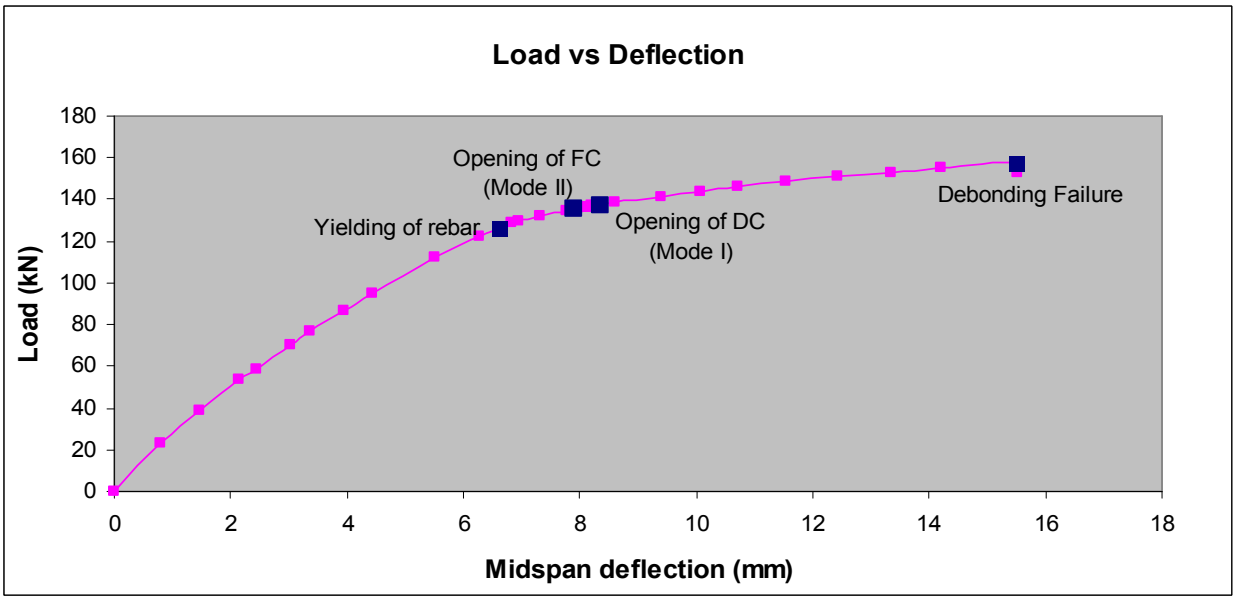

Figure 6.7: Load-deflection response of control model.

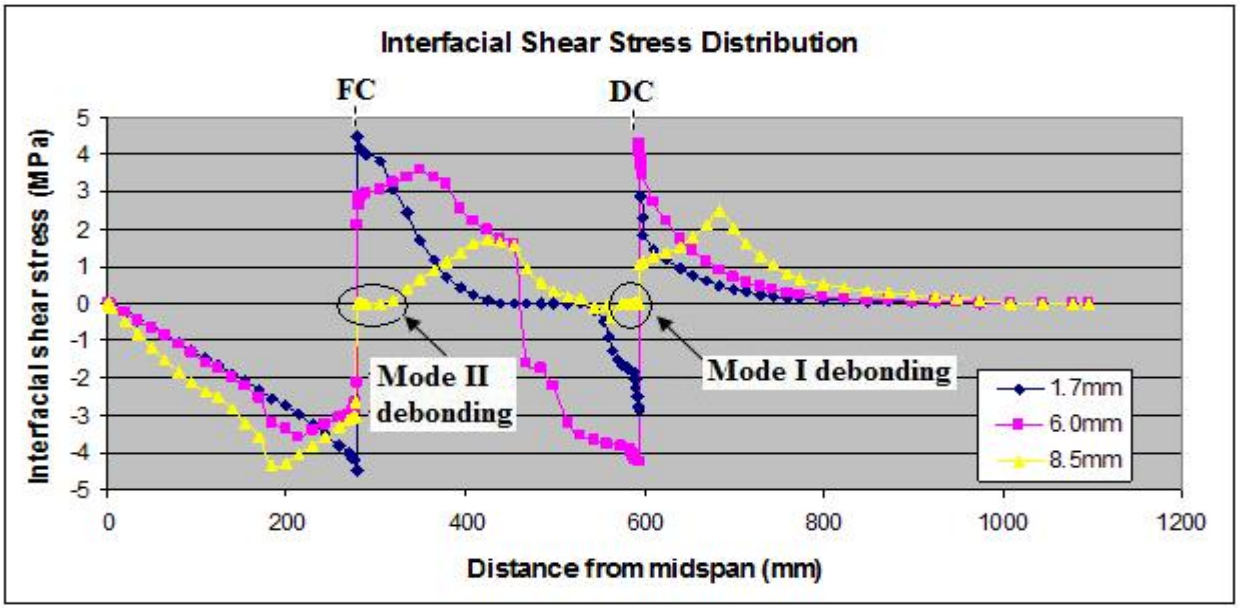

Figure 6.8: Development of interfacial shear stresses for various deflection levels.

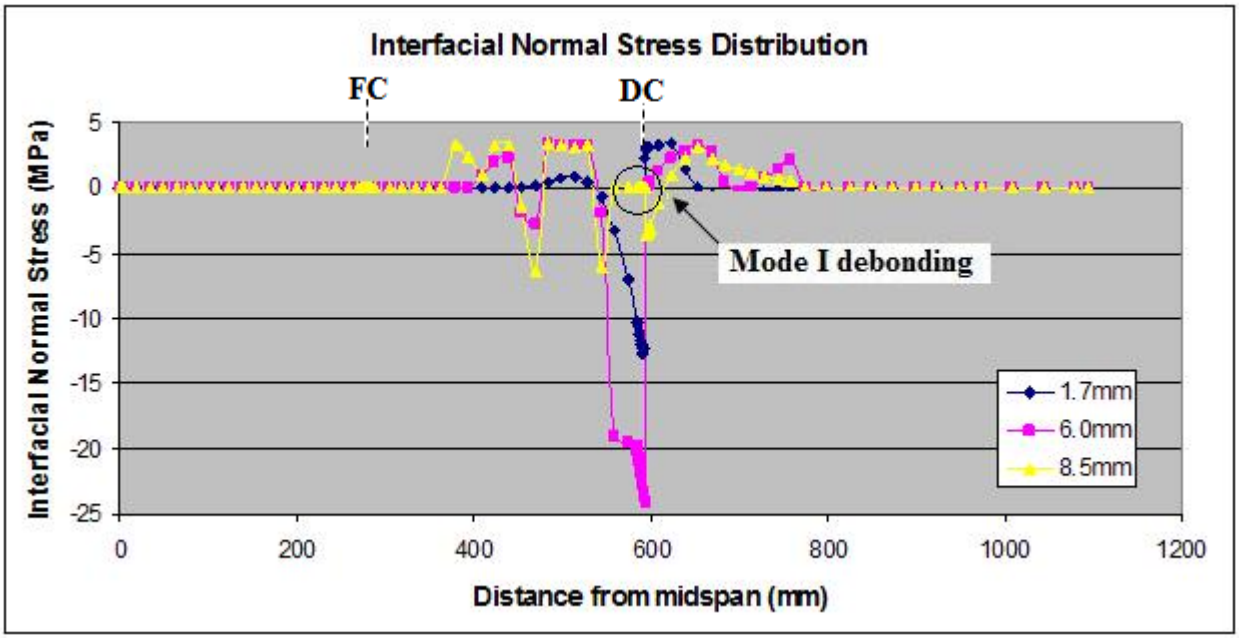

Figure 6.9: Development of interfacial normal stresses for various deflection levels.

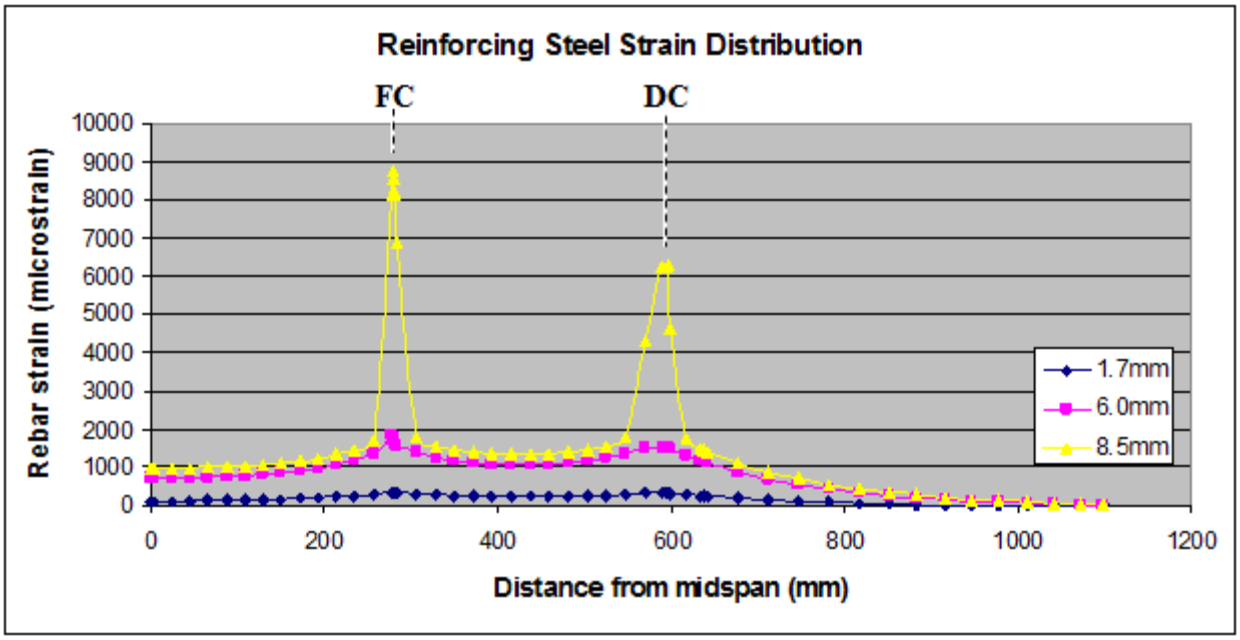

Figure 6.10: Development of steel reinforcement strain for various deflection levels.

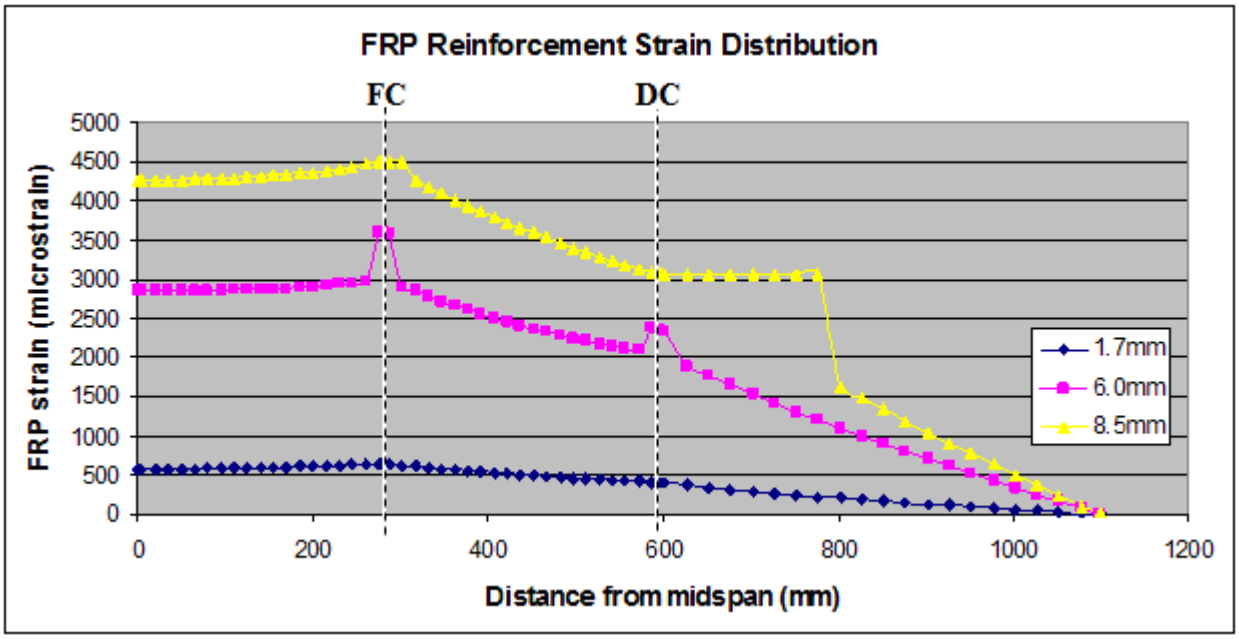

Figure 6.11: Development of FRP reinforcement strain for various deflection levels.

6.3.2 Effect of Interfacial Shear Stiffness

Interfacial stiffness refers to the rigidity of adhesive in contact with the concrete as well as the initial layer of concrete substrate where debonding in found to occur. In Chapter 5.0 an effort was made to investigate its effects on strengthening capacity and debonding mechanisms when subjected to mode II debonding and it was found that low interfacial shear stiffness reduces the load transfer efficiency between the concrete substrate and FRP materials, thereby limiting the effectiveness of the strengthening system. This portion of the analysis investigates the effect of interfacial shear stiffness under mixed-mode fracture behaviour. By predefining the flexural and diagonal crack as shown in Figure 6.2, local bond strength at τ_b=*4*.5MPa, interfacial normal stiffness k_n^{int}=1000MPa/mm and interfacial fracture energy at G_f^{int}=0.5N/mm, the effect of interfacial shear stiffness is studied by varying it for three cases: k_s^{int}=50, 160, and 500MPa/mm. These cases represent low, average, and high stiffness materials that may be employed in practice. The analyses are evaluated based on the response of the model in terms of load-

deflection, interfacial shear stress distribution, interfacial normal stress distribution, FRP strain distribution, and reinforcing steel strain distribution.

Figure 6.12 shows the load versus midspan deflection results for the three stiffness values. While no significant difference is found prior to the yield load, the figure clearly demonstrates its effect immediately after. The low value of interfacial shear stiffness results in a slow rate of load transfer and a lower level of structural stiffness after yielding in comparison to the higher stiffness models with a load ratio of 1.19 as summarized in Table 6.2. The low rate of stress transfer forces the concrete to carry a higher level of load resulting in earlier formation and opening of the FC, which consequently leads to the initiation of debonding at the FC itself, as shown in Figure 6.13. At the other extreme, the higher values results in faster stress transfer at the interface. This is believed to be a contributing factor in the increase of ultimate load and structural stiffness as the FRP is utilized to a further extent, enabling the model to achieve a load ratio of 1.36. No evidence of debonding of the FRP plate was observed until after yielding of the steel reinforcement in all stiffness models. Complete debonding was found to occur at a midspan deflection of 15.2, 15.5, and 18.6mm for stiffness values of 50, 160, and 500MPa/mm, respectively.

Figure 6.13 captures the interfacial shear stress distribution along the interface at deflection values of 1.7, 6.0 and 8.5mm. These deflection values are consistent throughout the analysis as they are selected in an attempt to capture the critical points in the analysis, such as the initiation of micro-debonding, softening of the interface, and the initiation/propagation of macro-debonding along the interface, while maintaining a standard by which all models can be fairly judged. The results of from the interfacial shear stress distribution suggest that employing a low stiffness material at the interface may facilitate micro-debonding. For instance, at the deflection

level of 6.0mm the interfacial shear stress concentration at the toe of the FC is still in its elastic stage for the low stiffness model, whereas the interface of the control model is softening. Debonding is found to initiate and propagate from the FC in mode II fracture behaviour at a deflection of 7.6mm, which is prior to the opening of the FC in the control model (i.e. at 7.9mm). This may be attributed to the fact that the concrete beam is initially required to contribute more to the load-carrying capacity of beam, which results in earlier formation and opening of the FC in comparison to the other models. Despite the fact that macro-debonding initiates at an earlier stage than the control model, the rate at which the debonding crack propagates along the interface appears to be reduced in the low stiffness model. This is exemplified by comparing the shear stress distribution of the low stiffness and control models at the deflection value of 8.5mm. In the low stiffness model, the FRP plate has debonded 5mm from each side of the FC, whereas the control model has debonded 45mm to the right of the FC. Additionally, the stress concentration in the vicinity of the DC is still in its elastic stage at the midspan deflection of 8.5mm in the low stiffness model, where as it is approaching the initiation of mode II macro-debonding in the control model.

Figure 6.14 captures the interfacial shear stress distribution along the interface at deflection values of 1.7, 6.0, and 8.5mm. The results from the figure suggest that a higher stiffness interface does not inhibit the initiation of macro-debonding. This is demonstrated by comparing the shear stress concentration at the FC in the control and high stiffness model at the midspan deflection of 1.7mm. In the control model, the interface at the toe of the FC is still in its elastic stage whereas in the high stiffness model the interface has began to soften. This may be attributed to the notion that high stiffness materials initially increase the rate of stress transfer at the interface, thereby resulting in earlier formation of micro-cracking. However, as loading is

further increased the high stiffness interface appears to inhibit the initiation of mode II macro-debonding as more external loading is required to exceed the shear capacity at the interface. However, by keeping the interfacial normal stress constant and only increasing the shear stress, the initiation of the debonding mechanism appears to have changed. Whereas in the low stiffness and control models macro-debonding was found to initiate from the FC in mode II fashion, the higher stiffness model debonds at the DC in mode I fashion as shown in Figure 6.18. However, the final debonding failure is still dominated by mode II facture.

Figures 6.16-6.18 compare the interfacial normal stress distribution between the low and high stiffness values at three deflection values of 1.7, 6.0 and 8.5mm, respectively. For the cases of the deflection values of 1.7 and 6.0mm, the normal stress distribution for the low stiffness value is negligible. This may be attributed to the fact that low shear stiffness initially results in a slower stress transfer rate between concrete and FRP. However, as loading is further increased the normal stress at the DC is found to increase, as shown in Figure 6.18. These findings suggest that interfacial shear strength directly influences the development of normal stresses along the interface by affecting the rate of transfer at the interface.

Low interfacial stiffness was found to influence the development of strain of the internal rebar. Figure 6.19 presents the strain of the rebar at a midspan deflection of 8.5mm for all stiffness models. At this point, the strain development in the low interfacial stiffness model is 62.7 and 29.8% greater than the higher stiffness value at the FC and DC, respectively. This may be attributed to the low stress transfer rate between concrete and FRP plate which in turn yields a higher strain distribution in the internal rebar. The internal rebar is required to contribute more to the load carrying capacity of the structure as the transfer of stresses at the interface is relatively lower.

Figure 6.20 also supports the notion that low interfacial stiffness affects the rate of transfer at the interface and the efficiency of the FRP material. This notion is supported by considering the strain development in the FRP material at the midspan deflection of 8.5mm. The FRP strain in the higher stiffness model was found to be 46.8 and 45.4% greater that the low stiffness interface at the FC and DC, respectively. This may contributed to the increase in ultimate load, deflection and opening of the FC and DC, as well as relieving the internal rebar from unnecessary strain, which may lead to disastrous results if the rebar is undergoing corrosion. Additional graphs can be found in the appendix.

Interfacial shear stiffness is thus seen to affect stress transfer, initial structural stiffness, ultimate load, initiation of debonding, and strain development in reinforcing materials. However, despite the value of the interfacial shear stiffness, the mode final debonding failure is still dominated in mode II fashion.

Table 6.2: Response of models for various interfacial shear stiffness values.

k_s^{int}	**Opening of Flexural Crack**		**Opening of Diagonal Crack**		**Yield Load**		**Ultimate Load**		**LR***	**Debonding mode of failure**	
(MPa/ mm)	**P (kN)**	**Δ (mm)**	**P (kN)**	**Δ (mm)**	**P (kN)**	**Δ (mm)**	**P (kN)**	**Δ (mm)**		**Initial Mode**	**Final Mode**
50	130.2	7.6	138.4	11.4	117.5	5.1	151.3	15.2	1.19	Mode II	Mode II
160	135.5	7.9	137.1	8.35	126.3	6.6	157.8	15.5	1.25	Mode II	Mode II
500	144.2	9.1	138.2	8.1	134.9	7.4	171.1	18.6	1.36	Mode I	Mode II

*LR - Load ratio defined as maximum applied load resisted by specimen divided by yield load for control specimen.

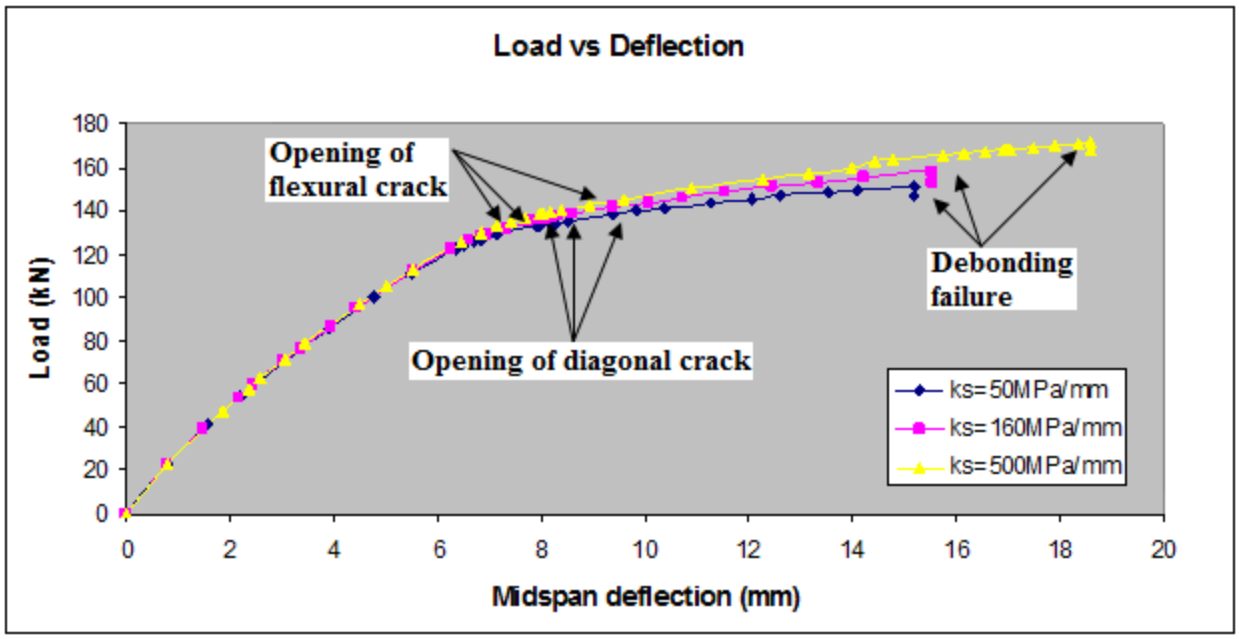

Figure 6.12: Effect of interfacial stiffness on load-deflection response.

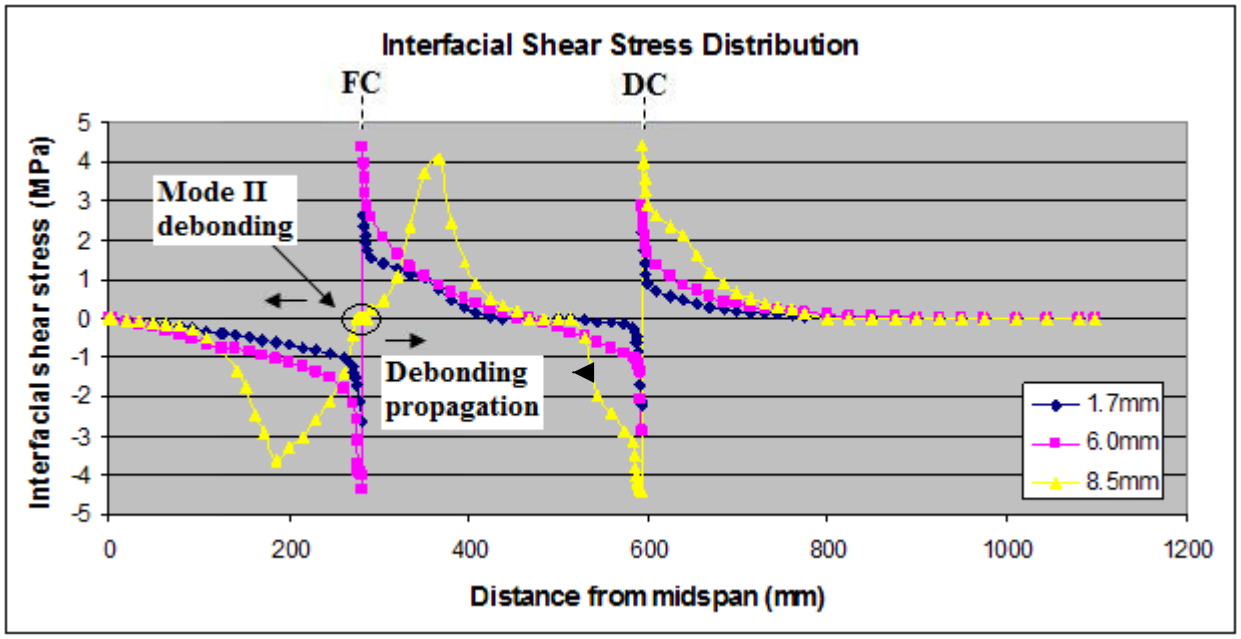

Figure 6.13: Development of interfacial shear stresses for various deflection levels (ks=50MPa/mm).

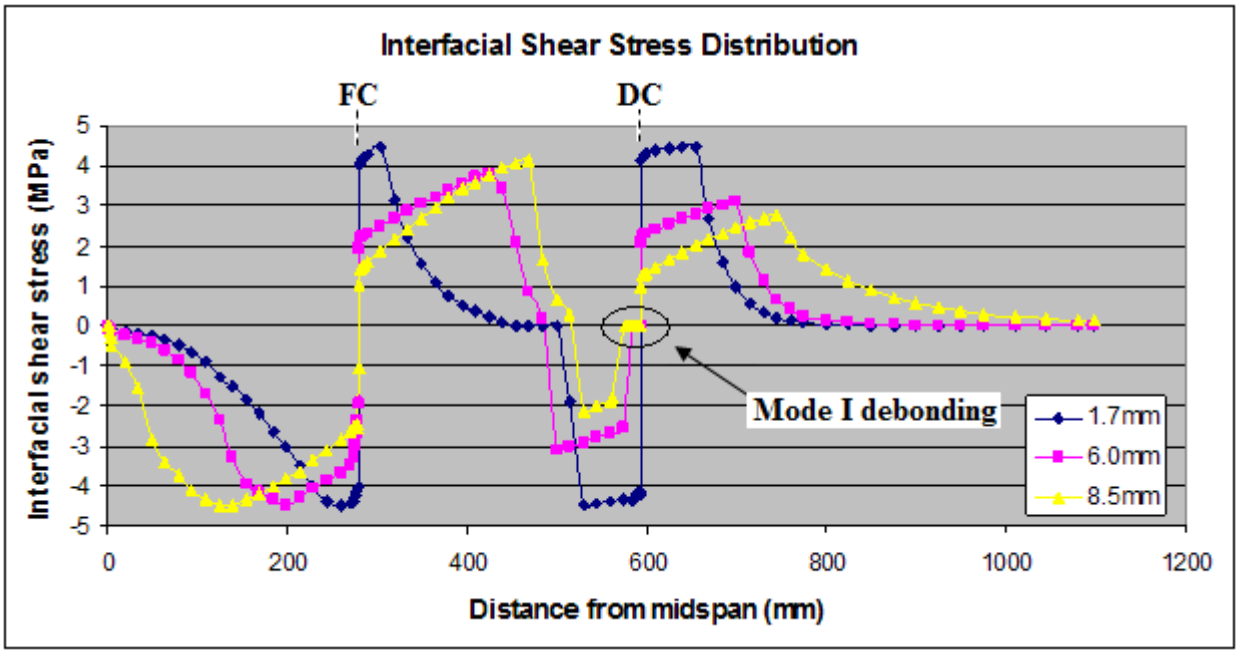

Figure 6.15: Development of interfacial shear stresses for various deflection levels (ks=500MPa/mm).

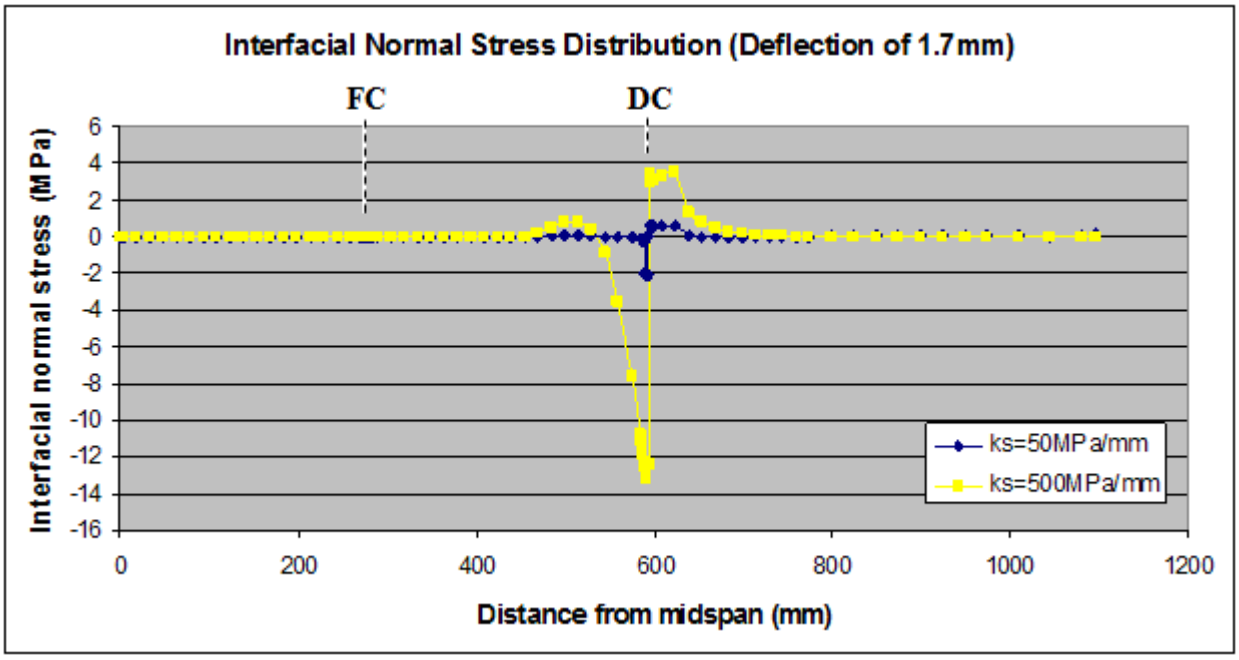

Figure 6.16: Development of interfacial normal stresses at deflection level of 1.7mm.

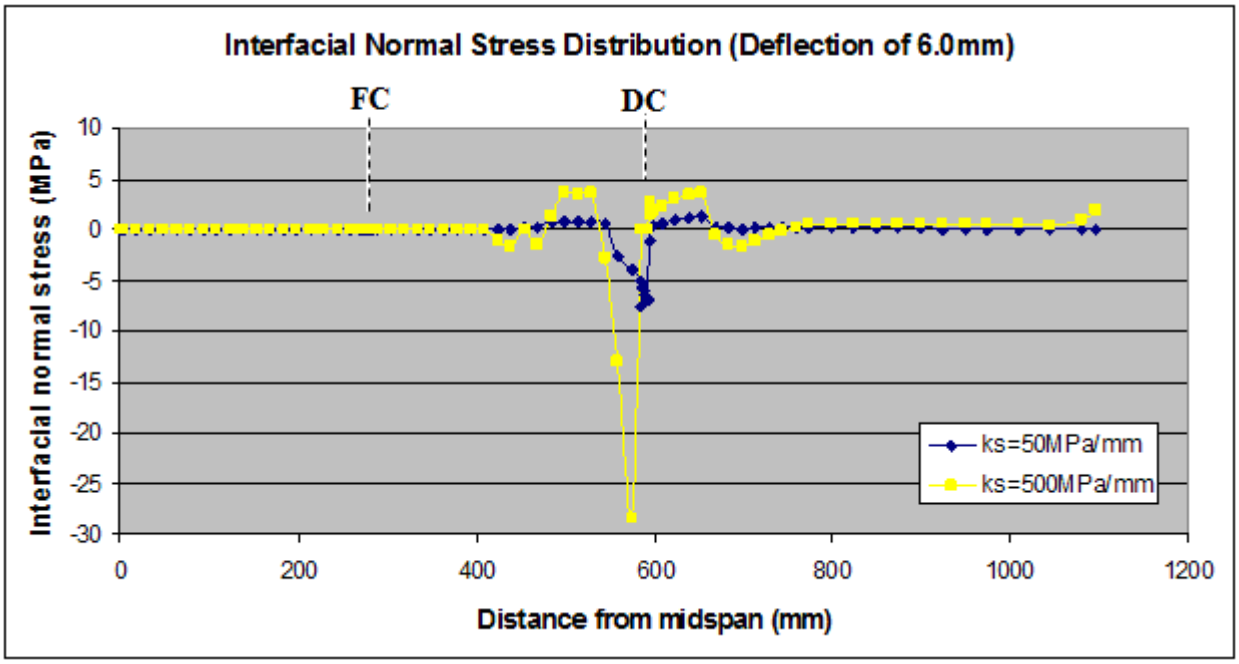

Figure 6.17: Development of interfacial normal stresses at deflection level of 6.0mm.

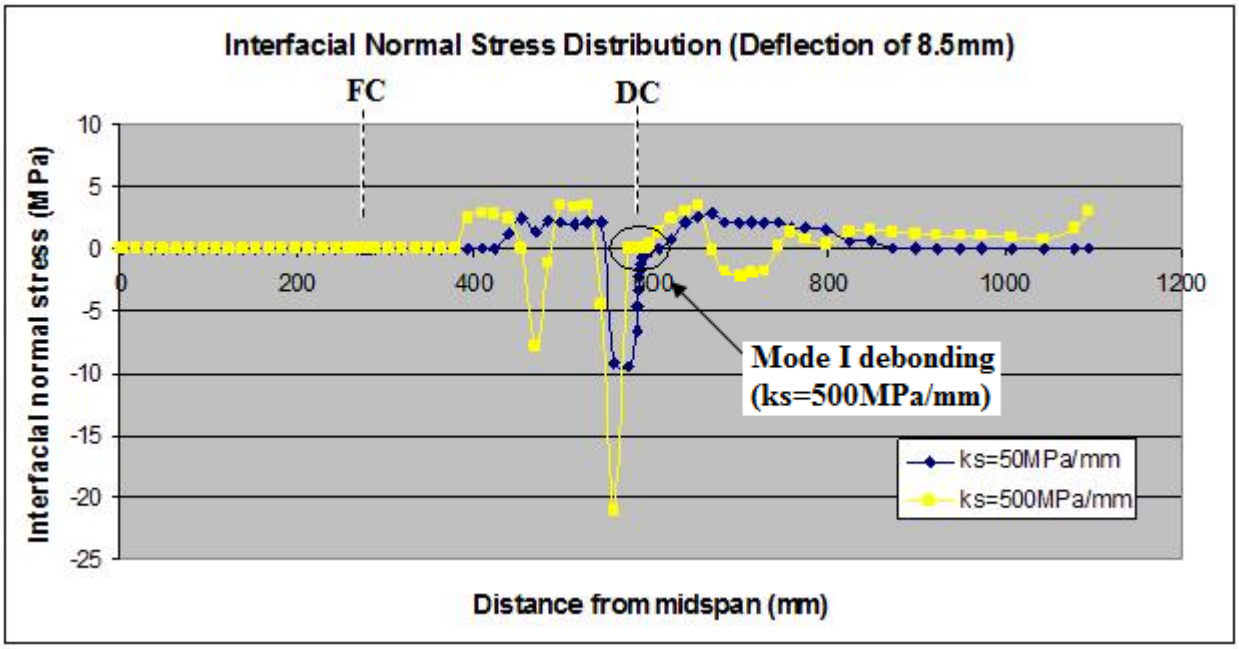

Figure 6.18: Development of interfacial normal stresses at deflection level of 1.7mm.

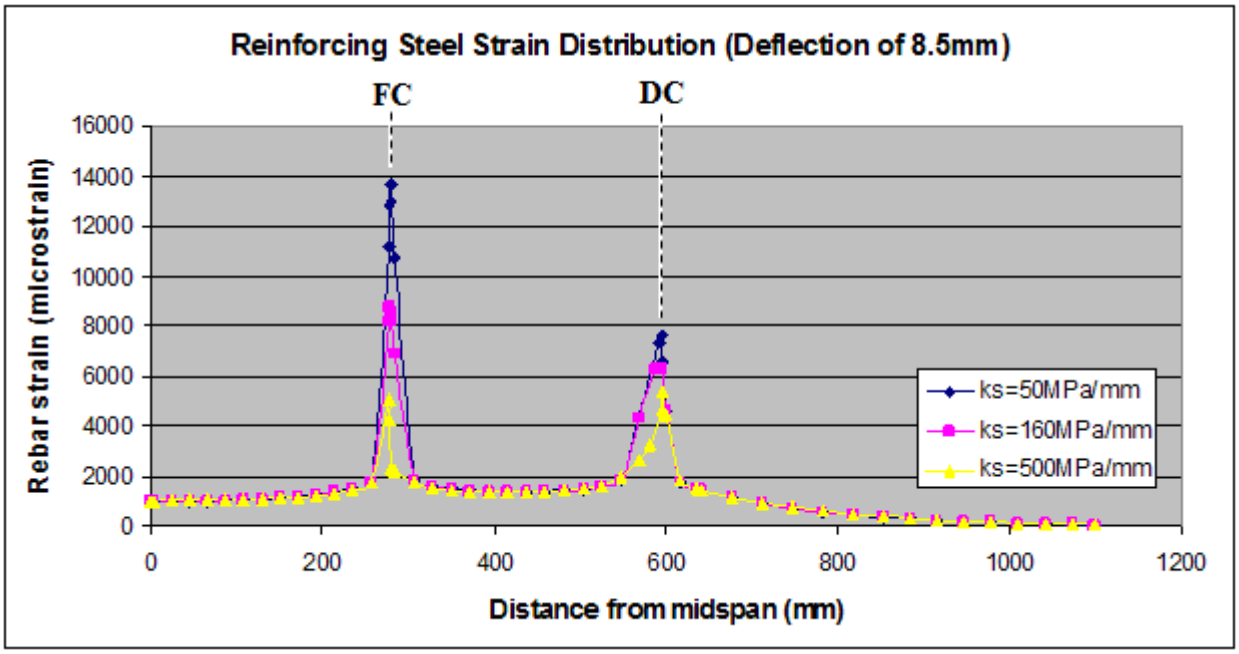

Figure 6.19: Development of reinforcing steel strain for various interfacial stiffness values at a deflection of 8.5mm.

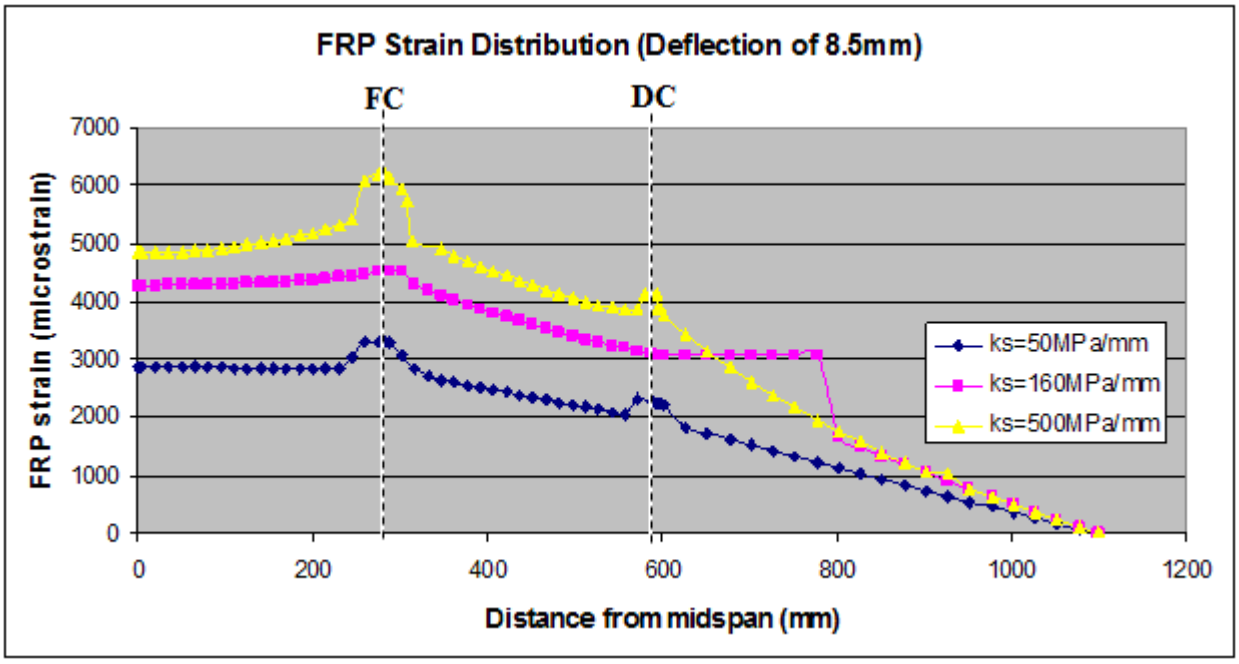

Figure 6.20: Development of FRP strain for various interfacial stiffness values at a deflection of 8.5mm.

6.3.3 Effect of Bond Strength

As noted in Chapter 5.0, the effectiveness of a FRP strengthened RC member is highly dependent on the bond stresses that exist between the adhesive and the member. Bond stresses are generated along the interface due to changes of internal moments along the length of the beam, and through the transfer of forces at plate-ends and/or across intermediate cracks (Neubauer and Rostasy, 1999). Chapter 5.0 focused on how bond stresses are affected by multiple flexural cracks that develop under applied loading. The investigation is now focused on how bond stresses are affected by a critical shear/diagonal crack that develops along the interface. Section 2.6 outlined the importance of considering bond strength to ensure composite action. However, researchers have been unable to come to a common consensus on interfacial bond strengths, with reported values being as low as 0.5MPa and as high as 12MPa. Nishida et al. (1999) reported ranges of bond strength between 3 and 4.3MPa, while Nababa et al. (2001) found it to be between 6 and 8MPa, and Yoshizawa et al. (2000) reported it to range from 4.7 to 12MPa. For the purposes of the current study, a set of three values are used: 1.5, 4.5, and 10MPa, which are representative of low, average, and high interfacial bond strength. The interfacial shear stiffness is fixed at k_s^{int}=160MPa/mm, interfacial normal stiffness at k_n^{int}=1000MPa/mm, interfacial fracture energy at G_f^{int}=0.5N/mm, and the positioned of the predefined cracks as shown in Figure (Sketch). The analyses are evaluated based on the response of the model in terms of load-deflection, interfacial shear stress distribution, interfacial normal stress distribution, FRP strain distribution, and reinforcing steel strain distribution.

Figure 6.21 shows the load versus midspan deflection response of the model for the three bond strength values. The low interfacial bond strength values leads to premature crack opening and lower overall levels of strengthening as summarized in Table 6.3. The FC in the lower bond

model opens earlier than the other models due to the reduced rate of stress transfer at the interface. As a result, the concrete beam is forced to contribute more to the load-carrying capacity causing the FC to open at a midspan deflection of 5.4mm, compared to 7.9mm for the control model. On the other hand, high interfacial bond causes a significantly more effective rehabilitation with greater yield and ultimate load, as well as prolonged crack opening as summarized in Table 6.3. The higher bond strength increases composite action and prevents the crack opening at the FC. The faster stress transfer at the interface is believed to significantly contribute to the increase in strengthening. This is supported by not only the increase in ultimate load but also by the increase in load ratio from 1.14 to 1.34 for the low to the high bond strength models, respectively.

Figure 6.22 captures the interfacial shear stress distribution along the interface at deflection values of 1.7, 6.0, and 8.5mm. The figure captures the initiation of debonding at the FC caused by premature crack opening at the midspan deflection of 6.0mm. This causes debonding to occur at the FC, without the occurrence of the debonding at the DC, causing only mode II response. However, the rate at which the debonding crack propagates along the interface was found to be lower than in higher bond strength models. For instance, at the midspan deflection of 8.5mm the debonding crack has propagated 45mm to the right of the FC whereas it has only debonded 7mm to the right of the FC in the low bond model. The reduced rate of debonding in the lower bond model may be attributed to the reduced stresses generated along the interface when a lower bonding material is employed. The debonding crack propagates in mode II fashion towards the DC and eventually debonds completely from the beam at a midspan deflection of 14.9mm.

Figure 6.23 captures the interfacial shear stress distribution along the interface also at deflection values of 1.7, 6.0, and 8.5mm. Employing higher interfacial bond stress was found to delay the initiation of macro-debonding at the interface. This may be attributed to the FRP plate providing more resistance to the opening of the FC and DC, since interfaces with higher bond strength require more energy (i.e. load) to exceed the strength capacity of the interface. The DC was activated prior to the opening of the FC, which is considered unique to higher bond strength interfaces. This may be attributed to the normal (or peeling) stresses that exist at the toe of the DC. Even though the opening of the FC initiated at a later loading stage than the lower bond models, the normal (or peeling) stresses that exist at the toe of the DC were found to contribute to the initiation of debonding, caused by faster load transfer. As a result, debonding initiated from the DC in mode I fashion at a midspan deflection of 7.8mm, and was then followed by the initiation of mode II debonding at the FC at a deflection of 8.25mm. Despite debonding initiating in mode I fashion, the ultimate debonding failure was dominated by mode II fracture at a midspan deflection of 16.5mm.

Figures 6.24-6.26 illustrate the interfacial normal stress distribution along the interface for each of the bond strength models at deflection levels of 1.7, 6.0, and 8.5mm. The figures suggest that low interfacial bond produces negligible peeling stress concentrations in comparison to higher bond models. This may be attributed to the delayed activation of the DC in the model along with the low rate of stress transfer along the interface. The behaviour of such low bond strength models produced similar result to the findings of the analysis preformed in Chapter 5.0, where multiple flexural cracks were predefined in the model. In contrast, the use of materials with higher interfacial bond strength increased the rate of stress transfer, consequently producing

greater peeling stresses adjacent to the DC and ultimately dominating the initiation of debonding in mode I fashion at the DC.

The level of bond strength was found to influence the strain development of the internal rebar. Figure 6.27 illustrates the strain development at a midspan deflection of 6.0mm. As expected, strain of the rebar in the low interfacial bond is 25.4 and 36.8% greater than the 4.5 and 10MPa bond values at the FC, respectively. This is attributed to the low stress transfer at the interface when employing material with weak bond. Figure A6.8, in the appendix, includes the reinforcing steel strain distribution at various loading stages and similar trends are found throughout.

Figure 6.28 illustrates the FRP strain development along the interface for the three bond models at a midspan deflection of 6.0mm. The findings support the notion that the higher bond materials increase the rate of stress transfer along the interface, and utilize the FRP material to a higher extent. The strain in the FRP plate of the 10MPa model is found to be 43.4 and 68.4% greater than the 4.5 and 1.5MPa bond values at the FC, respectively. Figures A6.7 and A6.10 in the appendix find similar trends in FRP strain development at various loading stages in the analysis. However, despite the value of the bond strength, the mode final debonding failure is still mode II dominated.

Table 6.3: Response of models for different bond strengths.

Bond str.	**Opening of Flexural Crack**		**Opening of Diagonal Crack**		**Yield Load**		**Ultimate Load**		**LR***	**Debonding mode of failure**	
(MPa)	**P (kN)**	**Δ (mm)**	**P (kN)**	**Δ (mm)**	**P (kN)**	**Δ (mm)**	**P (kN)**	**Δ (mm)**		**Initial Mode**	**Final Mode**
1.5	103.2	5.4	133.6	11.4	101.6	5.15	143.6	14.9	1.14	Mode II	Mode II
4.5	135.5	7.9	137.1	8.35	126.3	6.6	157.8	15.5	1.25	Mode II	Mode II
10	142.0	8.25	143.7	7.8	141.2	7.35	169.3	16.5	1.34	Mode I	Mode II

*LR - Load ratio defined as maximum applied load resisted by specimen divided by yield load for control specimen.

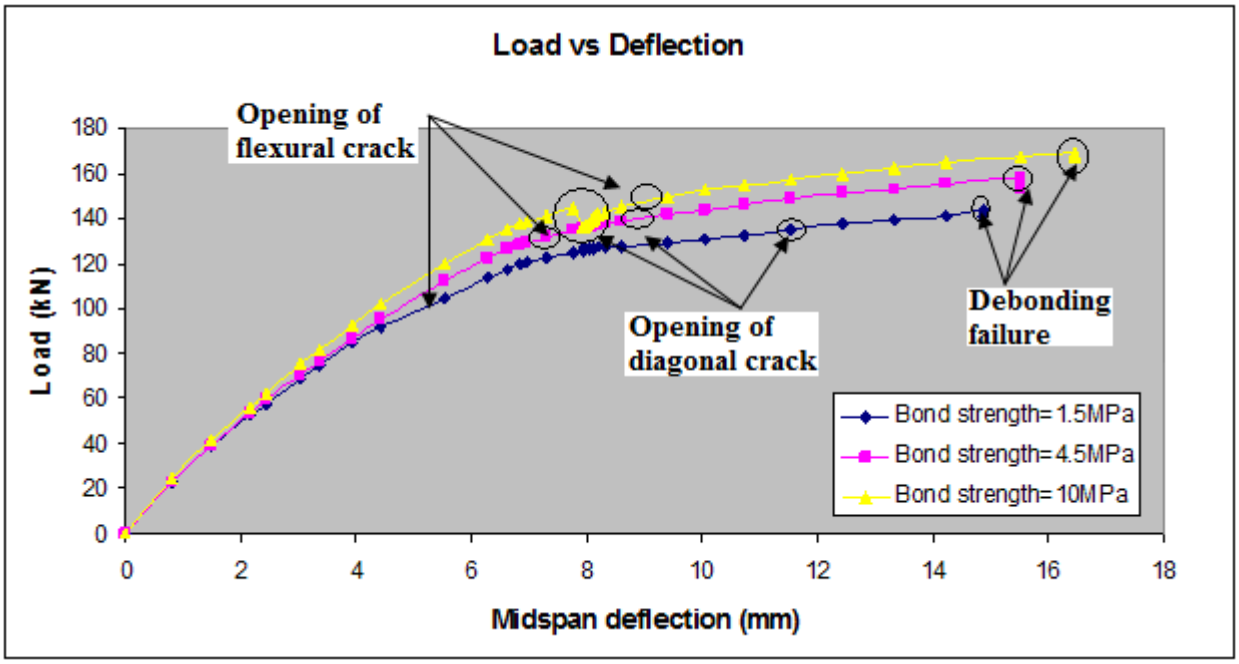

Figure 6.21: Load-deflection response for various bond strengths.

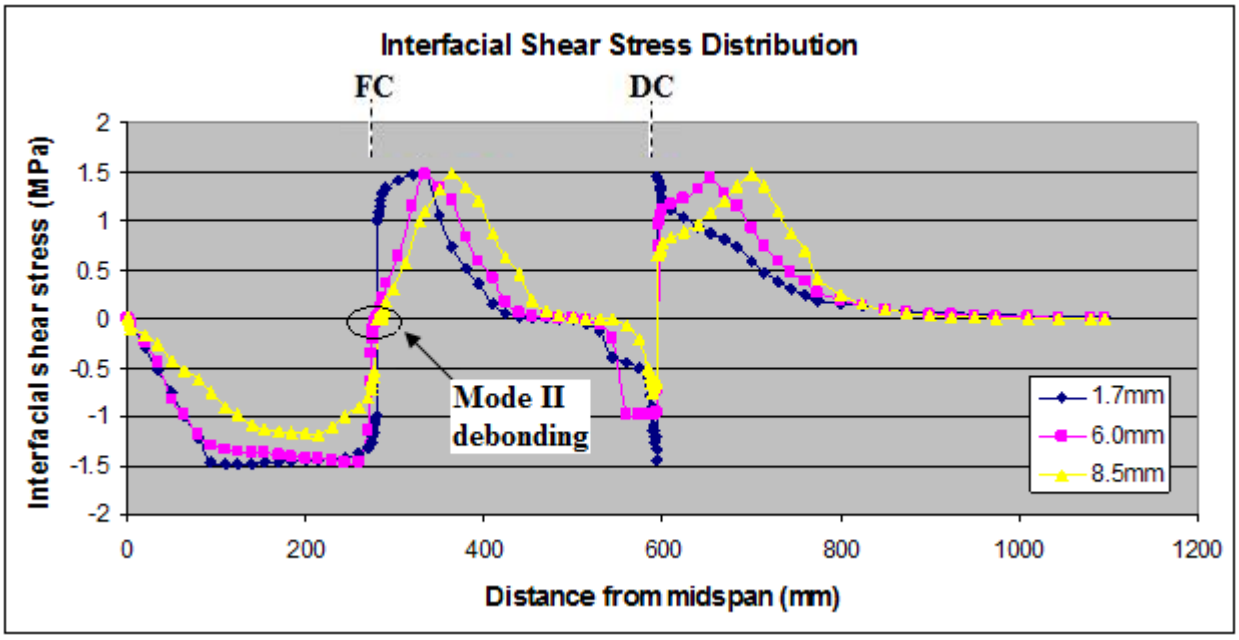

Figure 6.22: Development of interfacial shear stress for various deflection levels (τ_b=1.5MPa).

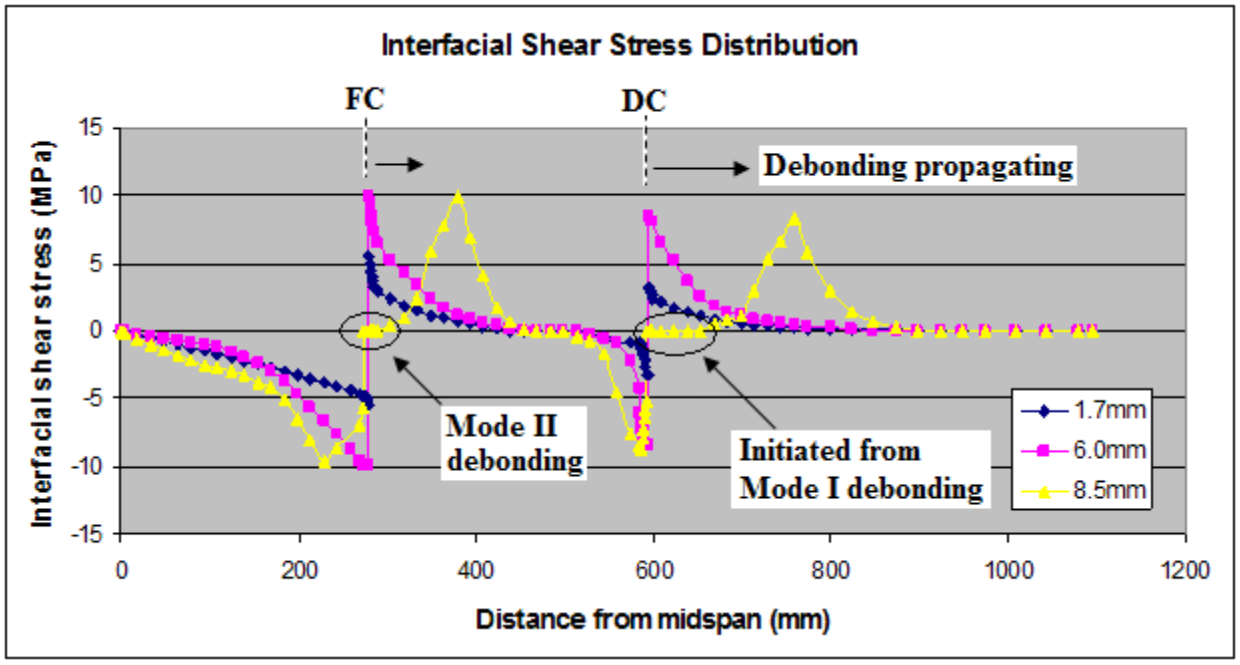

Figure 6.23: Development of interfacial shear stress for various deflection levels (τ_b=10MPa).

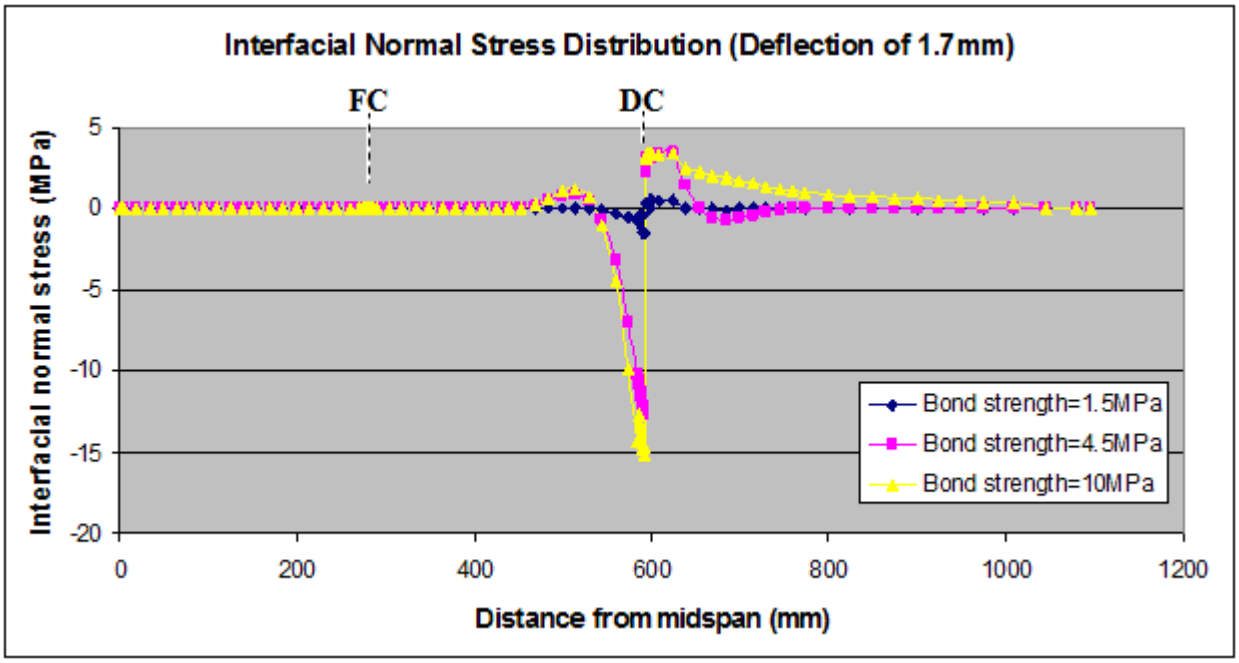

Figure 6.24: Effect of bond strength on interfacial normal stress (midspan deflection of 1.7mm).

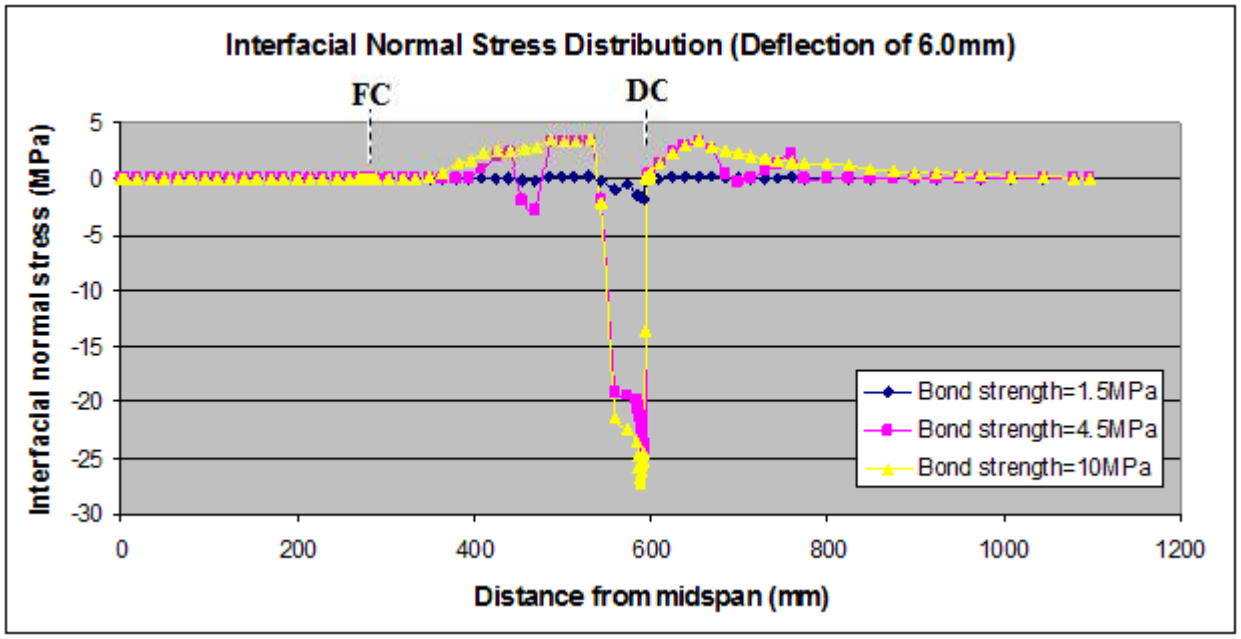

Figure 6.25: Effect of bond strength on interfacial normal stress (midspan deflection of 6.0mm).

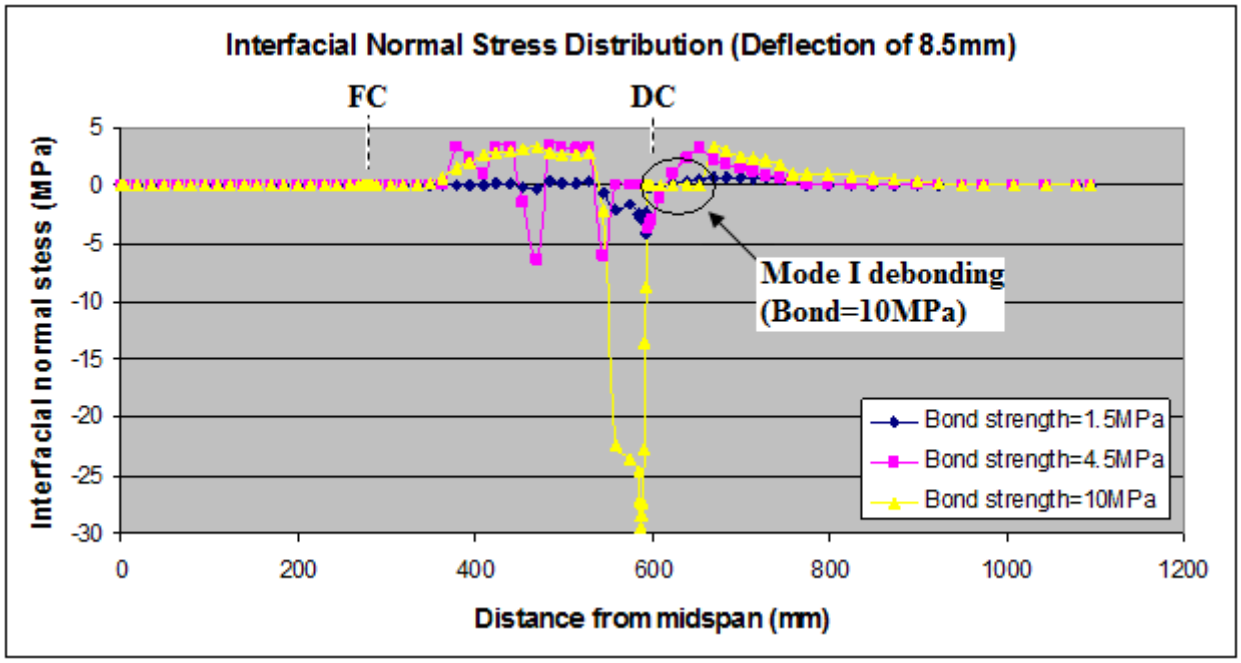

Figure 6.26: Effect of bond strength on interfacial normal stress (midspan deflection of 8.5mm).

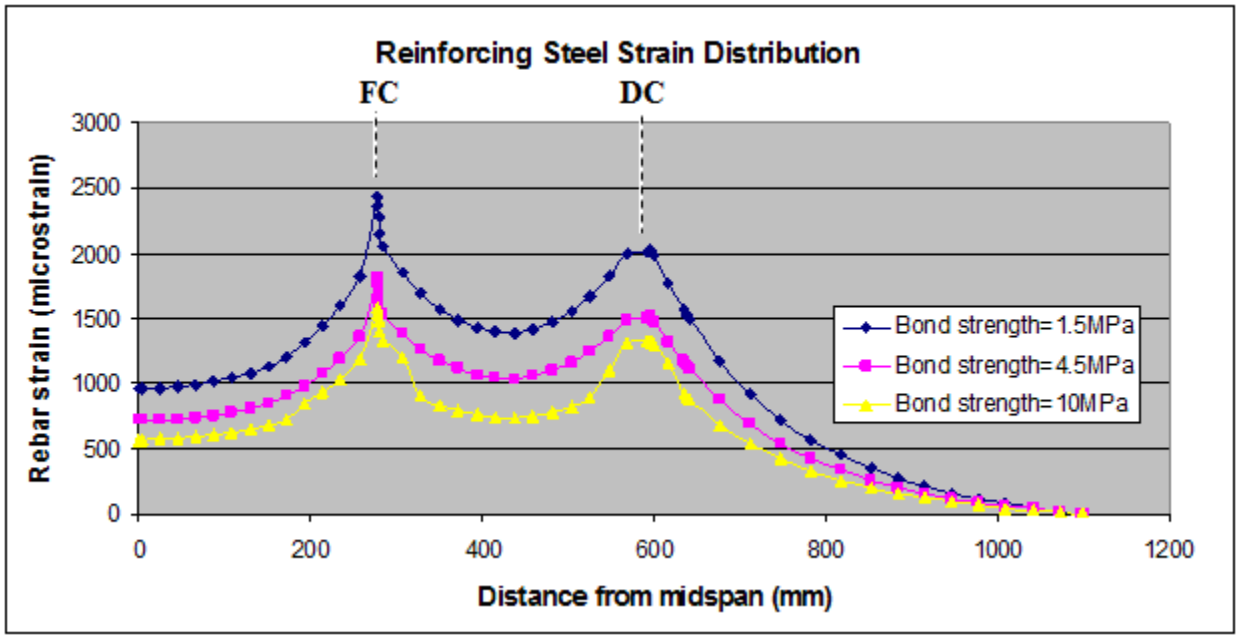

Figure 6.27: Effect of bond strength on reinforcing steel strain distribution (midspan deflection of 6.0mm).

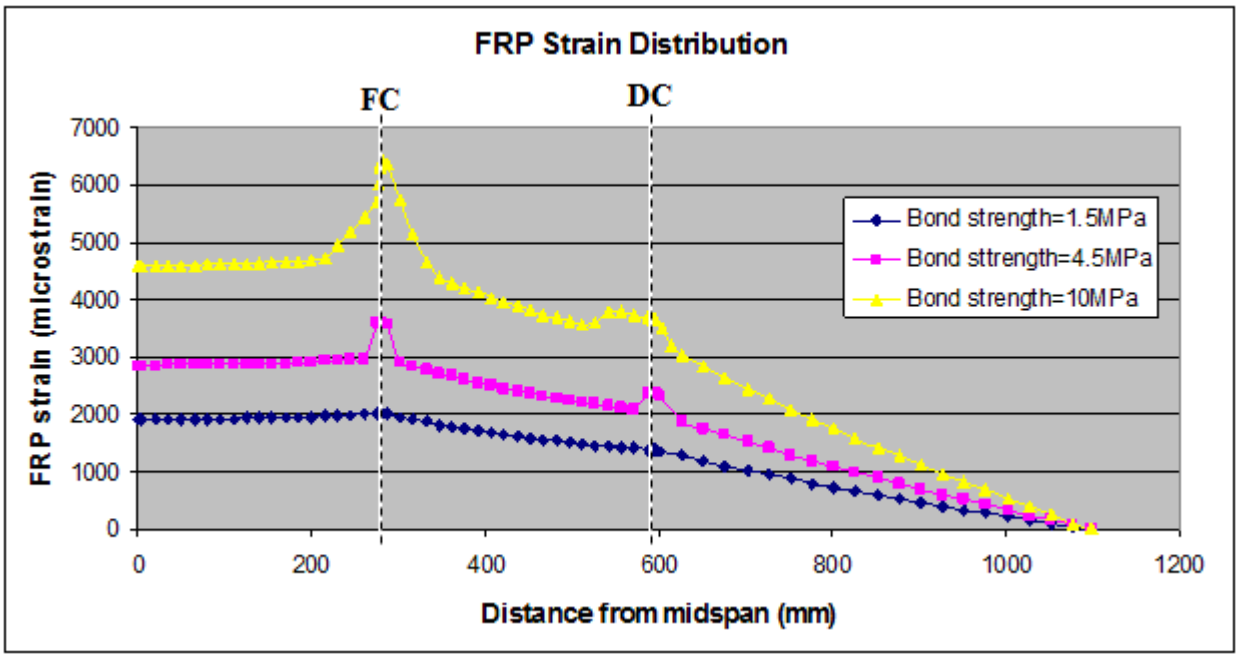

Figure 6.28: Effect of bond strength on FRP strain distribution (midspan deflection of 6.0mm).

6.3.4 Interfacial Fracture Energy

Interfacial fracture energy refers to the amount of energy (applied load) in order to produce a unit area of crack. The results in Chapter 5.0 indicate that interfacial fracture energy significantly affects the ultimate load-carrying capacity of a beam undergoing mode II debonding. These findings are further studied to focus on how fracture energy affects debonding mechanism and strengthening effect when subjected to normal (or peeling) stresses at the toe of a critical shear crack. By fixing the predefined cracks as shown in Figure 6.2, local bond strength at τ_b=*4*.5MPa, interfacial shear stiffness at k_s^{int}=160MPa/mm, interfacial normal stiffness k_n^{int}=1000MPa/mm, the effect of interfacial fracture energy is studied by varying it for three cases: G_f^{int}=0.3, 0.5 and 1.0N/mm, representative of low, average and high values. Its effect evaluated based on the response of the model in terms of load-deflection, interfacial shear stress distribution, interfacial normal stress distribution, reinforcing steel strain distribution and FRP strain distribution.

Figure 6.29 shows the load versus midspan deflection for the parametric analysis. The figure clearly shows that the load carrying capacity and ultimate load increase with interfacial fracture energy. Complete debonding was found to occur at a midspan of 10.66, 15.53, and 19.13mm for fracture energy values of 0.3, 0.5, and 1.0N/mm, respectively, as summarized in Table 6.4. While no significant difference in load carrying capacity can be found prior to the yield load, immediately following it one can be seen. Low interfacial fracture energy makes it easier for debonding initiation and propagation from the maximum moment region to the FRP plate-end, as shown in Figure 6.30, in mode II fashion. This can be attributed to the fact that low interfacial fracture energy cannot endure the stresses generated from the debonding crack initiating from the FC. Unlike the case of high fracture energy, the low interfacial fracture energy level severely limits tress transfer and is thus unable to distribute effects of cracking

resulting in very low efficiency of use of the FRP, confirmed by its low load ratio of 1.08. On the other hand, higher interfacial fracture energy delays the initiation of mode II debonding and results in more efficient use of the FRP material and overall strengthening by reaching a load ratio of 1.34.

Figure 6.30 captures the development of interfacial shear stress at the deflection values of 1.7, 6.0, and 8.5mm. Prior to the initiation of micro-debonding no significant difference in the stress development is found between the models, as can be seen by comparing the shear stress concentration at deflection values 1.7 and 6.0mm. However, subsequent to the initiation of micro-debonding, the rate of softening at the interface appears to be affected by the value of interfacial fracture energy with macro-debonding occurring much earlier than the other models at a midspan deflection of 6.8mm (occurring from the FC in mode II fracture behaviour). As shown in the figure at the midspan deflection of 8.5mm, the low energy model is found to debond at much faster rate than the other models. At this point, the FRP plate has debonded 105mm to the right of FC, whereas the control model has only debonded 45mm to the right of the crack. These findings suggest that the interface is unable to tolerate the stress development during the softening stage to the same extent as higher energy models. It should also be pointed out that debonding at the DC was initiated at dominated by mode II fracture, whereas the in the control model it was initiated in mode I fashion. This is attributed to the fact that the shear capacity at the DC was exceeded before the normal stress capacity. Thus, complete debonding was dominated in mode II behaviour initiating from the FC towards the plate-end.

Figure 6.31 illustrates the interfacial shear stress development at various loading stages in the analysis. The results indicate that higher fracture energy prolongs mode II debonding in comparison to the two lower energy models. While no significant difference in shear stress

development can be found prior to the initiation of micro-debonding at the interface, higher interfacial fracture energy reduces the rate of softening of the interface thereby prolonging the initiation of macro-debonding. This is exemplified by considering the shear stress concentration at the FC at the midspan deflection of 8.5mm. At this point, the interface is still intact whereas the lower energy models are undergoing mode II debonding. The interface is only undergoing debonding initiated at the DC in mode I fashion. This suggests that interfacial fracture energy is shear dominated. The first sign of mode II debonding was found to occur at the FC at a midspan deflection of 9.8mm. Despite that debonding initiated in mode I behaviour from the DC, debonding failure was still dominated by mode II fracture behaviour. This may be attributed to the fact that mode I debonding propagates in a very slow rate compared the mode II debonding.

Figure 6.32 captures the effect of interfacial normal stress distribution for the various models at a midspan deflection of 8.5mm. The figure suggests that interfacial fracture energy is shear dominated as no significant effect on the results are found. This may be attributed to the fact that interfacial normal stress is dominated by the strength of the concrete, rather than the bond stresses between the two materials. Similar trends are found at other loading stages, as found in Figures A6.13-A6.14 of the appendix.

Figures 6.33 and 6.34 shows the strain distribution in the FRP and rebar materials at deflections of 6.0 and 8.5mm. The trends in both materials appear to be similar, indicating that prior to yield load there is no significant difference in strain development. However, following the yield load, low interfacial fracture energy is found to limit the stress transfer at the interface and the concrete beam is required to contribute more to the load-carrying of the structure. At the other extreme, high fracture energy is found to do a better job at keeping the interface intact and providing adequate stress transfer at the interface. As a result, high efficiency of use of the FRP

material and the rebar is not needed to be strained to the same extent. However, despite the energy value at the interface, the mode final debonding failure is found to be mode II dominated in all models.

Table 6.4: Response of models for different interfacial fracture energy models.

G_f^{int}	Opening of Flexural Crack		Opening of Diagonal Crack		Yield Load		Ultimate Load		LR*	Debonding mode of failure	
N/mm	P (kN)	Δ (mm)	P (kN)	Δ (mm)	P (kN)	Δ (mm)	P (kN)	Δ (mm)		Initial Mode	Final Mode
0.3	125.9	6.8	129.2	7.3	122.5	6.55	135.8	10.7	1.08	Mode II	Mode II
0.5	135.5	7.9	137.1	8.35	126.3	6.6	157.8	15.5	1.25	Mode II	Mode II
1.0	147.1	9.8	139.7	8.1	138.6	8.0	169.2	19.6	1.34	Mode I	Mode II

*LR - Load ratio defined as maximum applied load resisted by specimen divided by yield load for control specimen.

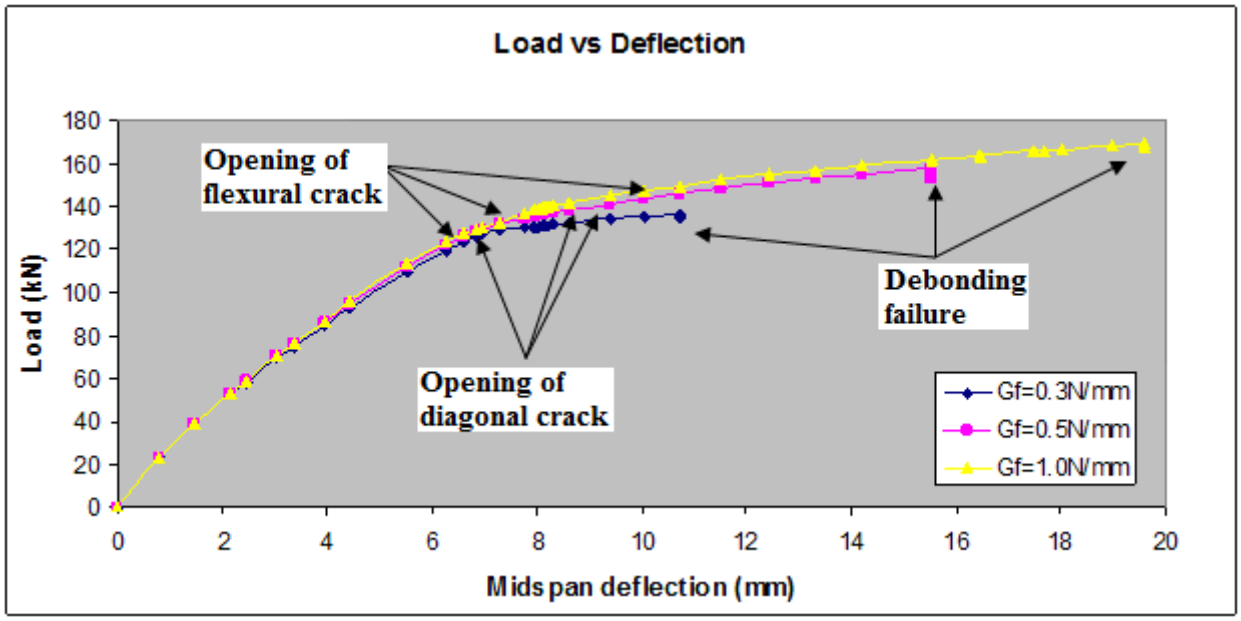

Figure 6.29: Effect of interfacial fracture energy on load-deflection response.

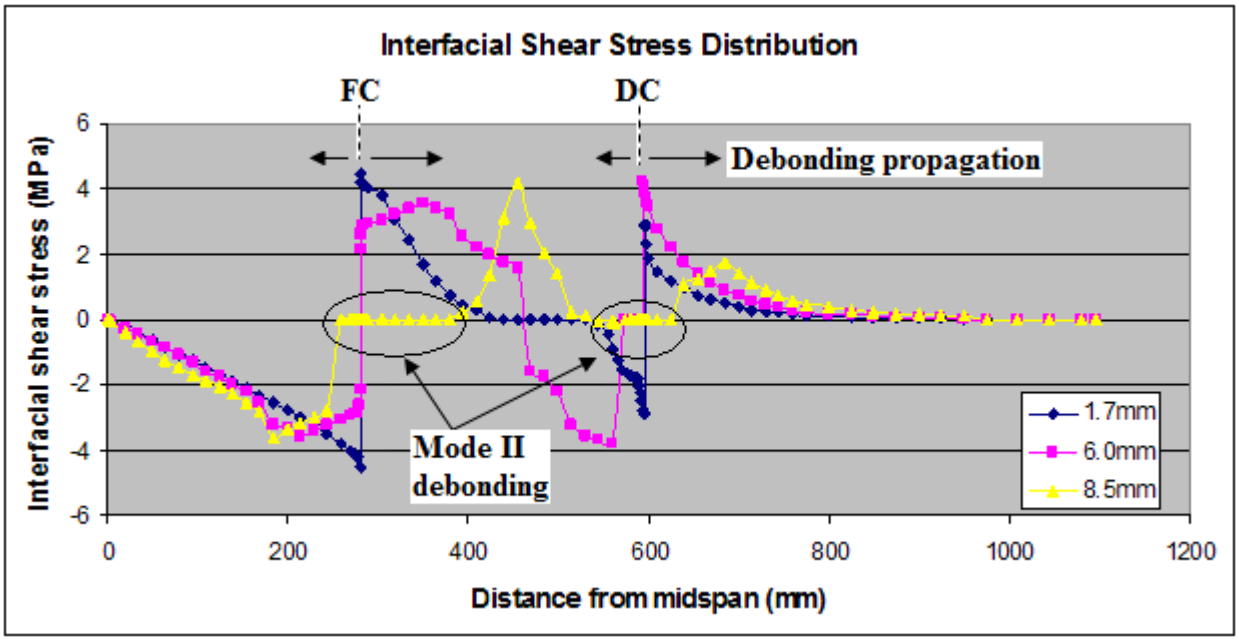

Figure 6.30: Development of interfacial shear stress for various deflection levels (G_f^{int}=0.3N/mm).

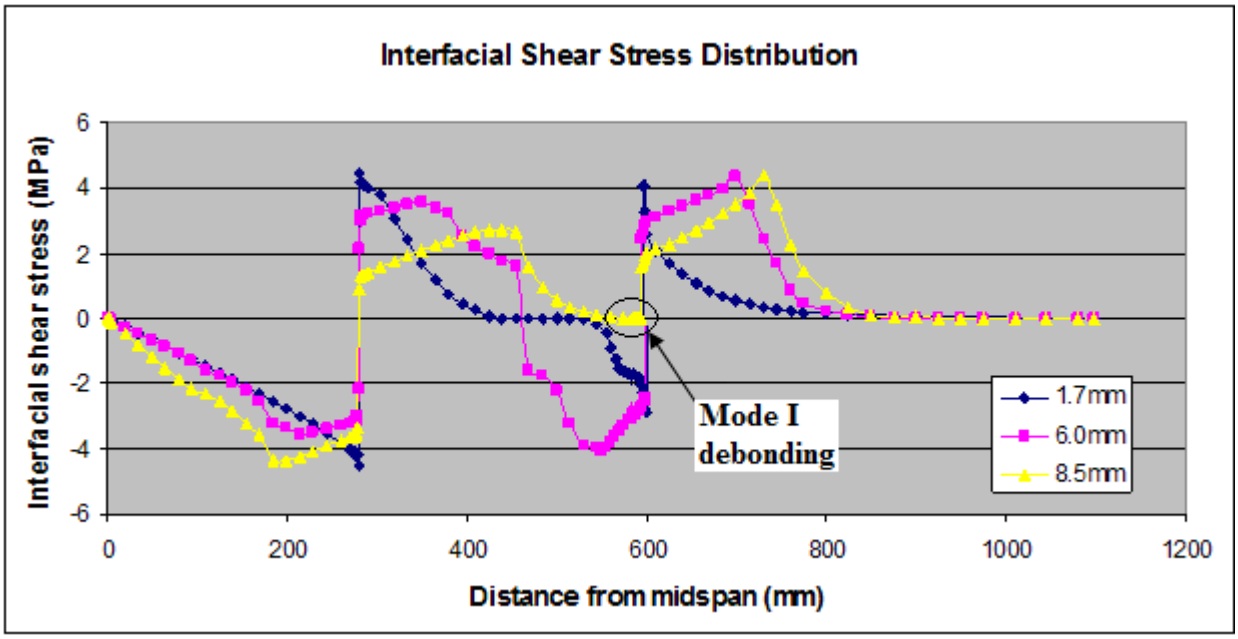

Figure 6.31: Development of interfacial shear stress for various deflection levels (G_f^{int}=1.0N/mm).

-

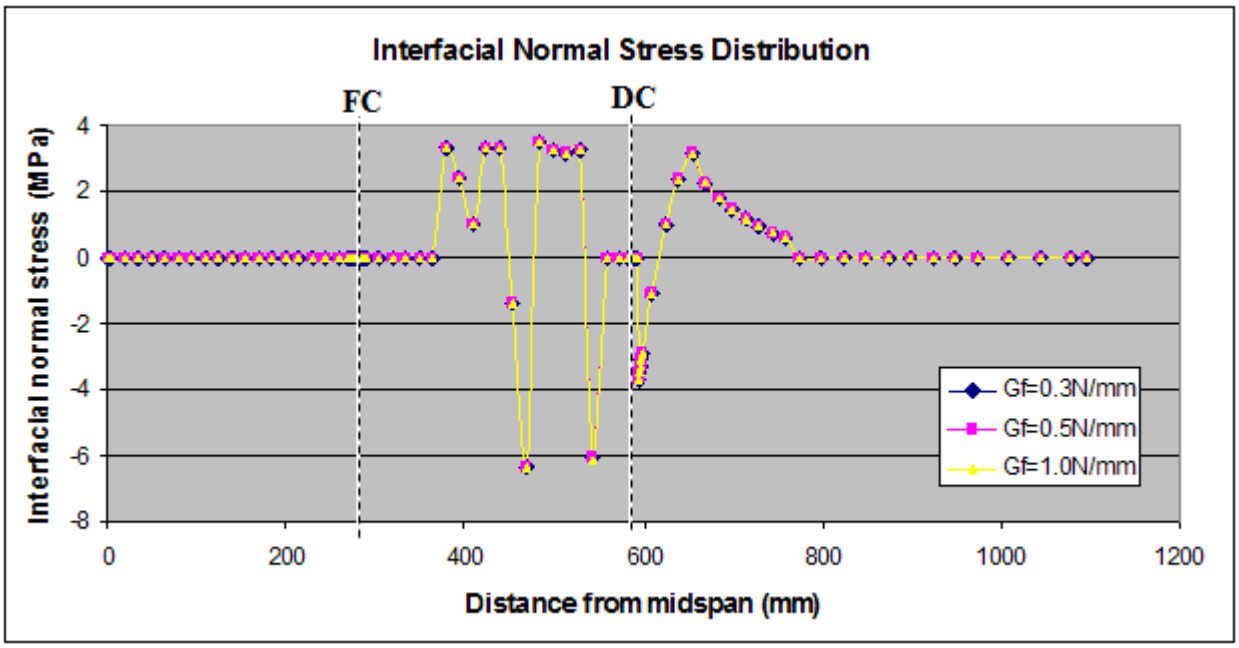

Figure 6.32: Effect of fracture energy on interfacial normal stress (midspan deflection of 8.5mm).

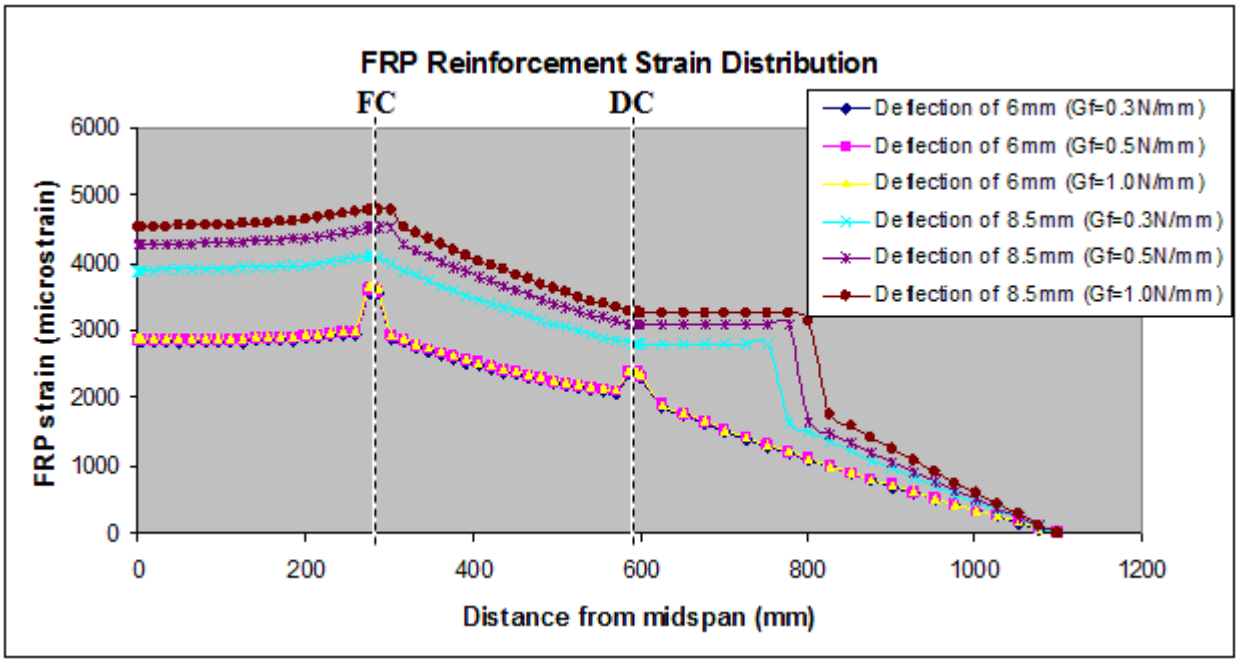

Figure 6.33: Effect of interfacial fracture energy on FRP reinforcement distribution.

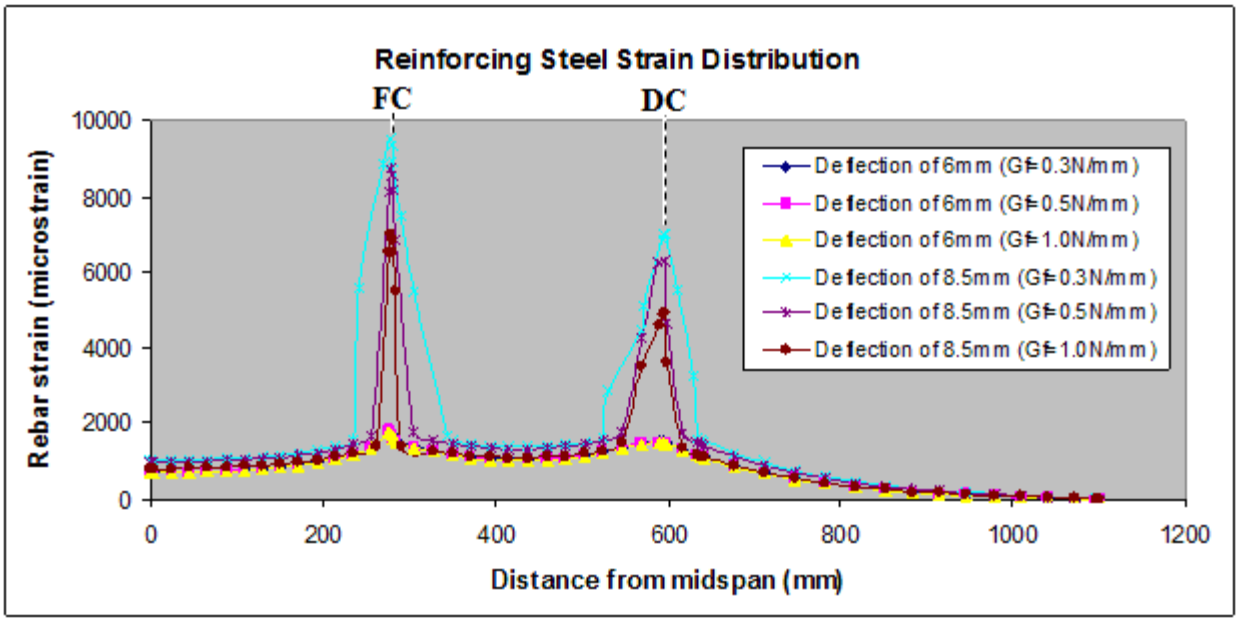

Figure 6.34: Effect of interfacial fracture energy on reinforcing steel strain distribution.

6.3.5 Interfacial Normal Strength

Shear-flexural or shear cracks induce high normal and shear stresses creating horizontal and vertical displacements near the toe of the crack, as shown in Figure 6.1. This portion of the study focuses on the interfacial normal strength of the FRP-concrete interface to investigate its effect on debonding mechanism and strengthening effect. By fixing the FC and DC as shown in Figure 6.2, bond strength at τ_b=4.5MPa, interfacial shear stiffness at k_s^{int}=160MPa/mm, and interfacial fracture energy at G_f^{int}=0.5N/mm, the interfacial normal stiffness is investigated using a set of three values: 500, 1000, and 1500MPa/mm, which are representative of low, average, and high normal stiffness values. The analysis was evaluated based the results of load-deflection, interfacial shear stress distribution, interfacial normal stress distribution, reinforcing steel strain distribution, and FRP strain distribution.

Figure 6.35 shows the load versus midspan deflection response of the models. Prior the yield load, there is no significant difference in the load-deflection response for different stiffness

values, but the ultimate load appears to be slightly higher for the higher normal stiffness model, with an increase of only 1.8% from the control model. The fact that there is no significant increase in the load-deflection response can be explained by examining the debonding mechanism of the models. Figures 6.36 and 6.37 capture the interfacial shear stress distribution of the interface at various loading stages. The figure indicates that the shear stress distribution at the FC is not affected by the change in interfacial normal stress value. This is attributed to the fact that at the toe of the FC, mode II debonding dominates, as proven by various researchers previously mentioned in Chapter 2.0. However, at the toe of the DC a difference in shear stress is distribution found. The case of the control model at midspan deflection of 8.5mm, the plate has debonded in mode I fashion at the toe of the DC over a 35mm span as shown in Figure 6.8. The low interfacial stiffness model on the other hand, has only debonded over a 5mm span at the same loading stage. This may be attributed to the low stress transfer rate at the interface when employing a low stiffness material. At the other extreme, the higher stiffness model also debonds over a 35mm span from the DC similar to the case of the control beam, indicating that with further increase of interfacial normal stiffness beyond a threshold does not result in any increase in modifying the interfacial normal stiffness.

Figures 6.38 and 6.39 illustrate the FRP and reinforcing steel strain distributions at a midspan deflection of 8.5mm. Both figures follow a similar trend, with there being only a slight difference in strain values in the vicinity of the DC. This can be attributed to the interfacial normal strength affecting the rate of transfer at the interface. In the case of the low stiffness model, the reinforcing steel is strained 8.0% more than the control specimen since the concrete beam is required to contribute more the load carrying capacity. The FRP plate at the same loading stage is utilized 6.4% more than the control specimen at the DC. This is due to the faster

stress transfer rate when employing a stiffer material at the interface. Similar trends were found at various loading stages as shown in Figures A6.19-A6.22 of the appendix.

Figures 6.40-6.42 show the interfacial normal stress distributions of the stiffness models at three loading stages: 1.7mm, 6.0mm, and 8.5mm, respectively. The trend is similar in all cases: the lower stiffness model results in lower interfacial normal stress distribution and the higher stiffness models result in higher normal stress. These findings further support the notion that higher stiffness models increase the transfer rate at the interface, which directly influence the utilization of the FRP plate.

Interfacial normal stress is thus seen not found to have a significant effect on the strengthening response of the specimen and only slightly on the strain development in the reinforcement materials. Despite the difference in the development of normal stresses surrounding the DC, the final mode of debonding failure is still found to be dominated by mode II fracture.

Table 6.5: Response of models for different interfacial fracture energy models.

k_n^{int}	Opening of Flexural Crack		Opening of Diagonal Crack		Yield Load		Ultimate Load		LR*	Debonding mode of failure	
MPa/ mm	P (kN)	Δ (mm)	P (kN)	Δ (mm)	P (kN)	Δ (mm)	P (kN)	Δ (mm)		Initial Mode	Final Mode
500	134.1	7.8	136.7	8.5	123.7	6.4	156.3	15.3	1.24	Mode II	Mode II
1000	135.5	7.9	137.1	8.35	126.3	6.6	157.8	15.5	1.25	Mode II	Mode II
1500	136.1	7.9	137.1	8.3	128.6	6.7	159.4	15.8	1.26	Mode II	Mode II

*LR - Load ratio defined as maximum applied load resisted by specimen divided by yield load for control specimen.

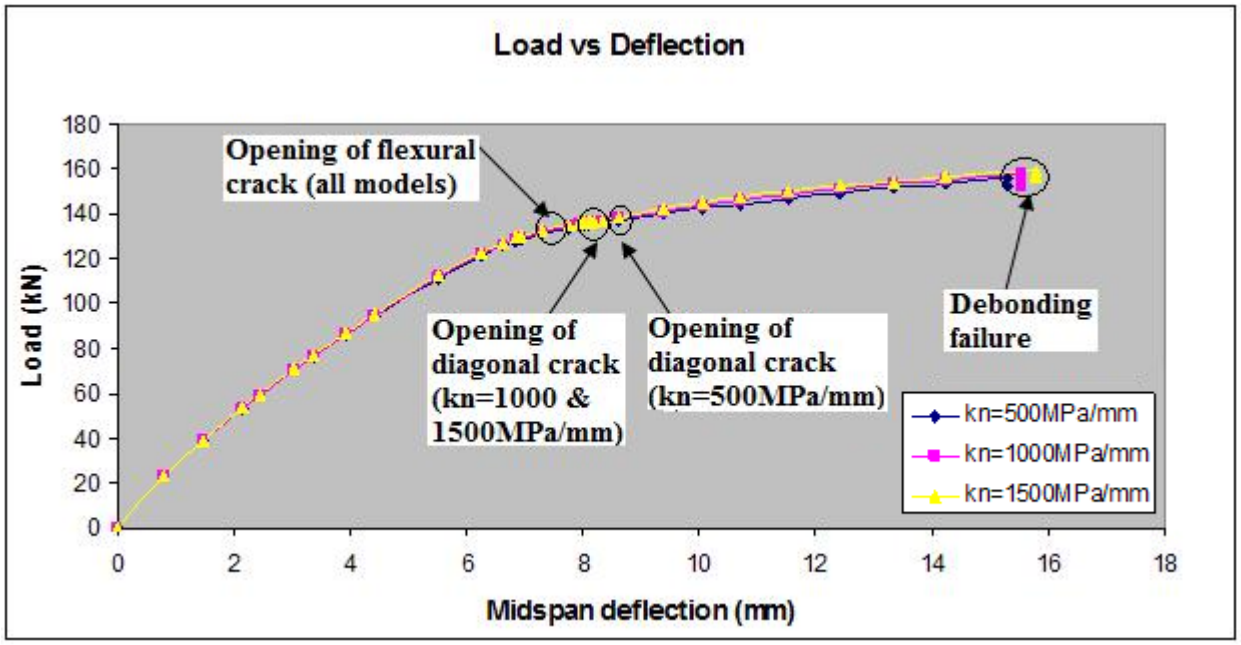

Figure 6.35: Effect of interfacial normal stiffness on load-deflection response.

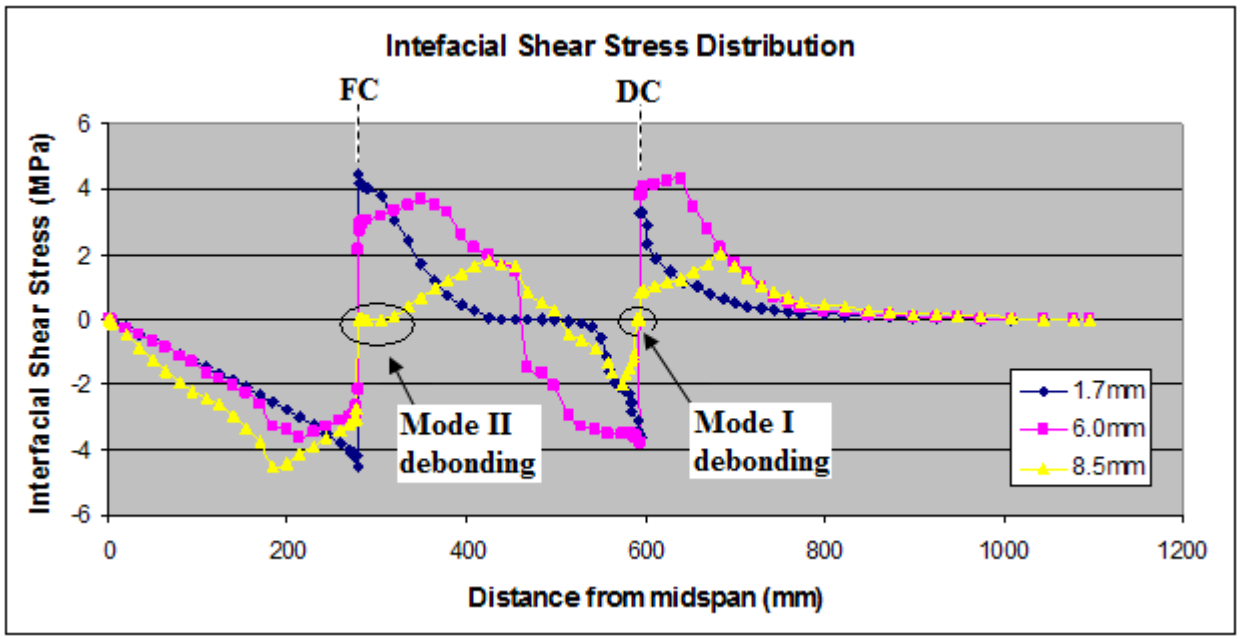

Figure 6.36: Development of interfacial shear stress distribution at various deflection levels (k_n^{int}=500N/mm).

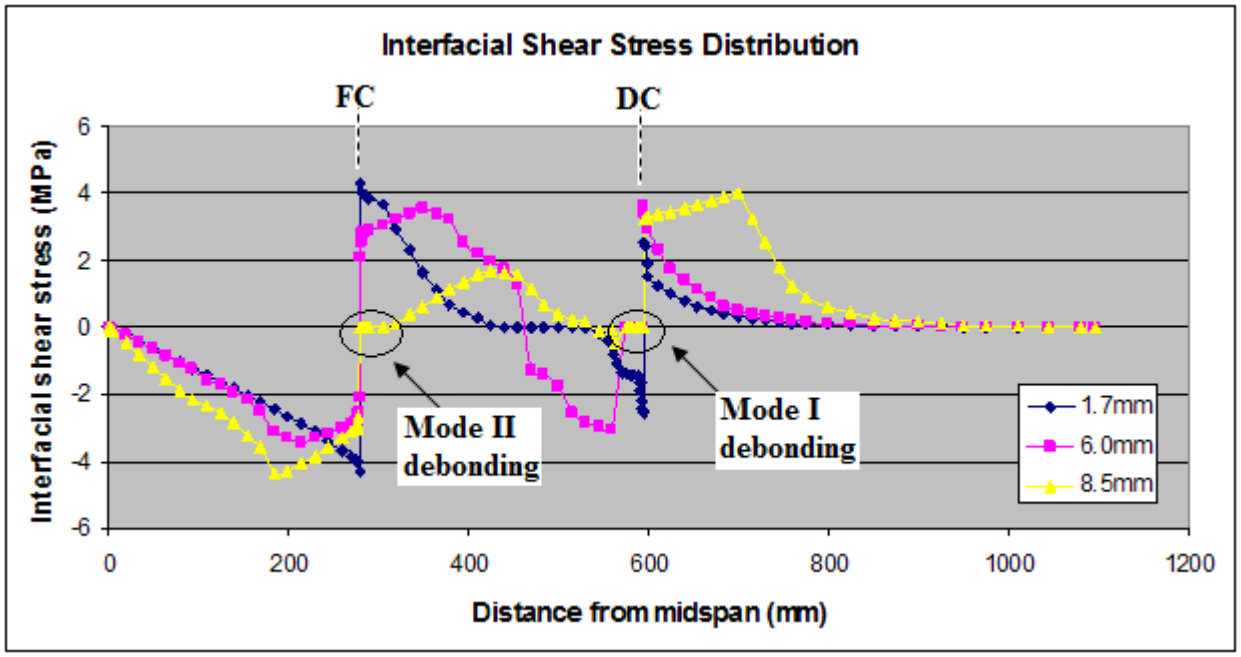

Figure 6.37: Development of interfacial shear stress distribution at various deflection levels (k_n^{int}=1500MPa/mm).

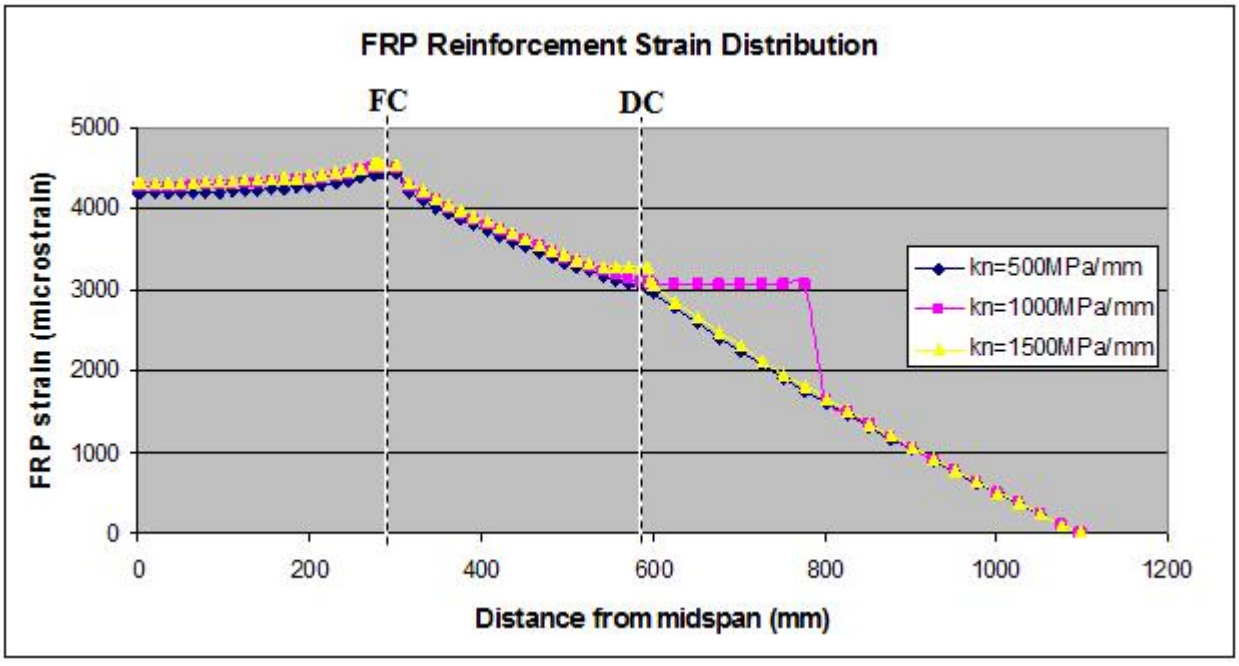

Figure 6.38: Effect of interfacial normal stiffness on FRP reinforcement distribution (deflection of 8.5mm).

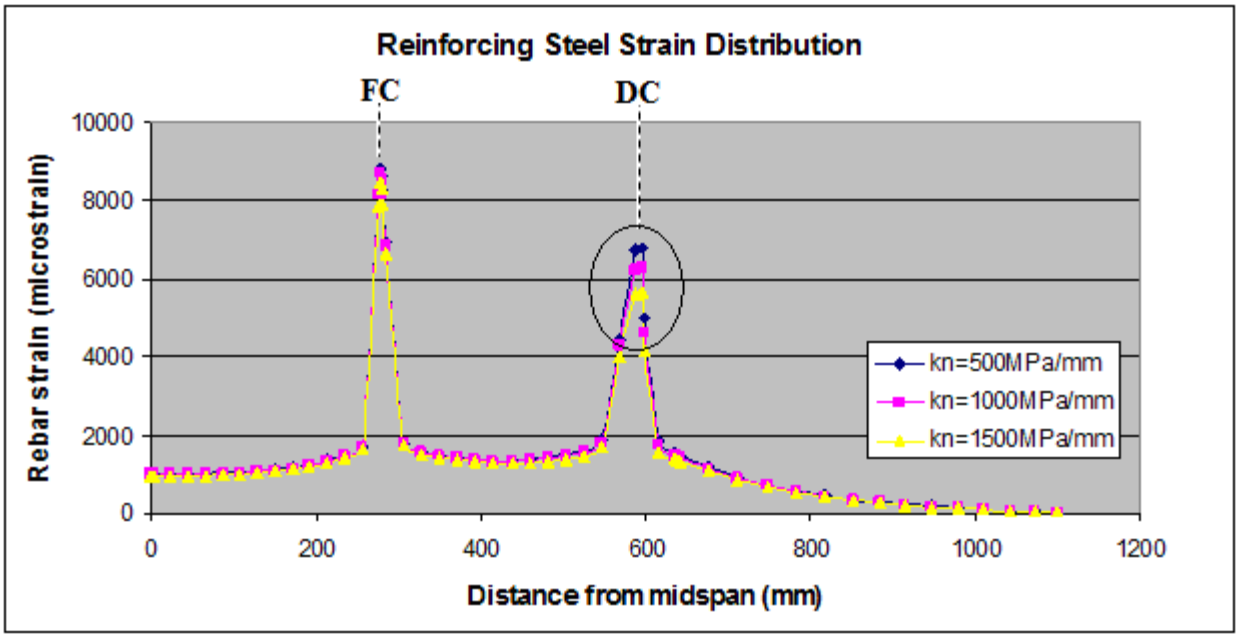

Figure 6.39: Effect of interfacial normal stiffness on steel reinforcement distribution (deflection of 8.5mm).

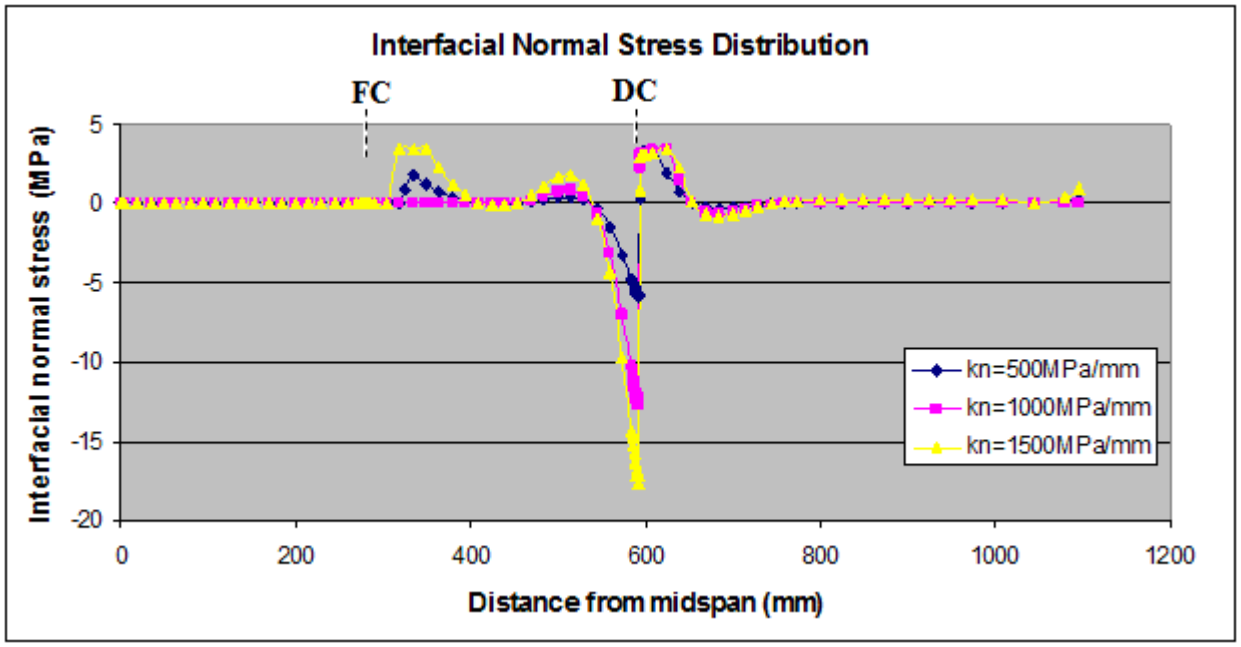

Figure 6.40: Interfacial normal stress distribution (deflection of 1.7mm).

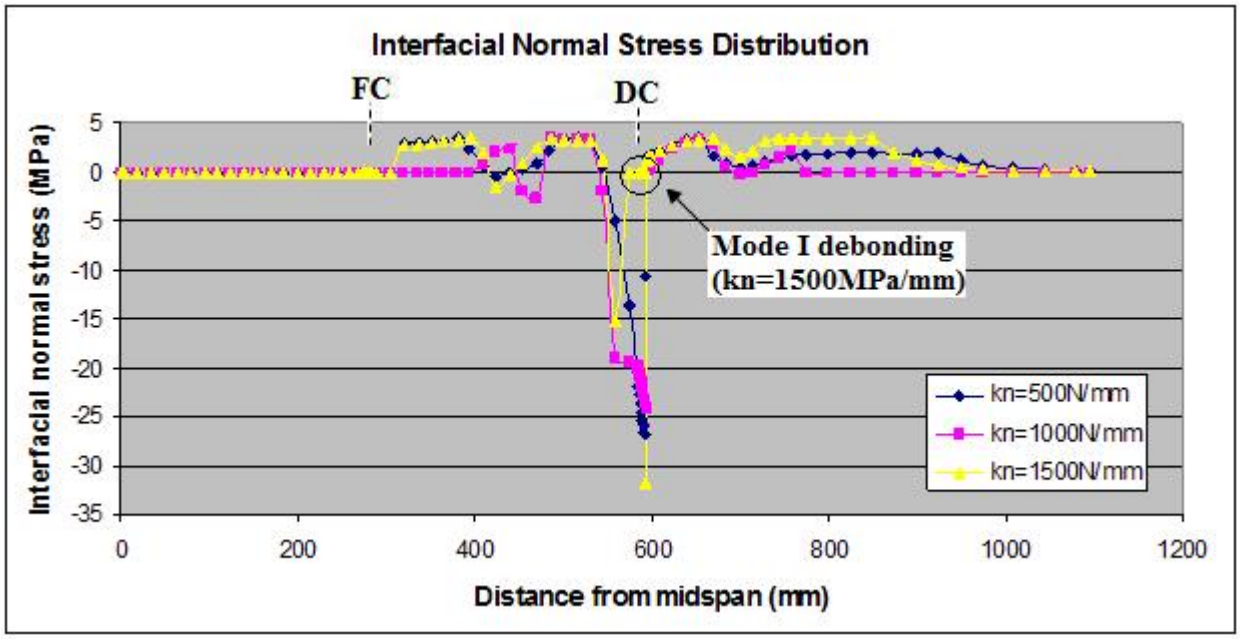

Figure 6.41: Interfacial normal stress distribution (deflection of 6.0mm).

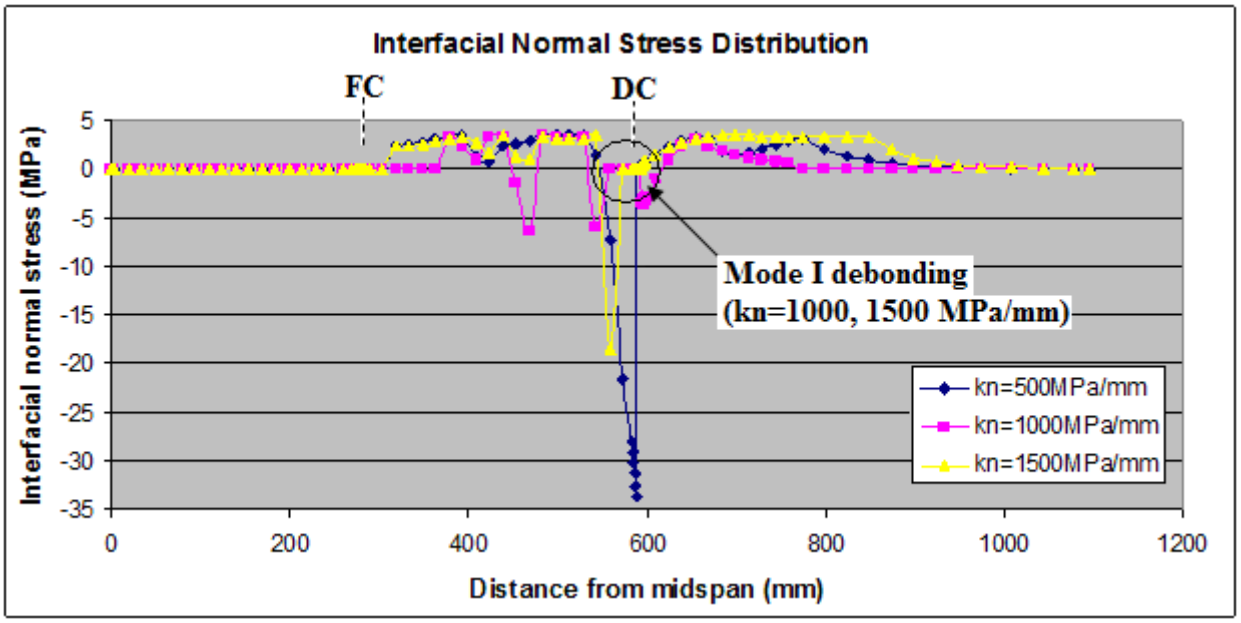

Figure 6.42: Interfacial normal stress distribution (deflection of 8.5mm).

6.4 SUMMARY

In this chapter, a numerical investigation into deboning mechanics caused by flexural and shear macro-cracks in a FRP-RC strengthened beam is studied through the use of a cohesive zone

model. Using the results of Brena et al. (2003) a suitable model was developed using ABAQUS finite element program, and then modified to study the interfacial behaviour. The debonding at the interface is modeled using two kinds of assumed interfacial stress-slip curves, shear and normal, depending on the displacements at the interface. A detailed parametric study was preformed to access how interfacial parameters affect fracturing procedures (such as initiation of interfacial micro- and macro-debonding), crack propagation, shear stress distribution, load-carrying capacity, and strain development in reinforcing materials. By comparing the initiation and propagation of the debonding crack at the interface, it can be concluded that shear cracks induce local bond fracture (mode I debonding) due to high peeling stress concentrations and provide a possible failure path. However, the final debonding failure is mainly governed by mode II fracture behaviour rather than the mode I component due to the fact that mode I debonding propagates in a very slow rate as compared to mode II debonding. Thus, the findings suggest that while mode I debonding mechanics are responsible for initial local bond failures at the shear crack, mode II mechanisms govern the subsequent propagation of debonding. This confirms the commonly accepted assumptions of using mode II mechanisms derived from mode II bond tests in determining debonding loads, as covered in Chapter 2.0.

A parametric study was preformed to study the effect of interfacial properties such as: interfacial shear stiffness, interfacial bond strength, interfacial fracture energy, and interfacial normal stiffness. The numerical simulations indicate interfacial stiffness is seen to affect, stress transfer, initial structural stiffness, ultimate load, initiation of debonding, and strain development in reinforcing materials. Interfacial bond strength and fracture energy are directly related, and thus it was expected that an increase one will have a similar effect on the other. Interfacial bond strength and fracture toughness were both found to be critical parameters influencing both

debonding mechanisms and ultimate failure load. The increase in their magnitudes results in a more effective FRP rehabilitation scheme with greater load capacity, faster load transfer, and activation of slower mechanisms of debond progression. Interfacial normal stress was not found to have a significant effect on the debonding failure and ultimate load, indicating that debonding failure is dominated by mode II fracture behaviour regardless of the type of crack that develops along the interface. This chapter provides insight into the mechanisms related to debonding and failure initiating from commonly found cracks occurring within the rehabilitation length and may be of interest to researchers and design engineers looking to successfully apply FRP products in civil engineering applications.

7 SUMMARY AND RECOMMENDATIONS

7.1 SUMMARY

Before FRP composites can be widely utilized in field applications, engineers must be confident about the performance of RC members externally reinforced with this material. As well, they must be able to predict the behaviour of such members using simple analytical equations for preliminary design, or with finite element analysis for more detailed studies. Although the experimental database for RC members strengthened in flexure with FRP composites is extensive, a review of the state-of-the-art in the applications of FRP to concrete structures concluded that further investigations are imperative in the domain of crack-induced debonding. The failure modes of flexural-strengthened members have been analyzed thoroughly by numerous researchers, but the complexities involved with crack-induced debonding behaviour require more attention. Information on how interfacial properties affect the debonding mechanism and strengthening capacity is not completely understood and the modelling techniques employed in past investigations were done without a sound theoretical basis. Furthermore, a detailed study on how of interfacial properties influence mixed-mode debonding is not readily available. For these reasons, this study embarked on a comprehensive review of the previous studies into FRP strengthened RC beams, which lead to the development of an appropriate finite element model to perform a detailed parametric analysis of the debonding behaviour and failure mechanisms caused by different types of crack distributions and the interfacial behaviour that governs crack propagation.

A nonlinear finite element model was developed and calibrated with the experimental results of Brena et al. (2003). In FRP strengthened RC beams, debonding of the FRP plate can be found to occur under the presence of multiple cracks along the span. In the first portion of the

thesis, an effort was made to clarify the effect of multiple cracks on debonding behaviour and failure mechanisms caused by different types of flexural cracks distributions. Flexural cracks create stress concentrations at the interface of the FRP plate and concrete beam, leading to horizontal displacements that are regarded as mode II fracture behaviour. Crack spacing was found to have a significant effect on structural stiffness, initiation of debonding, load-carrying capacity and efficiency of the reinforcement materials. Structural stiffness was found to decrease with crack spacing, contrary to previously reported numerical investigations. The onset of micro- and macro-debonding, as well as yield load was delayed in models with more closely spaced cracks. This is believed to be attributed to the abrasion effect and increased shear transfer length along the interface as more energy is required for debonding to propagate through the closely spaced cracks. However, subsequent to the initiation of macro-debonding, the more closely spaced cracks were found to quicken the debonding propagation as the debonding crack would join adjacent flexural cracks, resulting in delamination of the FRP system. From the results, it is found that the maximum FRP strain for the beams in the presence of multiple cracks is higher than that for a strengthened beam with a single crack.

Interfacial properties such as interfacial stiffness, bond strength, and fracture energy were investigated through a parametric analysis with a constant flexural crack spacing of 100 mm c/c. The stiffness of the FRP-concrete interface was found to influence the load-carrying capacity, initiation of micro- and macro-debonding, and strain development in reinforcement materials. Higher interfacial stiffness increases the rate of stress transfer at the interface resulting in a higher yield and ultimate load. Local bond strength was only found to affect the structural behaviour prior to the initiation of macro-debonding and have no effect on the ultimate load-carrying capacity. Low bond strength facilitates micro-debonding whereas, high bond strength

may accelerate the initiation of macro-debonding and reduce the ductility of the structure. The results suggest that interfacial fracture energy plays a critical role in the rehabilitation system. While it was not found to have an effect on the initiation of micro-debonding, an increase in fracture energy was found to increase the efficiency of the rehabilitation system by increasing yield and ultimate load.

The final portion of the study focused on how debonding mechanisms and interfacial properties are influenced under mixed-mode debonding. By predefining a flexural crack (representative of mode II fracture) and a critical shear crack (representative of mixed-mode fracture), the initiation and propagation of debonding crack at the interface was investigated through a detailed parametric analysis. A comprehensive parametric study was preformed to study the following interfacial properties under mixed-mode debonding: shear stiffness, bond strength, fracture energy and normal stiffness. A comparison of the initiation and propagation of the debonding crack at the interface indicates that shear cracks induce local bond fracture (mode I debonding) due to high peeling stress concentrations and thus provide a possible failure path. However, the final debonding failure is mainly governed by mode II fracture behaviour rather than the mode I component due to the fact that mode I debonding propagates in a very slow rate as compared to mode II debonding. The findings of the analysis indicate that interfacial shear stiffness affects stress transfer, initial structural stiffness, ultimate load, initiation of debonding, and strain development in reinforcing materials. Interfacial bond strength and fracture energy were found to have similar effects in the analysis. Both were found to be critical parameters influencing both debonding mechanisms and ultimate failure load. The increase in their magnitudes results in a more effective FRP rehabilitation scheme with greater load capacity, faster load transfer, and activation of slower mechanisms of debond progression. Interfacial

normal stress was not found to have a significant effect on the debonding failure and ultimate load, indicating that final debonding failure is dominated by mode II fracture behaviour regardless of the type of crack that develops along the interface. Based on the findings of the numerical results, some suggestions concerning the effect of interfacial properties are made for practical engineering applications in Section 7.3.

7.2 CONTRIBUTIONS

This investigation focused on crack-induced debonding failure in FRP strengthened RC beams. The contributions in this current research to the state of the art can be summarized as follows:

1. A numerical analysis model was developed that is capable of accurately simulating the load-carrying capacity and interfacial behaviour of a FRP strengthened RC beam, in a computationally efficient manner based on sound engineering principles.
2. A detailed explanation into how load-capacity, debonding behaviour, and failure mechanisms are influenced by various flexural crack distributions in FRP strengthened RC beams. Typical trends in the composite behaviour were also pointed out.
3. A complete explanation on how interfacial properties influence the efficiency of the rehabilitation system under mode II or mixed-mode fracture at the interface.

7.3 ENGINEERING IMPLICATIONS

The findings of this study may have practical implications of interest to researchers and engineers looking to improve the efficiency of FRP strengthened RC beams. The results from the numerical study, suggest that debonding failure can be avoided or delayed by ensuring that the interface consists of a material that is high in initial stiffness, bond strength, and fracture energy regardless of the crack distribution or mode of failure initiated by the intermediate crack. Contractors and engineers have been undertaking advanced surface processing and bonding

procedures in an attempt to inhibit debonding within the adhesive resin. While ensuring adequate surface preparation such as removing deteriorated, contaminated or damaged concrete will promote bonding of the repair materials, these procedures have not been entirely successful in restraining interfacial debonding along concrete substrate. One of the first studies on this topic by Asakura et al. (1998) pointed out that despite providing adequate surface preparation techniques to a railway tunnel lining, the FRP strengthening project was unsuccessful because a localized crack in the tunnel lining facilitated interfacial debonding along concrete substrate. The authors reported that improving the interfacial bond condition does not help much since the crack propagating in the concrete depends to a great extent on the original properties of the concrete. The findings of this study triggered researchers to look for new ways of inhibiting interfacial debonding. A review of empirical studies on this topic reveals that the following procedures can be employed to avoid/delay intermediate crack-induced debonding:

- Applying FRP material in U-wrap configurations to limit shear stress concentrations along the interface.
- Increase concrete toughness, not just in the weak concrete cover but also when patching is done to the concrete substrate. This may be done by using high tensile strength mortar/concrete prior to rehabilitation or by incorporating concrete composed of small amounts of short fibres into the concrete. Short fibres such as feather-fibres, wood-fibres, steel-fibres, and man-made polymeric-fibres could be used to significantly increase the concrete toughness, which will consequently increase interfacial properties such as initial stiffness, bond strength and fracture energy. An experimental study performed by Yin and Wu (2003) investigated the effect of mixing short fibres into fresh concrete in an attempt to avoid or delay the propagation of interfacial debonding induced by an

intermediate crack. The findings of the study suggest that increasing the concrete toughness changed the failure mode from intermediate crack-induced debonding to FRP rupture, confirming that the FRP plate was able to be used to its full potential without premature debonding failure.

7.5 FUTURE RESEARCH WORK

In the present thesis research, crack-induced debonding in the FRP strengthened RC beams has been systematically studied. The following recommendations are made for future studies:

- This study focused on the behaviour of the crack distribution, mode of debonding failure and interfacial properties under the effect of increasing monotonic loads. These same areas of study should be performed to under cyclic loading, as it has not yet been addressed in literature. Therefore, an experimental investigation to first study these parameters should be first performed to established fatigue crack growth propagation models and then a finite element model can be calibrated to perform a parametric investigation.
- The finite element analysis performed in this study emphasized the debonding failure and did not consider other possible modes of failures. Hence, future numerical simulation studies should be expanded to include more advanced modes for the concrete substrate and to take into consideration the friction that may take place between the FRP and concrete as debonding progresses.
- More work is required in the area of sequential analyses where repair or strengthening takes place after initial loading. In practice, many cracks will have already formed with some spacing before the application of FRP composites. Previous loading must be accounted, but the accuracy of such considerations for bond elements, such as how these

cracks affect the failure behaviour and bond properties of the structure, must first be established experimentally. Since a quantitative evaluation of these detrimental effects is still unavailable, more empirical studies on this topic are required so that their findings can be applied to numerical analyses.

- A numerical analysis into the debonding mechanisms associated with FRP strengthened RC beams under extreme loading conditions, such as torsion, as yet to be attempted.

REFERENCES

ABAQUS (2007). User's Manual version 6.7. Pawtucket (RI): Hibbit, Karlsson & Sorensen.

ABAQUS (2007). Theory Manual version 6.7. Pawtucket (RI): Hibbit, Karlsson & Sorensen.

ACI 440.2R-02. (2002). Guide for the Design and Construction of Externally Bonded FRP Systems for Strengthening Concrete Structures, *American Concrete Institute,* Michigan, USA.

Alexander, J.G.S., and Cheng, J.J.R. (1996). Field Application and Studies of Using CFRP Sheets to Strengthen Concrete Bridge Girders. *Advanced Composite Materials in Bridged and Structures: Proceedings of the 2nd International Conference on Advanced Composite Materials in Bridges and Structures,* 465-72.

Arduini, M., and Di Leo, A. (1996). Composite Behavior of Partially Plated Beams in the Linear Range. *American Concrete Institute,* 43-53.

Arduini, M., and Nanni, A. (1997). Parametric Study of Beams with Externally Bonded FRP Reinforcement. *ACI Structural Journal,* 94, 5, 493-01.

Arduini, M., Di Tommaso, A., and Nanni, A. (1997). Brittle Failure in FRP Plate and Sheet Bonded Beams. *ACI Structural Journal,* 94, 4, 363-70.

Baky, H.A., Ebead, U.A., and Neale, K.W. (2007). Flexural and interfacial behaviour of FRP-strengthened reinforced concrete beams. *Journal of Composites for Construction,* 11, 6, 629-638.

Barenblatt, G.I. (1962). The mathematical theory of equilibrium cracks in brittle fracture. *Advanced application mechanics,* 7, 55-129.

Brena, S.F., Bramblett, R.M., Wood, S.L., and Kreger, M.E. (2003). Increasing Flexural Capacity of Reinforced Concrete Beams Using Carbon Fiber-Reinforced Polymer Composites. *ACI Structural Journal*, 100, 1 36-46.

Chen, J.F., and Teng, J.G. (2001). Anchorage Strength Models for FRP and Steel Plates Bonded to Concrete. *Journal of Structural Engineering,* 127, 1, 784-91.

Chicoine, T. (1997). Conception et Analyse des Ancrages sur les Poutres Renforcees en Flexion a l'aide des Materiaux Composites. *M.A.Sc thesis,* University of Sherbrooke.

De Rose, D., and Sheikh, S.A. (1997). Rehabilitation of a Concrete Structure Using Fiber Reinforced Plastics. *Research Paper,* University of Toronto, 170 pp.

Dugdale., D.S. (1960). Yielding of steel sheets containing slits. *J. Mech. Phys. Solids,* 8, 100-104.

Ebead., U.A., and Neale, K.W. (2007). Mechanics of fibre-reinforced polymer-concrete interfaces. *Canadian Journal of Civil Engineers*, 34, 367-377.

fib Bulletin 14. (2001). Design and Use of Externally Bonded FRP Reinforcement for RC Structures.

Garden, H.N., and Hollaway, L.C. (1998). An Experimental Study of the Influence of Plate End Anchorage of Carbon Fiber Composite Plates used to Strengthen Reinforced Concrete Beams. *Composite Structures,* 42, 2, 175-88.

Grace, N.F., Sayed, G.A., Soliman, A.K., and Saleh, K.R. (1999). Strengthening Reinforced Concrete Beams Using Fiber Reinforced Polymer (FRP) Laminates. *ACI Structural Journal,* 96, 5, 865-75.

Hein, V.L., and Erdogran, F. (1971). Stress Singularities in a Two-Material Wedge. *International Journal of Fracture Mechanics,* 7, 3, 317-30.

Hillerborg, A. (1985). The theoretical basis of a method to determine the fracture energy of concrete. *Mater. Struct.,* 18, 291-296.

Irwin, G.R. (1957). Analysis of stresses and strains near the end of a crack traversing a plate. *Journal of Applied Mechanics,* 24, 361-364.

JSCE. (2001). Recommendations for the Upgrading of Concrete Structures with Use of Continuous Fiber Sheets. *Concrete Engineering.* Series 41, JSCE, Tokyo, Japan.

Janssen, M., Zuidema, J., and Wanhill, R.J.K (2006). Fracture Mechanics. The Netherlands: VSSD.

Kishi, N., Zhang, G., and Mikami, H. (2005). Numerical Cracking and Debonding Analysis of RC Beams Reinforced with FRP Sheets. *Journal of Composites for Construction,* 9, 6, 507-514.

Leung, C.K.Y. (2001). Delamination Failure in Concrete Beams Retrofitted with a Bonded Plate. *Journal of Materials in Civil Engineering,* 13, 2, 106-13.

Liu, Z., and Zhu, B. (1994). Analytical Solutions for Reinforced Concrete Beams Strengthened by Externally Bonded Steel Plates. *Journal of Tongji University,* 22, 1, 21-26.

Lu, X.Z., Ye, L.P., Teng, J.G., and Jiang, J.J. (2005). Meso-Scale Finite Element Model for FRP Sheets/Plates to Concrete. *Engineering Structures, 27, 564-75.*

M'Bazaa, I. (1995). Reinforcement en Flexion des Poutres en Beton Arme a l'aide des Lamelles en Materiaux Composites: Optimisation de la Longueur des Lamelles. *M.A.Sc thesis,* University of Sherbrooke.

Maalej, M., and Bian, Y. (2001). Interfacial Shear Stress Concentration in FRP-Strengthened Beams. *Composite Structures,* 54, 417-26.

MacGregor, J.G., and Bartlett, F.M. (2000). *Reinforced concrete: mechanics and design.* Toronto: Prentice Hall.

Malek, A.M., Saadatmanesh, H., and Ehsani, M.R. (1998). Prediction of Failure Load of R/C Beams Strengthened with FRP Plate Due to Stress Concentration at the Plate End. *ACI Structural Journal,* 95, 1, 142-52.

Miannay, D.P. (1998). *Fracture Mechanics.* New York: Springer-Verlag.

Meirer, U., and Winistorfer, A. (1995). Retrofitting of Structures Through External Bonding of CFRP Sheets. *Non-Metallic Reinforcement for Concrete Structures,* 465-472.

Morita, S., Muguruma, H., Tomita, K. (1967). Fundamental Study on Bond Between Steel and Concrete. *Transaction of the Architecture Institute of Japan,* 131, 1, 1-8.

Mufti, A.A., Erki, M.A., and Jaeger, L.G. (1991). Advanced Composite Materials with Application to Bridges. *Canadian Society of Civil Engineers,* 297 pp.

Mukhopadhyaka, P., and Swamy, N. (2001). Interface Shear Stress: A New Design Criterion for Plate Debonding. *Journal of Composites for Construction,* 5, 1, 35-43.

Nanni, A. (1995). Concrete Repair with Externally Bonded FRP Reinforcement. *Concrete International, ACI,* 17, 6, 22-26.

Neubauer, U., and Rostasy, F.S. (1999). Bond Failure of Concrete Fiber Reinforced Polymers Plate at Inclined Cracks – Experimental and Fracture Mechanics Model. *Proc., 4th International Symposium on Non-Metallic Reinforcement for Concrete Structures (FRPRCS4),* 369-392.

Ngo, D., and Scordelis, A.C. (1967). Finite element analysis of reinforced concrete beams. *ACI Journal, Proceedings*, 64, 3, 152-163.

Ngujen, D.M., Chan, T.K., and Cheong, H.K. (2001). Brittle Failure and Bond Development Length of CFRP-Concrete Beams. *Journal of Composites for Construction,* 5, 1, 12-17.

Nitereka, C., and Neale, K.W. (1999). Analysis of Reinforced Concrete Beams Strengthened in Flexure with Composite Laminates. *Canadian Journal of Civil Engineering,* 646-54.

Niu, H., and Wu, Z. (2005). Numerical Analysis of Debonding Mechanisms in FRP-Strengthened RC Beams. *Computer-Aided Civil and Infrastructure Eningeering,* 20, 354-68.

Niu, H., Karbhari, V.M., and Zhishen, W. (2006). Diagonal Macro-Crack Induced Debonding Mechanisms in FRP Rehabilitated Concrete. *Composites Part B: Engineering,* 37, 627-41.

Oehlers, D.J., and Seracino, R. (2004). Design of FRP and Steel Plated RC Structures: Retrofitting Beams and Slabs for Strength, Stiffness, and Ductility. Oxford*: Elsevier Science.*

Rabinovich, O., and Frostig, Y. (2000). Closed-Form High-Order Analysis of RC Beams Strengthened with FRP Strips. *Journal of Composites for Construction,* 4, 2, 65-74.

Rahimi, R., and Hutchinson, A. (2001). Concrete beams strengthened with externally bonded FRP plates. ASCE Journal of Composite Construction, 5, 1, 44-56.

Roberts, T.M. (1989). Approximate Analysis of Shear and Normal Stress Concentrations in the Adhesive Layer of Plated RC Beams. *Structural Engineering,* 67, 12, 229-33.

Roberts, T.M., and Haji-Kazemi, H. (1989). Theoretical Study of the Behaviour of Reinforced Concrete Beams Strengthened by Externally Bonded Steel Plates. *Proceedings of the Institution of Civil Engineers,* 87, 2, 39-55.

Ross, A., Jerome, D.M., Tedesco, J.W., and Hughes, M.L. (1999). Strengthening of Reinforced Concrete Beams with Externally Bonded Composite Laminates. *ACI Structural Journal,* 96, 2, 212-21.

Taljsten, B. (1997). Strengthening of Beams by Plate Bonding. *Journal of Materials in Civil Engineering,* 9, 4, 206-12.

Tan, Z. (2002). Experimental Research for RC Beam Strengthened with GFRP. *Master Thesis,* Tsinghua University.

Teng, J.G., Zhang, J.W., and Smith, S.T. (2002). Interfacial Stresses in Reinforced Concrete Beams Bonded with a Soffit Plate: A Finite Element Study. *Construction and Building Materials,* 16, 1-14.

Triantafillou, T., and Plevris, N (1991). Post-Strengthening of Reinforced Concrete Beams with Epoxy-Bonded Fiber Composite Materials. *Advanced Composites Materials in Civil Engineering Structures,* Proceedings of Specialty Conference, ASCE Materials Engineering Division, Nevada, USA, 245-256.

Tripi, J., M., Bakis, C.E., Boothby, T.E., and Nanni, A. Deformation in Concrete with External CFRP Sheet Reinforcement. *Journal of Composites for Construction,* 4, 2, 153-60.

Sebastian, W.M. (2001). Significance of Midspan Debonding Failure in FRP-Plated Concrete Beams. *Journal of Structural Engineering,* 127, 7, 792-98.

Shen, H.S., Teng, J.G., and Yang, J. (2001). Interfacial Stresses in Beams and Slabs Bonded with Thin Plate. *Journal of Engineering Mechanics,* 127, 4, 399-06.

Smith, S.T., and Teng, J.G. (2001). Interfacial Stresses in Plated Beams. *Engineering Structures,* 23, 857-71.

Smith, S.T., and Teng, J.G. (2002). FRP-Strengthened RC Beams I: Review of Debonding Strength Models. *Engineering Structures,* 24, 4, 385-95.

Ueda, T., Sato, Y., and Asano, Y. (1999). Experimental Study of Bond Strength of Continuous Carbon Fiber Sheet. *Proceedings of 4th International Sym. on Fiber Reinforced Polymer Reinforcement for Reinforced Concrete Structure,* 407-16.

Vilnay, O. (1988). The Analysis of Reinforced Concrete Beams Strengthened by Epoxy Bonded Steel Plates. *International Journal of Cement Composites Lightweight Concrete,* 10, 2, 73-78.

Vecchio, F.J., and Bucci, F. (1999). Analysis of Repaired Reinforced Concrete Structures. *Journal of Structural Engineering,* 125, 6, 644-52.

Wang (2006). Cohesive zone model of intermediate crack-induced debonding of FRP-plated concrete beam. *International Journal of Solids and Structures,* 43, 6630-6648.

Wong, R. (2001). Towards Modeling of Reinforced Concrete Members with Externally-Bonded Fiber Reinforced Polymers (FRP) Composites. *M.A.Sc Thesis,* University of Toronto, Canada, 2001, 298 p.

Wong, R., and Vecchio, F.J. (2003). Towards Modeling of Reinforced Concrete Members with Externally Bonded Fiber-Reinforced Polymer Composites. *ACI Structural Journal,* 100, 1, 47-55.

Wu, Z.S., Yaun, H., Yoshizawa, H., and Kanakubo, T. (2001). Experimental/Analytical Study on Interfactial Fracture Energy and Fracture Propagation Along FRP-Concrete Interface. *ACI International,* 201, 8, 133-52.

Yang, Z.J., Chen, J.F., and Proverbs, D. (2003). Finite Element Modeling of Concrete Cover Separation Failure in FRP Plated RC Beams. *Construction and Building Materials,* 17, 3-13.

Yao, J., Teng, J.G., and Lam, L. (2004). Experimental Study on Intermediate Crack Debonding in FRP-Strengthened RC Flexural Members. *Advances in Structural Engineering*, 11, 4, 365-395.

Yoshizawa, H., Myojo, T., Okoshi, M., Mizukoshi, M., and Kliger, H. Effect of Sheet Bonding Condition on Concrete Members Having Externally Bonded Carbon Fiber Sheet.

Materials for the New Millennium:Proceedings of the Fourth Materials Engineering Conference, 2, 1608-16.

Yuan, H., Teng, J.G., Seracino, R., and Wu, Z.S. (2004). Full-range behaviour of FRP-to-concrete bonded joints. *Engineering Structures,* 36, 99-113.

Yuan, H., Teng, J.G., Seracino, R., Wu, Z.S., and Yao, J. (2004). Full Range Behavior of FRP-to-Concrete Bonded Joints: A Closed-Form Analytical Solution. *Engineering Structures,* 26, 5, 553-64.

Zarnic, R., Gostic, S., Bosiljkov, V., and Bokan-Bosiljkov, V. (1999). Improvement of Bending Load-Bearing Capacity by Externally Bonded Plates. *Specialist Techniques and Materials for Concrete Construction, Proceedings of the International Conference on Creating with Concrete,* 433-42.

APPENDIX

CHAPTER 4.0

Investigation of State of Stress

The solution for a single edge cracked body under pure bending specimen was used to calculate the stress intensity factor (K):

$$K_I = \frac{6M}{tW^2}\sqrt{\pi a}\cdot F_I(\alpha)$$

where: $F_I(\alpha) = 1.122 - 1.4\alpha + 7.33\alpha^2 - 13.08\alpha^3 + 14\alpha^4$

$$\alpha = \frac{a}{W}$$

a – notch crack depth

W – depth of specimen

t – thickness of specimen

M – applied bending moment

Solution:

a = 6.35 mm
t = 200 mm
W = 350 mm
M = 75.725 kN·m

$$\alpha = \frac{a}{W} = \frac{6.35}{350} = 0.01814$$

$$F_I(\alpha) = 1.122 - 1.4\alpha + 7.33\alpha^2 - 13.08\alpha^3 + 14\alpha^4 = 1.0989$$

$$K_I = \frac{6*75.725(10^6)}{200*350^2}\sqrt{\pi*0.00635}*1.0989 = 2.878MPa\sqrt{m}$$

$$2r_y = \frac{1}{\pi}\left(\frac{K_I}{\sigma_{ys}}\right)^2 = \frac{1}{\pi}\left(\frac{2.878}{23}\right)^2 = 4.98mm < \frac{200}{10} = 20mm \quad \therefore \text{plane strain}$$

∴ Plane stain conditions prevail as per Janssen et al. (2006) empirical rules.

Mesh Sensitivity Analysis: 3D Model

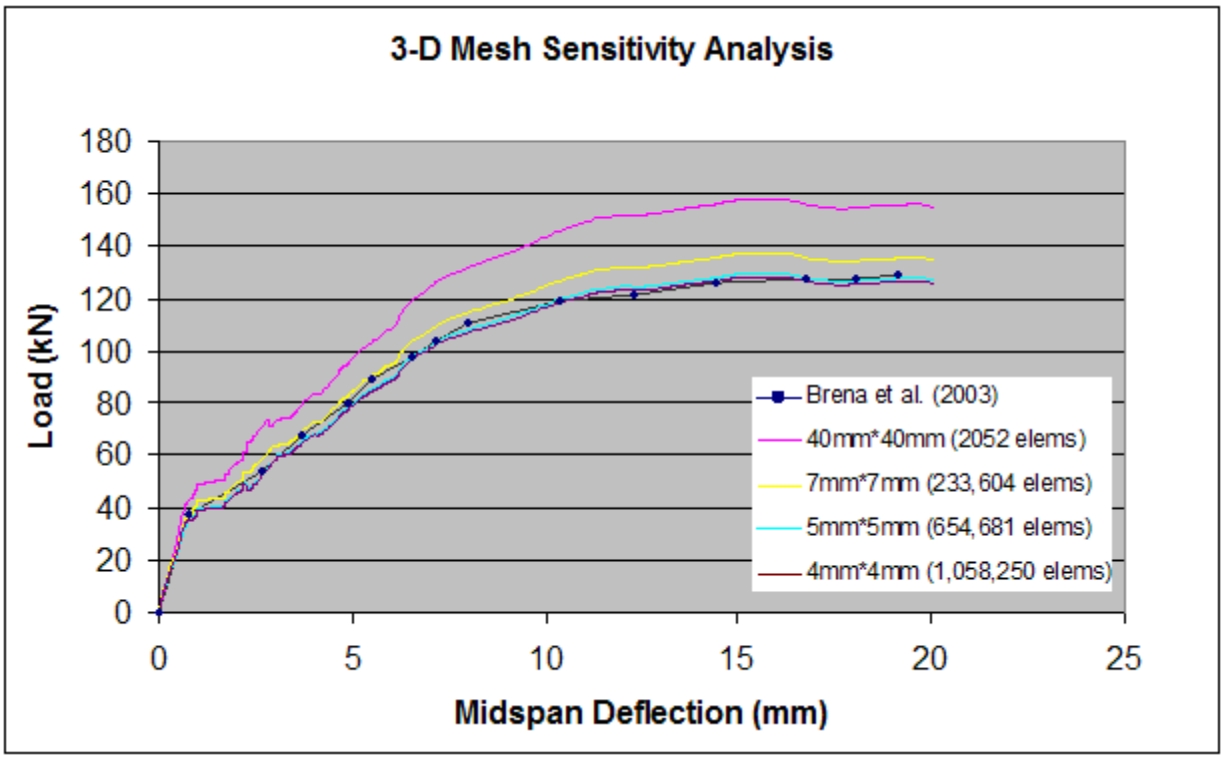

Figure A4.1: Mesh sensitivity analysis of 3-D model.

Mesh Sensitivity Analysis: 2D Model

Mesh sensitivity was investigated based on the load-deflection response of the FRP-RC beam using different levels of mesh refinement as shown in Figure 4.2. It can be seen that the structural performance is overestimated with the use of the coarse mesh, while refining the mesh leads to convergence of the response. It is clear that the fine mesh of size 4mm by 4mm gives acceptable results while still enabling high computational efficiency. The results shown in Figure 4.4 with the fine mesh compare very well with the experimental results reported by Brena et al. (2003), and thus were deemed acceptable to proceed with the in the calibration model.

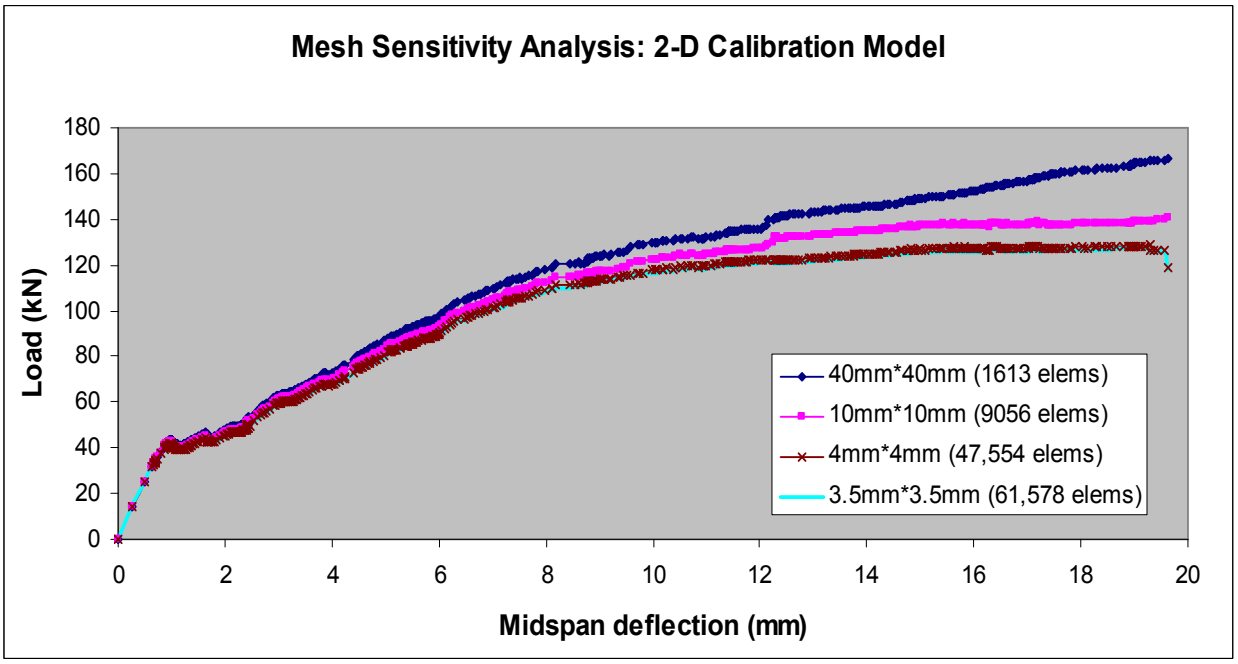

Figure A4.2: Mesh sensitivity analysis of 2-D model.

Material Validation

To ensure that the compressive behavior of the model is simulated properly, a material calibration model was created to test the compressive strength of a concrete cylinder in accordance with CSA Standard A23.2-9C *Compressive Strength of Cylindrical Concrete Specimens*. The standard acceptance test for measuring the strength of concrete involves testing cylinders 150mm in diameter by 300mm high. The model consisted of reduced-integration linear elements to be consistent with the composite model. Mesh sensitivity was investigated based on the stress-strain response of the concrete cylinder using three different levels of mesh refinement as shown in Figure A4.3. The results shown in Figure 4.3 indicate that mesh sensitivity was a minor issue.

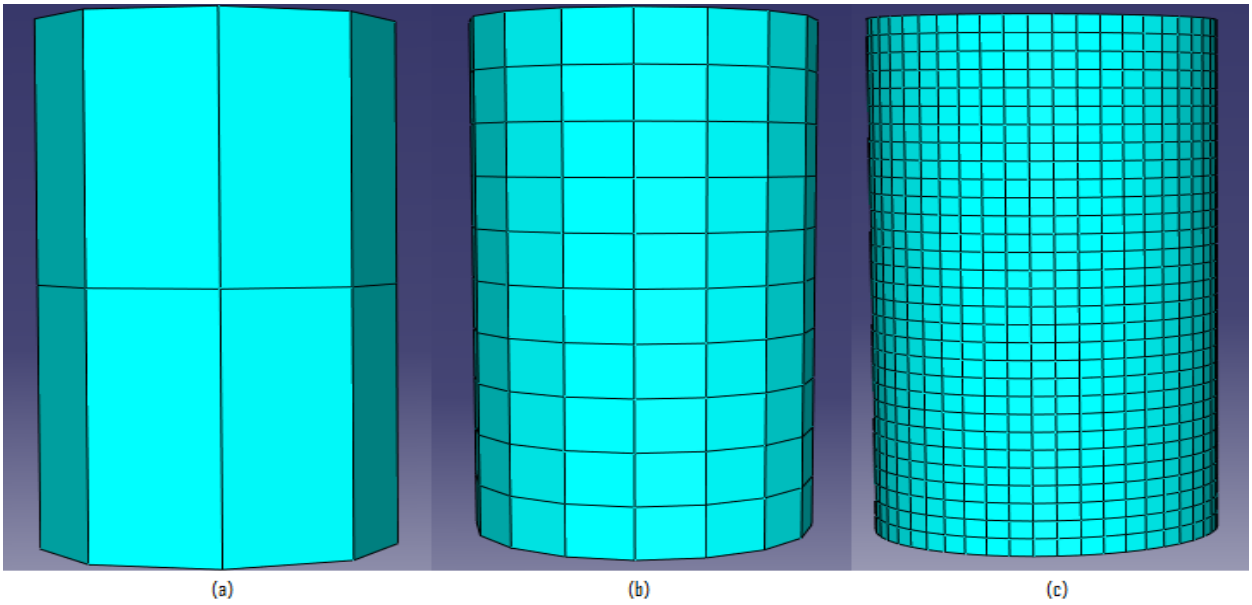

Figure A4.3: Mesh refinements: (a) coarse mesh with 8 elements, (b) medium mesh with 300 elements, (c) very fine mesh with 7320 elements.

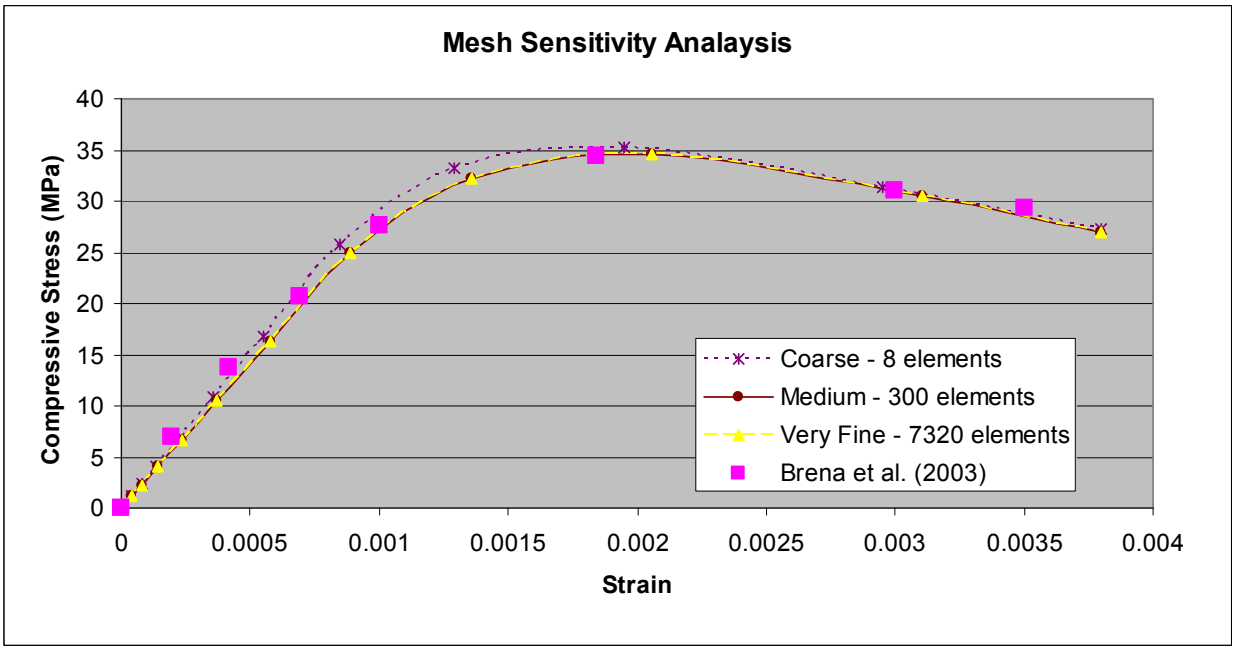

Figure A4.4: Mesh sensitivity analysis for concrete compressive behaviour.

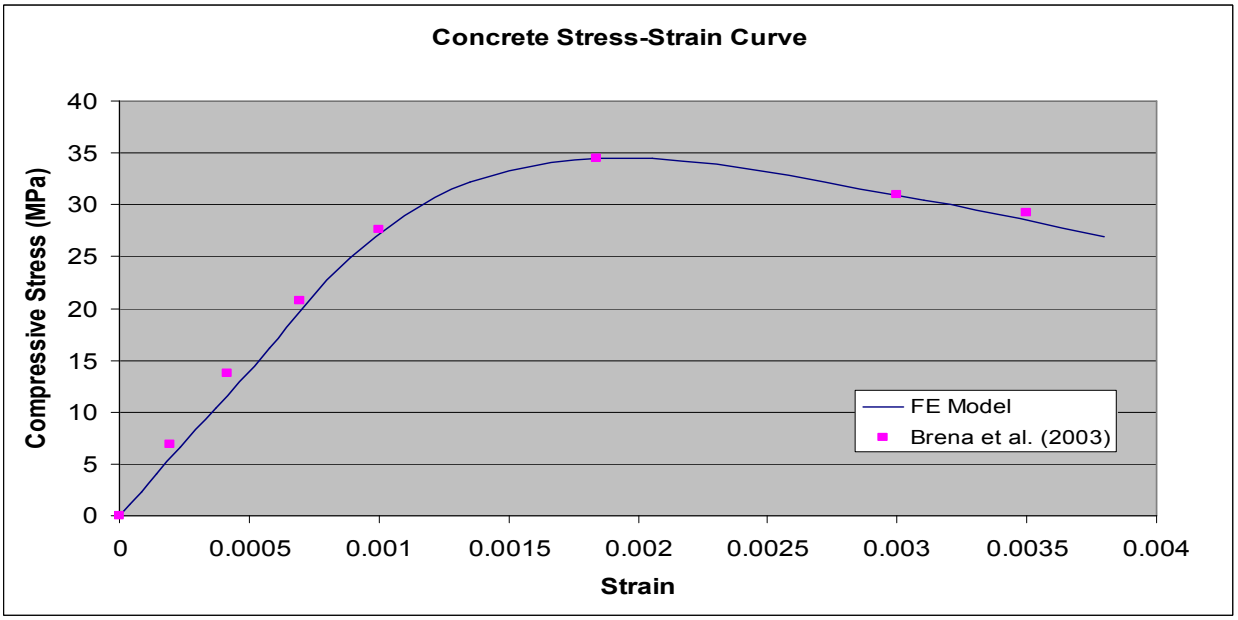

Figure A4.5: Concrete compressive stress-strain material model validation.

It is important to define the mechanical behaviour of the reinforcing steel properly to ensure that the concrete structure does not fail during the analysis due to a lack of reinforcement in key regions and to limit mesh sensitivity that occurs with tensile cracking of the concrete during loading. Thus, a finite element material calibration analysis was preformed to determine the yield stress and strength of the reinforcing bars used to fabricate the specimen as reported by Brena et al (2003). Stress-strain curves were determined by subjecting the reinforcing steel to tension tests in accordance with CSA G30.18. The results of the analysis compare well with the experimental results of Brena et al (2001) as shown in Figure A4.6.

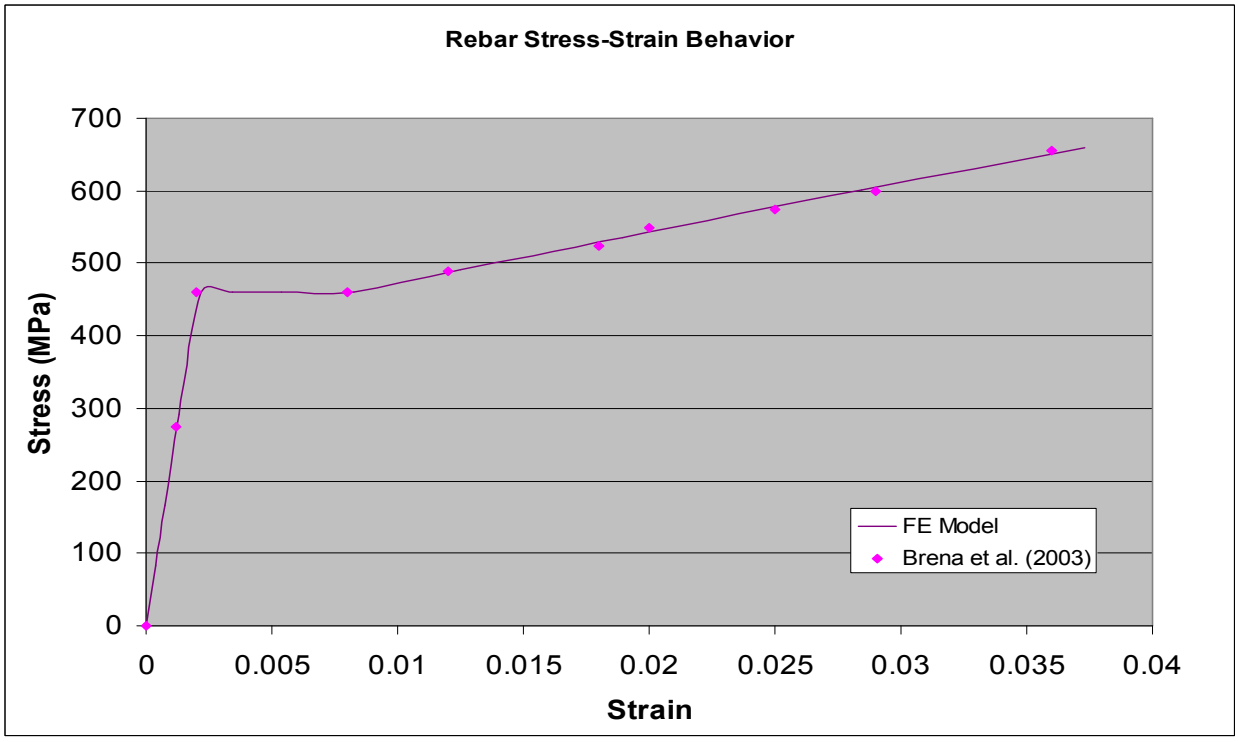

Figure A4.6 Reinforcing steel material validation.

Effect of Stirrup Removal

Strains at maximum load for model with and without stirrups are shown below.

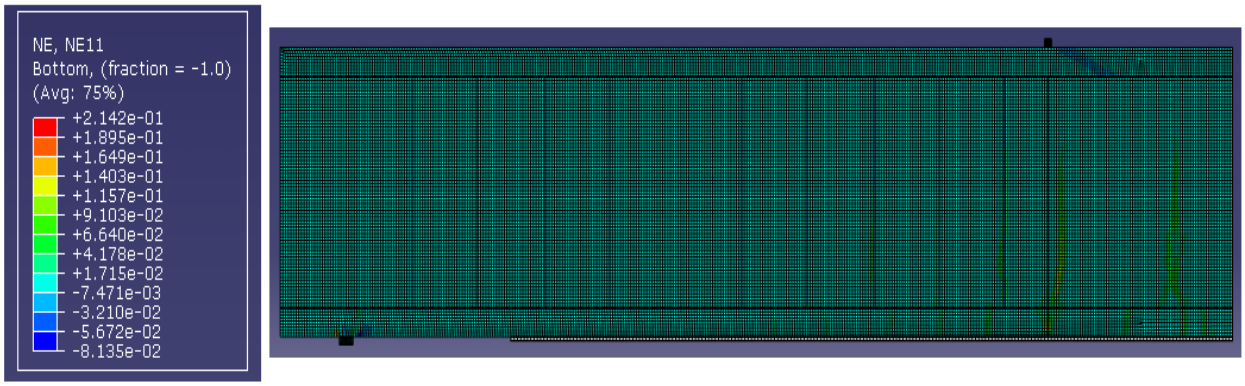

Figure A4.7: Longitudinal strains at maximum load in model with stirrups.

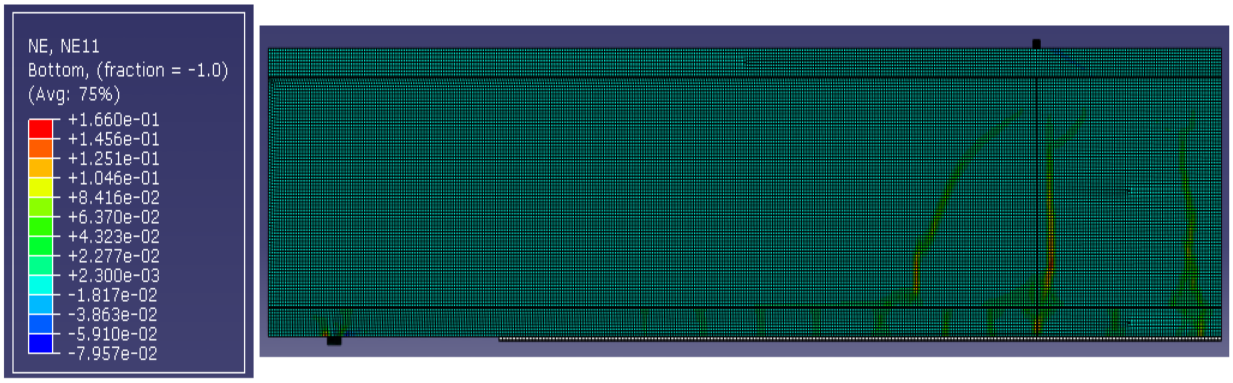

Figure A4.8: Longitudinal strains at maximum load in model without stirrups.

2.0 CHAPTER 5.0

Mesh Sensitivity Analysis

Snapshots of coarse, medium, and all fine meshes employed in the mesh sensitivity analysis are shown below.

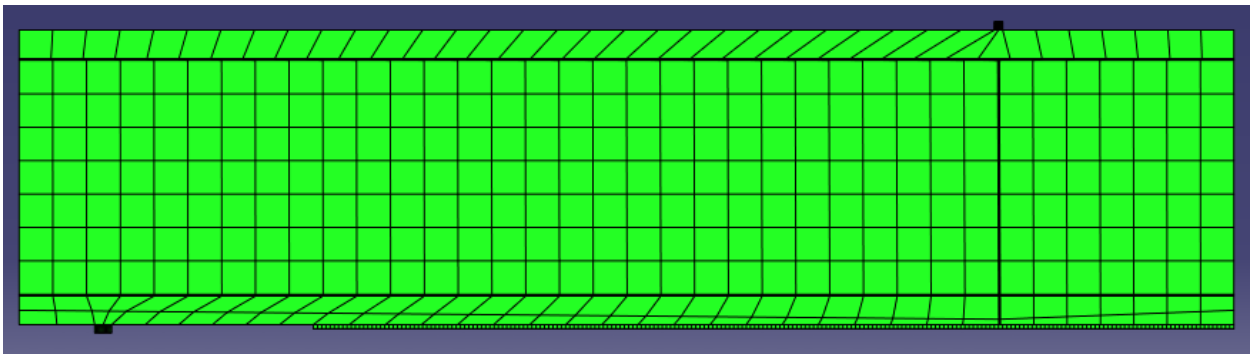

Figure A5.1: Coarse mesh of element size 40mm*40mm (1120 elements).

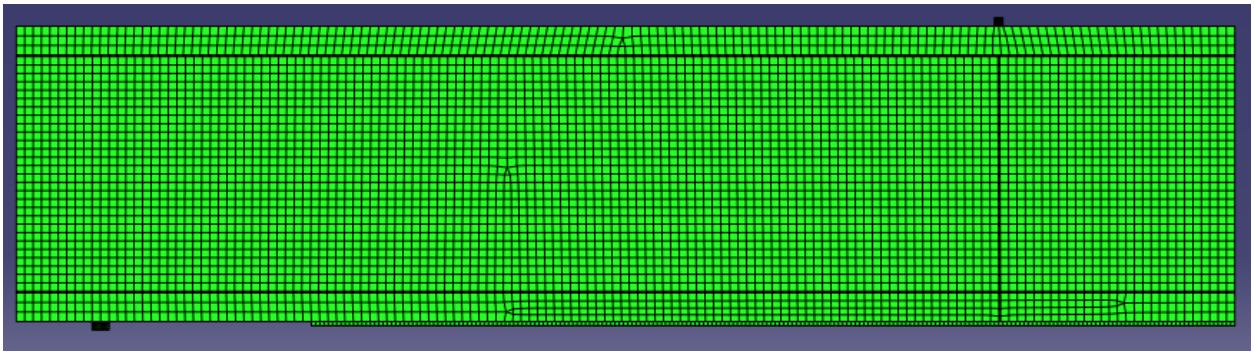

Figure A5.2: Medium mesh of element size 10mm*10mm (6231 elements).

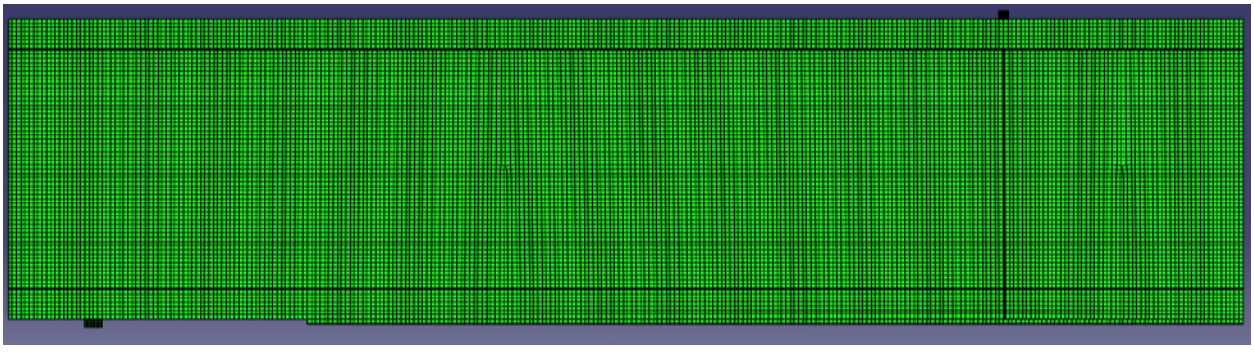

Figure A5.3: Fine mesh of element size 5mm*5mm (22,050 elements).

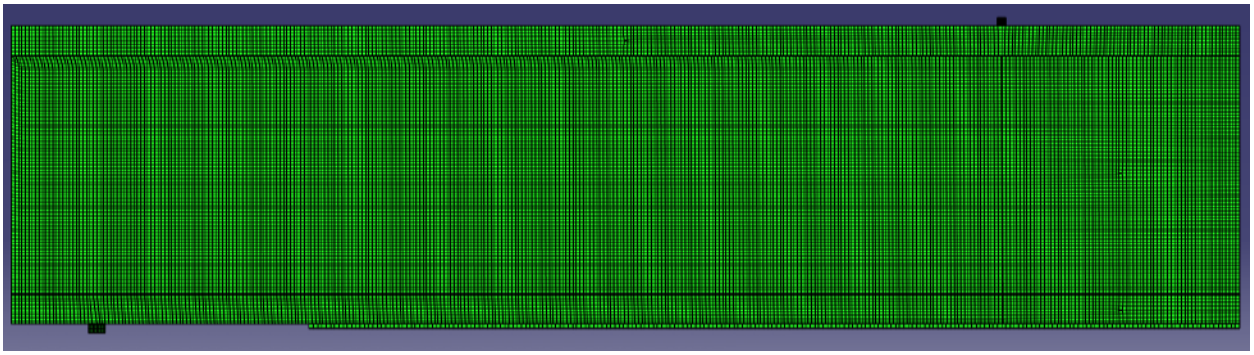

Figure A5.4: Fine mesh of element size 4mm*4mm (33,632 elements).

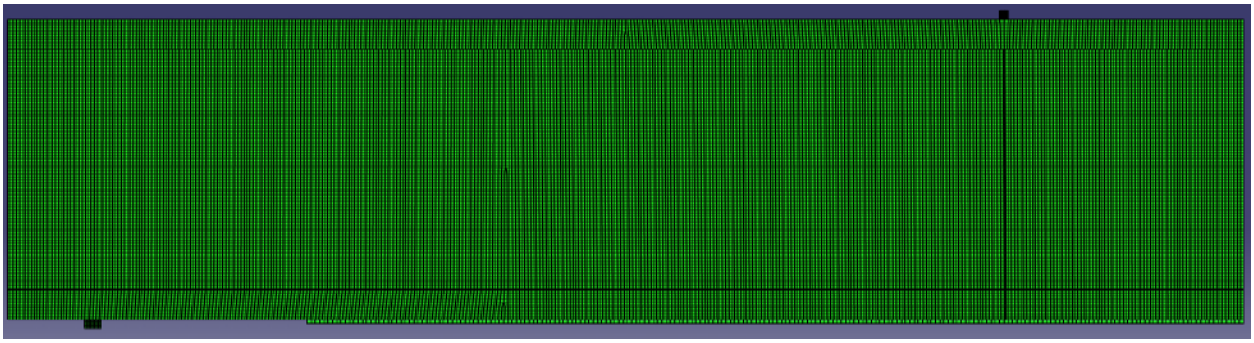

Figure A5.5: Refined mesh of element size 3.5mm*3.5mm (43,181 elements).

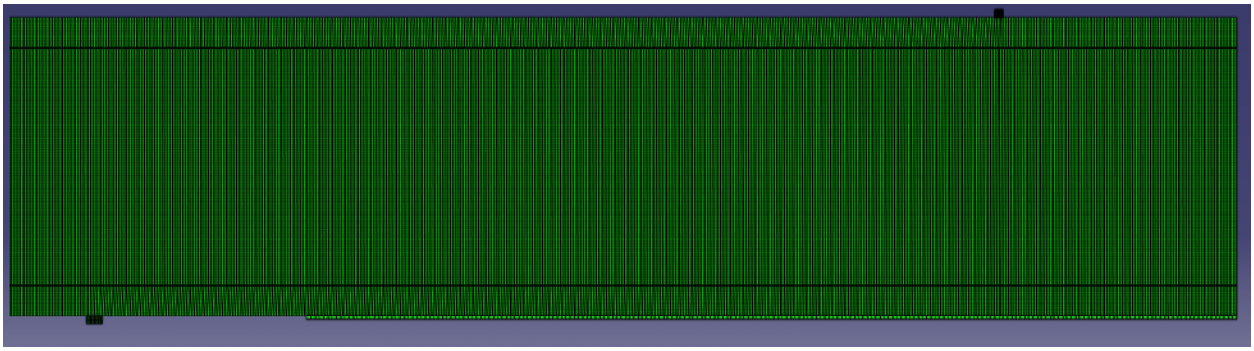

Figure A5.6: Highly refined mesh of element size 3mm*3mm (58,065 elements).

Mesh Analysis for crack spacing of 50mm

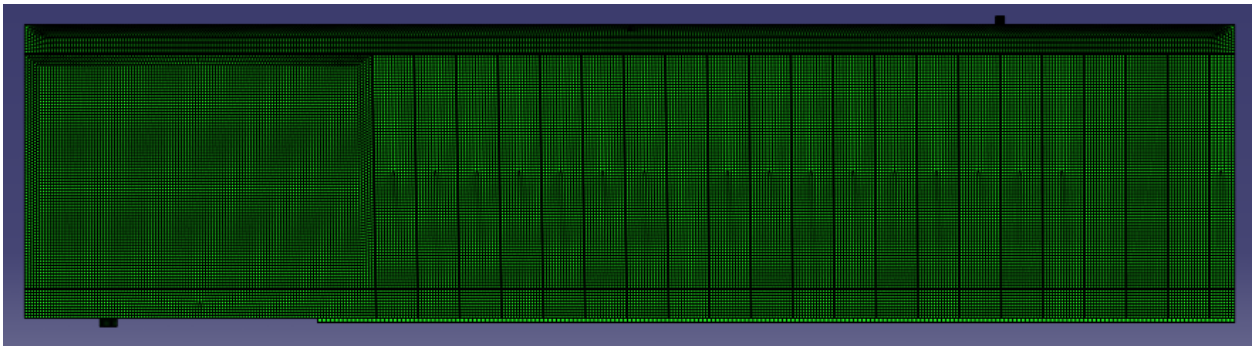

Figure A5.7: Refined mesh of element size 3.5mm*3.5mm.

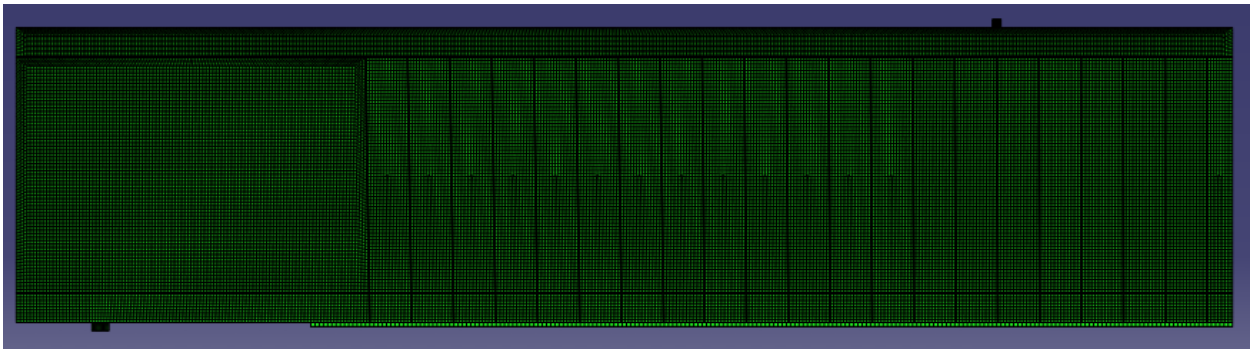

Figure A5.8: Highly refined mesh of element size 3mm*3mm.

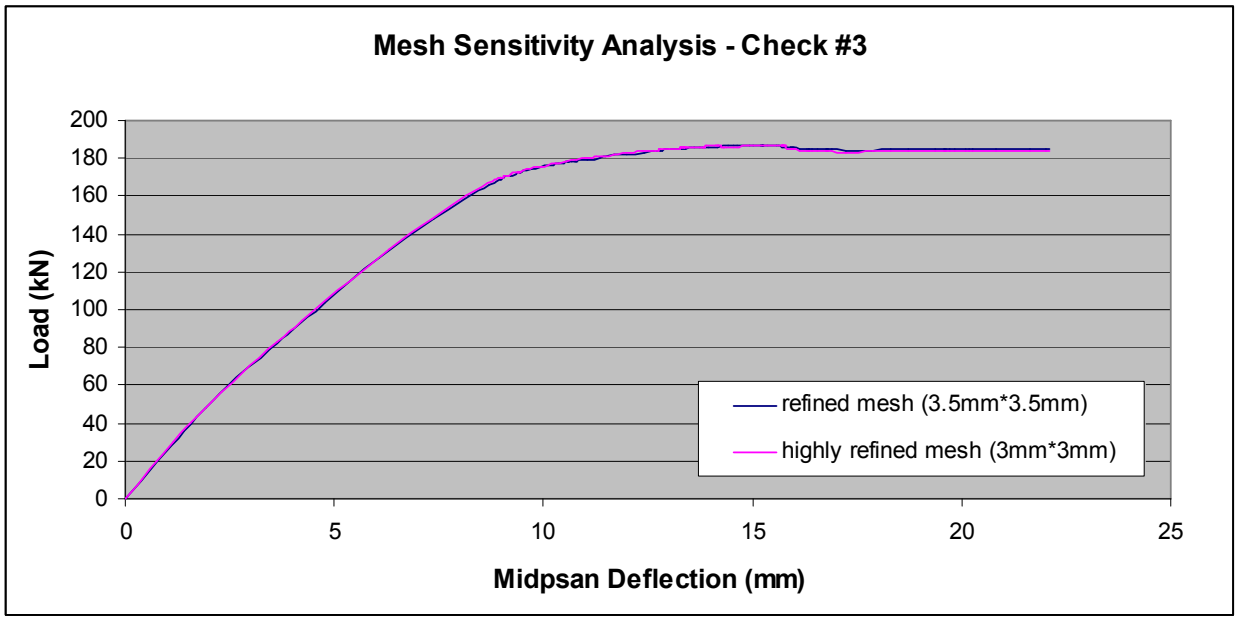

Figure A5.9: Effect of mesh refinement in terms of load versus deflection (x_c=50mm).

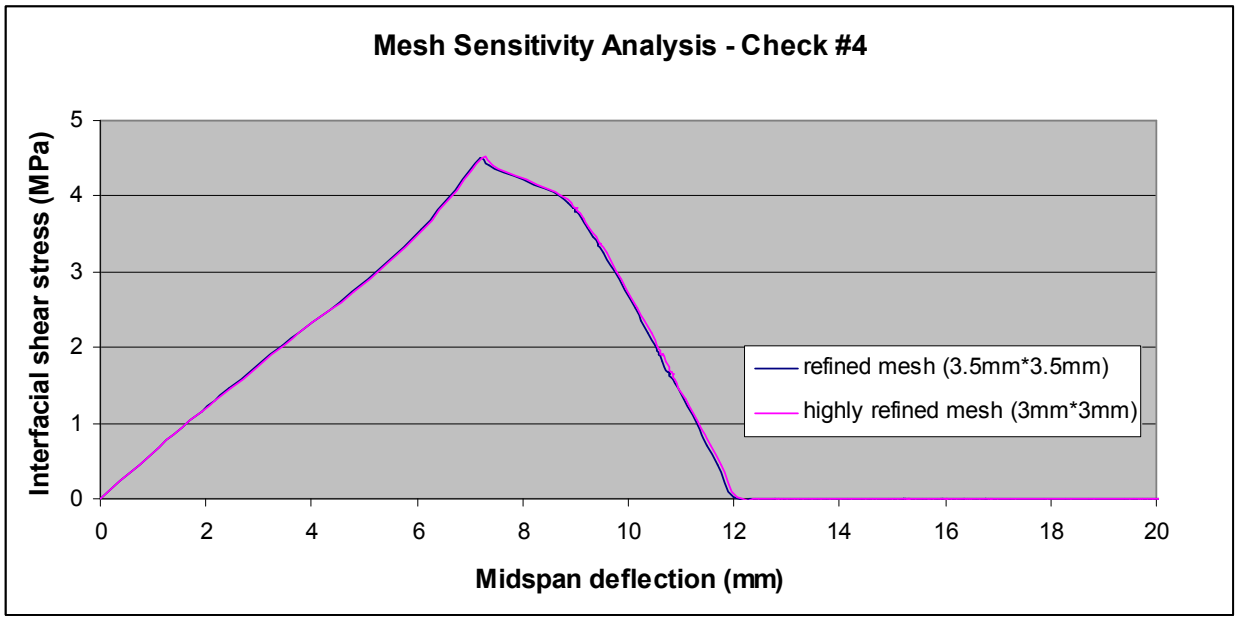

Figure A5.10: Effect of mesh refinement for fine meshes in terms of interfacial shear stress versus deflection (x_c=50mm).

Effect of Crack Spacing

Snapshots of the six crack spacing model setups are shown below.

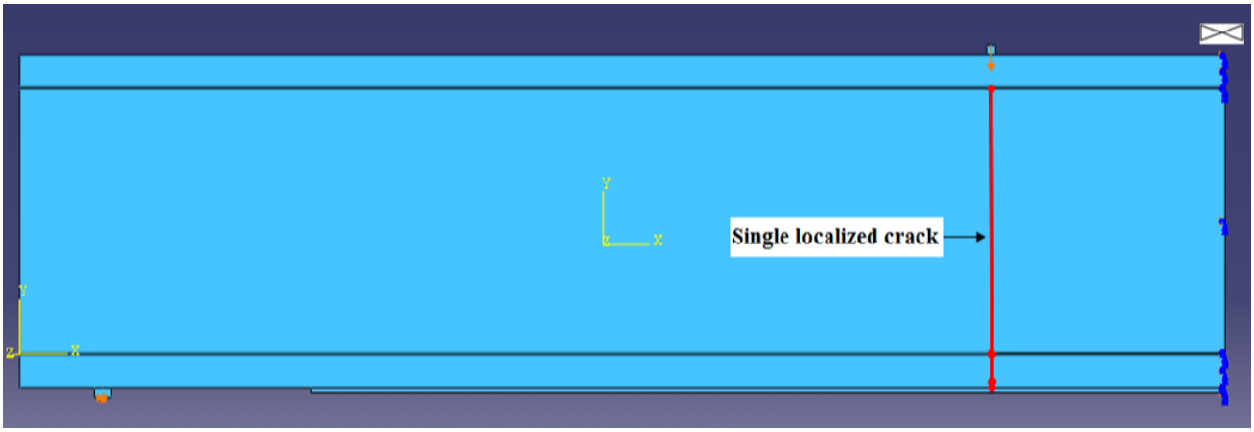

Figure A5.11: Snapshot of single localized flexural crack.

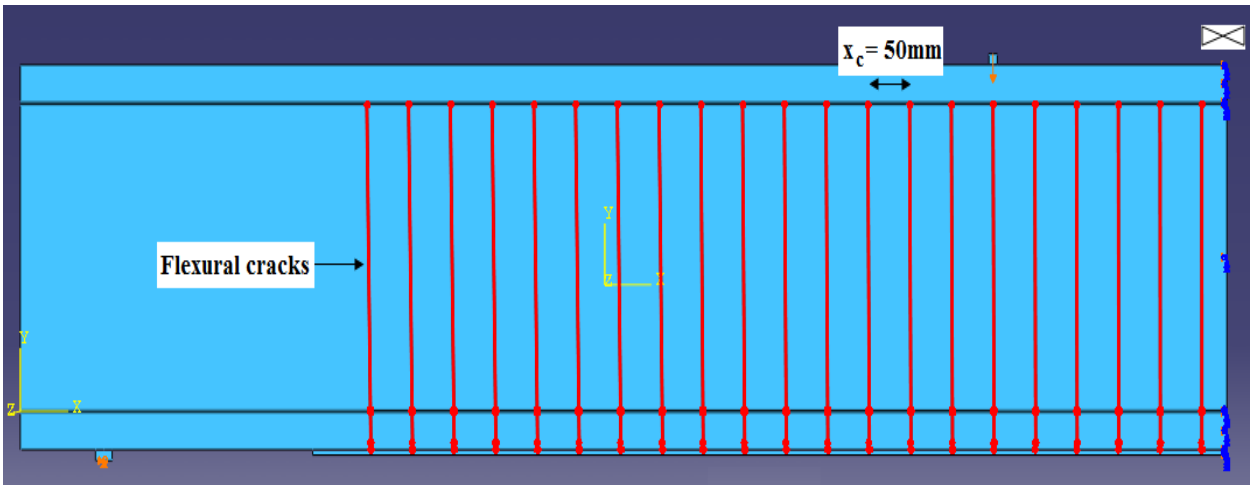

Figure A5.12: Snapshot of x_c = 50mm.

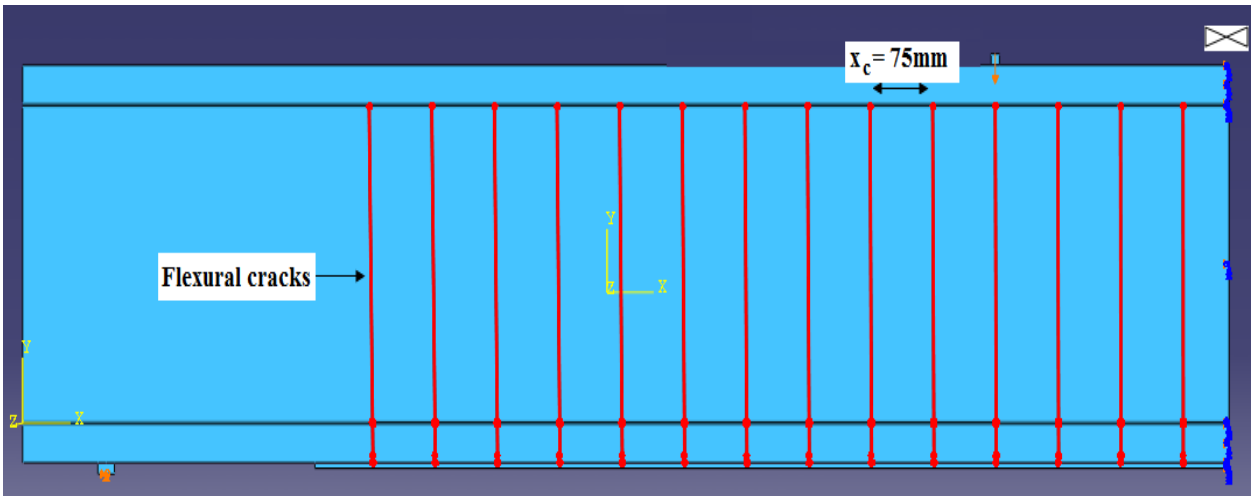

Figure A5.13: Snapshot of x_c = 75mm.

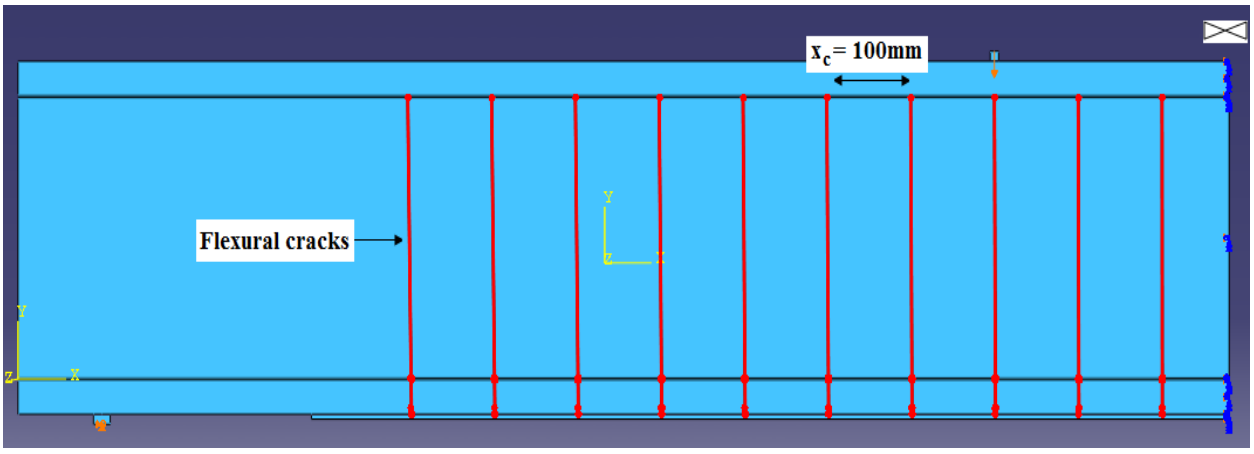

Figure A5.14: Snapshot of x_c = 100mm.

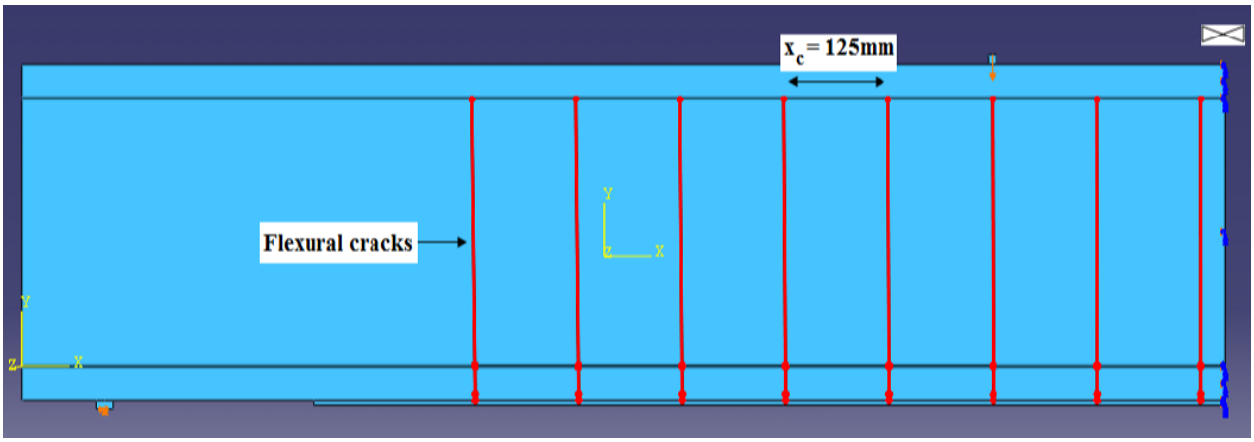

Figure A5.15: Snapshot of x_c = 125mm.

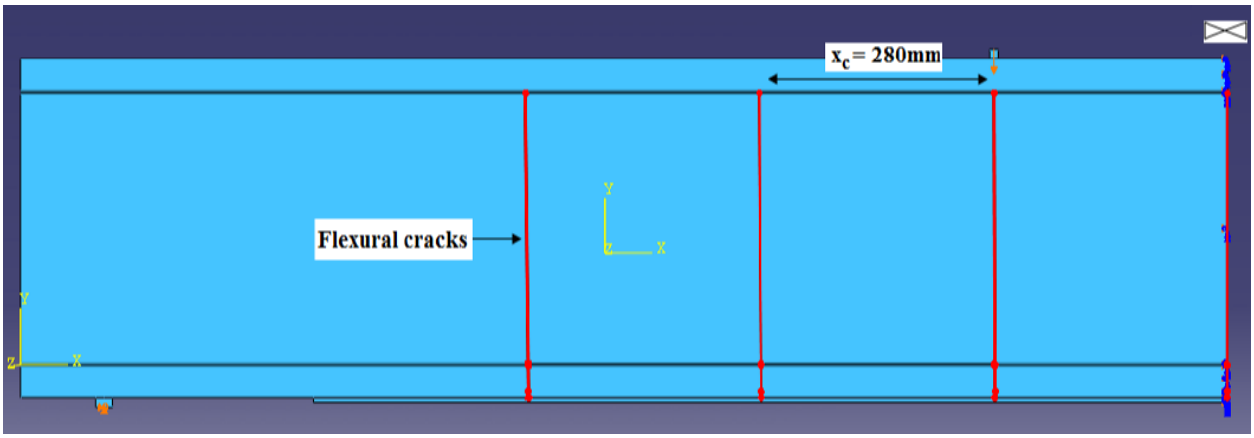

Figure A5.16: Snapshot of x_c = 280mm.

3.0 CHAPTER 6

Interfacial Shear Stiffness, k_s^{int} **=500MPa/mm**

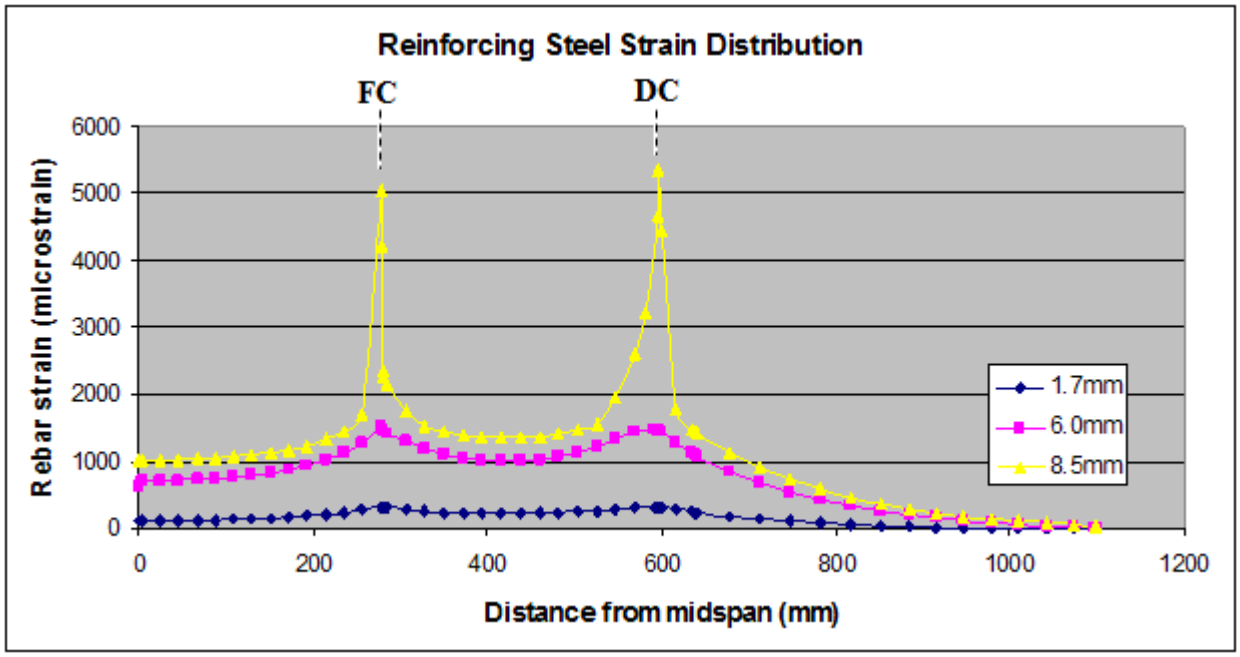

Figure A6.1: Development of steel reinforcement strain for various deflection levels.

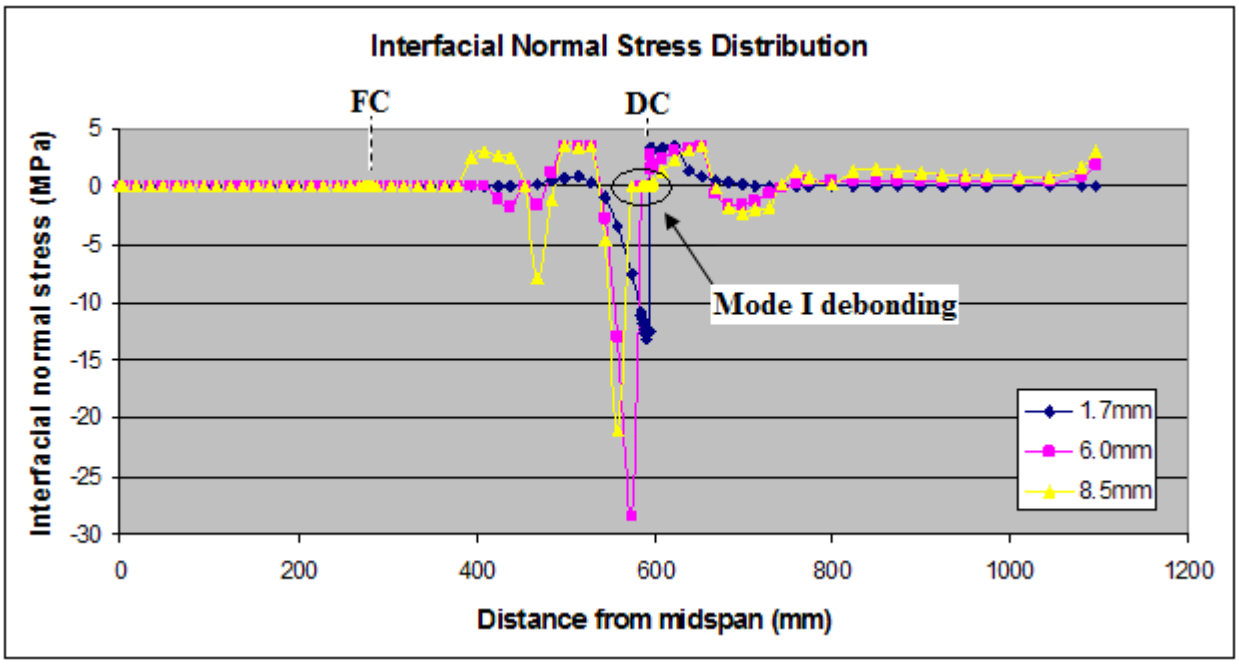

Figure A6.2: Development of interfacial normal stresses for various deflection levels.

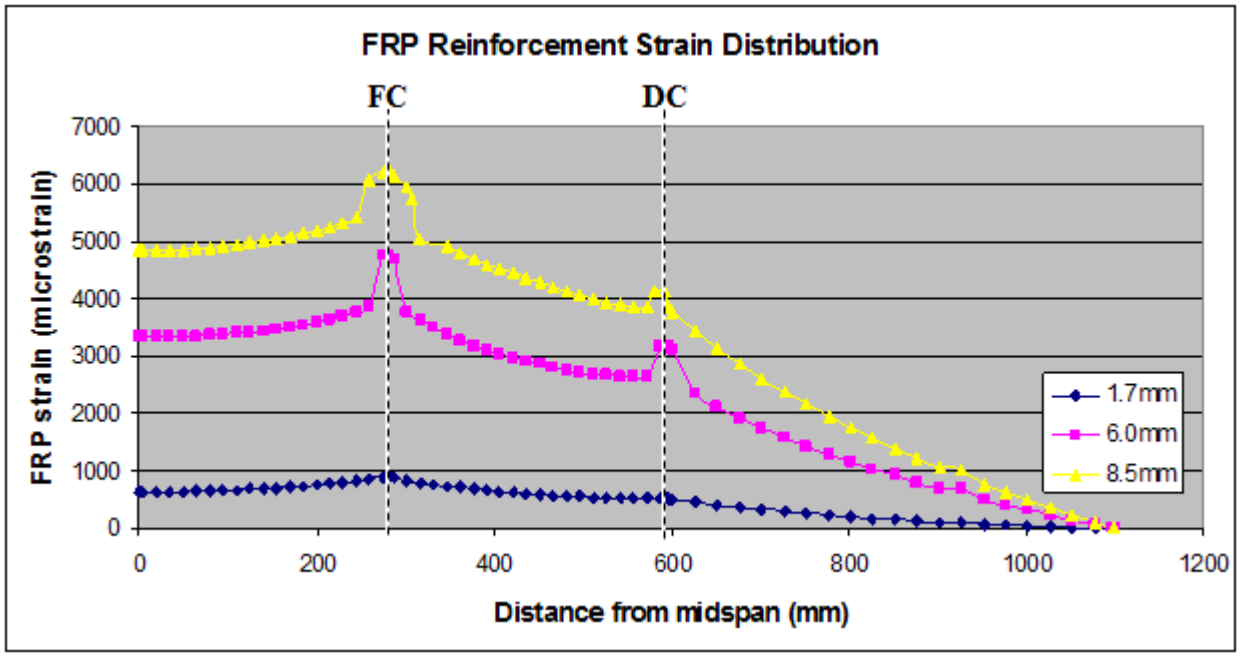

Figure A6.3: Development of FRP reinforcement strain for various deflection levels.

k_s^{int} **=50MPa/mm**

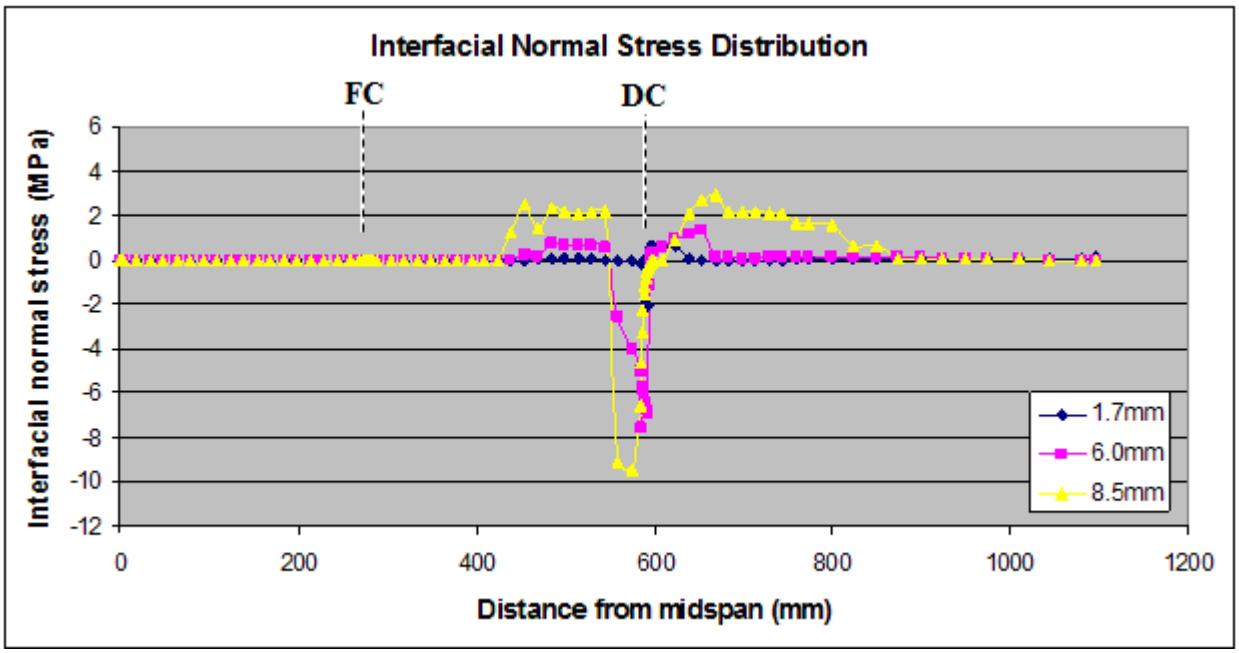

Figure A6.4: Development of interfacial normal stresses for various deflection levels.

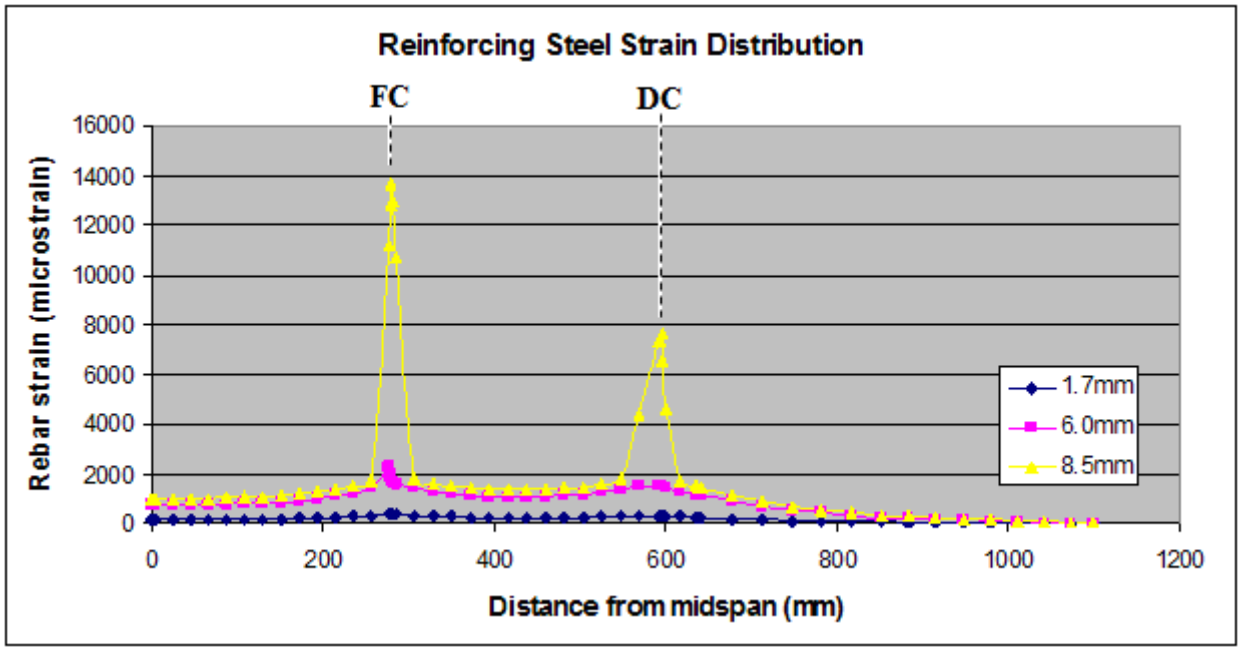

Figure A6.5: Development of steel reinforcement strain for various deflection levels.

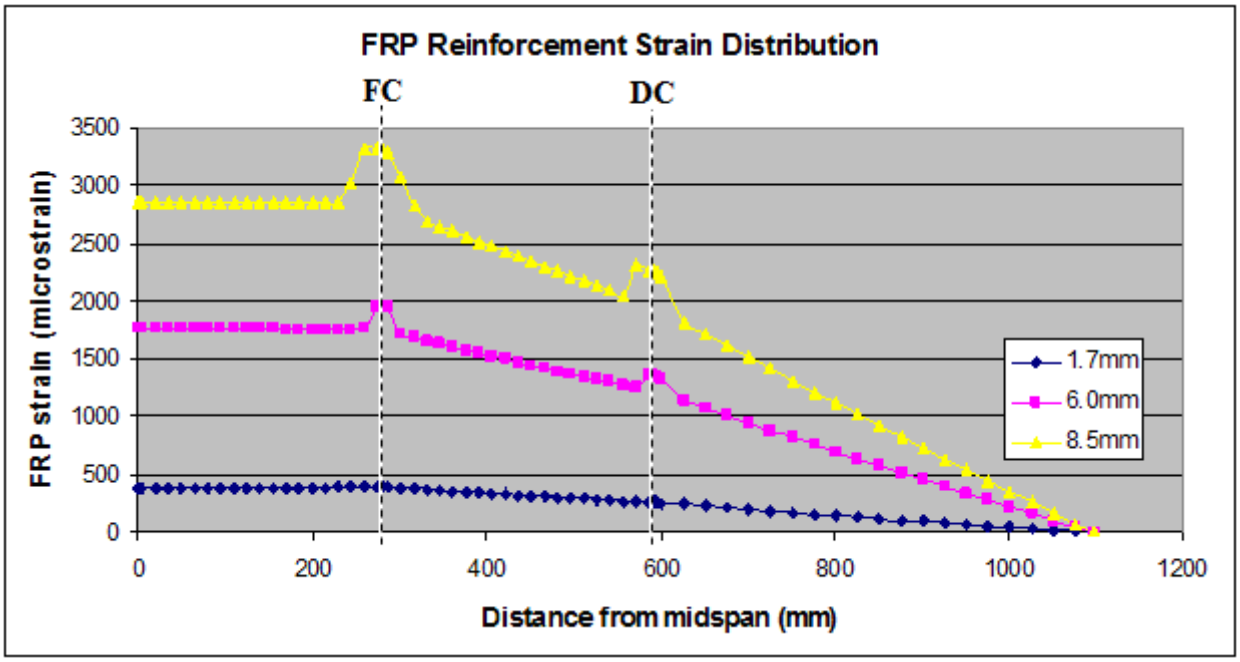

Figure A6.6: Development of FRP reinforcement strain for various deflection levels.

Local Bond Strength, τ_b=1.5MPa

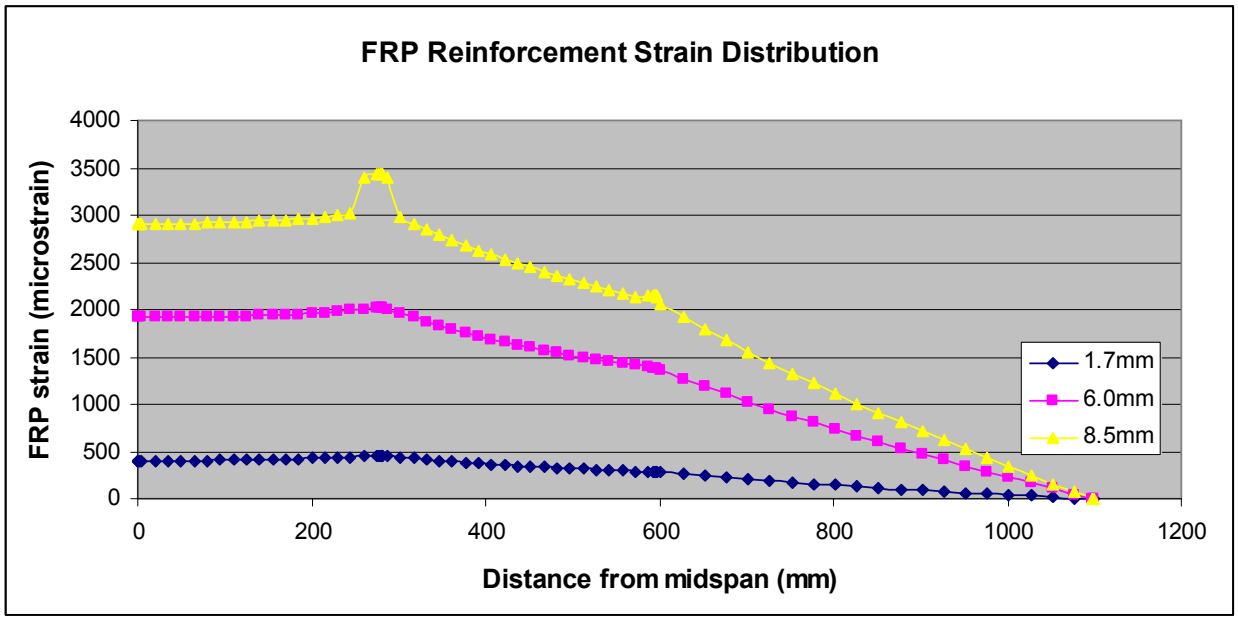

Figure A6.7: Development of FRP reinforcement strain for various deflection levels (τ_b=1.5MPa).

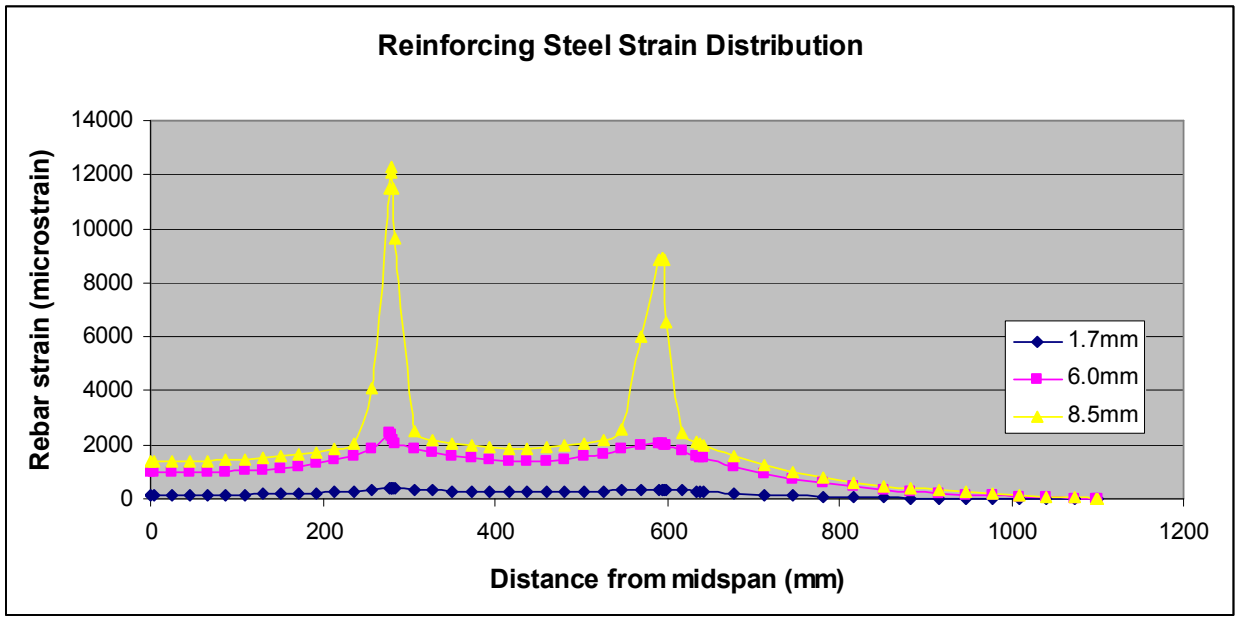

Figure A6.8: Development of reinforcing steel strain for various deflection levels (τ_b=1.5MPa).

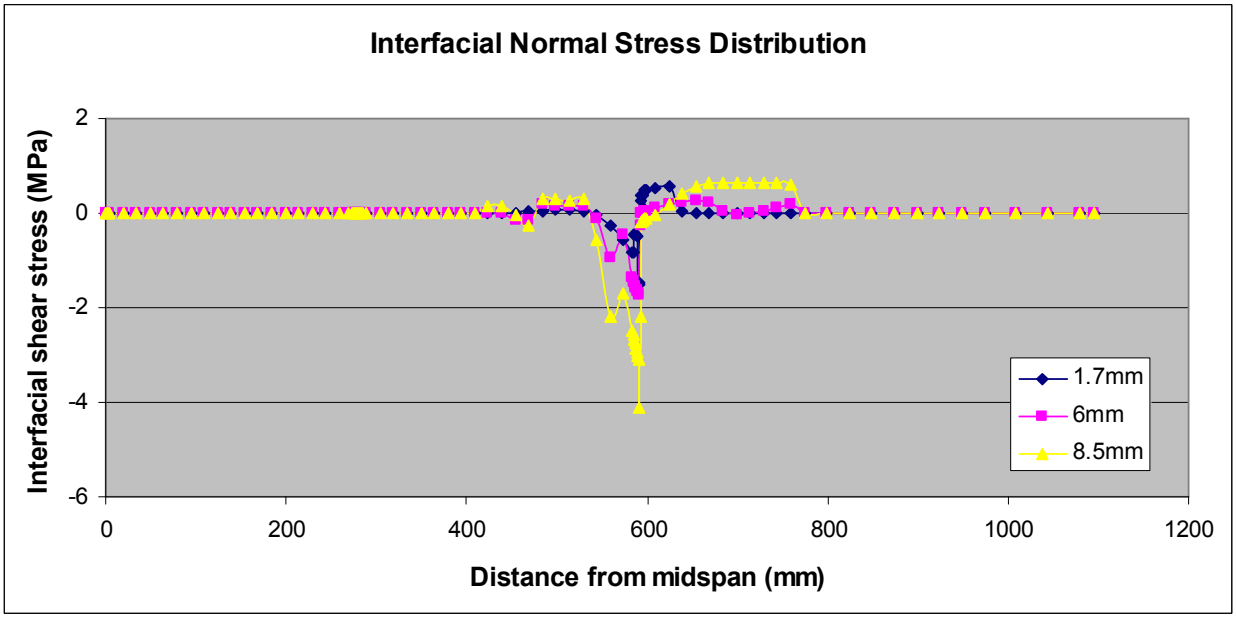

Figure A6.9: Development of interfacial normal stress for various deflection levels (τ_b=1.5MPa).

τ_b=10MPa

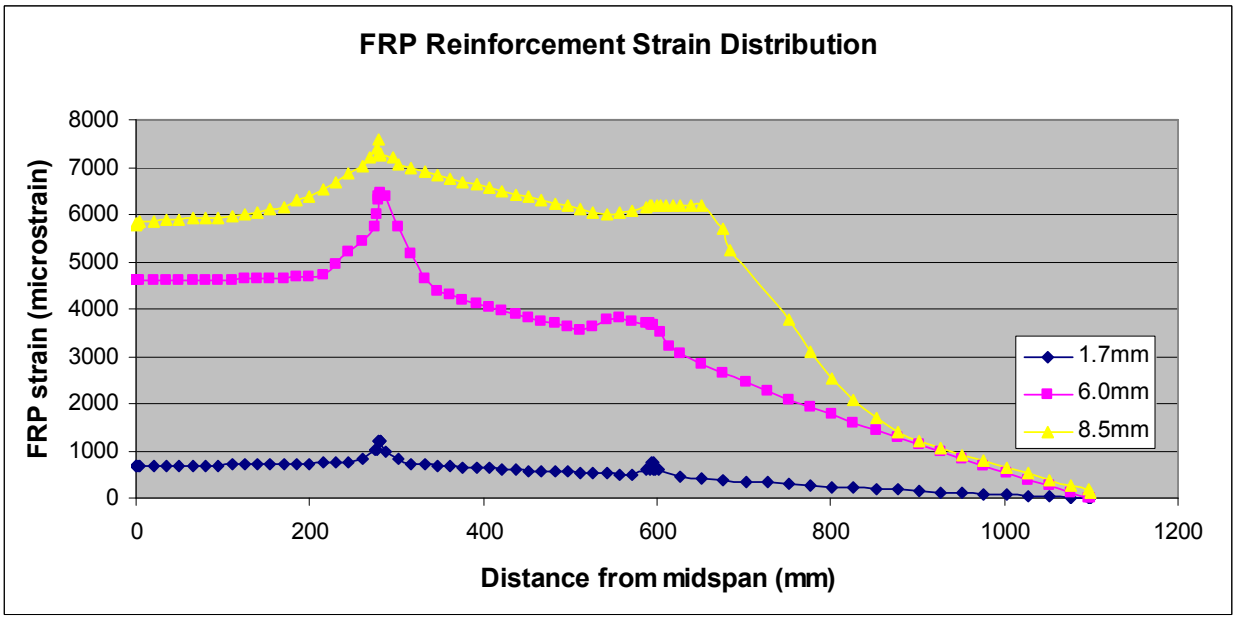

Figure A6.10: Development of FRP reinforcement strain for various deflection levels (τ_b=10MPa).

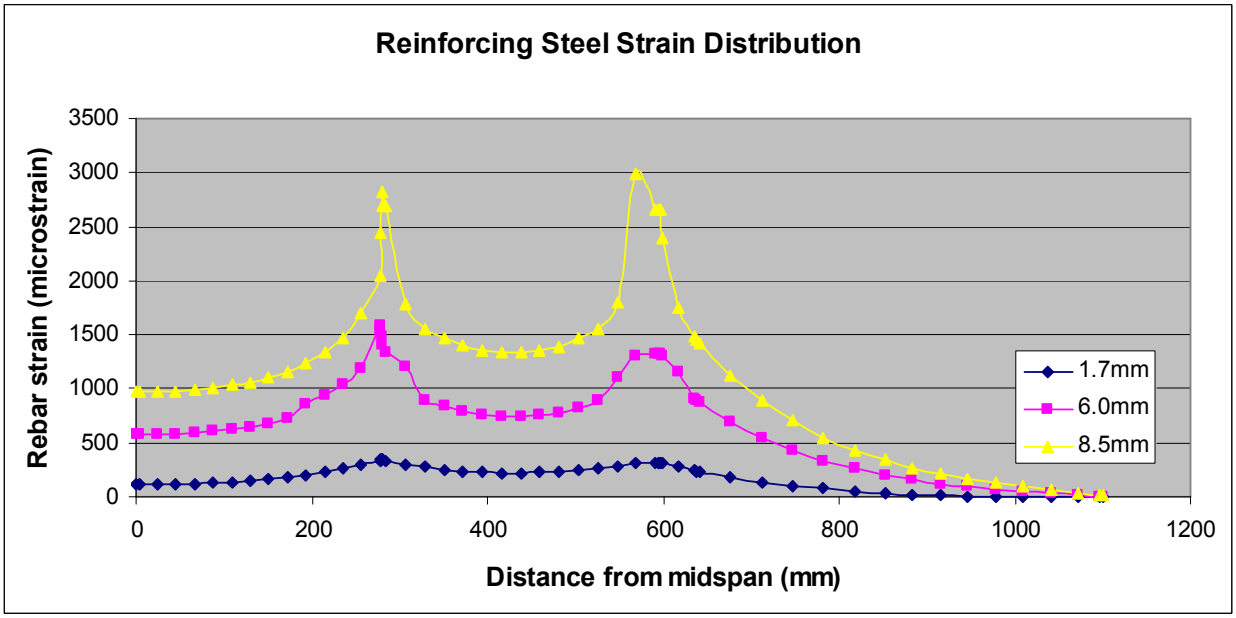

Figure A6.11: Development of reinforcing steel strain for various deflection levels (τ_b=10MPa).

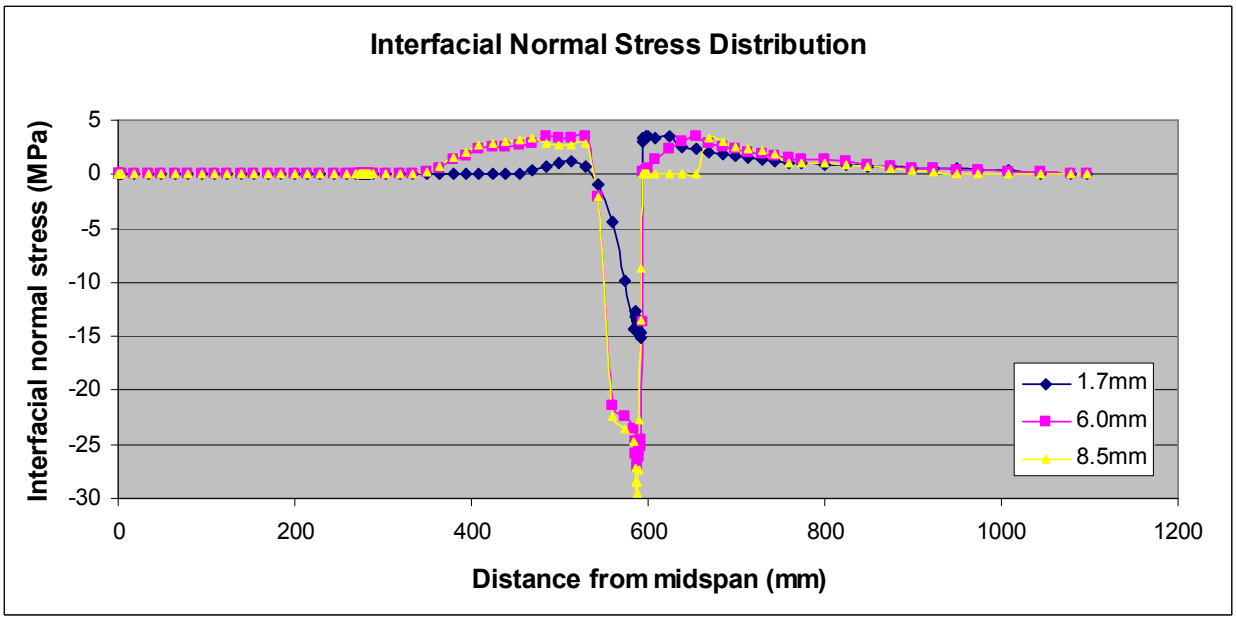

Figure A6.12: Development of interfacial normal stress for various deflection levels (τ_b=10MPa).

Interfacial Fracture Energy

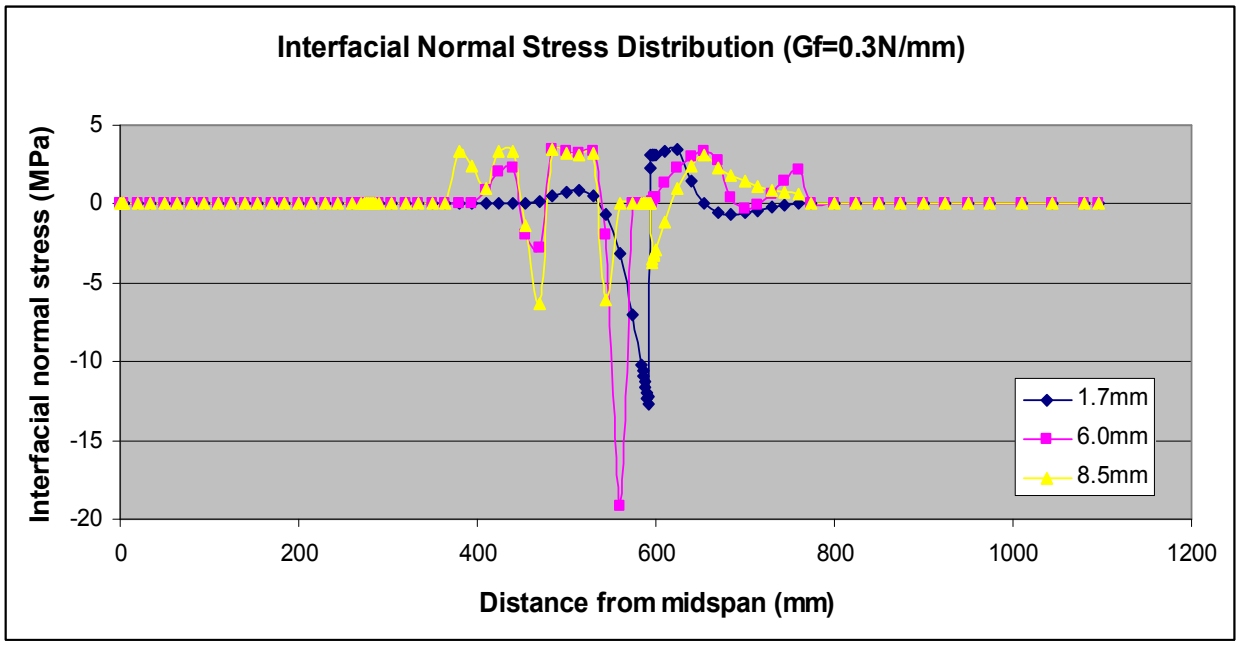

Figure A6.13: Development of interfacial normal stress for various deflection levels (G_f^{int}=0.3N/mm).

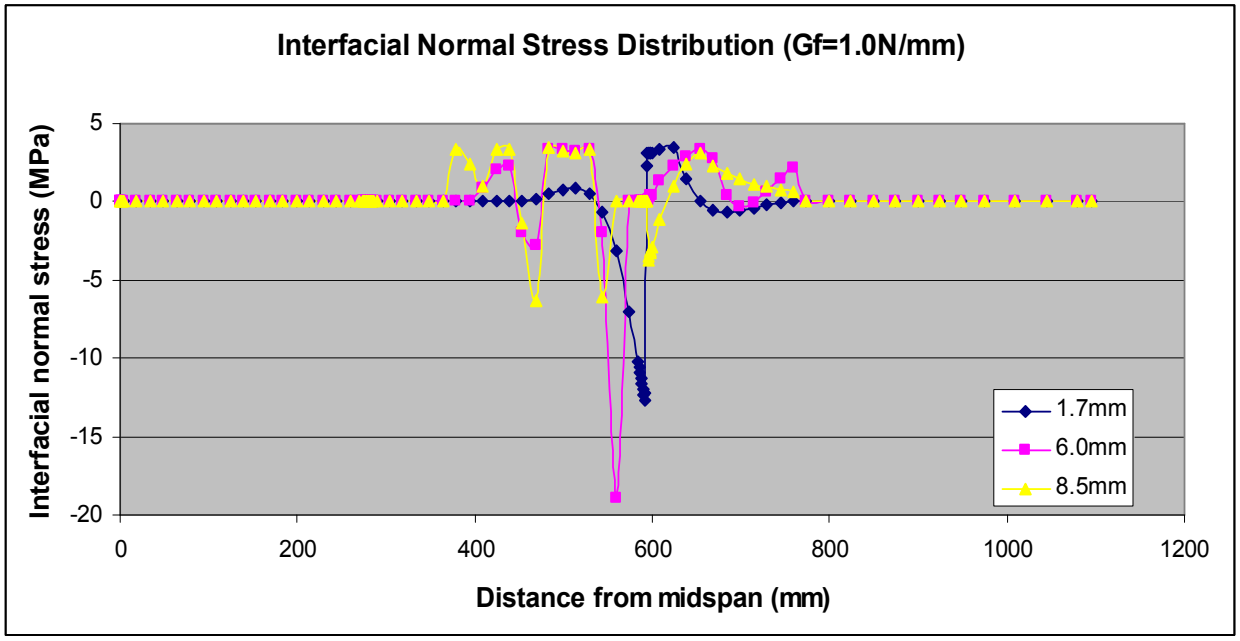

Figure A6.14: Development of interfacial normal stress for various deflection levels (G_f^{int}=1.0N/mm).

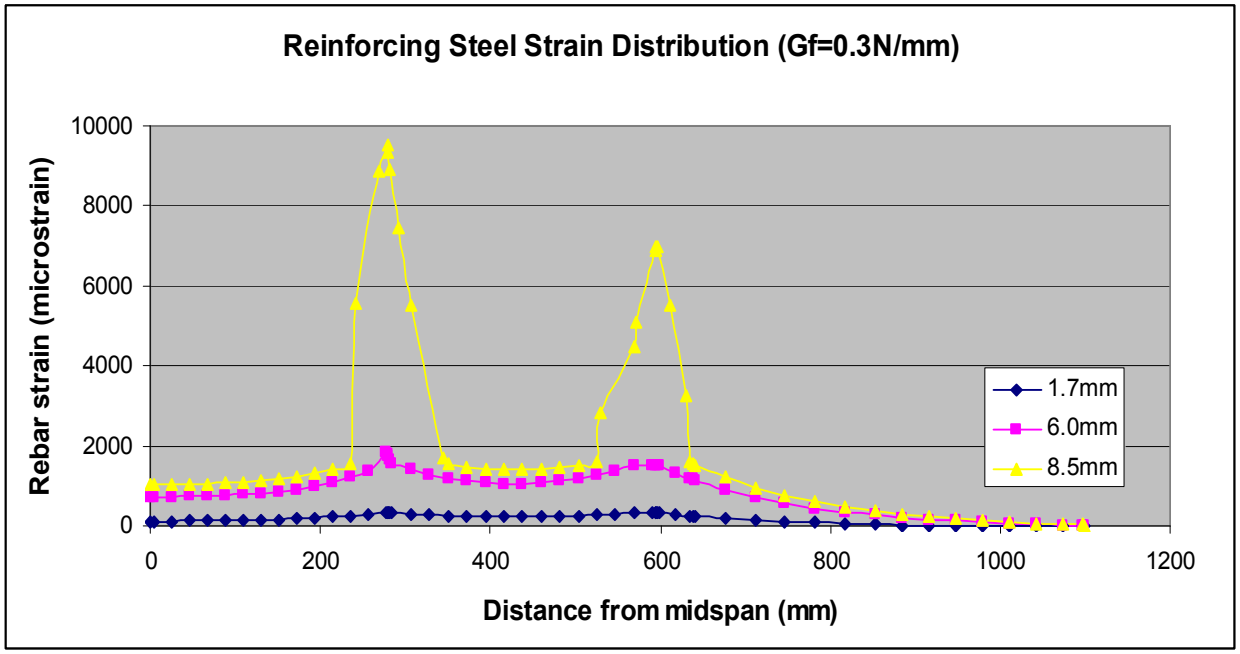

Figure A6.15: Development of reinforcing steel strain for various deflection levels (G_f^{int}=0.3N/mm).

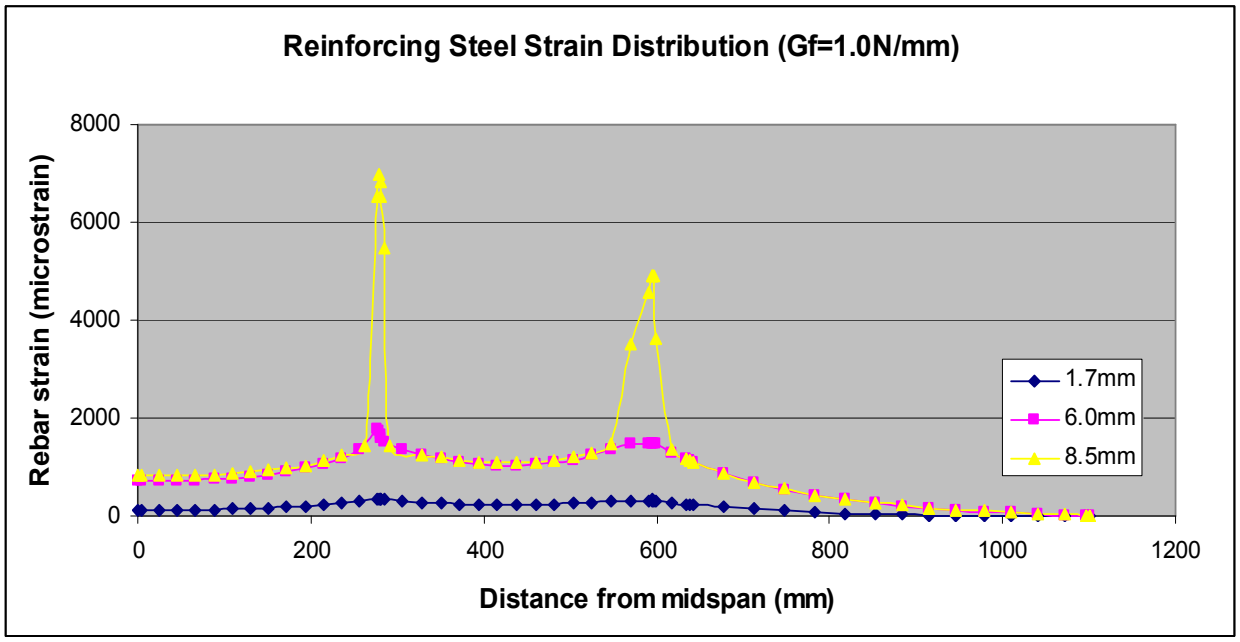

Figure A6.16: Development of reinforcing steel strain for various deflection levels (G_f^{int}=1.0N/mm).

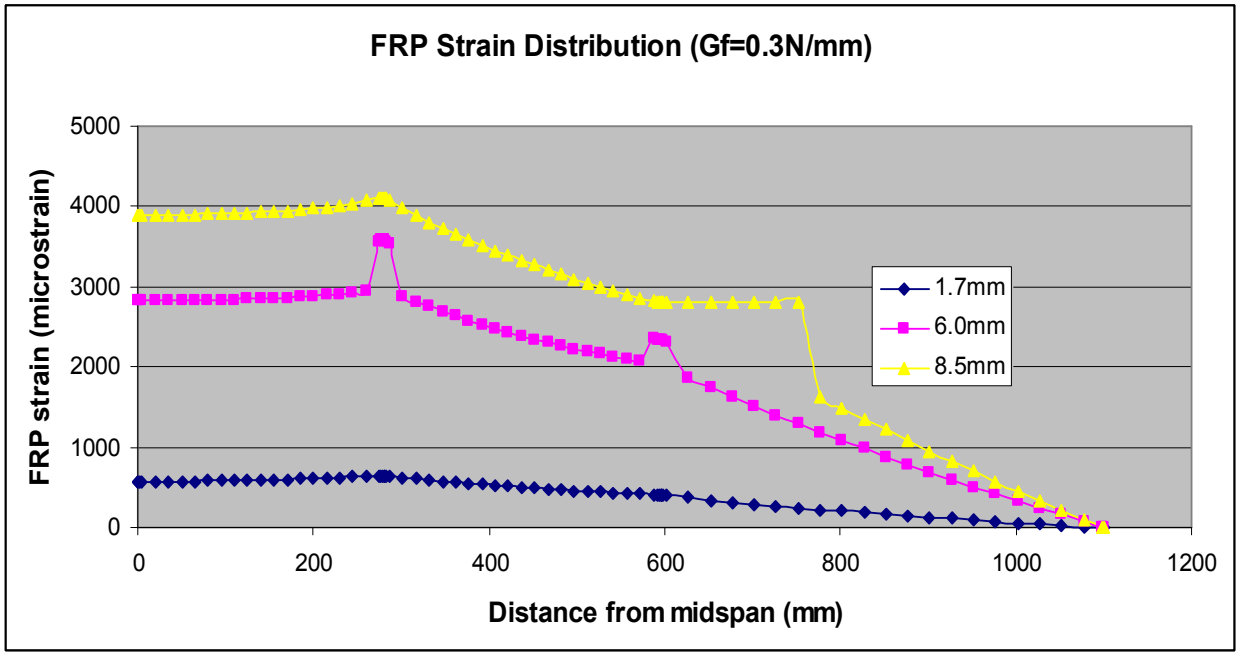

Figure A6.17: Development of FRP strain for various deflection levels (G_f^{int} =0.3N/mm).

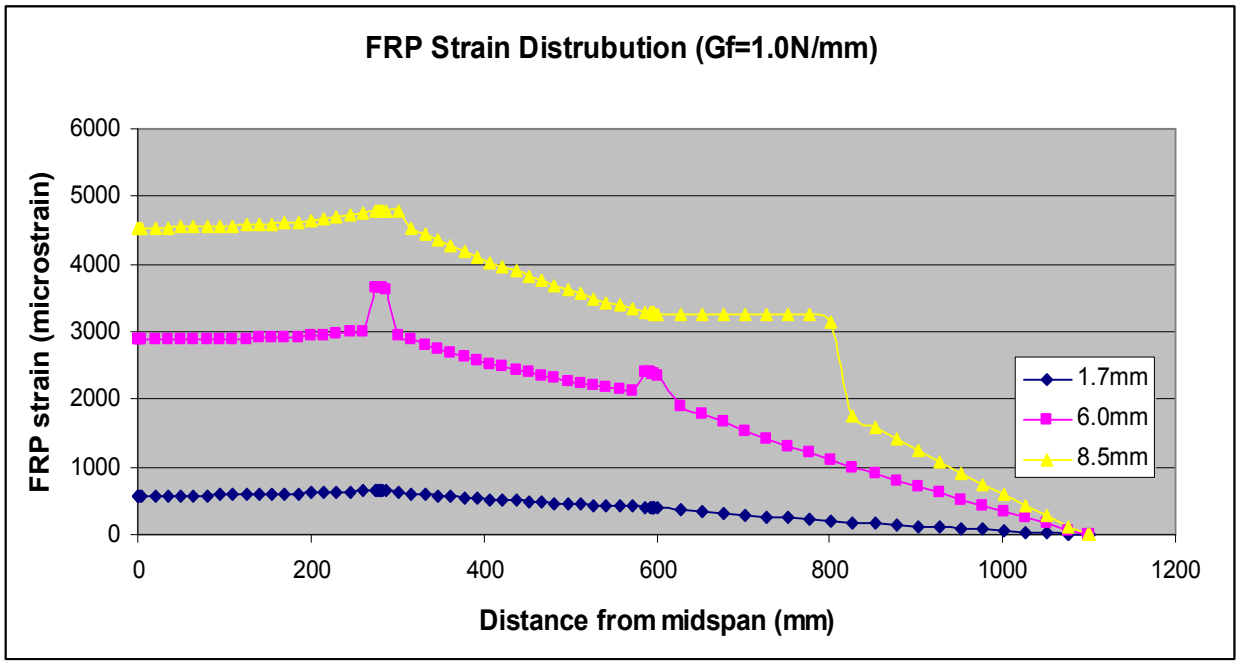

Figure A6.18: Development of FRP strain for various deflection levels (G_f^{int} =1.0N/mm).

Interfacial Normal Stiffness

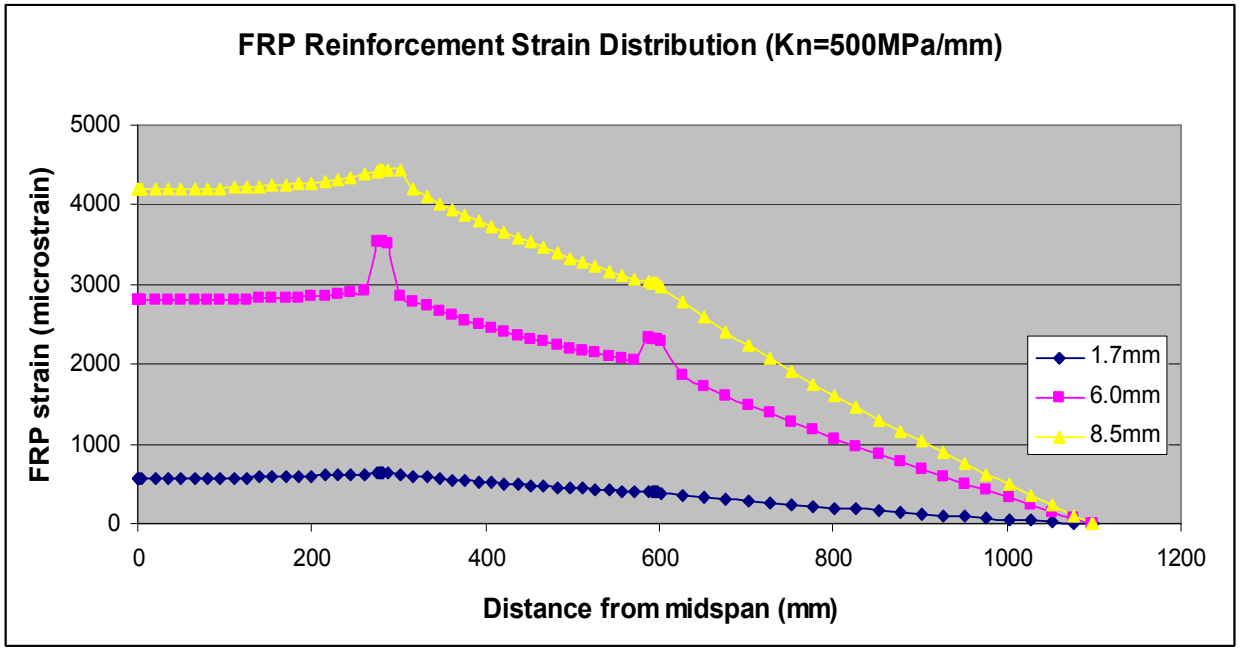

Figure A6.19: Development of FRP strain for various deflection levels (k_n^{int} =500N/mm).

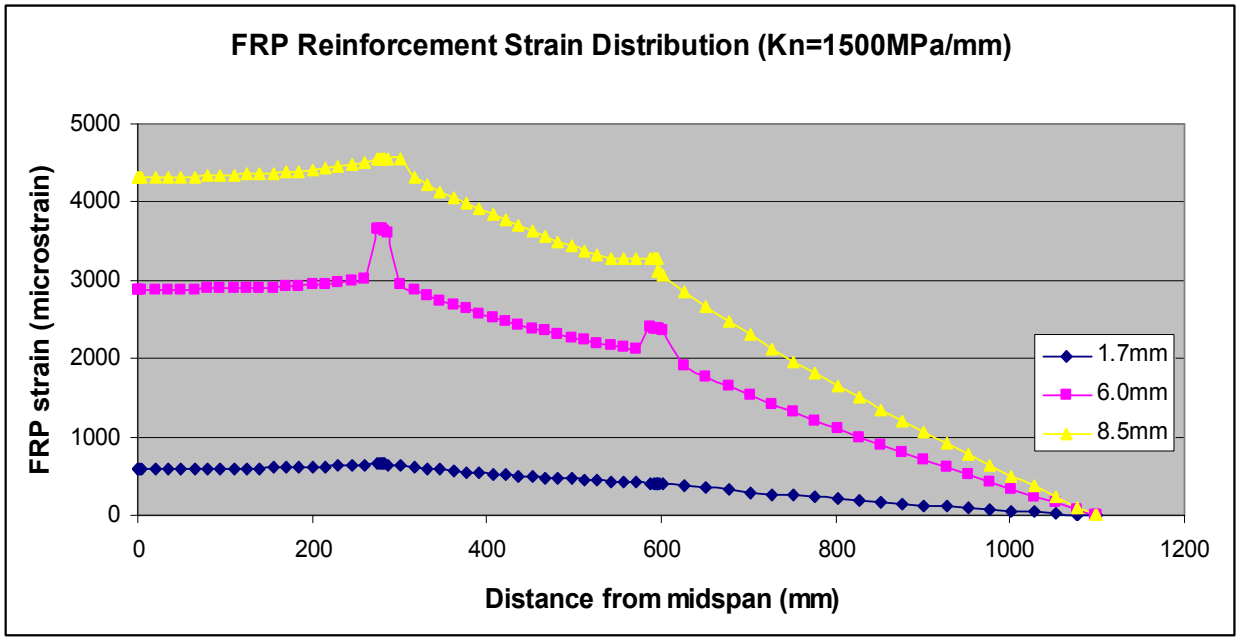

Figure A6.20: Development of FRP strain for various deflection levels (k_n^{int} =1500N/mm).

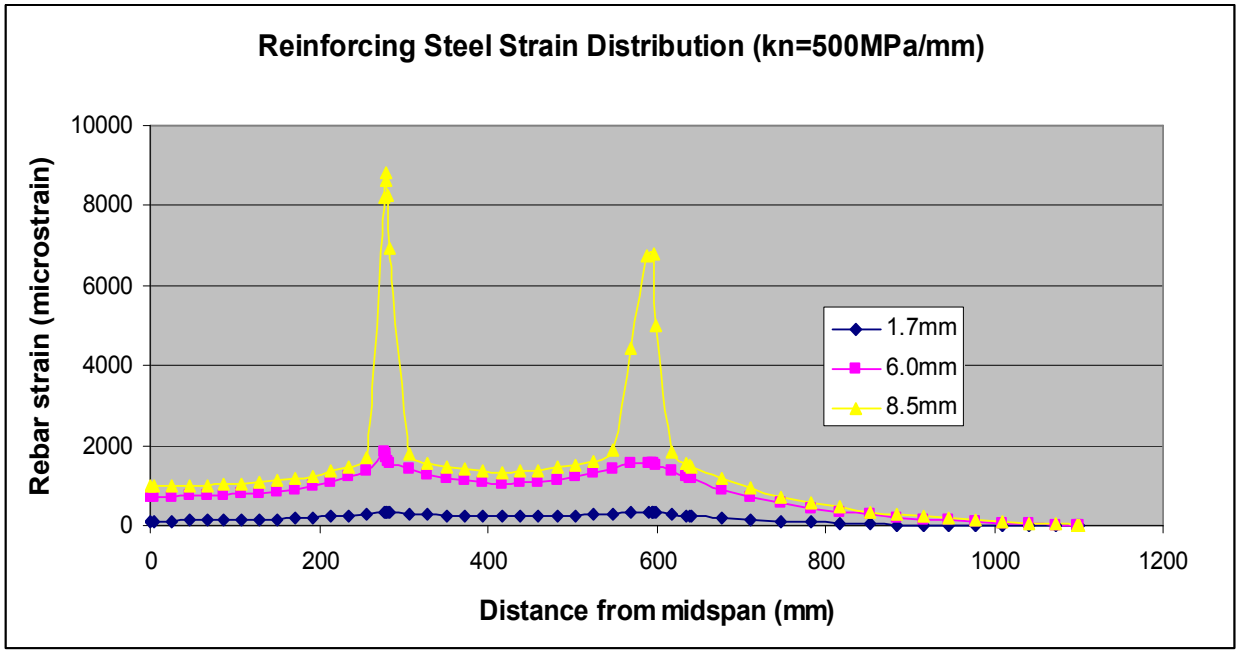

Figure A6.21: Development of reinforcing steel strain for various deflection levels (k_n^{int}=500N/mm).

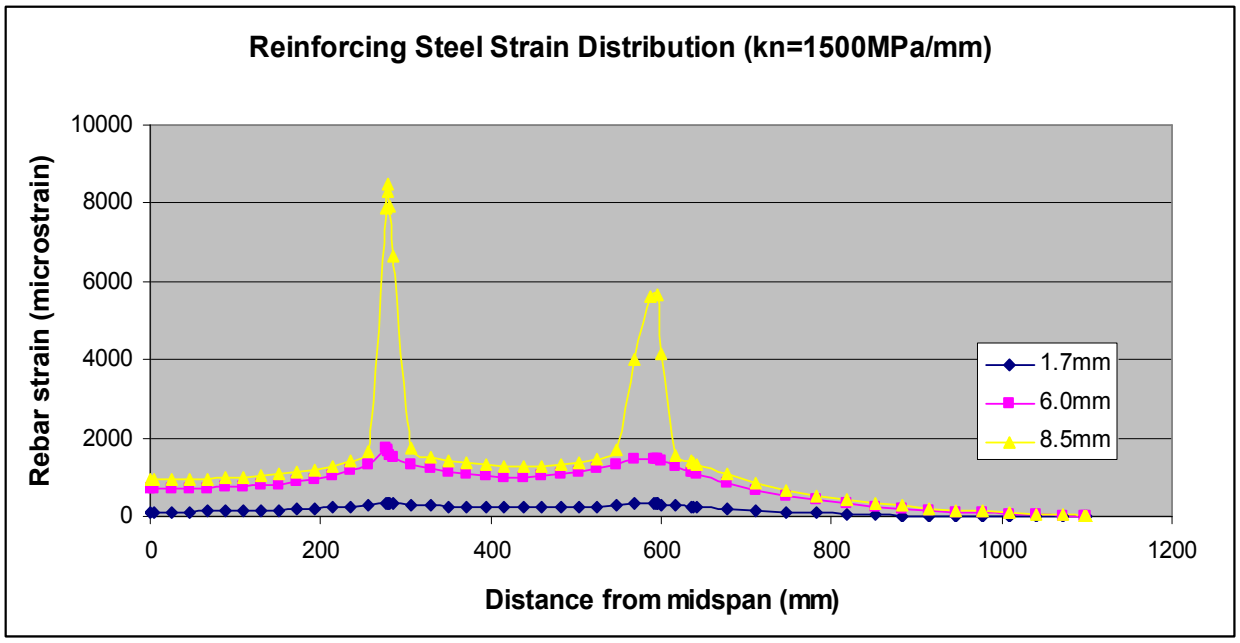

Figure A6.22: Development of reinforcing steel strain for various deflection levels (k_n^{int}=1500N/mm).